

MODEL DEVELOPMENT AND ANALYSIS OF SOLID ORAL DOSAGE
MANUFACTURING PROCESSES INVOLVING PARTICLE SIZE CHANGE

by

NIRUPAPLAVA METTA

A dissertation submitted to the

School of Graduate Studies

Rutgers, The State University of New Jersey

In partial fulfillment of the requirements

For the degree of

Doctor of Philosophy

Graduate Program in Chemical and Biochemical Engineering

Written under the direction of

Marianthi G. Ierapetritou,

Rohit Ramachandran

And approved by

New Brunswick, New Jersey

January, 2020

ABSTRACT OF THE DISSERTATION

Model development and analysis of solid oral dosage manufacturing processes involving
particle size change

By NIRUPAPLAVA METTA

Dissertation Director(s):

Marianthi G. Ierapetritou,

Rohit Ramachandran

Continuous pharmaceutical manufacturing offers advantages in cost, efficiency and acceleration in process development, particularly in the time of increasing research and development, and production costs. A science-based approach to process development promoted by the Quality by design paradigm requires incorporating the effect of variability in material properties and process conditions on product properties. This has increased focus on development of detailed and complex models capturing phenomenon from several scales, which led to an increase in computational expense. The limitations are exacerbated when several such models are integrated to simulate a continuous manufacturing process. This dissertation explores several modeling methods for the development of hybrid models of particulate processes. Milling operation is used as a case study for hybrid model development that supports the Quality by design approach and also addresses

computational limitations. Several unit operation models are integrated to simulate a wet granulation continuous manufacturing process leading to a computationally expensive model with several variables. This dissertation also establishes efficient methodologies to utilize the high dimensional and computationally expensive integrated process models for obtaining the space in which process needs to operate, thus supporting continuous pharmaceutical process development.

Acknowledgement

Working for this dissertation is the most rewarding and fulfilling journey I have taken, and several people have supported and cheered for me along the way. This acknowledgement is an expression of gratitude for their contribution.

First and foremost, I would like to express my sincere gratitude to my advisors Dr. Marianthi Ierapetritou and Dr. Rohit Ramachandran. Your mentorship, guidance and support both professionally and personally have driven me to keep going forward. Marianthi, thank you for believing in me. You have been an inspiration and a mentor to look up to. Rohit, thank you for your wisdom. You have taught valuable lessons that will remain with me. Working with you both has been a privilege.

I would also like to thank my committee members Dr. Dana Barrasso, Dr. Benjamin Glasser and Dr. Ravendra Singh for their insightful comments during the thesis proposal defense and dissertation defense. You have provided a perspective that led me to carefully evaluate my research and communicate it more effectively.

My research work is financially supported by FDA, National Science Foundation Engineering Research Center for Structured Organic Particulate Systems (ERC-SOPS) and a Consortium Agreement between Janssen Pharmaceutica, University of Ghent and Rutgers University. Through the collaborations, I am thankful for the valuable inputs I have received, and the several opportunities I had to present my work and strengthen my research and public speaking skills. I would also like to thank Dr. Sarang Oka for the internship opportunity at Hovione.

I am thankful for the camaraderie I have with several fellow graduate students at Rutgers. Dr. Zilong Wang, Dr. Lisia Dias, Atharv Bhosekar, Subhodh Karkala, Abhay Athaley, Pooja Bhalode and Indu Mutancheri, thank you for the good times and lending an ear when I needed to share my frustrations. I am fortunate to have known several people at Rutgers who contributed to making my time at Rutgers a memorable one. Thank you, Dr. Parham Farzan, Dr. Sebastian Escotet, Dr. Anik Chaturbedi, Dr. Ashu Tamarkar, Chaitanya Sampat, Ou Yang, Shashank Venkat Muddu, Yingjie Chen, Lalith Kotamarthy, Clara Hartmanshenn, Isabel Liberis and Alaina Howe.

I cannot imagine this taking this ride without all the fun, support and good times from friends and family. My friends for life, Ramya, Samyuktha and Renuka, thank you for always being with me in spirit. Ram, Abrar, Safa, Anusha, Vishwas, Veena, Naren, thank you for all the laughs, board game nights, holiday trips and being my family away from home. Neeraj and Sayali, thank you for cheering me on at every turn. The countless dinners, coffees, snow days and UNOs pizzas we have shared made difficult times tolerable and good times great.

I would like to express my heartfelt gratitude to my mother-in-law for the support especially during the final stages of my research work. I would not have been able to drive my work towards completion without the support and encouragement from her. Undeniably, I would not have had the conviction to pursue a PhD without the upbringing and confidence instilled in me by my parents and sister. Amma, I cannot thank you enough for your perseverance and inspiring me to always give my best. A special thank you to my baby girl, Arya, who teaches me every day and drives me to be better. Last but not the least, I would like to acknowledge the role of my love Anveshan, who has known me for the better part of my life and has a role in making me who I am. Anveshan, for being my best friend, greatest critic and champion, thank you.

Table of Contents

ABSTRACT OF THE DISSERTATION.....	ii
Acknowledgement.....	iv
List of Tables	x
List of Figures.....	xii
Chapter 1 Introduction.....	1
1.1 Continuous solid oral dosage manufacturing	1
1.2 Quality by design framework.....	3
1.3 Outline of the dissertation	6
Chapter 2 Literature review	8
2.1 Milling.....	8
2.1.1 Types of mill and granule characterization.....	9
2.1.2 Models for milling	13
2.2 Unit operations and integrated process models.....	16
2.2.1 Integrated process models.....	30
2.3 Design space of pharmaceutical processes.....	35
Chapter 3 Multi-scale model development of a continuous comilling process	38
3.1 Background	38
3.2 Modeling methods.....	39
3.2.1 Multiscale modeling framework	39
3.2.2 Population balance model (PBM).....	40
3.2.3 Discrete element method model.....	42
3.3 PBM-DEM framework.....	46

3.3.1	Energy based kernel	46
3.3.2	Sensitivity analysis.....	50
3.4	Qualitative comparison with experiments.....	53
3.5	Case studies.....	59
3.6	Summary	68
Chapter 4	A computationally efficient surrogate-based reduction of multi-scale comill process model	70
4.1	Background	70
4.2	Modeling methods.....	71
4.2.1	Discrete element method model.....	71
4.2.2	Population balance model.....	73
4.2.3	Surrogate model.....	75
4.2.4	Hybrid model framework.....	80
4.2.5	Model integration.....	83
4.3	Case studies and model integration.....	86
4.3.1	Case study with fixed flow rate simulations	86
4.3.2	Case study with fixed impeller speed simulations	91
4.3.3	Implementation in integrated process modeling	93
4.4	Comparison between kriging and ANN surrogate models.....	101
4.5	Summary	102
Chapter 5	Hybrid model development for prediction of milled granule quality attributes	
	104	
5.1	Background	104
5.2	Experiments.....	105

5.2.1	Design of Experiments.....	105
5.2.2	Test Methods.....	108
5.3	Modeling methods.....	109
5.3.1	Population balance model.....	109
5.3.2	Partial least squares model.....	115
5.4	Results and discussion.....	116
5.4.1	Experimental results.....	116
5.4.2	PBM calibration and validation	123
5.5	Summary	130
Chapter 6 Integrated model development and analysis of wet granulation continuous pharmaceutical tablet manufacturing process		132
6.1	Background	132
6.2	Model development and analysis	134
6.2.1	Flowsheet Modeling.....	135
6.2.2	Scenario Analysis.....	155
6.2.3	Sensitivity Analysis	158
6.3	Simulation results.....	162
6.4	Case studies.....	173
6.4.1	Step change in feeder flow rate.....	173
6.4.2	Step change in dryer air temperature	179
6.5	Scenario analysis of the integrated model.....	183
6.6	Sensitivity analysis of the integrated model.....	188
6.7	Summary	197

Chapter 7	Design space identification of continuous pharmaceutical manufacturing processes	200
7.1	Background	200
7.2	Feasibility analysis methodology	202
7.2.1	Kriging based feasibility analysis	204
7.2.2	Artificial neural networks based feasibility analysis	206
7.3	Test problems	211
7.3.1	Two dimensional test problems	217
7.3.2	Higher dimensional test problems.....	229
7.4	Design space of a continuous direct compaction process	234
7.4.1	Unit process models.....	235
7.4.2	Feasibility problem for the continuous direct compaction process.....	237
7.5	Design space of a continuous wet granulation process	240
7.5.1	Unit process models.....	241
7.5.2	Feasibility problem for the continuous wet granulation process.....	244
7.6	Summary	247
Chapter 8	Conclusions and future work.....	249
	Acknowledgement of prior publications.....	253
	Bibliography.....	255

List of Tables

Table 2.1 Mills classified on the basis of milled particle size [29] -----	10
Table 3.1 Range for model parameters used for sensitivity analysis -----	52
Table 3.2 Formulation components and percentages -----	54
Table 3.3 Batch Granulation settings -----	55
Table 3.4 Particle size distribution of the feed used in the DEM simulations -----	57
Table 3.5 Parameters of PBM used to generate milling data -----	62
Table 3.6 Iterations for case study 1 showing convergence to targeted E_{const} and f_{mat} values with starting guess values for $E_{const} = 0.002 \text{ J m/kg}$ -----	65
Table 3.7 Iterations for case study 2 showing convergence to targeted E_{const} and f_{mat} values with starting guess values for $E_{const} = 0.001 \text{ J m/kg}$ -----	66
Table 4.1 Details on DEM simulation parameters and runs for two case studies -----	73
Table 4.2 Parameters used in PBM -----	75
Table 4.3 Parameters used in the tablet press model -----	84
Table 4.4 Maximum and minimum absolute percentage errors for specific energy and collision frequency surrogate models for case study 1, validation: 850 rpm and case study 2, validation: 3.25 kg/h -----	90
Table 4.5 Metrics to compare performance of Kriging, ANN and constant kernel based particle size distribution and holdup predictions for case study 1, validation: 850rpm and case study 2, validation: 3.25 kg/h -----	91
Table 4.6 Kriging model parameters for case study 1 -----	95
Table 4.7 Kriging model parameters for case study 2 -----	95
Table 4.8 ANN model parameters for case study 1 -----	97
Table 4.9 ANN model parameters for case study 2 -----	98

Table 5.1 Overview of different milling experiments conducted in this study -----	108
Table 5.2 List of parameters in the PBM -----	113
Table 5.3 Overview of experiments used for the external validation of the empirical PLS models -----	116
Table 5.4 List of estimated parameter values in PBM using experimental data from RMC 1.4% and 6.4% granule feed, Experiment IDs G and H -----	124
Table 5.5 Statistical significance of parameters estimated in the PBM, using data from Experiment ID I-----	130
Table 6.1 Formulation used for model development -----	135
Table 6.2 Process setting ranges of validated twin-screw granulator model [191]-----	140
Table 6.3 State of unit models used in flowsheet model development-----	155
Table 6.4 Factors and responses for scenario analysis and sensitivity analysis -----	158
Table 6.5 Values of process variables used for simulating the flowsheet model-----	163
Table 6.6 Morris method sensitivity analysis results -----	190
Table 7.1 Two-dimensional test problems with variable bounds and constraints -----	212
Table 7.2 Standard high dimensional test problems with variable bounds and constraints-----	216
Table 7.3 Surrogate model accuracy metrics for two-dimensional test problems-----	218
Table 7.4 Surrogate model accuracy metrics for high dimensional test problems -----	231
Table 7.5 Variable bounds for the continuous direct compaction process feasibility case study	239
Table 7.6 Constraints for the continuous direct compaction process feasibility case study -----	239
Table 7.7 Variable bounds for the continuous wet granulation process feasibility case study---	246
Table 7.8 Constraints for the continuous wet granulation process feasibility case study -----	246

List of Figures

Figure 1.1 Schematic showing major drug-product manufacturing routes [16] -----	3
Figure 2.1 Schematic showing the flow of information in a generic flowsheet model -----	31
Figure 2.2 Schematic of an integrated flowsheet model for direct compaction, dry granulation and wet granulation routes of pharmaceutical manufacturing -----	33
Figure 2.3 Schematic of an integrated model developed in gPROMS™ -----	34
Figure 3.1 PBM-DEM framework for modeling continuous comill process -----	40
Figure 3.2 Geometry of the comill used in DEM simulations-----	43
Figure 3.3 Modeling breakage in DEM using particle replacement-----	45
Figure 3.4 Breakage model implementation in EDEM API [129]-----	46
Figure 3.5 PBM-DEM framework-----	51
Figure 3.6 Total sensitivity index plot with energy data from DEM simulations with $E_{const} = 0.03$ J m/kg and impeller speeds of 1750 rpm and 2500 rpm-----	53
Figure 3.7 Particle size distribution of feed and milled granules (at 90 s 300 s) for Batch 1 (high strength, solid lines) and Batch 2 (low strength, dashed lines)-----	55
Figure 3.8 Geometry used in the DEM simulations-----	57
Figure 3.9 Prediction of evolution of particle size distribution from the DEM-PBM framework, High threshold energy 0.8 J m/kg-----	58
Figure 3.10 Prediction of evolution of particle size distribution from the DEM-PBM framework, Low threshold energy 0.6 J m/kg -----	58
Figure 3.11 Workflow used in Case study 1 and 2 to demonstrate the algorithm-----	61
Figure 3.12 Particle size distributions of milled product at steady state -----	62
Figure 3.13 Snapshot of DEM simulation showing particles of different sizes inside and exiting the mill-----	64

Figure 3.14 Collision and mass specific energy of 1 mm particles from DEM simulations for case study 1 and 2 at various Econst values and impeller speeds 1750, 2500 rpm-----	65
Figure 3.15 Comparison of experimental and predicted milled particle size distribution at 1000 rpm from Econst = 0.025 J m/kg and fmat = 0.14 kg/J m -----	67
Figure 4.1 Schematic of an artificial neural network example -----	80
Figure 4.2 Schematic for the hybrid model framework -----	82
Figure 4.3 Schematic of the integrated mill and tablet press model developed in gPROMS™----	86
Figure 4.4 Percentage error surface plots for Energy and Collision surrogate models from Kriging (first row) and ANN (second row) for case study 1, Validation: 850 rpm -----	89
Figure 4.5 Comparison of PSD and holdup plots, DEM Vs SM Vs Constant kernel for case study 1, Validation: 850 rpm. Kriging based surrogate (First row) and ANN based surrogate (second row).-----	90
Figure 4.6 Percentage error surface plots for Energy and Collision surrogate models from Kriging (first row) and ANN (second row) for case study 2, Validation: 3.25 kg/h -----	92
Figure 4.7 Comparison of PSD and holdup plots, DEM Vs SM Vs Constant kernel for case study 2, Validation: 3.25 kg/h. Kriging based surrogate (First row) and ANN based surrogate (second row).-----	93
Figure 4.8 Comparison of evolution of milled product percentile diameters predictions from gPROMS and MATLAB, 850 rpm -----	99
Figure 4.9 Profile of milled granule bulk density evolution with time from SM-PBM framework -----	100
Figure 4.10 Profiles tablet hardness (left axis) and tablet weight (right axis) evolution with time from SM-PBM framework-----	100
Figure 5.1 Modeling framework to predict milling product CQAs-----	116

Figure 5.2 Particle size distributions of material prior to and after milling at different impeller speeds for oven-dried granules with, prior to milling, a friability of a) 19.19% b) 9.90% and c) 4.00%-----	118
Figure 5.3 Particle size distributions of material prior to and after milling at different impeller speeds, for oven-dried granules with a friability of 9.90% on the first row (1) and 4.00% on the second row (2), classified in size fractions prior to milling of < 1000 μm (a), 1000-2000 μm (b) and >2000 μm (c).-----	119
Figure 5.4 Particle size distributions of material prior to and after milling at different impeller speeds, for fluid bed dried granules after a fluid bed drying time of 400 μm (a), 600 μm (b) and 800 μm (c).-----	121
Figure 5.5 Particle size distributions of material after milling at different impeller speeds, for air dried granules with an RMC of 6.43% (a) and 1.41% (b).-----	122
Figure 5.6 Comparison of predicted and experimental milled product PSD at (a) 500 rpm, (b) 1000 rpm and (c) 1500 rpm, granule feed RMC 1.4% -----	126
Figure 5.7 Comparison of predicted and experimental milled product PSD at (a) 500 rpm, (b) 1000 rpm and (c) 1500 rpm, granule feed RMC 6.4% -----	127
Figure 5.8 Comparison of predicted and measured D10, D50 and D90 of milled product at various impeller speeds (a) Feed RMC 1.4% (b) Feed RMC 6.4% -----	128
Figure 5.9 Comparison of predicted and measured D10, D50 and D90 of milled product at various impeller speeds. Red color refers to validation impeller speed of 900 rpm -----	129
Figure 5.10 Comparison of predicted and measured milling times at various impeller speeds. Red color refers to validation impeller speed of 900 rpm -----	129
Figure 6.1 Schematic showing transfer of information between units required for flowsheet model development-----	136

Figure 6.2 Schematic showing interaction between units and various modeling approaches ----	153
Figure 6.3 gPROMS Formulated Products schematic of the full flowsheet model developed---	154
Figure 6.4 Schematic of the flowsheet model used for scenario analysis and sensitivity analysis -----	157
Figure 6.5 (a) Component feeder fill levels (b) Component feeder flow rates (c) Powder blend feeder and granule feeder fill levels and flow rates -----	165
Figure 6.6 (a) Granulator flow rate, mass of granules from the dryer and holdup in mill (b) Moisture content of wet and dry granules -----	166
Figure 6.7 Profiles of milled granules (a) bulk density, tapped density and true density (b) LOD, span and API concentration-----	168
Figure 6.8 Profiles of (a) bulk density, tapped density and true density (b) LOD, span and API concentration of granules from the granule feeder. -----	170
Figure 6.9 Profiles of (a) bulk density, tapped density and true density (b) LOD, span and API concentration of granules entering and leaving the feed frame.-----	171
Figure 6.10 Profiles of (a) tablet hardness, weight and potency (b) tablet press fill depth and main compression height-----	172
Figure 6.11 Step change in API 2 feeder flow rate setpoint showing an effect on the feeder flow rate -----	175
Figure 6.12 Comparison of API concentration profiles from simulations with fixed and step change in API 2 feeder flow rate setpoint for (a) blender and powder blend feeder (b) granulator and dryer (c) mill and granule feeder (d) granule blender and feed frame. -----	178
Figure 6.13 Comparison of tablet potency profiles from simulations with fixed and step change in API 2 feeder flow rate -----	179

Figure 6.14 Comparison of dried granule moisture content profiles from simulations with fixed and step change in dryer air temperature -----	181
Figure 6.15 Comparison of moisture content of granules entering and leaving the feed frame from simulations with fixed and step change in dryer air temperature -----	182
Figure 6.16 Comparison of tablet hardness profiles from simulations with fixed and step change in dryer air temperature-----	183
Figure 6.17 Scenario analysis plots for (a) wet granule d50 (b) dry granule d50 (c) dry granule LOD (d) tablet hardness -----	188
Figure 6.18 Total sensitivity index STi plots for (a) Granulator (b) Dryer (c) Mill (d) Tablet press (e) Blender-----	197
Figure 7.1 Schematic of a three-layer Artificial Neural Network-----	207
Figure 7.2 Algorithm for ANN and Kriging based feasibility analysis methodology -----	210
Figure 7.3 Illustration of surrogate model accuracy validation metrics-----	211
Figure 7.4 True feasible region boundaries of the test problems (a) branincon (b) camelback (c) sasenacon (d) ex3-----	214
Figure 7.5 High dimensional test problems formulated (a) 4Dcomp (b) 6Dcomp -----	217
Figure 7.6 Visual comparison of the original model and surrogate model feasible region boundaries (a) ANN for branincon (b) Kriging for branincon (Initial samples are represented with dots and adaptive samples are represented with red circles. True feasible region boundary is represented as black dashed line and feasible region boundary predicted by the surrogate model is represented as red line) -----	219
Figure 7.7 Visual comparison of the original model and surrogate model feasible region boundaries (a) ANN for ex3 (b) Kriging for ex3 (Initial samples are represented with dots and adaptive samples	

are represented with red circles. True feasible region boundary is represented as black dashed line and feasible region boundary predicted by the surrogate model is represented as red line) -----220

Figure 7.8 Visual comparison of the original model and surrogate model feasible region boundaries

(a) ANN for camelback (b) Kriging for camelback (Initial samples are represented with dots and adaptive samples are represented with red circles. True feasible region boundary is represented as black dashed line and feasible region boundary predicted by the surrogate model is represented as red line) -----221

Figure 7.9 Visual comparison of the original model and surrogate model feasible region boundaries

(a) ANN for sasenacon (b) Kriging for sasenacon (Initial samples are represented with dots and adaptive samples are represented with red circles. True feasible region boundary is represented as black dashed line and feasible region boundary predicted by the surrogate model is represented as red line) -----223

Figure 7.10 Comparison of ANN and Kriging model accuracy metrics for different levels of initial samples (a) branincon (b) camelback (c) sasenacon (d) ex3-----226

Figure 7.11 Comparison of number of adaptive samples required by ANN and Kriging based methodologies for different levels of initial samples -----227

Figure 7.12 Comparison of ANN and Kriging model accuracy validation metrics by number of adaptive samples for branincon (a) CF% (b) CIF% (c) NC% -----228

Figure 7.13 Comparison of ANN and Kriging model accuracy validation metrics by number of adaptive samples for camelback (a) CF% (b) CIF% (c) NC% -----229

Figure 7.14 Comparison of ANN and Kriging model accuracy validation metrics by number of adaptive samples for sasenacon (a) CF% (b) CIF% (c) NC%-----229

Figure 7.15 Comparison of ANN and Kriging model accuracy validation metrics by number of adaptive samples for ex3 (a) CF% (b) CIF% (C) NC% -----229

Figure 7.16 Comparison of ANN and Kriging model accuracy validation metrics by number of adaptive samples for qcp4con (a) CF% (b) CIF% (C) NC% -----232

Figure 7.17 Comparison of ANN and Kriging model accuracy validation metrics by number of adaptive samples for 4Dcomp (a) CF% (b) CIF% (C) NC% -----233

Figure 7.18 Comparison of ANN and Kriging model accuracy validation metrics by number of adaptive samples for g4con (a) CF% (b) CIF% (C) NC% -----233

Figure 7.19 Comparison of ANN and Kriging model accuracy validation metrics by number of adaptive samples for 6Dcomp (a) CF% (b) CIF% (C) NC% -----233

Figure 7.20 Comparison of ANN and Kriging model accuracy validation metrics by number of adaptive samples for Hesse (a) CF% (b) CIF% (C) NC% -----233

Figure 7.21 Schematic of a continuous direct compaction process-----234

Figure 7.22 Comparison of ANN and Kriging model accuracy validation metrics by number of adaptive samples for the direct compaction process model (a) CF% (b) CIF% (C) NC%-----239

Figure 7.23 Matrix of feasibility function contour plots representing the feasible region of the continuous direct compaction process case study (Feasible region boundary from the original model and predicted by the ANN model are represented as red dashed lines and red solid lines respectively)-----240

Figure 7.24 Schematic of a continuous wet granulation process-----241

Figure 7.25 Matrix of feasibility function contour plots representing the feasible region of the continuous wet granulation process case study (Feasible region boundary from the original model and predicted by the ANN model are represented as green dashed line and red line respectively) -----247

Chapter 1

Introduction

1.1 Continuous solid oral dosage manufacturing

Currently, batch manufacturing is the predominant method for the production of small-molecule drug products. Several limitations of batch manufacturing such as difficulty in scale-up, long processing times, need for large manufacturing facilities for large volume product production are recognized [1]. Drug product recalls and shortages are still high, nearly two-thirds of which are attributed to issues with product manufacturing i.e., quality of product and manufacturing facility. Lack of agility, flexibility and robustness in the pharmaceutical manufacturing sector that may lead to drug shortages is seen as a potential public health threat [2]. This is particularly evident in the event of emergencies and pandemics when the industry is required to produce large volumes of the drug product in a short time. The U.S. Food and Drug Administration (FDA) has recognized a need for modernizing the pharmaceutical manufacturing sector on par with other industries such as semi-conductors, chemicals and petroleum [3]. The U.S. FDA pharmaceutical quality for 21st century initiative promotes a

“a maximally efficient, agile, flexible pharmaceutical manufacturing sector that reliably produces high quality drugs without extensive regulatory oversight”

Continuous manufacturing is an innovation that is promoted to advance the pharmaceutical manufacturing sector and has attracted attention of the pharmaceutical industry in the past several years. In continuous manufacturing, material produced in each step is directly sent to the next step [2]. Continuous manufacturing promises to meet manufacturing demands through cost savings from simplified process, reduced space and fewer product failures [4]. It inherently involves higher

level of process design to ensure adequate process control and quality. There have been significant advancements in science and engineering over the past decade to support continuous manufacturing implementation [5]. With the available equipment capacity, it has potential to provide much higher throughput per unit volume per unit time which is highly required in time of drug shortages. Another factor driving greater interest in continuous manufacturing is the competition-free life span of the drug product. Companies have a great economic incentive to move quickly from drug discovery to drug product production phase as they incur significant investment costs in the drug discovery phase. Following this, there is a need to accelerate process development phase and bring the drug product to the market in order to secure significant returns in the early phase before similar drugs are launched [6]. Companies also incur reduced profit margins due to patent life expiry and subsequent increased competition from generic product manufacturers. Continuous manufacturing supports fewer scale-up studies and decrease in time-to-market by expediting process development. Recent drug product approvals by the U.S. FDA have already placed Continuous Manufacturing as a viable alternative. In July 2015, the U.S. FDA approved the use of Continuous Manufacturing technology for production of Vertex's Orkambi®. In April 2016, the FDA also approved switching production of Prezista® from batch to continuous process in a Janssen facility in Puerto Rico [7, 8]. Several studies evaluating the economic performance of batch and continuous technologies have been published [9, 10]. The conversation has shifted from "Should we do continuous manufacturing?" to "How to best implement continuous manufacturing?" [11].

In this dissertation, the focus is on continuous manufacturing of solid oral dosage products as they constitute about 60% [7] of global drug consumption. Manufacturing routes for tablet consumption can be broadly classified as direct compaction, dry granulation and wet granulation routes. A general schematic illustrating the routes is given in Figure 1.1. In the tableting process, raw materials such as Active Pharmaceutical Ingredient (API) and excipients in powder form are introduced through feeding units into a blending unit. Prior to this, a conical screen mill may be

used for delumping the powder. The powder blend may be granulated using a twin screw granulation unit by addition of a liquid binder. Granulation may also proceed through a dry granulator (or roller compactor). The purpose of granulating powders is improving flow properties of the powders. The use of wet granulation requires a drying step through a fluidized bed dryer. The granulated material is passed through a milling unit to break the granules into the required size distribution. Following this, the granules are compacted to form tablets in a tablet press unit. In the absence of the granulation step, the powders may be directly compacted to produce tablets. The work done in this dissertation primarily focuses on the wet granulation route. Several studies in the past focused on the direct compaction [12-14] and dry granulation routes [15]. A holistic study of the wet granulation manufacturing route is a research gap which is intended to be addressed in this dissertation.

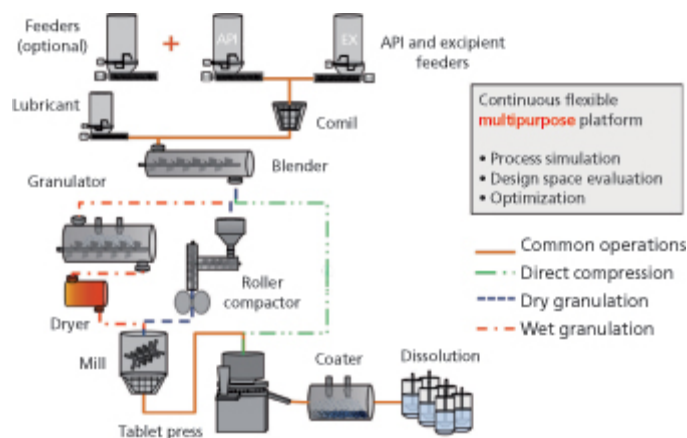


Figure 1.1 Schematic showing major drug-product manufacturing routes [16]

1.2 Quality by design framework

The Quality by design (QbD) initiative by FDA [17] was introduced to support the vision of advancing pharmaceutical manufacturing sector. Pharmaceutical QbD drives a systematic science-based approach to product design and process development [18]. QbD states that the identification

of the elements namely, Critical Quality Attributes (CQAs), Critical Material Attributes (CMAs) and Critical Process Parameters (CPPs) is central to the approach. A CQA is a final product or intermediate product property that needs to be within appropriate limits to ensure product quality. Examples of CQAs are content uniformity, moisture content, color, size etc. CPPs are input operating variables to the process such as impeller speed, flow rate or state variables such as temperature, pressure etc. Typical examples of input CMAs are powder true density, electrostatic properties, granule porosity etc. QbD advocates a thorough understanding of the process by linking CMAs and CPPs to CQAs. It requires that companies demonstrate the ability to predict the effect of material properties and process parameters on product attributes. The QbD concept has evolved over the years with regulatory guidelines from the International Congress on Harmonisation (ICH) Q8 R2 (Pharmaceutical development), ICH Q9 (Quality risk management) and ICH Q10 (Pharmaceutical quality system). The guidelines discuss the use of process modeling and other mathematical tools for pharmaceutical process understanding and process development. In this direction, tremendous research is ongoing to utilize various modeling approaches such as residence time distribution models, semi-empirical models, population balance models, discrete element method models, reduced order models and flowsheet models [19]. The approaches vary significantly in terms of the computational expense incurred and the level of process understanding that is demonstrated. Empirical models, though predictive in nature and computationally inexpensive, carry limitations in applicability to a different set of operating conditions or drug formulation. On the other hand, detailed and predictive modeling approaches such as discrete element method modeling simulate processes at a particle scale. However, they are computationally expensive. This dissertation aims to explore various modeling approaches for simulating particulate processes to support the QbD framework and address issues with computational limitations. The various modeling approaches are explored to simulate a conical screen milling process where particles undergo breakage, as this is one of the unit operations in the wet granulation route of tablet

manufacturing. A unified approach to utilizing strengths from various modeling approaches, addressing computational limitations and implementation in simulating continuous processes is a research area that merits focus.

The science-based approach to process development driven by the QbD framework ultimately aims to achieve greater control over producing products in specification. This is in contrast to a ‘Quality by testing’ approach, as increasing testing does not necessarily improve product quality. The goal is to shift from a procedural and inspection-based compliance to demonstration of methodologies and ability to remain in specification. The ICH Q8 [17] guideline within QbD framework introduced the concept of design space as

“the multidimensional combination and interaction of input variables (e.g., material attributes) and process parameters that have been demonstrated to provide assurance of quality”

From a regulatory stand point, the design space is proposed by the applicant and is subject to regulatory assessment and approval. This provides the applicant with the flexibility to change the processing conditions without needing any further approval, as long as it remains within the design space. Several publications used a design of experiments approach to identify this design space. This requires several initial and subsequent confirmatory experiments. The task is expensive, both in terms of raw materials as well as resources needed if the number of parameters in the experiments are high. Process systems engineering tools can be used effectively to complement an experiments based approach. In this dissertation, mathematical foundations are utilized to identify a ‘feasible region’ of CPPs and CMAs that is expected to yield a process satisfying requisite production and safe operability demands, and a product that adheres to the quality specifications. The goal is to develop efficient methodologies that can fully utilize the potential of the tremendous efforts in developing detailed process models. The design space can subsequently be identified by designing experiments within the identified ‘feasible region’. It is worth noting that the term ‘design space’

is used by the pharmaceutical industry and is the operating envelope identified with an experimental basis. 'Feasible region' is a term used by the process systems engineering community to identify this envelope using mathematical tools. In this dissertation, are used interchangeably.

1.3 Outline of the dissertation

Each of the five main chapters in this dissertation aims to further exemplify and advance research in the areas discussed thus far. Chapter 2 provides a literature review of the milling process, the existing body of work in modeling unit operations involved in continuous manufacturing through the wet granulation route, namely, feeding, blending, wet granulation, fluidized bed drying, comilling and tablet compaction. Following this, the concept of integrated modeling or flowsheet modeling is introduced in this chapter. Chapter 3 describes development of multi-scale modeling methodology utilizing the discrete element method modeling and population balance modeling. This chapter aims to provide an efficient methodology to include material properties in the comill modeling to aid QbD framework. Chapter 4 addresses computational limitations of the multi-scale process model through development a reduced model that aids utilization of the multi-scale model in applications that require several function calls. Chapter 4 further explores hybrid modeling utilizing a population balance modeling and a partial least squares modeling methodology to simulate the milling process and predicting milled granule CQAs. Chapter 5 focuses on utilization of several modeling approaches used for simulating individual unit operations in developing an integrated model that represents a plant scale wet granulation manufacturing process. Process systems engineering tools such as sensitivity analysis are implemented on the developed model to identify the CPPs. In Chapter 6 the concept of feasibility analysis is discussed. Following this, a novel feasibility analysis methodology that aids design space identification of pharmaceutical manufacturing processes is described. The methodology is applied to a number of case studies, including continuous pharmaceutical manufacturing processes. Finally chapter 7 discusses major

conclusions from the work presented in the dissertation and also provides directions for future work.

Chapter 2

Literature review

2.1 Milling

Milling is an intrinsically continuous unit operation common to the direct compaction, wet granulation, and dry granulation routes for continuous pharmaceutical manufacturing. In the direct compaction route, mills are used for material delumping and for API silication, whereas in the granulation routes, mills are used for granule size reduction. In the wet granulation route, mills reduce the size of oversize granules after the granulation and drying unit operations. In the case of dry granulation route, mills are used to break the compacted ribbons.

In this section, the focus is on mills as a particle size reduction tool. The granulation process is primarily required in drug product manufacturing in order to alleviate issues related to powder handling such as poor flowability. However, granulation may also produce particles with undesirable size distributions. This may downplay the positive benefits of granulation and also affect further processing during tablet compaction. The presence of large particles might lead to formation of tablet with pitted surfaces and poor strength, whereas an excess amount of fines leads to poor granule flow and weight variability [20]. In addition, the particle size distribution also impacts drug bioavailability [21]. Milling can also improve the dissolution of poorly soluble drugs, thereby improving their bioavailability [22, 23]. In this case, API is milled into ultrafine (micronized) particles to increase the surface area, leading to improvement in dissolution kinetics. Hence, an understanding of the effects of mill design and operation is critical.

2.1.1 Types of mill and granule characterization

Classification of milling equipment is generally performed on the basis of type of force applied to break the particles; impact, attrition and shear-compression [24]. The choice of equipment depends on the properties of the feed material (hardness, elasticity etc.) and the finished product specifications like particle size, particle shape, etc. Table 2.1 shows the most commonly used mills and their size reduction capacities. Only the impact mill and the shear-compression mill are discussed in detail, since these mill types are commonly integrated with roller compactors.

2.1.1.1 Impact Mill

The main mode of breakage in an impact mill is via mechanically induced high force collisions. Examples of impact mills are hammer mill and pin mill. Hammer mills are capable of significant size reduction and can reduce the size of particle down to about 10 μ m. The force imparted by the hammers, the feed rate, and the screen opening size are the critical parameters that control the degree of particle size reduction. Particle size distributions of granules produced by impact mills generally are relatively narrow, with fewer fines, because of self-classification of particles in screens. Pin mills operate similar to hammer mills, but typically with faster tip speeds and lower mechanical tolerances between rotating and stationary pins [25].

2.1.1.2 Shear-Compression Mill

The conical screen mill (comil) is a popular type of shear compression mill as it can be used for delumping as well as granule breakage. It has been found to be suitable for milling a wide range of products [26]. In a comil, the intense shear applied on the material in the gap between the impeller and the screen leads to creation of inter-particle and particle-wall frictional contacts and subsequent reduction in size. The force imparted due to the impeller also plays a part in particle breakage. The size-reduced particles escape through the screen. The size and shape of the screen holes, type of

screen, shape of the impeller, and the speed of the impeller are the important mill parameters that control the quality attributes of milled granules. Another type of shear compression mill is an oscillating granulator [27], which is generally used for roller compacted ribbons, which are passed through an assembly of wire mesh screen and oscillating rotors. The particle size of the milled granules is controlled by screen size, speed of the rotor and rotational angle of rotors [28]. They generally produce coarser granules than the comil. There are many roller compactors available commercially with an oscillating granulator incorporated after the rolls. This is easy to use as it allows continuous processing from powder blend to granules. For example, the Gerteis roller compactors employ one oscillating granulator under the compaction zone after the rolls, whereas the Alexanderwerk roller compactors employ two granulators for better control over the particle size. Often, a comil is integrated in after an oscillating granulator for secondary milling.

Table 2.1 Mills classified on the basis of milled particle size [29]

Mechanism	Particle Description	Size(μm)	Impact		Attrition	Impact & Attrition		Shear-Compression	
			Pin Mills	Hammer Mills	Jet Mills	Ball Mills	Conical screen mill	Oscillating Granulator	
	Medium fine	500-1000	Yes	Yes	No	No	Yes	Yes	
	Fine	150-500	Yes	Yes	No	No	Yes	Yes	
	Very Fine	50-150	Yes	Yes	No	No	Yes	Yes	
	Super Fine	10-50	Yes	Yes	Yes	Yes	No	No	
	Ultra Fine	<10	No	No	Yes	Yes	No	No	
	Colloidal	<1	No	No	No	No	No	No	

2.1.1.3 Granule characterization

Since milled granules are further processed to manufacture tablets or capsules, it is important to characterize the milled granules. The milling process is generally assessed by its ability to achieve the required particle size distribution. Sieve analysis and laser diffraction are the most common techniques used to measure particle size of granules [30].

Sieve analysis involves passing the granulated product by mechanical agitation through a series of sieves arranged in the order of decreasing sieve aperture size. The portion retained on each screen is then weighed and a mass-based PSD is obtained from the mass on each sieve. Major advantages of sieve analysis are its cost effectiveness and ease of use. However, it is time consuming and requires large amount of sample [31]. The sample size used for sieve analysis depends upon the sieve diameter used, i.e. the diameter of the sieve pan. For a small sieve diameter, from a few grams to a few tens of grams can be used, while for a large sieve diameter, generally a sample mass of few hundred grams is required. In addition, friable materials can give unreliable results, as the granules can experience significant breakage as they pass through the sieves.

Unlike sieve analysis, laser diffraction requires very little sample and the time required for analyzing the sample is short. In laser diffraction, a monochromatic laser light scattered by the particles in the sample is detected at various angles. A volume-based PSD is developed out of the scattered intensities data using a system of linear equations [32], subjected to assumptions of sphericity. The scattering pattern can be explained by Mie's theory or by Fraunhofer approximation based on the ratio of particle size to wavelength. Two widely used laser diffraction types of equipment are Malvern Mastersizer and Helos Laser diffraction (Sympatec®), which use Mie's theory and Fraunhofer approximation respectively. This technique is able to measure particle sizes between 0.05 to 2000 μm [33], but as the particle size increases, there is a risk of choking the equipment, and photons increasingly experience multiple scattering, which might lead to inaccuracy in the measurement.

Sieve analysis and Laser diffraction techniques measure the performance of the milling step in an intrusive manner, i.e. they require the user to collect samples and perform analysis on the collected samples. In contrast, the continuous mode of manufacturing requires adoption of innovative techniques that can monitor system performance in real time. To ensure efficient drug

manufacturing, the USFDA launched a revision to the cGMPs (Good Manufacturing Practices) in the year 2002, and established more stringent regulatory quality controls, and developed expectations of a higher level of process understanding than previously achieved by many pharmaceutical companies [34]. QbD (Quality by Design) and PAT (Process Analytical Technology) methods were endorsed as a part of this paradigm shift to promote superior understanding and to embrace novel techniques for better control on the process and timely quality checks.

Evolution of process analyzers like NIR (near infrared), Raman Spectroscopy, and FBRM (focused beam reflectance measurement) facilitated the shift towards QbD [35]. The primary goal of PAT is to help understand the effect of process/equipment parameters by enabling timely checks of the critical material properties and quality attributes, thereby enhancing the understanding of the process. Over the last decade, many non-intrusive PAT techniques such as FBRM, Insitec®, dynamic image analysis (DIA) and spatial filtering technique (SFT) have been developed to measure PSD [24]. Non-intrusive methods have the advantage of allowing real time analysis, as these methods do not interfere with the process and provide nearly instantaneous measurements. For these methods, a small material stream has to be separated from the process, to prevent the main stream from flooding the detectors.

Bulk density, tapped density, friability, porosity are the other important CQAs for the milled granules. The ratio of mass of loosely packed (untapped) granules to its volume is known as the bulk density. The bulk density of a sample is determined by measuring the volume of a known weight of the sample in a graduated cylinder. This volume includes the volume of voids present between the particles. Hence, the bulk density depends on both the density of granules and the spatial arrangement of granules in the particle bed. The tapped density is an increased bulk density attained after mechanically tapping a container containing the sample, which forces the particles to

pack densely. Granule friability characterizes granule strength. If the granules are very weak, they might crumble before they are tableted, which can further lead to segregation of the sample. On the other hand, if the granules are too hard, their compactibility is affected. Granule friability can be determined using a friabilator [36]. Porosity gives insight into granule structure and strength, which affects the tablet compaction. Very low porosity values indicate dense granules, which could be difficult to compact. On the other hand, high porosity indicates brittle and weak granules which could break due to the stresses from tableting or packaging. Porosity is generally measured using helium and mercury pycnometers [37]. In addition to these measurements, milled granules can be analyzed for tableability by examining the tablets produced for weight variability, tableability profile, and compactibility profile [38].

2.1.2 Models for milling

The granule breakage mechanism in a comill is a complex phenomenon where fracture and eventual breakage occur due to a rotating impellor and the smaller sized granules are discharged through a screen. Schenck and Plank [39] studied the fundamental breakdown behavior of granules in a comill and proposed impact attrition as the primary breakage mechanism. Milling experiments in the absence of a screen suggested that the screen acts only as a classifier and does not affect the breakage mechanism. Verheezzen, van der Voort Maarschalk [40] modeled breakage in a comill through a size reduction ratio defined as the ratio of the median particle size of granules before and after breakage. The initial size of particles before granulation and the amount of binder used was found to have an effect on the breakage behavior. Samanta, Ng [41] presented detailed comilling experiments with compacted ribbons to study the effects of impeller shape, speed, screen type and concluded that the fines can be reduced considerably by choosing the correct impeller and screen type for the material milled. Whilst plenty of work has been published that studied the effects of various design and process variables for comilling, work published on modeling of the comilling

operation to predict milled product CQAs is limited. Kumar Akkisetty, Lee [42] used an Artificial Neural Network (ANN) surrogate model to establish a relationship between mill operating conditions, material properties selection and breakage functions of a population balance model (PBM). However, the experiments used for this work did not consider the effect of granules exiting the mill as the screen holes were closed. Reynolds [43] developed a PBM to predict the milled particle size distribution (PSD) through the use of a generalized daughter distribution function. A critical screen size ratio dependent on impeller speed was used to model the exit of granules. However, the d_{95} of the milled PSD was used, which limits the applicability of the model formulation as d_{95} is the required model output that is predicted and not a model input. In addition, the dynamics of the model i.e., flowrate of particles exiting the mill was not formulated, and as a result, the time required to mill the material could not be predicted. Barrasso, Oka [44] modeled the comilling of compacted ribbons through development of a PBM. A linear function was used to model the exit of particles from the mill through the screen which aided in predicting the dynamic holdup as well. However, the full effect of the impact of impeller speed on the model was not captured. In addition, the applicability of the model in simulating comminution of granules obtained from a wet granulation process was not established. Population balance models for milling processes generally use semi empirical breakage kernels. This limits its applicability when the milling conditions or the material processed is changed. In addition, a PBM does not capture particle-scale interactions that would add more accuracy to the model. Discrete element method (DEM) models on the other hand, have the potential to bridge this gap

The development of a DEM model for breakage processes so far has been focused on ball mills, grinding mills, crushers etc. [45-48]. This is possibly due to additional challenges posed in a comill such as continuous feeding, discharge of particles through screen, introduction of additional complexity in the particle-wall interactions from a rotating impeller and a dearth of published experimental data etc. Experimental data published for milling processes are for standard materials

such as silica glass, alumina, and materials used in the mining industry [49-51]. Despite its prevalence in the pharmaceutical industry, work on analysis of breakage of pharmaceutical granules in a comilling process is very limited. Deng, Scicolone [52] presented a discrete element method (DEM) simulation of the comilling process, where breakage of particles was not considered as the comill was used as a dry coating device. In addition, screen holes and screen thickness were excluded from the geometry of the mill and particles exited the mill based on their proximity to the screen wall. Capece, Bilgili [53] established a bi-directional PBM-DEM framework utilizing a mechanistically motivated kernel formulation Capece, Bilgili [54]. However, the framework was implemented for a ball milling process where particles were not considered to exit the mill. Capece, Bilgili [54] formulated and used an energy based kernel that exclusively identified contribution of material properties. A PBM-DEM framework utilizing the mechanistically motivated kernel formulation [53] was proposed to model milling processes. In this framework, DEM simulation was run for a short milling time and energy distribution data was collected. This data obtained is given as input to PBM where breakage is incorporated through use of the aforementioned mechanistic kernel. PBM updates the particle size distribution (PSD) of the material due to breakage. DEM simulation is run again with the updated PSD. Thus, a bi-directional coupling between DEM and PBM is established. The process is to be continued for the duration of the milling. The framework proposed is sensitive to the short milling time used for each iteration as it assumes absence of breakage and, a constant value of the breakage kernel in this time period. The framework is also sensitive to the position of the updated PSD of material in the mill. This is especially a limitation for the modeling of comill processes. In a comill process, the particle population inside the comill is greatly dependent on the proximity of the particles to the screen holes as particles closer to the screen may exit the mill. In addition, to implement the framework, the estimation of material specific parameters of the kernel requires tedious milling experiments from mono sized feed material.

In this dissertation, a DEM based model for a comill process is developed and a hybrid DEM-PBM multiscale framework is established. Full extent of the effect of mill geometry on particle population inside the comill through screen thickness, screen hole size, impeller shape and speed, is incorporated into DEM model. Following this, a surrogate model is introduced into the hybrid framework to address computational expense incurred due to the DEM model. The goal of the hybrid framework is to accurately incorporate effect of material properties and geometry into the model and also enable its utilization in flowsheet models that are used to simulate continuous tablet manufacturing processes.

Besides prediction of milled particle size distribution, mentions of prediction of other CQAs such as bulk density, tapped density, friability etc., of the milled product are limited in literature. It is important to note that these CQAs have an impact on the compaction behavior of granules and thus their effect on CQAs should be predicted. This dissertation addresses prediction of particle size distribution as well as other CQAs using a PBM and partial least squares hybrid modeling approach.

2.2 Unit operations and integrated process models

In this section, an overview of modelling approaches generally used for process model development is given. The literature review aims to establish existing work on simulating unit processes. This provides the required foundation to developing an integrated model simulating continuous tablet manufacturing processes. Attempt has been made to give relevant equations where applicable, and to explain the modeling strategies, along with references to the published work where more details on the model development can be found. Specifically, models for loss-in-weight feeder, blender, wet granulator, fluidized bed dryer, roller compactor and tablet press are discussed. Following this the concept of integrated models or flowsheet models is introduced.

Loss-in-weight feeder

Although variability in feeding performance can propagate downstream and affect the final product quality, dynamic models published for feeding equipment are limited when compared to other unit operations. In order to get stable and constant flow, loss-in-weight (LIW) feeders are operated under gravimetric mode where the flow rate is controlled by adjusting the screw speed inside the feeder. Wang, Li [55] used multivariate analysis to correlate feeding performance to powder flow properties. The feeding performance was quantified using relative standard deviation of mass flow rate from the feeder, which correlated to the powder flow properties using partial least squares regression. This approach is particularly useful if the new material to be fed is expensive, or is available in limited quantities. Boukouvala, Muzzio [56] developed data driven models from experimental data collected using LIW feeder provided by a Gericke feeder. Screw speed, screw size, screw configuration and powder flow index were the significant feeder variables identified from experimental data using an Analysis of Variance (ANOVA) method. Modeling approaches such as kriging, response surface methodology were used to correlate these variables to feeder flow rate standard deviation, which is a feeder performance metric. Such approaches are valuable, as a mechanistic understanding of powder behavior inside the screw feeders is still lacking.

Wang, Escotet-Espinoza [12] used a semi-empirical equation to dynamically model the mass flowrate out of the feeder $F_{out}(t)$ using Equation 2.1:

$$\dot{F}_{out}(t) = ff(t)\omega(t) \quad 2.1$$

where $\omega(t)$ is the screw speed; $ff(t)$ is the feed factor, defined as the maximum mass of powder fitting in a screw flight and is expressed in Equation 2.2:

$$ff(t) = \rho_{effective}(t)V_{ScrewPitch} \quad 2.2$$

where $\rho_{effective}$ is the effective density of materials in the screw pitch with a volume $V_{ScrewPitch}$. ff was found to be dependent on the amount of material in the hopper, as the effective density of powder entering the screws is expected to change due to change in pressure exerted by static head of the material above. This relationship was determined to be following a pseudo-first-order as expressed in Equation 2.3:

$$ff(W(t)) = ff_{level}^{sat} - e^{-BW(t)}(ff_{level}^{sat} - ff_{level}^{min}) \quad 2.3$$

Continuous blender

Powder blending is a crucial unit operation in pharmaceutical industry as the individual components in a formulation are effectively mixed in this unit, thus impacting the content uniformity in the final drug product. This section reviews various models that have been used to model continuous powder blenders. Discussion has been restricted to modeling tubular blenders, the most popular form of powder blenders that have been used in continuous processing of pharmaceuticals.

Numerous modeling techniques have been used to simulate the powder behavior in a continuous blender. The relative standard deviation of the concentration of the active ingredient at the blender exit is typically used as a blender performance metric, and is defined in Equations 2.4 and 2.5 [57]:

$$RSD = \frac{\sigma}{\bar{C}} = \frac{\text{standard deviation}}{\text{average concentration}} \quad 2.4$$

$$\sigma = \sqrt{\frac{\sum_{i=1}^N (C_i - \bar{C})^2}{N - 1}} \quad 2.5$$

where N is the number of samples collected and C_i is the concentration of sample i .

Several models in the literature for mixing processes used discrete element method (DEM) to simulate the mixing and segregation behavior [58, 59]. DEM models are used to capture the effects of blender geometry, material properties and operating conditions [57, 60] on the RSD. While mechanistic models such as DEM are computationally expensive, the Discrete Element-Reduced Order Modeling (DE-ROM) methodology has opened avenues to capture mechanistic effects in a unit modeling framework. In this methodology, the distributed parameter information from DEM simulations such as velocity profiles, are efficiently represented using a reduced order model. The lower dimensional velocity profiles are then correlated to blender performance predictors such as RSD using partial least squares modeling. Sen, Chaudhury [61] coupled population balance models (PBM) with DEM models to predict the concentration of API at the blender exit. Velocity profiles obtained from a periodic section of the DEM blender model was used to define the change in the number of particles with time in the PBM equation.

In addition to RSD, the residence time distribution (RTD) of particles in the blender is also of interest, it dictates the amount of time a material takes to exit the blender, thus enabling material traceability. In Wang, Escotet-Espinoza [12], a continuous blender was modeled as CSTRs in-series, which was used to characterize the RTD. The CSTR in series model uses multiple ideal stirred tanks in series to simulate mixing of powders along the length of the blender. A delay time τ_{delay} is used, that represents the time particles take to convectively move through the blender in axial direction. The blender RTD is then represented as given in Equation 2.6:

$$E(t) = \text{Unit Step}[\tau - \tau_{delay}] \frac{(t - \tau_{delay})^{n-1} e^{(-\frac{t - \tau_{delay}}{\bar{\tau}})}}{(n - 1)! \bar{\tau}^n} \quad 2.6$$

where n is the number of tanks and $\bar{\tau}$ is the mean residence time of one tank in the model. The blender's mean residence time then is, $\tau_{blender} = \tau_{delay} + n\bar{\tau}$.

The mass balance in the blender is modeled assuming the hold up in the blender reaches a steady state asymptotically i.e., it follows a first-order. The flowrate out of the system, which is used as an input in the downstream unit, can thus be modeled as given in Equations 2.7 and 2.8:

$$\bar{\tau} \frac{dM(t)}{dt} + M(t) = M_{ss} \quad 2.7$$

$$\frac{dM(t)}{dt} = F_{in}^{total} - F_{out}^{total} \quad 2.8$$

Continuous wet granulator

Population balance modeling is the most commonly used approach to model a continuous wet granulation process, both, when modeling a twin screw process or a high shear granulator, the two most common forms of continuous wet granulators. A general population balance model (PBM) equation is given in Equation 2.9.

$$\begin{aligned} \frac{\partial F(\mathbf{x}, t)}{\partial t} + \frac{\partial}{\partial \mathbf{x}} \left[F(\mathbf{x}, t) \frac{d\mathbf{x}(\mathbf{x}, t)}{dt} \right] \\ = R_{form}(\mathbf{x}, t) - R_{dep}(\mathbf{x}, t) + \dot{F}_{in}(\mathbf{x}, t) - \dot{F}_{out}(\mathbf{x}, t) \end{aligned} \quad 2.9$$

where, the number of particles F is the particle density and \mathbf{x} is the vector that represents the granule characteristic. The partial differential term with respect to \mathbf{x} accounts for property changes due to mechanisms such as layering, liquid addition or consolidation. R_{form} and R_{dep} are functions representing birth and death rates of particles with property \mathbf{x} . \dot{F}_{in} and \dot{F}_{out} are the flow rates of particles entering and exiting the granulator respectively.

A three dimensional (3-D) PBM is widely used to account for distributions in size, liquid content and porosity simultaneously. Granulation processes in pharmaceutical industry involve multiple solid components i.e., an API granulated with one or more excipients. In this case, the distribution of API in the granule population is of interest. Non-uniform API distribution is undesired as it can affect the uniformity of the final solid oral dosage form [62]. To model multi component granulation systems, a fourth dimension must be added to the 3-D PBM as given in Equation 2.10:

$$\begin{aligned} \frac{\partial}{\partial t} F(s_1, s_2, l, g, t) + \frac{\partial}{\partial l} \left[F(s_1, s_2, l, g, t) \frac{dl}{dt} \right] + \frac{\partial}{\partial g} \left[F(s_1, s_2, l, g, t) \frac{dg}{dt} \right] \\ = R_{nuc}(s_1, s_2, l, g, t) + R_{agg}(s_1, s_2, l, g, t) \\ + R_{break}(s_1, s_2, l, g, t) \end{aligned} \quad 2.10$$

where l, g indicate the liquid and gas volumes in the granule respectively. s_1 and s_2 are the solid volumes in the granule of the two different components used, typically API and excipient. The formation and depletion rates are governed by nucleation, aggregation and breakage processes, which constitute the right hand side of the PBM equation.

There is a lot of work that has been published and is ongoing to accurately model the mechanisms in a granulation process. Specifically, several aggregation and breakage kernels have been developed that are empirical, or mechanistic, or a combination of both [63-65]. The terms in the kernels may be estimated based on experimental data or data obtained from mechanistic models

such as discrete element method models. Nucleation process entails formation of nuclei as liquid droplets are added to the system and come in contact with powder particles. In drop controlled regime [66], each droplet forms one nuclei. Rate of nucleation is typically modelled as following zero or first order reaction [65]. Barrasso and Ramachandran [67] modeled rate of nucleation as R_{nuc} as ratio of rate of liquid added to powder and an assumed droplet volume, $\dot{L}_{in,powder}/V_{droplet}$. Here, the fraction of liquid added to the powder, $\dot{L}_{in,powder}$ is assumed as its volume fraction or the ratio of total powder volume to total volume of granules and powder.

Various aggregation kernels have been used and published in the literature. X. Liu and D. Litster [63], Cameron, Wang [68] provide a tabulated list of aggregation kernels used. As an example, aggregation kernel proposed by Madec, Falk [69] is given in Equation 2.11:

$$\beta((s_1, s_2, l, g, \acute{s}_1, \acute{s}_2, \acute{l}, \acute{g})) = \beta_0(V + \acute{V}) \left((LC + \acute{L}C)^\alpha \left(100 - \frac{LC + \acute{L}C}{2} \right)^\delta \right)^\alpha \quad 2.11$$

Aggregation rate is strongly dependent on liquid binder content and granule size, which explains the kernel structure. In this kernel, the two colliding particles are represented as (s_1, s_2, l, g) and $(\acute{s}_1, \acute{s}_2, \acute{l}, \acute{g})$. V and LC represent total volume and fractional liquid binder content. β_0 , α and δ are the parameters to be estimated from experimental data. For pharmaceutical processes, a composition dependent aggregation kernel proposed by Matsoukas, Kim [70] may be used, since distinct solid phases may attract or repel each other. This can be accounted for using a multiplication factor $\Psi(s_1, s_2, \acute{s}_1, \acute{s}_2) = \exp(-a_{ab}(x + x - 2x\acute{x}))$, where x is the mass fraction of the first component. Once the kernel is formulated, the rate of aggregation is included in the model through Equations 2.12 - 2.15:

$$R_{agg}(s_1, s_2, l, g, t) = R_{agg}^{form}(s_1, s_2, l, g, t) - R_{agg}^{dep}(s_1, s_2, l, g, t) \quad 2.12$$

$$\begin{aligned} R_{agg}^{form}(s_1, s_2, l, g, t) &= \frac{1}{2} \int_0^{s_1} \int_0^{s_2} \int_0^l \int_0^g \beta(s_1 - \acute{s}_1, s_2 - \acute{s}_2, l - \acute{l}, g \\ &\quad - \acute{g}, \acute{s}_1, \acute{s}_2, \acute{l}, \acute{g}) F(s_1 - \acute{s}_1, s_2 - \acute{s}_2, l - \acute{l}, g \\ &\quad - \acute{g}, t) F(\acute{s}_1, \acute{s}_2, \acute{l}, \acute{g}, t) d\acute{g} d\acute{l} d\acute{s}_2 d\acute{s}_1 \end{aligned} \quad 2.13$$

$$\begin{aligned} R_{agg}^{dep}(s_1, s_2, l, g, t) &= \frac{1}{2} \int_0^\infty \int_0^\infty \int_0^\infty \int_0^\infty \beta(s_1, s_2, l, g, \acute{s}_1, \acute{s}_2, \acute{l}, \acute{g}) F(\acute{s}_1, \acute{s}_2, \acute{l}, \acute{g}, t) dg dl ds_2 ds_1 \end{aligned} \quad 2.14$$

$$\begin{aligned} R_{agg}^{dep}(s_1, s_2, l, g, t) &= \frac{1}{2} \int_0^\infty \int_0^\infty \int_0^\infty \int_0^\infty \beta(s_1, s_2, l, g, \acute{s}_1, \acute{s}_2, \acute{l}, \acute{g}) F(\acute{s}_1, \acute{s}_2, \acute{l}, \acute{g}, t) dg dl ds_2 ds_1 \end{aligned} \quad 2.15$$

Similarly, breakage mechanism may be also be included in the model through the use of breakage kernels. Breakage kernels as discussed in models for milling for comminution processes are also applicable to granulation processes.

It is worth noting that the 4-D models as described above are computationally expensive to evaluate. This limits its applicability for model based control, or advanced model applications such as sensitivity analysis or flowsheet modeling. For practical purposes, the dimensionality of the model can be reduced and a lumped parameter approach can be used, that is, one or more granule

properties are lumped into the remaining distributions. A new equation is used for each lumped parameter to track its evolution with time. For example, if gas volume is taken as the lumped parameter, the 3-D reduced model is given by Equation 2.16 where nucleation and layering effects are not considered.

$$\frac{\partial}{\partial t} F(s_1, s_2, l, t) + \frac{\partial}{\partial l} \left[F(s_1, s_2, l, t) \frac{dl}{dt} \right] = R_{agg} + R_{break} \quad 2.16$$

Equation 2.17 is the gas balance equation where total volume of gas in each bin is given by $G(s_1, s_2, l, t) = g(s_1, s_2, l, t)F(s_1, s_2, l, t)$.

$$\frac{\partial}{\partial t} G(s_1, s_2, l, t) = F(s_1, s_2, l, t) \frac{dg}{dt} + R_{agg,gas} + R_{break,gas} \quad 2.17$$

Barrasso and Ramachandran [71] provided a detailed account of several model order reduction strategies and compared them to the full 4-D model. It was found that the 3-D model with gas volume as the lumped parameter showed most promising results in terms of accuracy and computational time, possibly due to low influence of gas phase on aggregation and breakage rates.

Among various continuous granulators available, the twin screw granulator (TSG) is the most widely used model in continuous manufacturing processes. Barrasso and Ramachandran [67] demonstrated the ability of a multi-dimensional PBM coupled with a DEM model to qualitatively predict effects of screw design and configuration on granule properties. A compartmental PBM was used where the TSG was represented as four well mixed axial, spatial compartments in series. Powder and liquid were introduced in the first compartment and the granulated product exited the last compartment. Within each compartment, the residence time of particles was evaluated using DEM simulations. In addition, collision and velocity data gathered from DEM simulations were

also used to evaluate mechanistic expressions for aggregation, breakage and consolidation. Despite its promise, the use of mechanistic models for predictive purposes is still not widely accepted due to the computational expense it carries. Use of surrogate modeling techniques such as artificial neural networks, kriging etc., [72] to represent and predict the high dimensional and computationally expensive mechanistic data, shows tremendous potential.

Fluidized bed dryer

Fluidized bed drying has been the widely adopted form of drying for pharmaceuticals, and discussions on modeling of dryers has thus been restricted to fluidized bed drying. It is important to note that some dryers operate in semi-continuous modes, and it is advised that the practitioner is cognizant of the mode of operation when adopting the drying models reviewed below.

Drying models with varying extent of detail ranging from empirical models to detailed mechanistic models are published in the literature. A detailed review of the mechanistic drying models available is published in Mortier, De Beer [73]. Drying of pharmaceutical material is typically described using single particle drying models, where pore structure is ignored and the porous material is treated as a whole. The single particle drying model can be used to predict the drying behavior of a population of granules using population balance model. The effect of fluidization of the particles can be thoroughly studied using computational fluid dynamics (CFD) models where the spatial distribution of the moisture content can be analyzed.

In single particle drying models, evaporation of liquid is described using a diffusion equation. In particular, Mezhericher, Levy [74] describes drying of a motionless single porous droplet in a flow of air in two phases. In the first phase, temperature of the water increases and water evaporates from the surface. This can be described using Equation 2.18:

$$\dot{m}_v = h_D(\rho_{v,s} - \rho_{v,\infty})A_d \quad 2.18$$

where \dot{m}_v is the mass transfer rate, h_D is the mass transfer coefficient, $\rho_{v,s}$ is the partial vapor density over the droplet surface, $\rho_{v,\infty}$ is the partial vapor density in the ambient air, and A_d is the surface area of the droplet.

When the radius of the droplet becomes equal to the radius of the drying particle, the second drying phase starts during which two regions, the wet core and the dry crust are formed. In this phase, water evaporates inside the particle at the receding interface between the crust and the wet core. The vapor generated over the interface diffuses and forms a thin boundary layer over the particle surface. The drying air then takes away the vapor on the particle surface through convection. The evaporation rate in the second phase is given by a complicated equation that is developed based on a moving evaporating interface. The equations from both drying phases are to be solved simultaneously with ODEs for decrease in droplet radius, temperature of the droplet, decrease in wet core radius, PDEs for temperature profile in the dry crust and wet core. The reader is referred to Mortier, De Beer [75] for details on the corresponding equations and their solution.

Mortier, Van Daele [76] proposed reduction of the complex single particle drying model to be used in a population balance equation. To reduce the complex drying model, a global sensitivity analysis is performed and the critical operating parameters that most impact the model outputs are chosen. Empirical relationships can then be used to represent the complex drying model as a function of the critical processing parameters. Based on the sensitivity analysis, particle radius was found to be important for the first drying phase and gas temperature for the second drying phase.

For constant ambient conditions, drying of a population of wet granules can be described by Equation 2.19:

$$\frac{\partial}{\partial t} n(R_w, t) + \frac{\partial}{\partial R_w} \dot{R}_w(R_w, Y) n(R_w, t) = 0 \quad 2.19$$

where $n(R_w, t)$ is the number density distribution of particles of wet radius R_w at time t . The growth term, $G_r = \dot{R}_w(R_w, Y)$ accounts for the decrease in moisture content. Here, Y represents the ambient conditions in the system such as gas temperature, gas velocity, air humidity etc.

It is worth paying attention to the empirical and Artificial neural network (ANN) based models that are published in literature [77] to predict the evolution of average moisture content of granules with time. The empirical models are generally expressed in exponential terms to represent the drying curves. While no mechanistic understanding of the process is incorporated in these models, they may serve as an easy way to predict moisture content evolution.

Tablet Press

Similar to the roller compaction, the tablet press unit operation is identical in both batch and continuous operations. The compaction process in a tablet press has thus been modeled since decades. Tablet press unit modeling constitutes modeling of powder residence in the feed frame as well as powder compaction behavior after flow from the feed frame in to the dies of a rotating turret. The uniformity of powder flow from the feed frame to the die impacts the tablet weight and its potency. Modeling of powder flow in the feed frame through discrete element method (DEM) simulations are published and have provided deeper understanding of powder flow patterns, potential particle attrition, over lubrication in the feed frame and effect on tablet weight variability [78, 79]. Mateo-Ortiz and Mendez [80] studied the effect of paddle wheel speed and disc speed on the residence time distribution of powder in the feed frame through laboratory experiments as well as DEM simulations. The experiments conducted showed that higher paddle wheel speeds lead to a lower mean residence time, narrow RTD profiles, and that the RTD profiles are similar to an ideal

CSTR. Boukouvala, Niotis [81] used experimental data published in Mendez, Muzzio [82], and developed response surface models for predicting mean residence time of powder as a function of turret speed and paddle wheel speed.

Compaction of powders has been modeled extensively. Patel, Kaushal [83] provides a review of the various models proposed to characterize powder compressibility. These models relate powder properties such as porosity, volume, density etc., which are a measure of the state of consolidation of powder, with compacting pressure. Among many such models proposed, the Heckel equation, the Kawakita equation and the Kuentz-Leunberger (KL) equation are the most commonly used in the pharmaceutical area. The Heckel equation given in Equation 2.20, assumes that the reduction in porosity e due to applied pressure P on the powder obeys a first order relationship.

$$\ln \frac{1}{e} = kP + A \quad 2.20$$

Here, constant k represents plasticity of the material and the constant A is the sum of two densification terms as given by Equation 2.21:

$$A = \ln \frac{1}{e_0} + B \quad 2.21$$

where the first term is related to initial die filling and B gives densification due to rearrangement of particles.

The Kawakita model, described by Equations 2.22 and 2.23 assumes that when subjected to load, the product of pressure and volume terms is constant, since the particles are in equilibrium at all stages of compression.

$$\frac{P}{C_1} = \frac{1}{ab} + \frac{P}{a} \quad 2.22$$

$$C_1 = \left(\frac{V_0 - V}{V_0} \right) \quad 2.23$$

Here, V is the volume of compact at pressure P and V_0 is the initial apparent volume of powder. a is the initial porosity and $1/b$ is the plasticity parameter.

The KL equation (Equation 2.24) was obtained by considering the pressure susceptibility of porosity reduction as a function of powder bed porosity [84].

$$P = \frac{1}{C_2} \left[(\varepsilon - \varepsilon_c) - \varepsilon_c \ln \left(\frac{\varepsilon}{\varepsilon_c} \right) \right] \quad 2.24$$

Here, ε_c denotes the critical porosity when the powder attains a state of mechanical rigidity and $1/C_2$ is the plasticity parameter.

All of the parameters can be determined experimentally through regression from force-displacement data. Paul and Sun [85] systematically evaluated the performance of these equations and suggested that the KL equation is superior to Heckel and Kawakita equations applied to powders exhibiting a wide range of mechanical properties. Singh, Gernaey [86] described a detailed model based on Kawakita equation. This model also incorporates prediction of tablet hardness as a function of compression force proposed by Kuentz and Leuenberger [84] as given in Equations 2.25 and 2.26:

$$H = H_{max}(1 - \exp(\rho_r - \rho_{r,cr} + \lambda_H)) \quad 2.25$$

$$\lambda_H = \ln\left(\frac{1 - \rho_r}{1 - \rho_{r,cr}}\right) \quad 2.26$$

where ρ_r is the relative density. The parameters $\rho_{r,cr}$ and H_{max} are to be fitted from experimental data. Escotet-Espinoza, Vadodaria [87] estimated these co-efficients from experimental data and developed empirical equations to relate these parameters to the original blend properties.

2.2.1 Integrated process models

Developing individual unit operation models enables a superior understanding of each unit operation, the relationship between the material properties, process and design parameters and the quality attributes of intermediate materials. However, equally important, it enables the development of a flowsheet model that simulates the continuous manufacturing line. A robust and detailed flowsheet simulation is an approximate representation of the actual plant operation [88]. Dynamic behavior of the entire manufacturing line with respect to disturbances or changes in the input factors can be simulated using a flowsheet model. In addition, flowsheet models can be systematically used to perform sensitivity analysis. Sensitivity analysis is a tool to identify the input factors that are most influential on the output of interest, such as tablet properties. Once the critical input factors are identified, a design space can be determined, within which all the process, product quality, equipment and production rate constraints are met. Thereafter, the optimal operating conditions in this feasible region that requires least operating and material costs can be determined. Another advantage of development of flowsheet model is enabling the traceability of material, which aids in identifying and discarding potential off-spec material. Lastly, it enables the testing of various control strategies on the process. The entire exercise can be performed in-silico, resulting in savings

in time, effort and money from performing laboratory experiments, or trials on the manufacturing setup.

Once the individual unit operation models are developed, and the required parameters are estimated, the integrated model is built via connecting the inlet of a unit to the outlet of the preceding unit. Relevant material properties, operating conditions and individual unit model variables are sent to the following unit. Figure 2.1 is a pictorial representation of information flow between unit operations in a generic flowsheet model.

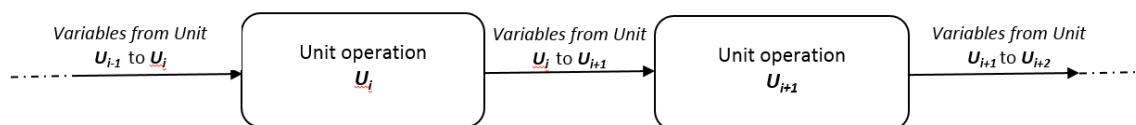


Figure 2.1 Schematic showing the flow of information in a generic flowsheet model

Process simulators such as gPROMSTM, ASPENTM facilitate the development of flowsheet models. The commercially available simulators aid in process simulation as well as the aforementioned advanced applications of flowsheet models such as design space identification, sensitivity analysis and process optimization. To further describe flowsheet model development, the required connections and flow of information in a direct compaction, dry granulation and wet granulation lines are shown in Fig (2). In the schematic, ρ , \dot{m} , PSD , x , z denote density, mass flow rate, particle size distribution of the powder or granules, concentration and moisture content in the granule respectively. The tablet weight, hardness and potency are denoted by w_{tablet} , λ_{tablet} and x respectively. It is important to note that connections of the same type are to have the same property set. For example, the text in red, blue, grey and green correspond to variables related to powder, granules, ribbons and tablets respectively. The variable set for each of these phases is to be maintained consistent throughout the flowsheet in order to avoid simulation errors. The schematic shown in Figure 2.2 is developed for a two-component system as an example. However, this can

be easily extended to a multi-component system. The readers are to note that the variables listed are shown as an example and the comprehensive list of variables, properties that need to be transferred from a unit model to another will depend on requirements and validity of the unit operation models for the specific manufacturing line in question.

The schematic shown in Figure 2.3 is an example of an integrated model of a direct compaction line developed in gPROMS™. The flowsheet model shown integrates the feeder, blender, feedframe and tablet press models. The feeder model also includes a refill unit and a controller. The controller manipulates the feeder screw speed in order to control feeder flowrate.

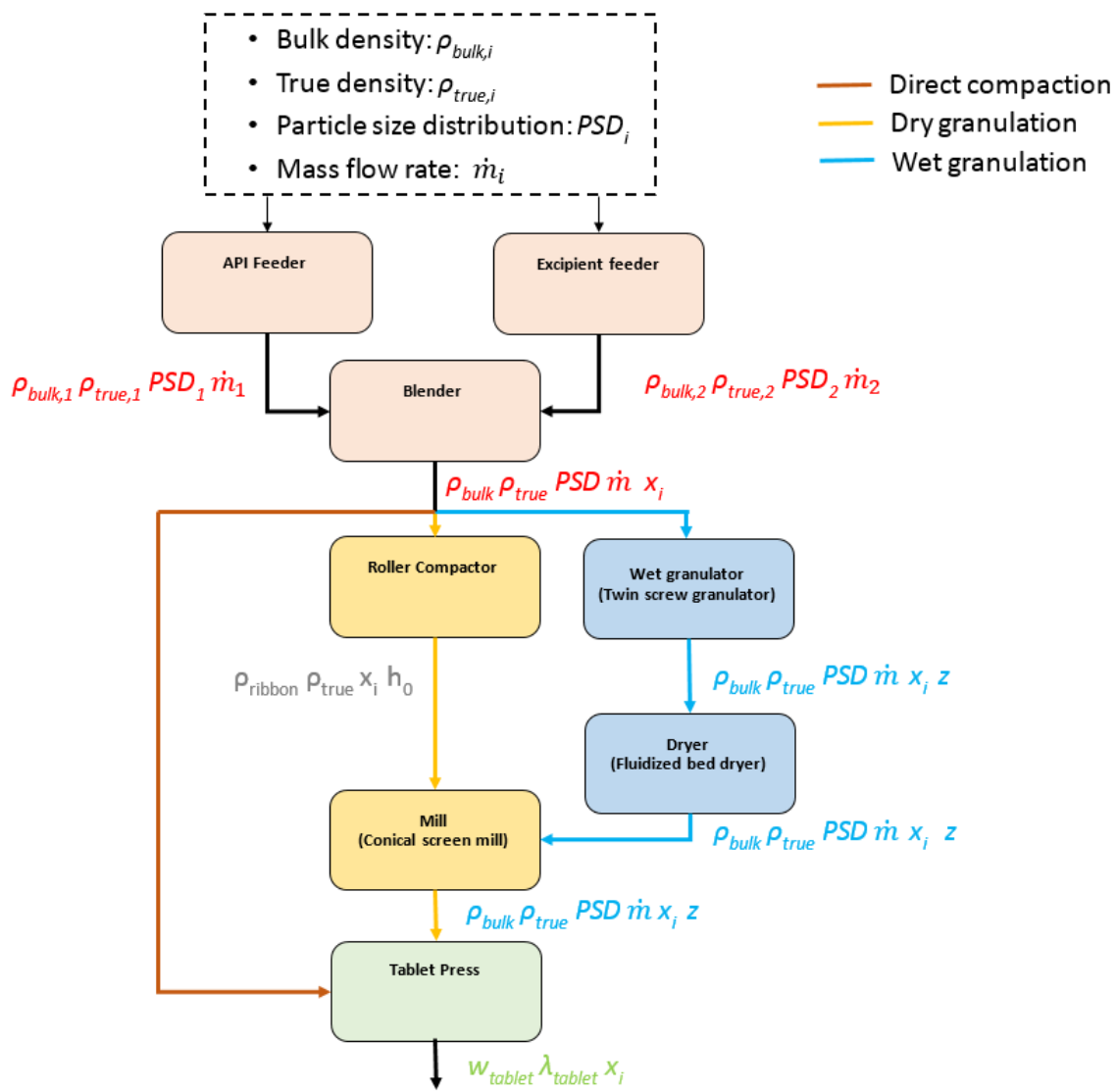


Figure 2.2 Schematic of an integrated flowsheet model for direct compaction, dry granulation and wet granulation routes of pharmaceutical manufacturing

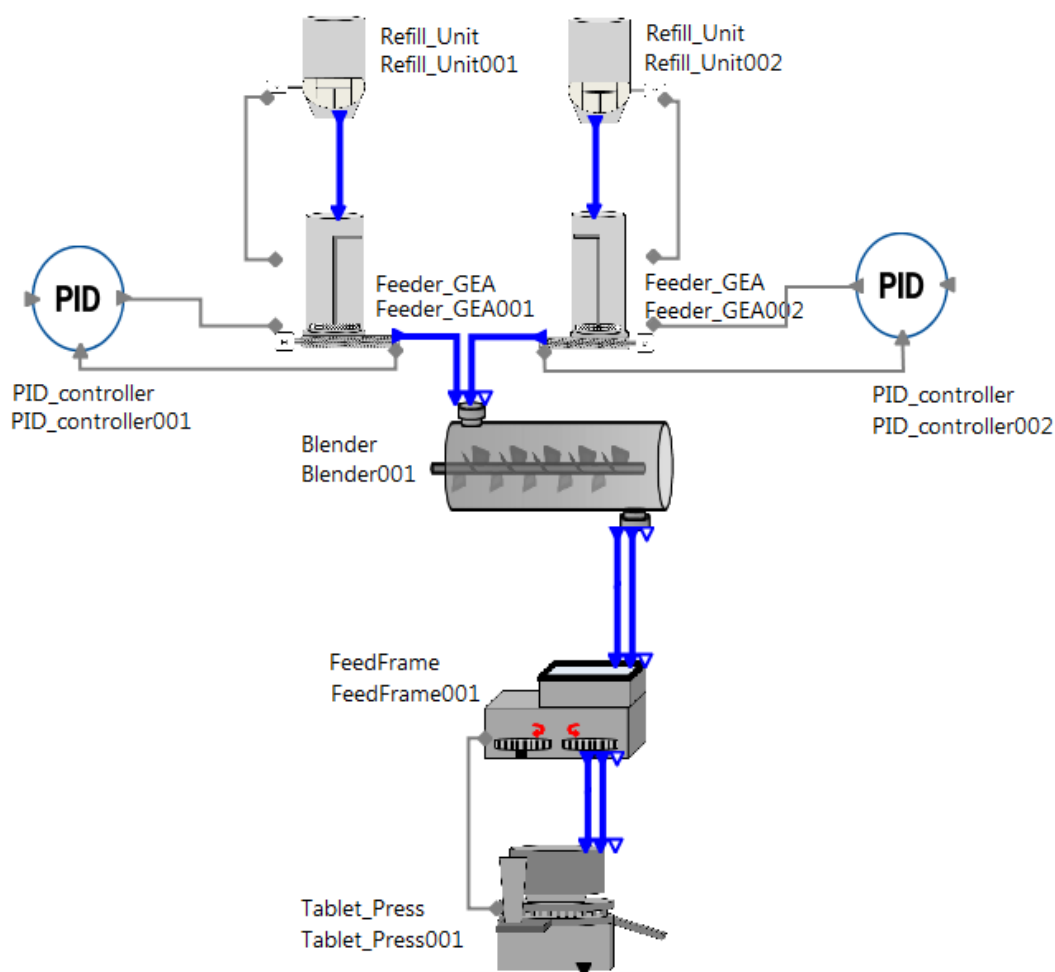


Figure 2.3 Schematic of an integrated model developed in gPROMS™

Previous work on the development of flowsheet models are restricted to direct compaction [12-14, 89] and dry granulation routes [15, 81] for continuous solid oral dosage manufacturing. Park, Galbraith [15] created a flowsheet model of a continuous dry granulation process and applied it for optimization. Boukouvala, Chaudhury [90] developed a flowsheet model for the wet granulation route. This model served as a proof-of-concept and with no connection to specific experimental data. The work done in this dissertation primarily focuses on the wet granulation route. A holistic study on the process development of the wet granulation manufacturing route is a research gap which is intended to be addressed in this dissertation.

2.3 Design space of pharmaceutical processes

A design space is the multidimensional combination and interaction of input variables (e.g., material attributes) and process parameters that have been demonstrated to provide assurance of quality [18]. Traditional methods for identification of design space of processes include designing experiments considering multiple responses to investigate all the factors considered and developing multiple response surface models [91, 92]. A ‘sweet spot’ or an optimal region is obtained where the acceptable regions of multiple responses overlap. The challenge is that if the resulting overlap is too small, the experimental design may need to be reconsidered, leading to waste of expensive material and sub-optimal use of resources. In addition, model parameter uncertainty and sensitivity to factor disturbances are not considered in this approach [93]. Design space of pharmaceutical processes is closely related to the concepts of process feasibility, flexibility and resiliency [94] generally applied for the chemical industry. The motivation for these concepts was to incorporate operability considerations at design stage. Feasibility is the ability of a process to satisfy all production, operating, safety and quality constraints. Early concept of process feasibility was formulated [95] in terms of a flexibility test problem. The flexibility index problem determines a quantitative measure which indicates the extent of flexibility that can be attained in a given parameter range. The term ‘design space’ is used by the pharmaceutical industry as an operating envelope identified with an experimental basis. The term ‘feasible region’ is used by the process systems engineering community to identify this envelope using mathematical tools. These terms are used interchangeably in this dissertation.

Analytical methods to solve for the flexibility problem includes the vertex solution method [96] which considers the vertices of the uncertain parameter set as the critical points under some convexity conditions. However, this method requires solving optimization problem at an exponential number of vertices for higher dimensional problem. Also, in cases of non-linear

constraints, the feasible regions could be nonconvex, and the vertices may not be the critical points. The active-set method [97] could be used where the flexibility test problem and the flexibility index problem are formulated as a two level optimization problem. However, this also requires the constraints to be differentiable and available in closed-form. Laky, Xu [98] applied the flexibility index concept to identify a probabilistic design space of pharmaceutical processes. Here, uncertainty in model parameters was considered to exist. The flexibility index problem was solved in terms of the model parameters and a probability map was generated over several process parameter values. Of more interest in this dissertation are data-based methodologies which do not require problems to be solved analytically, as the models for pharmaceutical are generally complex in nature and derivatives are difficult to evaluate. The simplicial approximation approach proposed by Goyal and Ierapetritou [99] measured the feasible region by evaluating inner and outer approximations of the feasible region. Points are determined at the boundary of the feasible region and a convex hull defined by these points is evaluated. However, this requires several function evaluations and is not applicable for nonconvex feasible regions. Building on this idea, Banerjee and Ierapetritou [100] proposed surface reconstruction approach by sampling points and constructing polygonal representation of the feasible region. While the method is successful in identifying disjoint and nonconvex feasible regions, large sampling costs are incurred which is a limitation for computationally expensive models.

During the past decade, the need to develop predictive models for complex processes accompanied by advances in computational capabilities has led to the evolution of higher fidelity models, which incur high computational cost. The feasibility analysis methods discussed so far cannot be applied to these models as they require high number of function calls which is prohibitive for such models. Also, they have constraints that are not available in closed-form or function derivatives are difficult to evaluate. Surrogate based methods have gained prominence to address problems of such nature as these methods treat the models as 'black-boxes'. In this class of methods, a surrogate model is

used to approximate the computationally expensive model for identifying the feasible region. Banerjee, Pal [101] used a HDMR surrogate model to approximate the original model and used the computationally inexpensive surrogate to identify the feasible region. Kucherenko, Giamalakis [102] used HDMR as a metamodel to represent the design space in case of uncertainty in model parameters. Rogers and Ierapetritou [103] used kriging as the surrogate model to approximate the original function for identifying disjoint and nonconvex feasible regions with limited sampling. Wang and Ierapetritou [104] used RBF surrogate model which performed comparable to kriging surrogate model. In some of these approaches, an adaptive sampling methodology is used, where samples are identified in regions that are of high interest such as regions where the surrogate model prediction errors are high or regions that are expected to be feasible. However, these approaches showed limitations or did not illustrate examples in identifying feasible regions in high dimensional problems. In this dissertation, the goal is to develop a methodology of identifying feasible regions in low as well as high dimensional problems. The methodology will be applied to the integrated continuous process models to support identification of design space.

Chapter 3

Multi-scale model development of a continuous comilling process

3.1 Background

The population balance model (PBM) approach is widely used to model breakage, crystallization and settling processes in various industries such as mining, food, chemical, metal, pharmaceutical etc. [105-108]. Modeling breakage processes through PBMs requires the formulation of a breakage kernel that represents the breakage phenomenon. Kernels used in the past [49, 109] are empirically formulated where material properties, process conditions are not explicitly incorporated in the equations. This limits its applicability when process parameters and/or material properties are changed. Per the QbD paradigm, companies are required to demonstrate the ability to predict the effect of material properties and process parameters on product attributes. The impact of variation in material properties or process conditions on product quality is more significant as disturbances can propagate downstream [110]. The use of semi-empirical breakage kernels in a PBM based approach to model comilling operation limits its applicability when the milling conditions or the material processed is changed. In addition, a PBM does not capture particle-scale interactions that would add more accuracy to the model. Discrete element method (DEM) models on the other hand, have the potential to bridge this gap.

In the current work, an iterative algorithm is proposed to estimate material specific parameters of an energy based mechanistic kernel [54]. Particle breakage is incorporated into the DEM model via a ‘threshold energy’ which is a material specific parameter used in the energy based kernel. Full extent of the effect of mill geometry on particle population inside the comill through screen

thickness, screen hole size, impeller shape and speed, is incorporated into DEM model. The specific purposes of this study are to:

- Develop a multi-scale framework for a milling process where material specific properties are explicitly incorporated.
- Demonstrate the structure and validity of the framework using two case studies.
- Determine the material specific kernel parameters for a given material and process variables known from experiments, such as milled product particle size distribution, hold up, process time required to reach steady state.
- Validate the proposed framework via comparing predicted and experimental process output variables.

3.2 Modeling methods

3.2.1 Multiscale modeling framework

An overview of the multiscale modeling framework involving DEM, PBM, and input from experimental data is shown in Figure 3.1. The DEM model implements particle breakage through particle replacement i.e., a particle is replaced by smaller size daughter particles when a breakage criteria is met. The breakage criteria in DEM is implemented through a ‘threshold energy’, which is a material specific parameter whereby a granule is replaced by smaller size granules when the impact energy of the granules exceeds the threshold energy. An iterative algorithm is used where the threshold energy is estimated for every iteration using PBM calibrated with experimental data. The PBM uses mechanistic data from DEM simulations. DEM simulations are run with the updated threshold energy value and mechanistic data obtained from the simulations are given as input to PBM through energy based kernel. Details of the PBM and DEM models used are discussed in

Sections 3.2.2 and 3.2.3 respectively, followed by details of the implementation of the iterative algorithm which forms the basis for the multiscale PBM-DEM framework.

To demonstrate the proposed framework, two case studies are considered. The first case considers 1 mm feed material with breakage implemented in DEM, assuming kernel values are known. The second case considers 1 mm feed material with breakage implemented in DEM, assuming kernel values are unknown and uses information from experiments including milled product particle size distribution, hold up amount, time required for the process to reach steady state, which hereafter will be referred to as ‘steady state time’. For this work, we utilize computer generated data from the PBM to be the virtual experimental data.

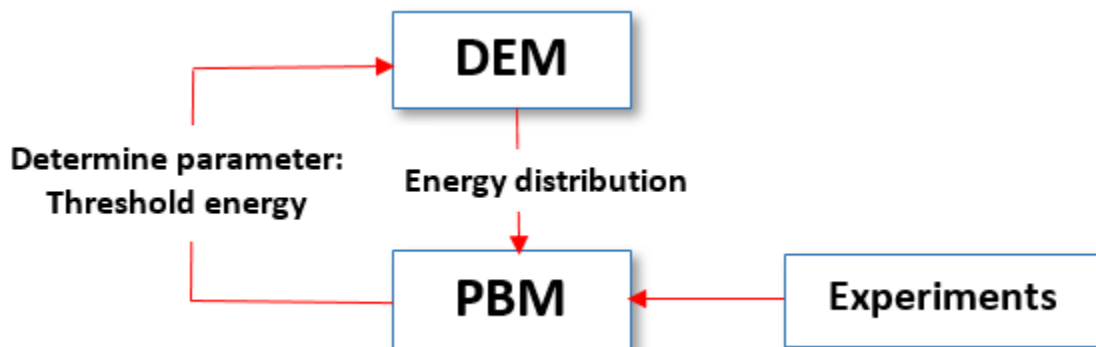


Figure 3.1 PBM-DEM framework for modeling continuous comminution process

3.2.2 Population balance model (PBM)

A PBM is used to track the change in the mass of particles of a certain property over time. For a milling process, the number of particles change due to breakage. A 1-D PBM model developed and validated previously [111] for ribbons from a roller compactor is used in this work. Equation 3.1 represents the change in mass of particles $M(x,t)$ of a certain diameter x with time t .

$$\frac{dM(x,t)}{dt} = \mathbb{R}_{form}(x,t) - \mathbb{R}_{dep}(x,t) + \dot{M}_{in}(x,t) - \dot{M}_{out}(x,t) \quad 3.1$$

A continuous feed rate of 4 kg/hr is used as $\dot{M}_{in}(x,t)$. Flow rate out of the mill is determined based on the use of a parameter $\Delta = d_{screen} * \delta$ where, δ is referred to as critical screen size ratio and d_{screen} is the screen size used. If the size of the particle is less than Δ , it exits the mill instantaneously. If the size of the particle is greater than the screen size, it does not exit the mill. If the size of particle is within these limits, a linear function is used to determine the flow rate out of the mill as given in Equations 3.2 and 3.3.

$$\dot{M}_{out}(x,t) = (\mathbb{R}_{form}(x,t) - \mathbb{R}_{dep}(x,t) + M_{in}(x,t))(1 - f_d(x)) \quad 3.2$$

$$\text{where } f_d(x) = \begin{cases} 0 & \text{for } x \leq \Delta \\ \frac{x - \Delta}{d_{screen} - \Delta} & \text{for } \Delta \leq x \leq d_{screen} \\ 1 & \text{for } x > d_{screen} \end{cases} \quad 3.3$$

The breakage distribution function $b(u,w)$ represents the distribution of the daughter particles formed when a particle of volume w undergoes breakage. A log-normal distribution function as given in Equation 3.4 is used in this work based on published work that successfully predicts milling process using this distribution [112, 113]. $C(w)$ is introduced to ensure mass conservation holds such that the sum of mass fractions of all daughter particles (volume u) formed from a parent particle (volume w) must be equal to 1 as given in Equation 3.6. The breakage kernel $K(w)$ defines the probability that a particle of volume w undergoes breakage. The kernel usually takes semi-empirical forms such as a shear rate or impeller speed based kernel as given in Equation 3.5, where v_{imp} is the impeller speed or power law based kernel [114]. The breakage kernel is used to formulate the rates of formation \mathbb{R}_{form} and depletion \mathbb{R}_{dep} . P_1, P_2, n, σ and δ in Equations 3.4 and 3.5 are

model parameters that are estimated from milling experiments. A cell average technique is used to discretize and solve the population balance equations. More details on the numerical solution can be found in Barrasso, Oka [111].

$$b(u, w) = \frac{C(w)}{u\sigma} \exp \left[\frac{-(\log u - \log \left(\frac{w}{n}\right))^2}{2\sigma^2} \right] \quad 3.4$$

$$K(w) = P_1 v_{imp} \frac{w^{P_2}}{w_{ref}} \quad 3.5$$

$$\int_0^w b(u, w) du = 1 \quad 3.6$$

3.2.3 Discrete element method model

DEM is used to simulate discrete matter via the use of contact laws to model inter-particle interactions. In this study, the Hertz-Mindlin (no slip) contact model is used as it is well suited for non-cohesive interactions between spherical materials. The contact model has been widely used in the literature [53, 115, 116]. More details on the contact model can be found in other sources [117-119]. Commercial DEM package EDEM (EDEM solutions, 2.7) is used and EDEM API (Advanced Programming Interface) is used to model particle breakage.

AutoCAD® software is used to develop the 3D drawing of the mill geometry consisting of the feed wall, screen, impeller and collection bin as shown in Figure 3.2. The dimensions of the geometry are set to represent the laboratory scale comill unit (Quadro 197-S, Quadro Engineering, Ontario, Canada). A screen of 990 µm hole size, screen thickness 0.7874 mm, 25% open area and a square edged impeller are used. A continuous feed rate of 4 kg/hr is introduced through the virtual feeder.

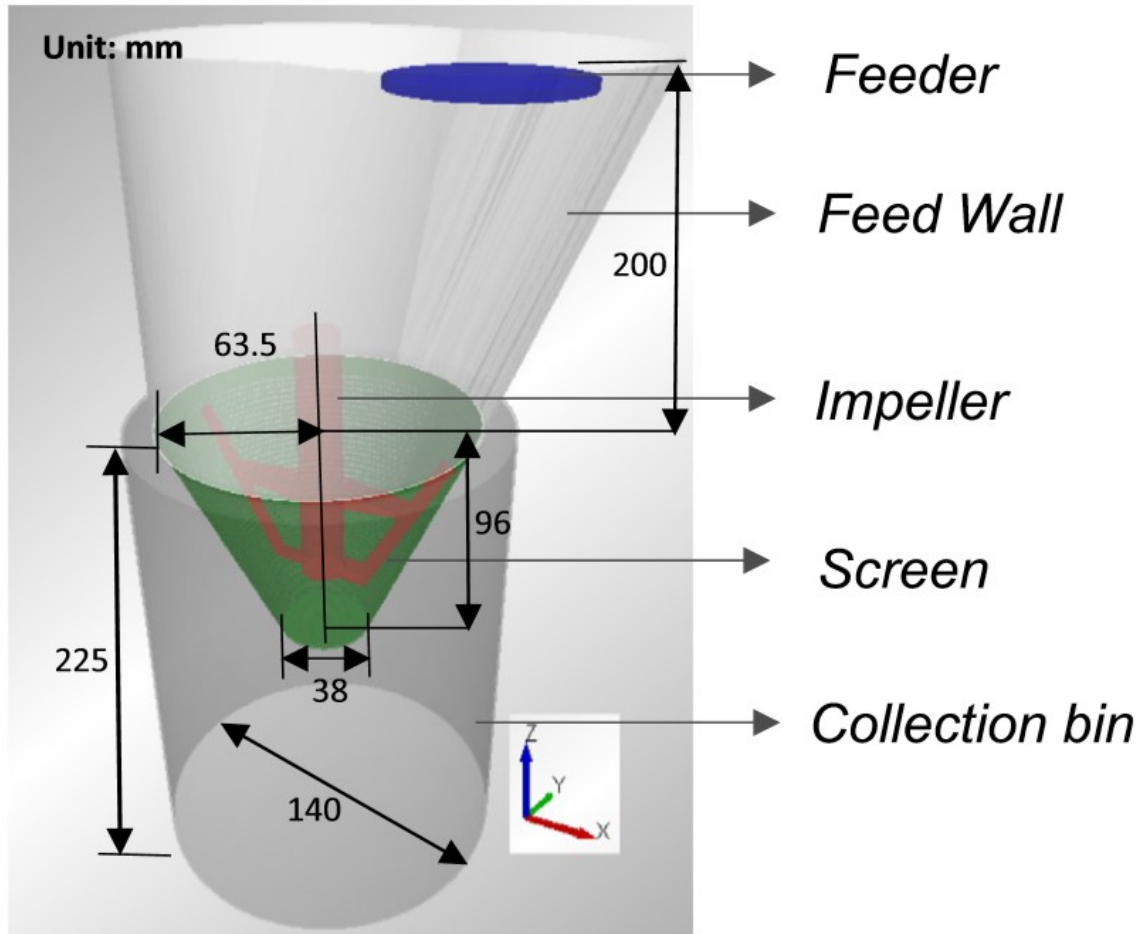


Figure 3.2 Geometry of the comill used in DEM simulations

For the equipment properties, typical steel properties are used [120] (density 7900 kg/m^3 , poisson's ratio 0.3, coefficient of restitution 0.5, shear modulus 77 GPa). For the particles, a density of 860 kg/m^3 is used to model pharmaceutical material. An effective particle density is used that is calculated from particle true density of 960 kg/m^3 and granular porosity of 0.1. Poisson's ratio, coefficient of restitution and shear modulus are taken as 0.3, 0.5, 1MPa respectively. The coefficient of static and rolling friction are taken as 0.5, 0.01 respectively for steel as well as particles based on values used in Marigo, Cairns [121] for particles. The effect of these parameters on DEM simulations is out of the scope of this work, however, these values can be changed based on calibration from experimental data as described in other sources [122-124].

Particles in the comill break as a result of being subjected to stresses from particle-particle collision, particle-impeller collision or particle-screen/wall collision. The profile of energy of each particle over time is a representation of the time history of collisions experienced by the particle. The energy distribution can be defined either as collision energy or dissipation energy, both of which are available in DEM. A study by Capece, Bilgili [54] showed that the collision energy does not differentiate between a small particle impacting a stationary larger particle and vice versa as the relative velocities and reduced mass is the same in both cases. However, when dissipation energy is considered, a lower value is obtained when a small particle impacts a stationary larger particle, thus differentiating between two scenarios. Hence, energy distribution in this work is defined as dissipation energy which is based on normal and tangential contact forces given in Equation 3.7 [125].

$$E = [F_{n,d} v_n + F_{t,d} v_t] \Delta t \quad 3.7$$

where F and v denote force and velocity respectively, subscript ' n ' and ' t ' denote their normal and tangential components respectively and subscript ' d ' denotes dissipation component of force over an incremental time period Δt .

In this work, breakage in DEM is modeled via particle replacement strategy [126]. The EDEM API is used to set a rule that a particle breaks if the energy (E) lost by a particle during contacts given by Equation 3.7 exceeds a minimum impact energy (E_{min}). Since, particles in the mill will be of various sizes, a size dependence of the minimum impact energy is used. If x is the diameter of the particle, $x E_{min}$ is taken as a constant material property (E_{const}) [127] i.e., a smaller particle needs higher energy to break when compared to a larger particle. When $E > E_{min}$, as calculated in EDEM API, the particle is removed from the simulation and instantaneously replaced by a group of daughter particles in the space occupied by the mother particle. The number and size of daughter

particles can be determined from experimental data or using mechanistic basis as described by Reynolds [43], Loreti, Wu [128]. However for the purposes of demonstration of the framework, the daughter particles in this work are chosen as two particles of half the volume each of parent particle. The geometric orientation of the daughter particles is determined using a random function in EDEM API. In addition, a minimum particle size limit of 350 μm is set in DEM as experimental particle size measurements showed that less than 1.5% of mass of milled product is below 350 μm .

An illustration of the particle replacement strategy and its implementation in EDEM API is shown in Figure 3.3 and Figure 3.4. At the beginning of a time step, impeller moves per the set rotation speed. Particles are generated or updated based on previous time step. Particle-particle, particle-geometry contacts are detected and the corresponding calculations are done. If the energy lost calculated is greater than the threshold energy for the particle, it is deleted and replaced by daughter particles. Once all the contacts are processed and particle population is updated, the next time step is processed. This loop is implemented till the final simulation time is reached.

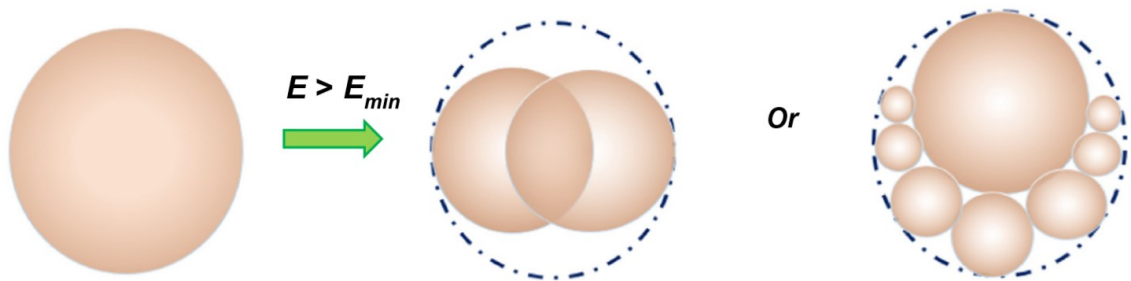


Figure 3.3 Modeling breakage in DEM using particle replacement

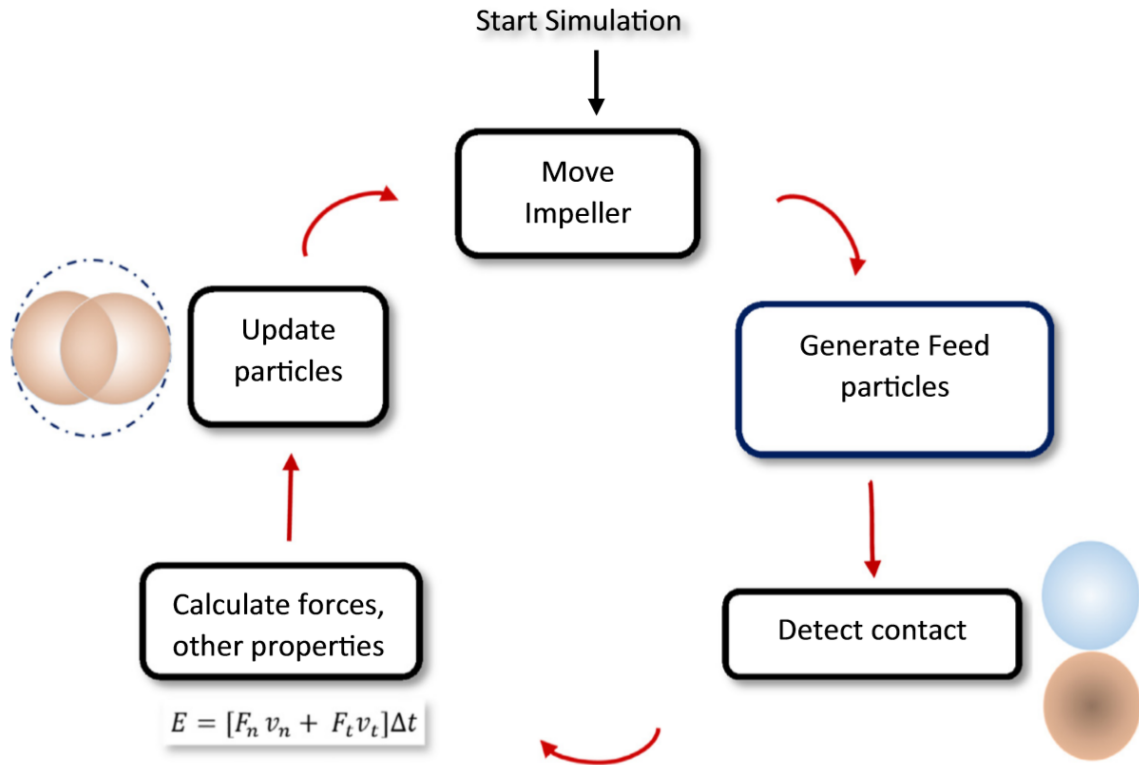


Figure 3.4 Breakage model implementation in EDEM API [129]

3.3 PBM-DEM framework

3.3.1 Energy based kernel

To establish a PBM-DEM framework for determining material specific kernel parameters the development of an energy based breakage kernel by Capece, Bilgili [54] is utilized. The energy term in this breakage kernel is multiplied by the frequency of collisions to account for multiple impacts on particles. For the i^{th} bin of diameter x_i , the breakage kernel is given by Equation 3.8 where, $f_{coll,i}$ is frequency of collisions of particles in i^{th} bin defined as number of collisions per particle per second as obtained from DEM simulations. Here, $E_{i,min} = \frac{E_{const}}{x_i}$ where x_i represents the size of particles in i^{th} bin. E_i is the mass specific energy of particles with energy greater than the

threshold energy. Only particles with ‘contributing energies’ i.e., energies of particles greater than threshold energy are considered in the kernel as these lead to breakage of particles.

$$K_i(t) = f_{mat} x_i f_{coll,i}(E_i - E_{i,min}) \quad 3.8$$

With the formulation of the energy based kernel as explained above, the impeller speed based empirical kernel as given in Equation 3.5 can be replaced by a kernel that captures particle scale information from the DEM model. This leads to the establishment of PBM-DEM framework to estimate material specific parameters f_{mat} and E_{const} . The non-kernel related parameters n , σ , and δ are set at the values used to generate the milling experimental data as explained in Section 3.5. The algorithm for the detailed framework is then explained in the following steps:

Step 1: Assume a value for E_{const} . A good starting point is to run short DEM simulations without breakage and study the energy values to guess a plausible E_{const} value.

Step 2: Run DEM simulations with breakage and threshold energy equal to E_{const} for at least two impeller speeds (say 1750, 2500 rpm) for about 40s, as experiments indicate this is approximately the time required to reach constant flow rate of milled product.

Step 3: Obtain energy distribution data from DEM simulations. These values are given as inputs to PBM for every size class and time interval Δt utilizing Equation 3.8.

Step 4: Steady state PSD, hold up, and steady state time from milling experiments are fit to the PBM and the parameters f_{mat} and E_{const} are estimated. The objective function given in Equation 3.9 is minimized to estimate the parameters f_{mat} and E_{const} .

$$\begin{aligned} \varphi(\theta) = \sum_{j=1}^2 [PSD_{j,expt} - PSD_{j,sim}]^2 + [holdup_{j,expt} - holdup_{j,sim}]^2 \\ + [SStime_{j,expt} - SStime_{j,sim}]^2 \end{aligned} \quad 3.9$$

where *SStime* refers to steady state time and subscripts '*j,expt*' and '*j,sim*' refer to experimental and simulated values for the *j*th impeller speed respectively.

Step 5: The estimated E_{const} in step 4 is used back in step 2.

The iterations continue until the convergence criterion is met. At the end of the algorithm, f_{mat} and E_{const} are estimated along with the energy distribution data which can now be used in PBM. The framework is graphically illustrated in Figure 3.5.

The purpose of using a PBM in this framework is as follows:

- **Estimate the constant material properties E_{const} and f_{mat} .** This is achieved via calibration of PBM from experimental data and estimation of parameters. If the value of E_{const} is not known, a valid DEM model cannot be setup as the breakage condition in DEM is dependent on E_{const} .
- Determination of E_{const} from experimental data alone was done by Capece, Bilgili [53]. However, this required additional experiments to be done in a batch process for all of the size fractions using mono sized feeds and measurement of broken particle mass at various time points. In the absence of such feed, an empirical kernel is assumed in the PBM and parameters of this kernel are estimated through least squares fitting of known experimental data such as milled product particle size distribution [109, 111]. However, this approach inherently accepts the empirical nature of the kernel and thus limits its applicability when material or any other experimental conditions such as feed rate are changed. Another issue

is the amount of material required to perform these experiments. To obtain a mono sized feed for lower size fractions, a large amount of material is required as the mass percentage of low size fractions in granulated product is relatively low. The proposed framework does not need milling experiments using mono sized feed material, while also replacing the empirical formulations of the kernel with mechanistic kernel. The circumvention of experiments with mono sized feeds is especially an advantage for pharmaceutical granules as the preparation of such feed is laborious as well as leads to wastage of large amounts of expensive pharmaceutical ingredients.

Hence, a combined DEM-PBM framework, where the parameters are determined via calibration of PBM model is more efficient as the number of experiments as well as quantity of raw material required is considerably low.

- **Design, control and optimization of the process.** Once the parameters E_{const} and f_{mat} are estimated and the relationship between energy distribution and impeller speed is captured, DEM simulations can be run in standalone for milled product PSD prediction. However, PBM is much faster to run than DEM, which is required for inline control and process optimization. Hence, PBM can be used to represent the particle scale energy distribution data obtained in DEM and thus the prediction of PSD can be achieved. While a surrogate model can be used to represent the relationship between impeller speed and particle size distribution obtained in DEM, this will reduce any mechanistic understanding achieved from a DEM model to a ‘black box’. This is undesirable as it limits the usability of the model. However, a PBM which is formulated using kernel and fragment distribution function representing a breakage process, retains the intuitive understanding of breakage and expands its applicability when process conditions or materials are changed. While energy distribution of granules at various impeller speeds is still needed, this can be

achieved via building a surrogate model that captures this relationship and can be used in PBM kernel, thus making the framework eventually independent of the DEM runs.

In order to ensure the identifiability of parameters f_{mat} and E_{min} , and support the choice of objective function given in Equation 3.9, sensitivity analysis is performed as described in the following section.

3.3.2 Sensitivity analysis

Sensitivity analysis is the study of attributing the cause and extent of variability in the model response to various input variables. It can be utilized to quantitatively analyse the importance of model parameters with respect to variability in the model response [130]. The use of sensitivity analysis in the context of parameter estimation for multi scale models has been explored by many researchers [131, 132]. In the current work, variance based sensitivity analysis is used to determine the extent of the effect of the material specific parameters f_{mat} , E_{const} and non-kernel related parameters n , σ , and δ on the outputs of the PBM model; particle size distribution, steady state time as well as objective function value as given in Equation 3.9. Sobol's method of computing sensitivity indices [133] to assess impact of each of the parameters is used. The sensitivity indices are computed based on evaluations of the model at various values of the parameters. The lower and upper bounds for the parameters used in this work are listed in **Error! Reference source not found.** $N(k+2)$ sampling points are taken for function evaluations, where k is the number of parameters used in this model ($k=5$) and $N=1000$ is used in this work based on recommended minimum number of 500 [134].

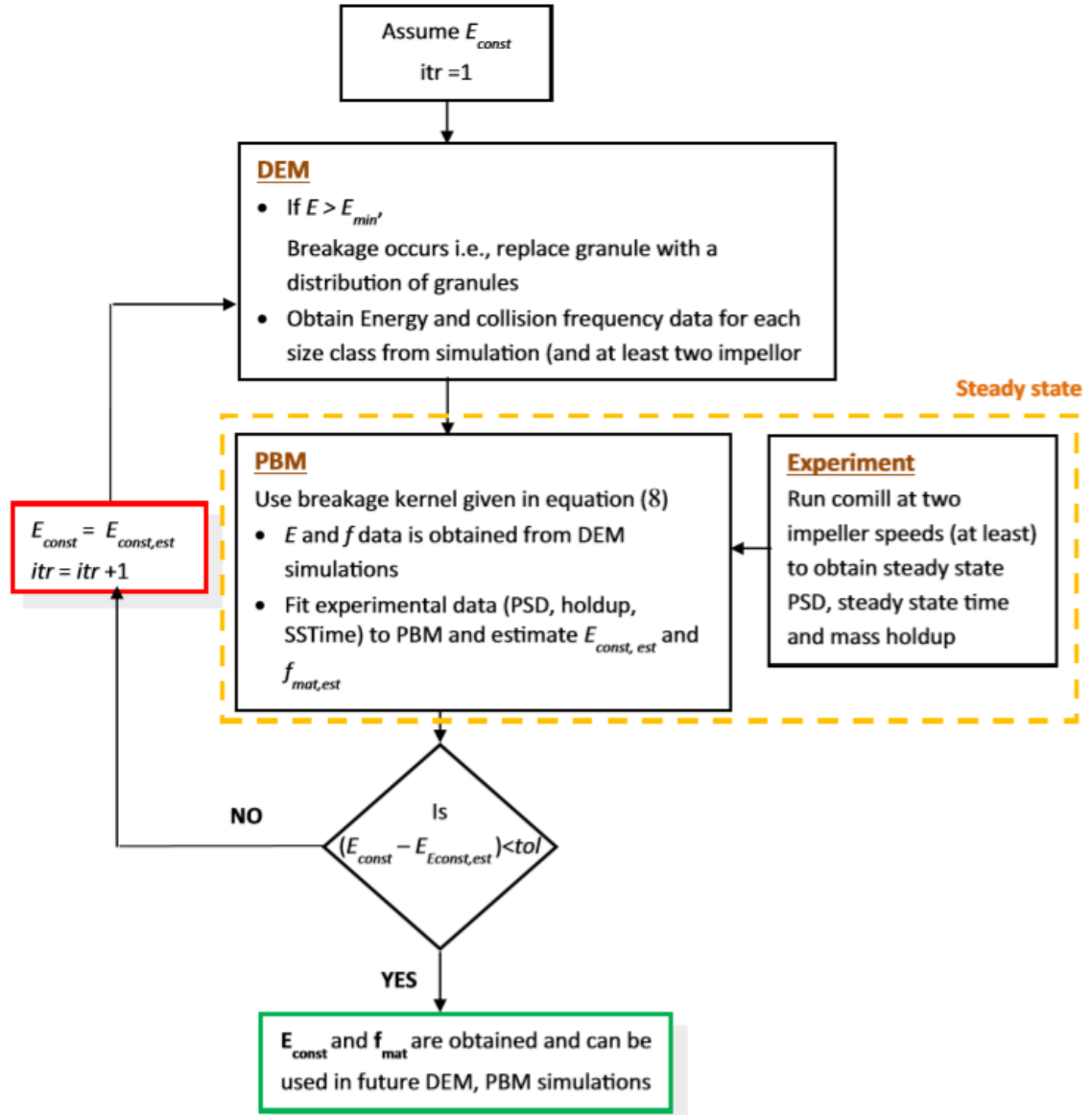


Figure 3.5 PBM-DEM framework

Let $Y=f(X_1, X_2, \dots, X_k)$ be a scalar model output i.e., a function of k model parameters. If X_i is i^{th} factor, \mathbf{X}_{-i} is matrix of all factors except i . If N is the total sample size, \mathbf{A} and \mathbf{B} are two sample matrices of input factors of size $N \times k$. \mathbf{A}_B^i is matrix where column i comes from matrix \mathbf{B} and all other $k-1$ columns come from matrix \mathbf{A} . More details on the choice of \mathbf{A} and \mathbf{B} matrices are explained by Saltelli, Annoni [133].

If V , E are variance and expected values respectively, then total sensitivity index S_{Ti} is given by Equation 3.10.

$$S_{Ti} = 1 - \frac{E_{\mathbf{X}_{\sim i}} [V_{\mathbf{X}_i}(Y|\mathbf{X}_{\sim i})]}{V(Y)} \quad 3.10$$

$$\text{where } E_{\mathbf{X}_{\sim i}}(V_{\mathbf{X}_i}(Y|\mathbf{X}_{\sim i})) = \frac{1}{N} \sum_{j=1}^N f(\mathbf{A})_j (f(\mathbf{A})_j - f(\mathbf{A}_B^i)_j) \quad 3.11$$

A higher value of sensitivity index S_{Ti} implies a higher effect on the response variable. Figure 3.6 shows a sensitivity index plot for the PBM-DEM model, where energy data corresponding to a threshold energy of 0.03 J m/kg and impeller speeds of 1750 and 2500 rpm are used in the PBM. The plots indicate E_{const} and f_{mat} are significant parameters in the PBM-DEM model. PSD(1), PSD(2), PSD(3) and PSD(4) shown in Figure 3.6, refer to the mass fraction in the smallest four bins of the milled product particle size distribution. The effect of these parameters is evident in particle size distribution, as well as holdup and steady state time output variables, which supports the choice of objective function as given in Equation 3.9 that includes all these output variables.

Table 3.1 Range for model parameters used for sensitivity analysis

	Lower bound	Upper bound
f_{mat}	1e-5	10
E_{const}	0	0.1
n	1	10
σ	0.5	5
δ	0	1

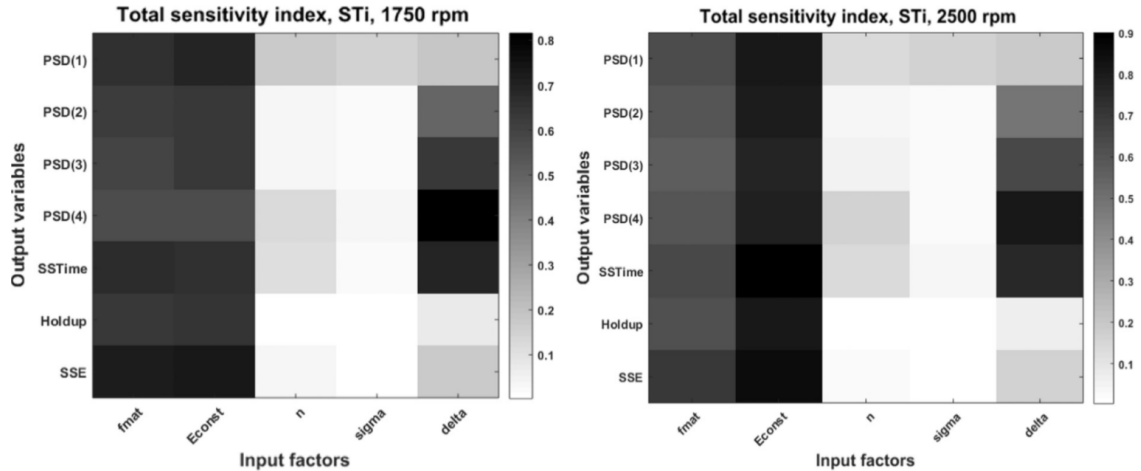


Figure 3.6 Total sensitivity index plot with energy data from DEM simulations with $E_{const} = 0.03$ J m/kg and impeller speeds of 1750 rpm and 2500 rpm

3.4 Qualitative comparison with experiments

In this section the effect of the threshold energy parameter on milling dynamics is demonstrated through experiments and the DEM-PBM framework developed. The threshold energy parameter reflects in the strength of granules or granule friability. Specifically, the goals are two-fold:

- Evaluate the effect of granule strength on the particle size evolution of granule through experiments
- Demonstrate that the DEM-PBM framework can qualitatively predict the effect of granule strength on breakage through particle size evolution profiles

Since a conical screen mill has a screen that allows exit of granules based on relative size of the granule to the screen, the effect of granule properties on particle size distribution is more apparent in the absence of a screen. Specifically, the screen holes were covered using an aluminium foil to eliminate exit of granules. It is important to note that the breakage of granules due to impact and

shear from the screen and the impeller is not affected. The experiments conducted were designed to reflect this.

Two batches of granules are prepared using a high shear granulator. The granule strength is varied between the two batches through liquid to solid ratio and wet massing time. The formulation used to prepare the granules using the high shear granulator is given in Table 3.2. Using the ingredients in the given formulation, the powders were blended in a tote blender (Glatt tumble tote blender) for 30 minutes. Following this, the pre blended powders were granulated in a 2.4 L batch granulator (Key-International table-top high shear granulator) at certain granulator settings. The granulation process parameters used in this work are given in Table 3.3. These settings are chosen based on work previously published [135]. Granule porosity is expected to be inversely proportional to granule strength. Based on this, the process parameters that yield low and high porosities are chosen. Batch 1 with low expected porosity (23.78%) has high strength granules and Batch 2 with high expected porosity (59.72%) has low strength granules. Particle size distributions of the batches are measured using sieve analysis measurement. The wet granules thus prepared in the high shear granulator are air dried for 48 hours before milling in a conical screen mill (Quadro® 197-R). In each milling experiment, a fixed mass of granules was milled at a fixed impeller speed. The purpose of fixing these parameters is to demonstrate the effect of granule strength. Each batch of granules are milled for 90 s and 5 min. Particle size distributions at the end of milling are measured using sieve analysis measurement.

Table 3.2 Formulation components and percentages

Ingredient	% w/w
Caffeine	8
Polyvinylpyrrolidone (PVP)	4
MCC Avicel PH 101	44
α -lactose monohydrate	44

Table 3.3 Batch Granulation settings

Batch	LS ratio	Wet massing time, min	Chopper speed, rpm	Expected Porosity, %
1	0.55	5	6000	23.78
2	0.35	1	6000	59.72

The evolution of particle size distributions as observed experimentally are plotted in Figure 3.7. The figure shows that the change in PSD for the Batch 1 (solid lines) proceeds at a slower rate when compared to the change in PSD for Batch 2 (dashed lines). This demonstrates the effect of granule strength on the dynamics of particle size evolution. The granule strength is synonymous to the ‘threshold energy’ parameter used in the DEM-PBM framework developed for the mill.

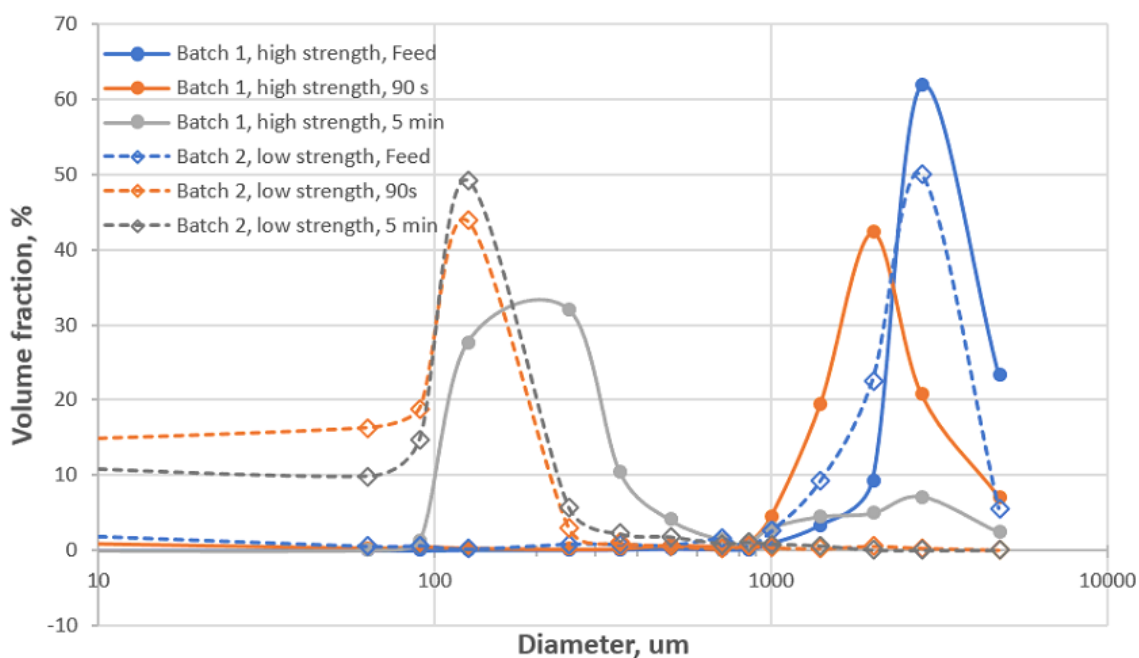


Figure 3.7 Particle size distribution of feed and milled granules (at 90 s 300 s) for Batch 1 (high strength, solid lines) and Batch 2 (low strength, dashed lines)

A successful implementation of the framework should show similar trends in the prediction of particle size distribution. To demonstrate this, DEM simulations are run using a geometry that

reflects the experimental setup i.e., the screen is only a hollow fulstrum and does not have holes for granules to exit. The DEM geometry used in the simulations is shown in Figure 3.8. 100 g of granules are introduced into the geometry through a virtual feeder. The particle size distribution of the granule feed used in the simulations is similar to the PSD measured experimentally. It may be observed that the PSD of feed for Batch 1 and 2 has a high volume fraction in the size bin of 2.8 mm. The particle size distribution of the feed used in the DEM simulations is given in Table 3.4. A high threshold energy is simulated using a hypothetical value of 0.8 J m/kg and a low threshold energy is simulated using a hypothetical value of 0.6 J m/kg. The DEM simulations are run for 10 s. Energy and collision frequency values are recorded and used in the PBM through the energy based breakage kernel. In addition, the PBM also reflects the conditions of batch feed i.e., $\dot{M}_{in} = 0$ and absence of exit of granules i.e., $\dot{M}_{out} = 0$. The resulting particle size distribution profiles for Batch 1 (high threshold energy) and Batch 2 (low threshold energy) are plotted in Figure 3.9 and Figure 3.10 respectively. For profiles with low threshold energy, the PSD at 90 s reflects much larger granule size compared to the profile at 300 s. However, the profiles with high threshold energy show minor change from 90 s to 300 s. From these comparisons, it is apparent that the DEM-PBM framework can predict qualitative trends in the PSD evolution as observed in the experiments.

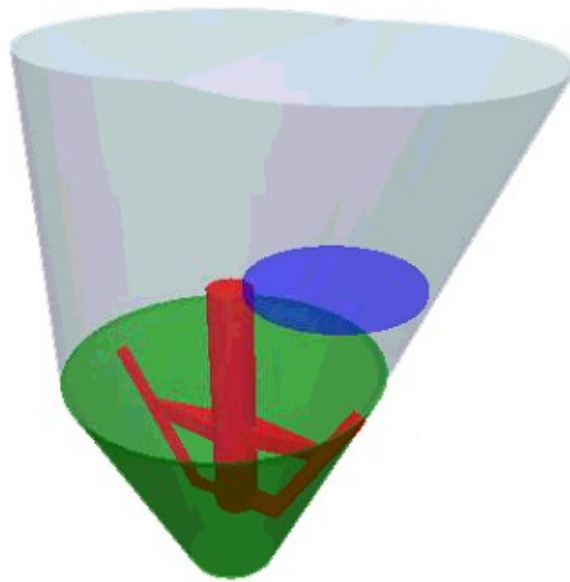


Figure 3.8 Geometry used in the DEM simulations

Table 3.4 Particle size distribution of the feed used in the DEM simulations

Mass %	Size, μm
25.4	1980
64.6	2800
10.0	3960

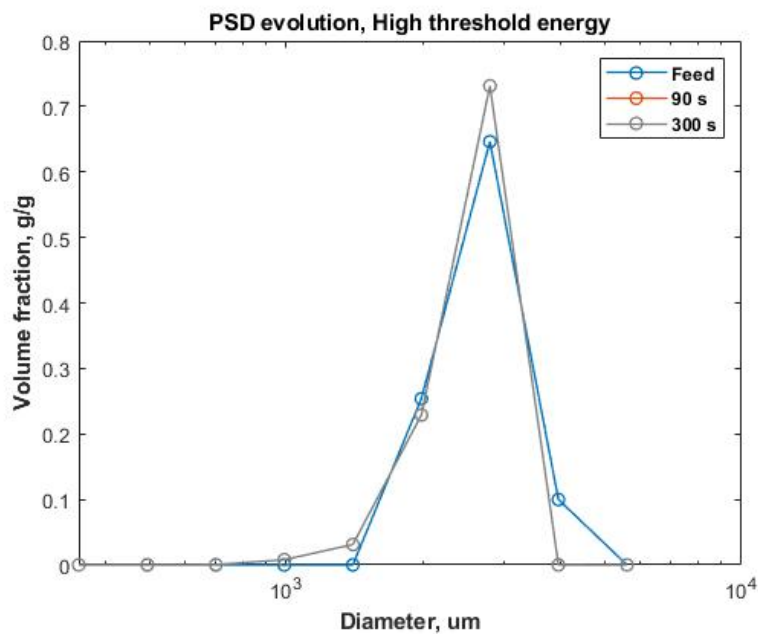


Figure 3.9 Prediction of evolution of particle size distribution from the DEM-PBM framework, High threshold energy 0.8 J m/kg

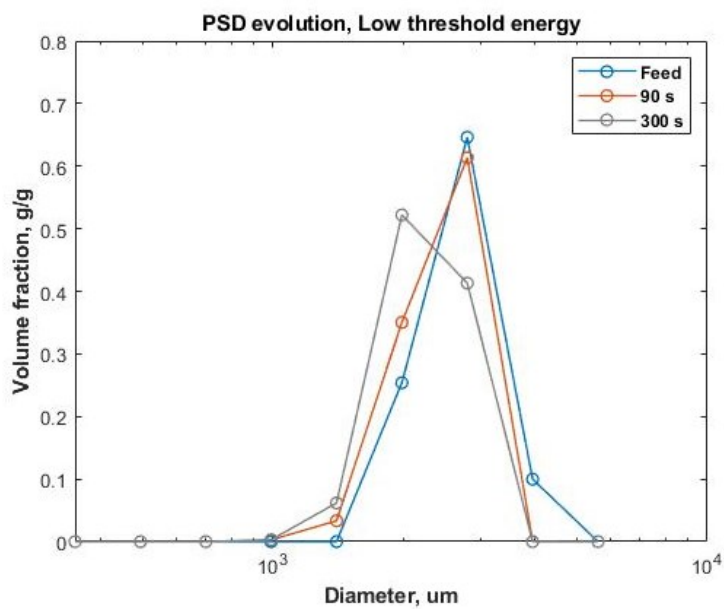


Figure 3.10 Prediction of evolution of particle size distribution from the DEM-PBM framework, Low threshold energy 0.6 J m/kg

3.5 Case studies

Two cases are discussed in this section with the aim to demonstrate the convergence of the proposed algorithm as well as provide an understanding of the significance of the structure of the framework. For the case studies and iterations, DEM simulations are run for 5 seconds and only ‘contributing energies’ i.e., energies of particles greater than threshold energy are considered in the energy distribution data.

In Case study 1, breakage is implemented in the DEM model as explained in Section 3.2.3. In this case study, the algorithm is demonstrated assuming breakage kernel values are known. Traditionally, kernel values of PBM are estimated from tedious milling experiments with narrowly distributed feeds or single particle breakage tests [49, 136]. In this work, kernel values ($K_{known, j}$) are assumed to be known for two impeller speeds i.e., $j = 1, 2$ based on hypothetical E_{const} and f_{mat} values. With the assumed f_{mat} value and DEM data corresponding to the assumed E_{const} , Equation 3.8 is used to compute the kernel value, $K_{known, j}$ for the two impeller speeds. The aim of this case study is to implement the algorithm with breakage incorporated into DEM. Convergence of the algorithm in this case study to the known material specific parameters shall demonstrate the validity of the framework to estimate material specific parameters in cases where breakage is significant. For each iteration, the objective function used is a sum of squared differences between known kernel values $K_{known, j}$ and kernel value obtained based on f_{mat} and E_{const} values estimated in each iteration. The iterative algorithm specific to the case study 1 is shown schematically for clarity in Figure 3.11.

For case study 2, breakage is implemented in the DEM model, as in the previous case study. However, kernel values are assumed to be unknown as is usually the case in any process. Instead, measurements from milling experiments are assumed to be known. For this case study, experimental data used, specifically particle size distribution of the milled product, holdup amount,

steady state time are virtually generated using a simulated PBM previously described in Section 3.2.2. The data are generated for 1750 rpm and 2500 rpm impeller speeds and the model parameters used to generate this data are listed in Table 3.5. The breakage distribution parameters n and σ are chosen as 2 and 0.5 respectively to replicate breakage of a parent particle into a distribution of daughter particles with mean of half the volume of mother particle. Experimental data thus generated is also listed in Table 3.5, with milled product particle size distribution plotted in Figure 3.12. The aim of this case study is to implement the algorithm with breakage incorporated into DEM and assuming only measurements from milling experiments are available. For each iteration, the objective function used is a sum of squared differences between experimental particle size distribution PSD, holdup, steady state time (designated as PSD_{expt} , $holdup_{expt}$ and $SStime_{expt}$ respectively) and simulated values obtained based on f_{mat} and E_{const} values estimated in each iteration. Convergence of the algorithm in this case study to the known material specific parameters shall demonstrate the validity of the framework to estimate material specific parameters. This is significant in cases where kernel values are unknown because of various limitations such as limited availability of material or limited manpower to perform tedious experiments with narrowly distributed feeds. Details and further discussion specific to each case study is explained in the next sections.

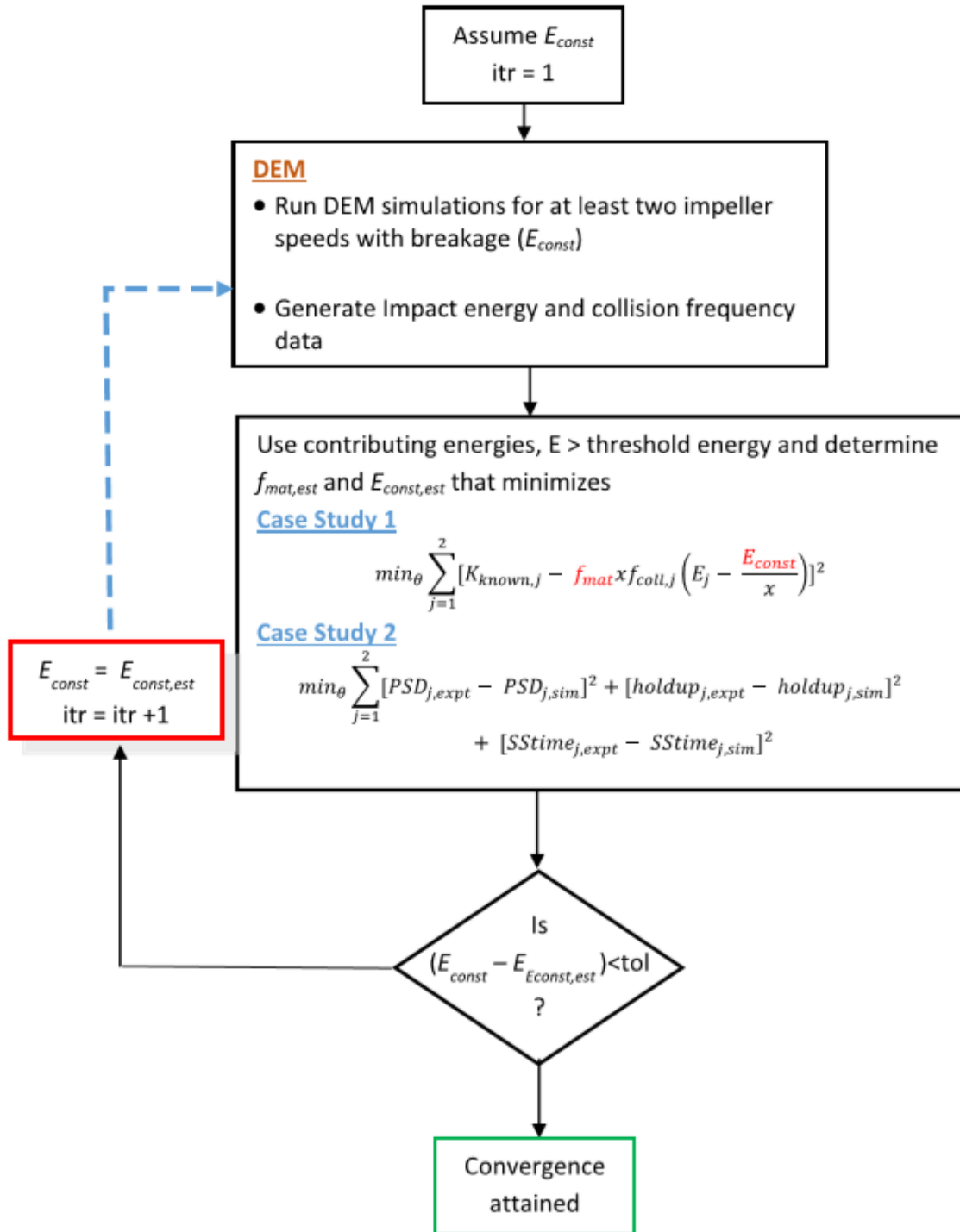


Figure 3.11 Workflow used in Case study 1 and 2 to demonstrate the algorithm

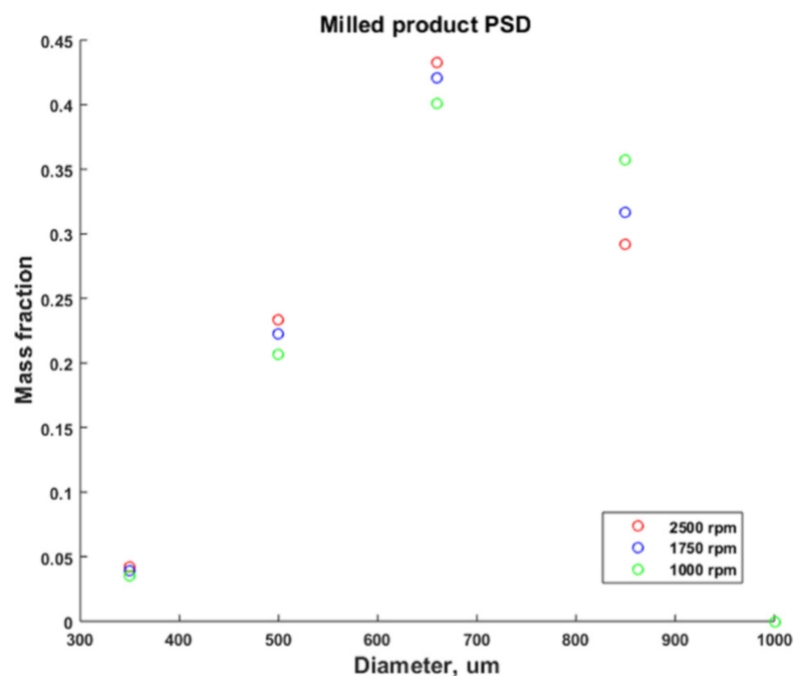


Figure 3.12 Particle size distributions of milled product at steady state

Table 3.5 Parameters of PBM used to generate milling data

PBM parameters					
Impellor speed, rpm			1000	1750	2500
<i>Non-kernel parameters</i>	Critical size ratio	δ	0.85	0.83	0.80
	Breakage distribution mean parameter	n		2	
	Breakage distribution standard deviation	σ		0.5	
<i>Breakage kernel</i>	Coefficient	P_1		0.45	
	Size dependence	P_2		1	
<i>Process variables</i>	Steady state time, s		55.83	38.65	36.07
	Hold up, g		3.39	2.99	4.24

Case study 1

Breakage of particles based on threshold energy is considered in DEM simulations i.e., particles break when ' E ' as given in Equation 3.7 is more than threshold energy. The validity of the algorithm in this case is important as studies have shown that kernel values are influenced by population and the distribution of particles, a phenomenon referred to as non-linear kinetics [137, 138],[139]. Breakage in DEM is implemented via deletion of the mother particle and replacement with two daughter particles of half the volume each as explained in Section 3.2.3. DEM simulations are run at a continuous feed rate of 4 kg/hr of mono sized 1 mm feed particles. Two simulations each at 1750 and 2500 rpm are run for E_{const} values of 0.03, 0.003, 0.0003 J m/kg. Simulations are run to $t=5$ s and the algorithm is implemented for impact energy data at $t=5$ s. A snapshot of DEM simulation at $t=1$ s showing particles of different sizes is given in Figure 3.13.

In order to demonstrate the implementation of the algorithm, targeted values for E_{const} and f_{mat} are chosen as 0.03 J m/kg 0.1 kg/J m respectively. The corresponding kernel values based on DEM simulation data and Equation 3.8 are 0.5199 and 0.2864 s^{-1} respectively for 1 mm particles. Since 1 mm particles have size greater than the screen size, breakage rate of 1 mm size class is studied. An arbitrary guess value for E_{const} is chosen for the first iteration. Energies above the threshold energy i.e., $E > E_{const}/\text{particle size}$ are only considered in kernel formulation as these contribute to breakage. Considering $\theta = [f_{mat}, E_{const}]$ as parameters, the objective function given in Equation 3.12 is used to estimate f_{mat} and E_{const} for the next iteration.

$$(\theta) = \min_{\theta} \sum_{j=1}^2 \left[K_{known,j} - f_{mat} x f_{coll} \left(E - \frac{E_{const}}{M} \right) \right]^2 \quad 3.12$$

The optimization yields a new threshold energy value $E_{const, est}$ and, $f_{mat, est}$. The new E_{const} value is used in the next iteration to find corresponding contributing energies. Since contributing energy

data from DEM simulations are dependent on E_{const} value, DEM simulations are run with the new E_{const} value at every iteration. The corresponding energy and collision data are analysed to estimate parameters for the next iteration. For this work, energy and collision data for E_{const} values within the bounds $[0.03, 0.003]$ or $[0.003, 0.0003]$ are obtained through linear interpolation. f_{coll} and mass specific energy values for the three E_{const} values and two impeller speeds are shown in Figure 3.14. The iterations are continued till the difference between $E_{const, est}$ from two consecutive iterations is lower than tolerance. If the final E_{const} converges to the targeted E_{const} , the algorithm is demonstrated. Details on iterations using objective function in Equation 3.12 are shown in Table 3.6. The work flow representation for this case study is given is Figure 3.11.

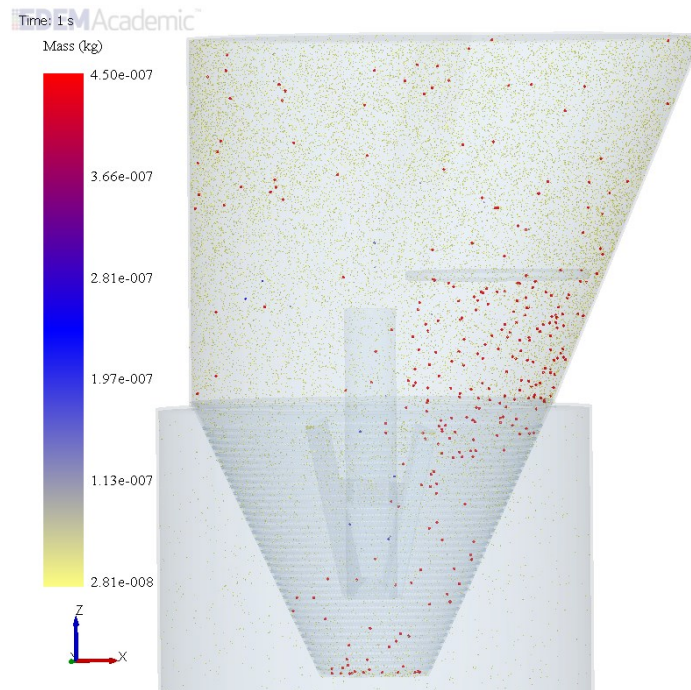


Figure 3.13 Snapshot of DEM simulation showing particles of different sizes inside and exiting the mill

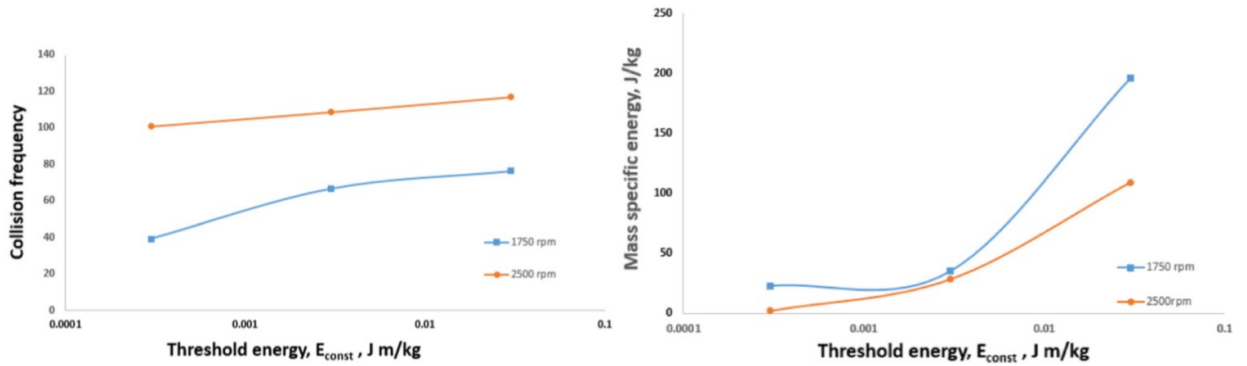


Figure 3.14 Collision and mass specific energy of 1 mm particles from DEM simulations for case study 1 and 2 at various E_{const} values and impeller speeds 1750, 2500 rpm

Table 3.6 Iterations for case study 1 showing convergence to targeted E_{const} and f_{mat} values with starting guess values for $E_{const} = 0.002$ J m/kg

Starting $E_{const} = 0.002$ J m/kg			
Iteration#	$E_{const, est}$	$f_{mat, est}$	Objective function
1	0.006671	0.98	3.01e-12
2	0.015115	0.55	1.29e-12
3	0.020636	0.21	4.55e-14
4	0.024148	0.15	1.44e-13
5	0.026357	0.12	1.18e-13

Case study 2

Case study 2 addresses the scenario where kernel values from milling experiments are not known, as it is usually the case. An alternative is to calibrate a PBM model with experimental data from multi sized feeds which is relatively easier, but requires the assumption of an empirical form of the breakage kernel. The empirical assumption is usually based on experience or is a form that is borrowed from breakage experiments from other industries. The disadvantage of this is the questionable validity of the assumed form, since the dependence of the kernel on size or speed of impeller or feed rate etc., may not be valid across different materials, sizes, speeds or feed rates. Hence, the framework in the current study proposes to use other process variables such as particle

size distribution, steady state time, hold up amount directly with DEM simulations which not only is devoid of making any empirical assumptions on the form of breakage kernel, but also eliminates the traditional path of performing experiments with mono sized or narrowly distributed feeds.

In this case study, conditions used for DEM simulations are the same as explained in the previous case study. However, objective function in Equation 3.9 i.e., a sum of squared errors between predicted and experimental PSD, steady state time and hold up is used. The experimental data is obtained as explained earlier, with the breakage rate values for 1 mm size class considered as 0.5199 and 0.2864 s⁻¹ for 1750 and 2500 rpm respectively. Hence, the iterations should converge to E_{const} of 0.03 J m/kg and f_{mat} of 0.1 kg/J m. The details of the iterations converging to E_{const} of 0.027 and f_{mat} of 0.12 is shown in Table 3.7.

Table 3.7 Iterations for case study 2 showing convergence to targeted E_{const} and f_{mat} values with starting guess values for $E_{const} = 0.001$ J m/kg

Starting $E_{const} = 0.001$ J m/kg			
Iteration#	$E_{const, est}$	$f_{mat, est}$	SSE
1	0.001217	0.82	1.22e-14
2	0.002337	0.83	3.05e-15
3	0.008638	1.11	3.04e-15
4	0.021619	0.57	212.314
5	0.024767	0.14	8.88e-14
6	0.026745	0.12	6.91e-14

The final E_{const} and f_{mat} values obtained from the algorithm i.e., 0.027 J m/kg and 0.12 kg/J m are considered as the known material specific parameters. Mass specific contributing energy from DEM simulation run at 1000 rpm is used to predict the particle size distribution, steady state time, holdup and compared with computer generated experimental data for 1000 rpm in Figure 3.12 and Table 3.5. A holdup of 3.08 g, steady state time of 55.84 s is predicted which compares well against experimental holdup value of 3.39 g and steady state time of 55.83 s. Comparison of predicted and

experimental milled particle size distribution for 1000 rpm is given in Figure 3.15. While the excellent agreement between experiment and simulated values is also in part due to the same value of n , σ and δ parameters considered in generating the data as well as PBM used for validation, the convergence of algorithm to the targeted E_{const} and f_{mat} values serve as proof of concept for the proposed multi scale framework to estimate the material specific parameters.

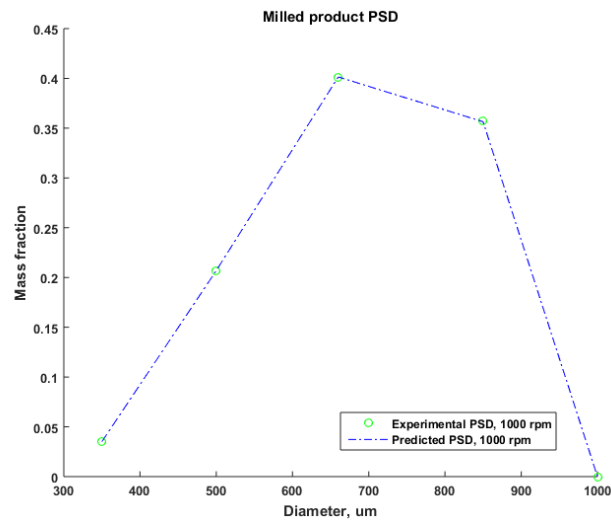


Figure 3.15 Comparison of experimental and predicted milled particle size distribution at 1000 rpm from $E_{const} = 0.025 \text{ J m/kg}$ and $f_{mat} = 0.14 \text{ kg/J m}$

The case studies thus demonstrate and explain the need and validity of the proposed framework where PBM, DEM and experimental data are treated together to estimate material specific kernel parameters. While the case studies are implemented and demonstrated for 1 mm particles, the validity of the framework is independent of the size distribution of the feed. In addition, for various impeller speeds and threshold energies, energy data at 5 s of milling time is collected, analyzed and used in the framework to utilize the advantage of computer generated milling data. With lab experiments, the energy data needs to be collected at various times to capture the breakage dynamics and given as input to the PBM through energy based kernel till the process reaches steady state. Since the framework is applied to continuous process, breakage can be implemented in DEM,

which is otherwise not computationally economical to apply in a batch process as the number of particles drastically increase with time. In contrast, for a continuous process, since there are also particles exiting the system, this is captured as an opportunity to incorporate breakage in DEM and thus include the effects of changing population dynamics in the framework.

3.6 Summary

In this work, a multi-scale DEM-PBM approach utilizing a breakage kernel that identifies material properties; and that is calibrated with experimental data to estimate these properties, is proposed. A rule based breakage of particles is implemented in the DEM model, where a particle breaks if the energy lost from contacts exceeds a minimum threshold energy. The DEM model implemented also accounted for the effect of mill geometry in particle breakage specifically through incorporation of screen holes, screen thickness and impeller design. Limited milling experiments with granular material are required with the proposed methodology, which eliminates the need for tedious experiments with mono-dispersed feeds or assumptions related to semi empirical formulation of breakage kernels for estimation of material specific parameters. The convergence of the proposed methodology is demonstrated for various cases and the need for a combined framework is established.

In the current work, instantaneous energy loss from contacts is considered to implement breakage in DEM. Incorporation of cumulative energy i.e., energy lost by particles from all the collisions over the time period of its existence is a potential area of investigation as it hypothesized that granular structure becomes weaker due to repeated collisions and hence the threshold energy is lower [140]. In addition, the proposed framework uses discrete energy data from DEM simulations at various time steps into PBM. A surrogate model can be developed as the energy distribution is dependent on process variables such as feed flow rate, impeller speed etc. The incorporation of mechanistic data into the PBM can be made more efficient through the use of surrogate model that

can capture this dependence. In terms of the computational power, while the expense for the proposed methodology is high due to incorporation of particle breakage in the DEM model, advances in the area of parallel computing is expected to alleviate limitations on computational complexity which is generally high in mechanistic models. Further work is also needed to incorporate measured material properties of granules such as porosity, friability etc., into mechanistic models and thus make these models more useful in understanding the effect of material properties on the process.

Chapter 4

A computationally efficient surrogate-based reduction of multi-scale comill process model

4.1 Background

In this chapter, the DEM-PBM multiscale framework for a comill process as established and explained in the previous chapter using a mechanistic breakage kernel developed by Capece, Bilgili [54] is applied. The purpose is to include the effect of material properties and processing conditions into the modeling framework and under the QbD paradigm. However, since particle scale phenomena are captured, DEM simulations are very computationally expensive. The issue of higher computational expense is exacerbated for units involving particle size and number change such as milling as the computation power needed is proportional to the number of particles in the system. This limits its use in flowsheet modeling, for instance, where the model needs to be evaluated quickly for dynamic simulation and control purposes. Surrogate modeling (SM) techniques can effectively bridge this gap.

Mechanistic data from DEM simulations at various processing conditions are collected. Following this, a SM-PBM framework is then established to replace the DEM-PBM framework by developing surrogate models for the mechanistic data obtained from the DEM simulations. The effect of the hybrid framework on the bulk property predictions such as steady state granule size distributions and dynamic holdup profiles are analyzed. The framework is implemented and shown for two case studies along with the supporting discussion. Following this, to demonstrate the applicability of the surrogate model based framework in flowsheet modeling, the mill and tablet press models are

integrated and the effect on tablet properties such as hardness and weight are analyzed. The work presented is then summarized along with discussion on prospects of future work.

4.2 Modeling methods

4.2.1 Discrete element method model

The DEM model as described in the previous chapter (Section 3.2.3) is used here. The model used is explained here briefly. The Hertz-mindlin contact model [118, 119] is used with a time integration step of 3.5×10^{-6} s. The criteria for breaking a particle in DEM is setup through the use of a ‘threshold energy’, which is a material specific parameter. A particle is considered broken, and is replaced by a distribution of smaller particles, if the impact energy of the particle exceeds a ‘threshold energy’. The implementation of particle breakage in DEM is done using the particle replacement strategy [126]. A rule based breakage is used whereby, if the energy lost by a particle exceeds the threshold energy, the particle is deleted from the simulation and is replaced by a distribution of daughter particles. The number and size of daughter particles can be determined from experimental data or using mechanistic basis [43, 128]. For the purposes of this work, it is assumed that a particle breaks into two particles of half the volume each. A minimum particle size limit of $350 \mu\text{m}$ is also set in DEM as experimental particle size analysis showed that less than 1.5% of granules inside the comill is below $350 \mu\text{m}$.

For the equipment properties, typical steel properties were used [120] (density 7900 kg/m^3 , poisson’s ratio 0.3, shear modulus 77 GPa). For the particles, a density of 860 kg/m^3 was used to model pharmaceutical material. An effective particle density was used that is calculated from particle true density of 960 kg/m^3 and granular porosity of 0.1 [141]. Poisson’s ratio and shear modulus were taken as 0.3, 1MPa respectively. Coefficient of restitution was taken as 0.2 for interaction of steel with particles and particles with particles. The coefficients of static friction for

steel-particle and particle-particle interactions were taken as 0.4 and 0.5 respectively and the coefficient of rolling friction for steel-particle and particle-particle interactions were taken as 0.01 based on values used in [121]. The DEM parameters used are also listed in Table 4.1. The effect of these parameters on DEM simulations is out of the scope of this work, however, these values can be changed based on calibration from experimental data as described in [122-124]. Simulations were setup such that the feed is introduced to the comill in a continuous mode. The feed particle size distribution was set by assuming a normal distribution with mean 1 mm and a standard deviation 0.2 mm. 13 particle size classes were generated using a geometric progression ratio of $2^{1/6}$ and ranging from 0.35 to 1.4 mm (i.e., $0.35 \cdot (2^{1/6})^n$ where n varies from 0 to 12), which are designated as bin 0, bin 1,...bin 12. The feed ranged from particle size 0.55 to 1.4 mm (i.e., bin 5 to bin 12). DEM simulations for two case studies were run. In the first case study, the feed flow rate is considered constant at 4 kg/h and mill impeller speed is varied. In the second case study, the mill impeller speed is fixed at 1000 rpm and eight simulations are run at various feed flowrates. For each of the case studies, additional simulations were run which were used to validate the modeling framework. The specific simulation conditions used for both case studies are tabulated in Table 4.1.

The data from DEM simulations is introduced to a PBM through the mechanistic breakage kernel, explained in the previous chapter (Section 3.2.3) and also given in Equation 4.1. Breakage kernel in a PBM defines the breakage rate or the breakage probability of particles and is used in formulating rates of formation and depletion of particles in population balance models. The goal of using the mechanistic kernel is to introduce particle scale information obtained from DEM simulations and utilize it to define breakage probability at a system level and obtain bulk property predictions such as milled particle size distribution. The post processing of data from DEM simulations for use in the mechanistic kernel for both case studies and their use in the framework is discussed in further sections.

Table 4.1 Details on DEM simulation parameters and runs for two case studies

DEM simulation parameters								
	Steel			Particle				
Density, kg/m ³	7900			860				
Poisson's ratio	0.3			0.3				
Shear modulus	77 GPa			1 MPa				
Interaction parameters	Steel-Particle			Particle-Particle				
Coefficient of restitution	0.2			0.2				
Coefficient of static friction	0.4			0.5				
Coefficient of rolling friction	0.01			0.01				
Case study 1: Fixed flowrate simulations								
Simulations at impeller speeds (rpm) used to build the model	400	700	1000	1300	1600			
Simulation at impeller speed (rpm) used to validate the model	850 rpm							
Flowrate, kg/h	4							
Threshold energy E_{const} , J m/kg	0.03							
Case study 2: Fixed impeller speed simulations								
Simulations at flowrates (kg/h) used to build the model	2.5	3	3.5	4	4.5	5	5.5	6
Simulation at flowrate (kg/h) used to validate the model	3.25 kg/h							
Impeller speed, rpm	1000							
Threshold energy E_{const} , J m/kg	0.03							

4.2.2 Population balance model

The PBM as described in the previous chapter is used here. The model used here applies the same model equations. Specifically, a log-normal breakage distribution function is used. The breakage kernel in a PBM reflects the probability or the rate at which a particle breaks due to collisions. PBM for a comilling process developed in [43, 111] used empirical breakage kernels based on shear rate, impeller speed, and particle size. However, the parameters of these kernels that are obtained from calibration with experimental data do not explicitly identify their dependence on particle properties

or processing conditions. This limits their applicability and does not support the QbD approach that the pharmaceutical industry is aligning to. In this direction, Capece, Bilgili [54] proposed the use of a breakage kernel with a mechanistic basis i.e., a kernel that is informed by DEM simulations and explicitly identifies terms that depend on material properties and milling environment. This mechanistic breakage kernel as given in Equation 4.1 is used in the model. For particles of diameter x_i the breakage kernel K_i at various times t is defined. The energy term in this breakage kernel is multiplied by the frequency of collisions to account for multiple impacts on particles. $f_{coll,i}$ is frequency of collisions of particles in i^{th} bin defined as number of collisions per particle per second as obtained from DEM simulations. Here, $E_{i,min} = \frac{E_{const}}{x_i}$ where x_i represents the size of particles in i^{th} bin. This represents the dependence of particle threshold energy on the particle size i.e., a smaller particle needs higher energy to break when compared to a larger particle. The parameter E_{const} is the ‘Threshold energy’ that is also used to setup DEM simulations (Table 4.1). E_i is the mass specific energy of particles with energy greater than the threshold energy. Only particles with ‘contributing energies’ i.e., energies of particles greater than threshold energy are considered in the kernel as these lead to breakage of particles.

$$K_i(t) = f_{mat} x_i f_{coll,i} (E_i - E_{i,min}) \quad 4.1$$

The parameters f_{mat} and E_{const} can be determined from experimental data and using DEM simulations. Chapter 3 explains an efficient way of using an iterative algorithm through which the material specific parameters f_{mat} , E_{const} can be estimated from experimental data and DEM simulations. In Capece, Bilgili [53], the parameters were estimated using experimental data alone, however this requires performing tedious experiments with mono sized material. In the current work, the values of f_{mat} and E_{const} are considered as 5 kg/J m and 0.03 J m/kg respectively as

given in Table 4.2. While these are hypothetical values, the approach in this paper is applicable to mechanistic data generated using any parameter values.

The remaining PBM parameters, n , σ , ε , α , f_{mat} , E_{const} are considered fixed. It is important to note that the value of E_{const} used is same as the threshold energy parameter used to implement breakage in DEM simulations and the values of n , σ are set to simulate binary breakage as in the DEM simulations. Table 4.2 gives the values of the parameters used in this work.

Table 4.2 Parameters used in PBM

PBM parameters			
Screen model	Critical size ratio coefficient	ε	1
	Critical size ratio exponent	α	0.2
Breakage distribution function	Parameter	n	2
	Standard deviation	σ	0.25
Breakage kernel	Kernel parameter, kg J/m	f_{mat}	5
	Threshold energy, J m/kg	E_{const}	0.03

4.2.3 Surrogate model

In surrogate modeling, models that incur high computational cost are reduced to lower cost models [142-144]. The reduction in computational cost enables the use of these models for process flowsheet simulations, process optimization and further analysis [12, 103, 104, 145, 146]. Jia, Davis [147] used surrogate models to predict loss-in-weight feeder flow variability as a function of unit flowability and feed rate. A specific class of surrogate modeling techniques known as Reduced Order Models (ROM) have been used to represent high fidelity CFD simulations. Lang, Malacina [148] demonstrated the effectiveness of ROM for process simulation and optimization using case studies from power generation processes. Fei, Black [149] demonstrated building of surrogate model based flowsheet model for an integrated gasification and combustion power generation process and the optimization of the flowsheet model for economic and environmental benefits was

also shown. CFD based ROM models are also used in optimizing operation of bioreactors [150]. Specific to pharmaceutical process modeling, the reducing order modeling methodology in combination with response surface models such as kriging was established in [60] and applied to a continuous blending process case study. In Rogers and Ierapetritou [57], DEM simulations were run for a continuous blender and reduced order models were developed for distributed parameters such as velocity. The reduced order model was used to ultimately predict blend uniformity through RSD i.e., relative standard deviation of the component concentration. A PLS model was developed to predict RSD, as a function of axial velocity and other design variables such as blade speed and shaft angle.

In the current work, the high cost DEM models are reduced to low cost models using surrogate modeling techniques, specifically Kriging and Artificial Neural Networks (ANN) in order to efficiently represent the mechanistic data into PBM. The primary purpose for the use of these techniques is to aid the use of the DEM-PBM framework into continuous process modeling. Kriging and Artificial neural networks are chosen in this work as they are known to effectively model non-linear data [151, 152]. The next two sections present a brief description of the two modeling methodologies.

4.2.3.1 Kriging

Kriging implemented in Design and Analysis of computer Experiment (DACE), is selected in this work [153]. Detailed background and derivation of this modeling technique can be found in [153, 154]. A brief description is given here. The kriging model prediction $\hat{f}(x^i)$ for a d dimensional input x^i is given as a realization of a regression model $\hat{\mu}(x^i)$ and an error term $\hat{\varepsilon}(x^i)$ as given in Equation 4.2. The error ε is represented by a Gaussian process with zero mean and covariance $\sigma_{krig}^2 \mathbf{R}(\theta, x^{(i)}, x^{(j)})$ between $\varepsilon(x^{(i)})$, $\varepsilon(x^{(j)})$ where \mathbf{R} is the correlation model. The correlation model \mathbf{R} indicates that the errors in the predicted values are correlated as a function of the

independent variables. In this work, the generalized exponential function is used to represent the correlation model as given in Equation 4.3, which indicates that when the distance between the points x^i and x^j is close to zero, the correlation is one and when the distance between the points increases, the correlation decreases.

$$\hat{f}(x^i) = \hat{\mu}(x^i) + \hat{\epsilon}(x^i) \quad 4.2$$

$$\mathbf{R}(\theta, x^{(i)}, x^{(j)}) = \exp\left(-\sum_{h=1}^d \theta_h |x_h^{(i)} - x_h^{(j)}|^{\theta_{d+1}}\right), \quad 0 < \theta_{d+1} \leq 2 \quad 4.3$$

The parameter θ_h relates to the significance of the variable. A large value of θ_h leads to a large value of correlation for small distances between the points x^i and x^j . For the parameter θ_{d+1} , a value of 2 or 1 gives the Gaussian and exponential function respectively. Usually, the correlation model has a large impact on the model fit to the data when compared to the regression terms. Hence, a constant term for $\mu=\beta$ is considered sufficient for a good model prediction [154].

The values of the parameters β , σ^2 , θ_i are estimated using the maximum likelihood of the observed response \mathbf{y} . The logarithm of the likelihood function is given by Equation 4.4.

$$\ln(L) = -\frac{n}{2}\ln(2\Pi) - \frac{n}{2}\ln(\sigma_{krig}^2) - \frac{1}{2}\ln(|R|) - \frac{(y - 1\hat{\beta})^T R^{-1}(y - 1\hat{\beta})}{2\sigma_{krig}^2} \quad 4.4$$

The optimal values of β , σ_{krig}^2 are given by Equations 4.5 and 4.6. Using the optimal values, the final kriging predictor is given by Equation 4.7, where \mathbf{r} is the correlation between the point to be correlated and sample design points $\mathbf{r} = \mathbf{R}(x^{new}, x^i)$. In this work, kriging model is built and applied to the framework in MATLAB 2017a.

$$\hat{\beta} = \frac{\mathbf{1}^T R^{-1} \mathbf{y}}{\mathbf{1}^T R^{-1} \mathbf{1}} \quad 4.5$$

$$\hat{\sigma}_{krig}^2 = \frac{(\mathbf{y} - \mathbf{1}\hat{\beta})^T R^{-1} (\mathbf{y} - \mathbf{1}\hat{\beta})}{n} \quad 4.6$$

$$\hat{f}(x^{new}) = \beta + r^T R^{-1} (\mathbf{y} - \mathbf{1}\beta) \quad 4.7$$

4.2.3.2 Artificial neural network

Artificial neural networks have been used successfully to model complex problems related to pattern recognition, classification, and prediction in various fields. ANNs have been used to successfully model pharmaceutical processes as well [155]. For example, Akkisetty, Lee [156] used ANN to establish relationship between mill operating conditions, material properties selection and breakage functions of a population balance model (PBM). Barrasso, Tamrakar [72] used ANN to represent collision information obtained from DEM simulations into PBM to simulate wet granulation process. In artificial neural networks, input-output dataset is connected using neurons or nodes. A basic neural network structure consists of three layers; an input layer for the input variables in the model, a hidden layer where the input variables are transformed and an output layer for the output variables in the model. Each input variable is weighed before it reaches the neuron in the next layer. An additional neuron is added with a unit weight to be included as bias. The weighed inputs to the neuron are summed and a transfer function is applied before reaching the next layer. This continues for any number of hidden layers in the network. In ANN, a learning rule is applied to choose the weights and biases that best predict the output variable. The optimal set of weights and biases are obtained by minimizing a performance function using an optimization algorithm. In this work, Levenberg-Marquardt algorithm is used and the performance function minimized is the sum of squared differences between the predicted and targeted output variable

values from the data set. The dataset provided to ANN is divided randomly into training, validation and testing datasets. The training dataset is used to optimize the weights and biases. The validation dataset is used to determine the optimum number of times (epochs) the dataset is provided to the network in order to prevent overfitting of the data. The test set is generally used to compare different architectures. An indication of the need for a different architecture can be known from test set error. If the optimum performance function value occurs at a significantly different epoch compared to the validation set, a different ANN architecture may need to be looked at.

An example of ANN architecture with one input layer, one hidden layer and one output layer is given in Figure 4.1. The architecture given in the figure has three input neurons (represented as yellow circles), four neurons (represented as blue circles) in the hidden layer and one neuron in the output layer (represented as the green square). In addition, a bias is added to the input and hidden layers with a constant weight of 1 (represented by yellow and blue squares). In this work, the input layer has three neurons and output layer has one neuron. Also, one hidden layer with ten neurons is used. A sigmoid transfer function as given in Equation 4.8 is used for hidden layer and a linear transfer function is used for output layer. The dataset is randomly divided into training, validation and testing set in the ratio of 0.65, 0.25, and 0.1 respectively as recommended in [157]. The MATLAB neural network toolbox [158] is used to build the ANN models and apply it to the framework.

$$tansig(i) = \frac{2}{1 + e^{-2i}} - 1 \quad 4.8$$

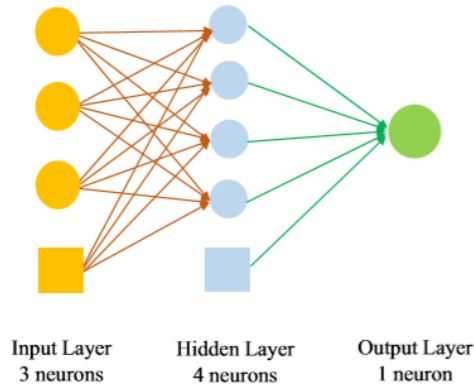


Figure 4.1 Schematic of an artificial neural network example

4.2.4 Hybrid model framework

The DEM-PBM framework is established through the use of the energy based kernel as given in Equation 4.1. The framework is pictorially shown in Figure 4.2. DEM simulations using the threshold energy constant are run to 10 s. Energy and collision frequency data are obtained by logging every collision event resulting in a breakage, and post processing this data. As the DEM simulation progresses, each collision event that results in energy of the particle exceeding the threshold energy is recorded in a text file automatically. For post processing the data, 13 particle size bins are set based on a geometric progression ratio of $2^{1/6}$ and mean particle diameters ranging from 0.35 to 1.4 mm. Collision frequency in this work is defined as number of collisions resulting in breakage per particle per second. For a size bin i , the total number of collisions of particles resulting in breakage divided by the number of particles for the time interval used gives the collision frequency $f_{coll, i}$ for the size bin i (Equation 4.9). Similarly, sum of energies of all particles from a particle size bin divided over total mass of particles gives the specific energy E_i for particle size bin i (Equation 4.10) as a function of particle size, time and processing condition. For simulations run at constant impeller speed, energy and collision frequency data is obtained as a function of particle size, time and flow rate. For simulations run at constant flowrate, energy and collision frequency data is obtained as a function of particle size, time and impeller speed.

$$f_{coll, i} = \frac{\text{Total number of collisions in time interval } t \text{ (from brekaing particles in bin } i)}{\text{Total number of particles (in bin } i) * \text{ time interval } t} \quad 4.9$$

$$E_i = \frac{\text{Sum of energies of particles (from brekaing particles in bin } i)}{\text{Total mass of particles (in bin } i)} \quad 4.10$$

For simulations at constant flowrate, this results in 450 data points (5 impeller speeds x 9 particle sizes x 10 time intervals). For simulations at constant impeller speed, this results in 720 data points (8 flowrates x 9 particle sizes x 10 time intervals). The particles in bin numbers 1, 11, 12 are not considered as particle with the lowest size i.e., bin number 1 is considered to exit the mill and is not expected to break. The particles in bins 11 and 12 (mean particle diameters 1.24 mm and 1.4 mm) resulted in variation of less than 10% in the data obtained from DEM. This is possibly due to low population of particles of this size in the feed and an even lower population in the broken mass. The matrix of DEM data is obtained through processing data from the text file using custom codes in MATLAB. In the DEM-PBM framework, mechanistic data resulting from DEM simulations are fed to PBM through the breakage kernel. In addition, for a new processing condition, say a different flowrate or impeller speed, the DEM simulation needs to be run at the new processing condition. On the contrary, in the SM-PBM framework, surrogate models for the specific energy and collision frequency are developed using the DEM simulation runs in the experiment design. For a new flowrate or impeller speed, the surrogate model is able to predict the specific energy and collision frequency for the required particle sizes and time intervals without having to run the DEM simulation. The limitation in computational expense from DEM simulation is addressed since the surrogate model takes few seconds to run when compared to a DEM model which takes days to run. In addition, the mechanistic information can be analytically represented using surrogate model

equations, which provides an effective way to incorporate particle scale information into process modeling. These serve as significant advantages of using the surrogate models.

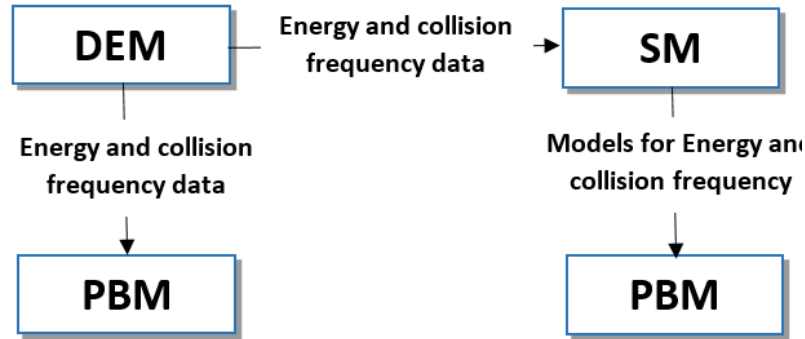


Figure 4.2 Schematic for the hybrid model framework

In order to utilize the hybrid model framework with a new material using experimental data, accurate estimation of DEM simulation parameters and breakage kernel parameters are required. Yan, Wilkinson [159] utilized angle of repose experiments and statistical analysis to understand the relative importance of the DEM simulation parameters (particle-particle and particle-wall static and rolling coefficients, coefficient of restitution, shear modulus) and facilitate their calibration in order to appropriately represent the material in DEM simulations. In addition, it is important to know the distribution of daughter particles obtained once a parent particle undergoes breakage. Loreti, Wu [128] proposed methodology to study particle breakage for impact milling of ribbons. To utilize the hybrid model framework, it is also important to estimate the breakage kernel parameter E_{const} , which signifies threshold energy needed for a particle to undergo breakage. Metta, Ierapetritou [160] proposed an iterative algorithm to estimate the threshold energy parameter. Once all the required DEM simulation parameters are obtained, DEM simulations need to be run to develop surrogate models that efficiently represent the DEM data, thus building the SM-PBM approach that can be utilized in continuous process modeling. While the DEM simulation parameters may change as milling progresses, from the authors' knowledge, there is limited work

that considers changes in particle properties as the breakage process progresses. Inclusion of such phenomenon remains to be a challenge to be addressed.

4.2.5 Model integration

Flowsheet models are developed using the individual unit models via connecting the inlet of a unit to the outlet of the preceding unit [89]. Relevant product properties, operating conditions and individual unit model variables are sent to the following unit. Process simulators such as gPROMSTM facilitate the development of flowsheet models. Previous work published in the area of pharmaceutical flowsheet model development for direct compaction line [12, 161], dry granulation line [81, 162] and wet granulation line [163] used unit operation models that are based on mass balance principles, empirical, semi-empirical approaches, population balance models. However, these models do not include mechanistic data obtained from computationally expensive simulations like DEM. Surrogate models provide an effective way to facilitate the inclusion of mechanistic models into integrated process models.

In this work, the mill model as described in Section 4.2.4 is integrated with a tablet press model [12]. In a tablet press, material from the mill unit is transferred to the dies. The geometry of the dies and depth to which material is filled, known as fill depth (FD) determines the weight of the tablet (w_{tablet}). Tablet hardness is modeled using the Kuentz-Luenberger equation [84] as given in Equation 4.11, where ρ_r is the relative density, $\rho_{r,cr}$ is the relative critical density and λ_H is an intermediate variable defined as given in 4.12. The relative density ρ_r is defined as the ratio of initial volume of solid in the die (V_{solid}) over tablet volume (V_{tablet}). The tablet volume is given by the length (L_{tablet}), diameter of the tablet (D_{tablet}). The initial solid volume (V_{solid}) in the die can be calculated based on the bulk density (ρ_{bulk}) and true density (ρ_{true}) of the milled granule product along with volume occupied by the granules in the die (V_0) as given in Equation 4.13. The volume occupied by granules in the die is dependent on the fill depth to which the granules are

filled and the diameter of the tablet (D_{tablet}) as given in Equation 4.14. V_0 is also used to determine the tablet weight as given in Equation 4.15. The parameter H_{max} is the maximum hardness which represents tablet hardness at zero porosity and $\rho_{r,cr}$ is the relative critical density. The parameters $\rho_{r,cr}$ and H_{max} need to be obtained from experimental data. The tablet press model parameters used in this work are listed in Table 4.3.

$$H = H_{max}(1 - \exp(\rho_r - \rho_{r,cr} + \lambda_H)) \quad 4.11$$

$$\lambda_H = \ln\left(\frac{1 - \rho_r}{1 - \rho_{r,cr}}\right) \quad 4.12$$

$$\rho_r = \frac{V_{solid}}{V_{tablet}} = \frac{\left(\frac{\rho_{bulk}}{\rho_{true}}\right)V_0}{L_{tablet} \frac{\pi D_{tablet}^2}{4}} \quad 4.13$$

$$V_0 = FD \frac{\pi D_{tablet}^2}{4} \quad 4.14$$

$$w_{tablet} = V_0 \rho_{bulk} \quad 4.15$$

Table 4.3 Parameters used in the tablet press model

Tablet Press model parameters		
Tablet diameter, m	D_{tablet}	8e-3
Fill depth, m	FD	8.1e-3
Tablet length, m	L_{tablet}	3.2e-3
Relative critical density	$\rho_{r,cr}$	0.3
Maximum hardness, N	H_{max}	200

It should be noted that the tablet press model requires bulk density of the milled granules as model input. Since the mill model predicts particle size distribution of the milled product, there is a need to connect this information with the milled granule bulk density. Previous work published for modeling this relation included the use of empirical models [164-167]. In this work, the empirical relationship developed by Yajima, Itai [168] is used to predict the granule bulk density. The authors realize that the applicability of such empirical models developed is limited and, for a new formulation or design condition, experiments need to be conducted again to rebuild the empirical relationships. However, in this article, to demonstrate the benefit of implementation of surrogate models, the empirical model as given in Equation 4.16 is considered, where $a_0 = 0.4747$, $a_1 = 0.2322$, $a_2 = -0.1277$, $a_3 = 0.0753$, $a_4 = -0.0846$. X_1 and X_2 are the mean and standard deviation of the particle size distribution when fitted to a lognormal distribution.

$$\rho_{bulk,g/cc} = a_0 + a_1X_1 + a_2X_2 + a_3X_1X_2 + a_4X_1^2 \quad 4.16$$

Overall, the mill operation simulated by the SM-PBM as described in Section 4.2.4, the tablet press model as described in this section, along with a bulk density prediction model as described in Equation 4.16 are used to build an integrated mill and tablet press model using gPROMSTM Modelbuilder 5.1. A schematic of the integrated model built in this platform is shown in Figure 4.3.

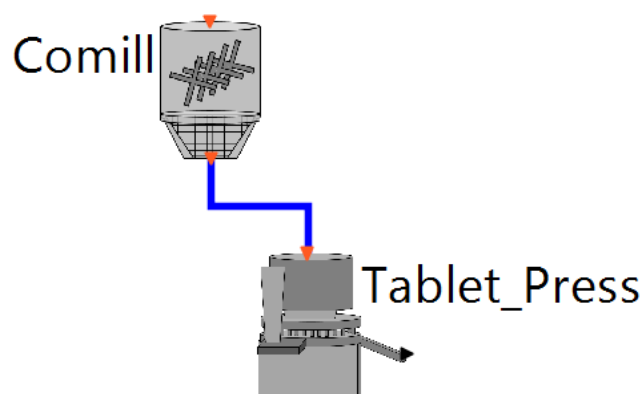


Figure 4.3 Schematic of the integrated mill and tablet press model developed in gPROMS™

In the next section, details on the surrogate models built for specific energy and collision frequencies, along with their effect on the bulk property prediction is discussed for two case studies. Following this, the implementation of the surrogate models in the mill and tablet press integrated model and its effect on tablet properties is discussed.

4.3 Case studies and model integration

4.3.1 Case study with fixed flow rate simulations

Kriging and ANN models are built for specific energy and collision frequency of particles as a function of particle size, time and impeller speed based on data obtained from five DEM simulations run as per the experimental design (Table 4.1). For the validation case (850 rpm), absolute percentage differences between the DEM value for specific energy and collision frequency, and Kriging model are plotted in Figure 4.4. Similarly, absolute percentage differences between the DEM value for specific energy and collision frequency, and ANN model for the validation case are also plotted in Figure 4.4. In addition, Table 4.4 lists the maximum and minimum errors in the developed Kriging and ANN models. The percentage error from the surrogate models as seen from the plots is less than 10% for most particle sizes and times. However,

the maximum error from a Kriging based energy and collision model is 25.6% and 15.8% respectively. Also, the maximum error from an ANN based energy and collision model is 20.8% and 27.4% respectively. To understand the acceptable error limit, it is important to see how the surrogate models affect predictions from the hybrid model framework. Particle size distributions and dynamic holdup are process responses from the hybrid model and also the bulk property predictions of interest in a milling process. In particular, breakage kernel effects the particle size distribution of the product inside the mill as well as exiting the mill. Hence, a comparison of model predictions from DEM-PBM and SM-PBM approaches should be analyzed through PSD of the product inside, exiting the mill and dynamic holdup. In addition, the aforementioned predictions are also compared with model predictions considering a constant kernel i.e., the kernel is assumed to be independent of particle size and time. The constant value considered is taken as the average of kernel values obtained from DEM simulations for all particle sizes and time intervals. The comparison to predictions from a constant kernel based model is done in order to show that is important to consider the effect of particle size and its evolution with time on particle breakage.

For case study 1, a comparison of particle size distribution of material inside and exiting the mill at steady state for kriging based model is shown in Figure 4.5 (first row). Figure 4.5 (second row) also shows the comparison for an ANN based model. A comparison of the dynamic holdup for kriging based model and ANN based model are also shown in Figure 4.5. It is apparent that the surrogate based model predictions agree well with DEM based model predictions. The constant kernel based predictions differ significantly from DEM based predictions in this case study.

To quantify the effect of the surrogate models on predictions, a sum of square errors is computed and reported. For PSD plots, the metric is computed as sum of squares of errors between DEM-PBM prediction and SM-PBM prediction for all particle size mass fractions inside and exiting the mill at steady state as given in Equation 4.17. For dynamic holdup plot, the metric is computed as

sum of square errors between DEM-PBM prediction and SM-PBM prediction of holdup for every second as given in Equation 4.18.

$$SSE_{PSD} = \sum_{bin=1}^{ns} (mass\ fraction_{bin,DEM-PBM} - mass\ fraction_{bin,SM-PBM})^2 \quad 4.17$$

$$SSE_{holdup} = \sum_{t=1}^T (holdup_{t,DEM-PBM} - holdup_{t,SM-PBM})^2 \quad 4.18$$

For case study 1, the sum of square errors for PSD from Kriging-PBM approach, ANN-PBM approach and constant kernel models are 2.6e-4, 2.5e-4 and 1.9e-2 respectively. For dynamic holdup, the sum of square errors for PSD from Kriging-PBM approach, ANN-PBM approach and constant kernel models are 0.36, 0.96 and 26.6 respectively. The metrics for case study 1 are also tabulated in Table 4.5. It is evident that that surrogate models are successful in predicting PSD and holdup. In addition, bulk property predictions from kriging based model is comparable to ANN based model.

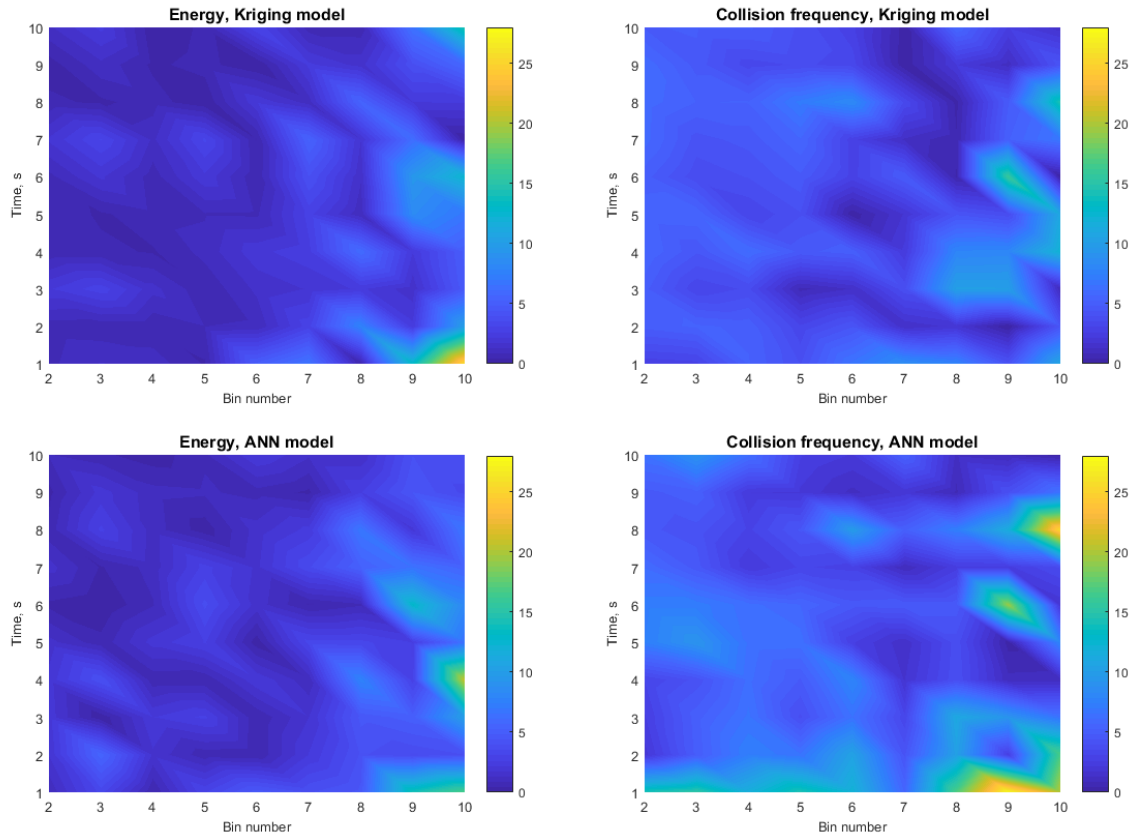


Figure 4.4 Percentage error surface plots for Energy and Collision surrogate models from Kriging (first row) and ANN (second row) for case study 1, Validation: 850 rpm

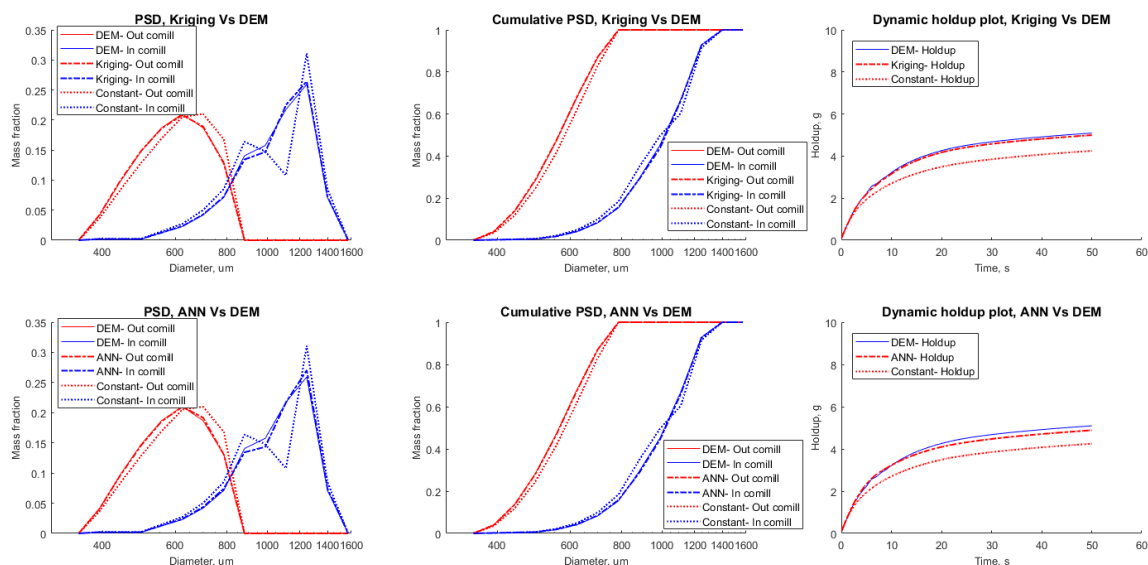


Figure 4.5 Comparison of PSD and holdup plots, DEM Vs SM Vs Constant kernel for case study 1, Validation: 850 rpm. Kriging based surrogate (First row) and ANN based surrogate (second row).

Table 4.4 Maximum and minimum absolute percentage errors for specific energy and collision frequency surrogate models for case study 1, validation: 850 rpm and case study 2, validation: 3.25 kg/h

Case study 1: Fixed flowrate simulations				
	Specific Energy SM		Collision frequency SM	
%error	Kriging	ANN	Kriging	ANN
Maximum	25.6	20.8	15.8	27.4
Minimum	2.8e-3	4.1e-2	1.4e-2	0.20
Case study 2: Fixed impeller speed simulations				
	Specific Energy SM		Collision frequency SM	
%error	Kriging	ANN	Kriging	ANN
Maximum	27.9	30.1	22.3	22.4
Minimum	5.6e-3	1.3e-2	9.9e-2	7.8e-2

Table 4.5 Metrics to compare performance of Kriging, ANN and constant kernel based particle size distribution and holdup predictions for case study 1, validation: 850rpm and case study 2, validation: 3.25 kg/h

Case study 1: Fixed flowrate simulations			
	Kriging	ANN	Constant kernel
PSD, SSE	2.6E-4	2.5E-4	1.9E-2
Holdup, SSE	0.36	0.96	26.6
Case study 2: Fixed impeller speed simulations			
	Kriging	ANN	Constant kernel
PSD, SSE	2.9E-4	1.2E-3	1.1E-2
Holdup, SSE	0.04	0.97	4.56

4.3.2 Case study with fixed impeller speed simulations

Similar to case study 1, Kriging and ANN models are developed for specific energy and collision frequency of particles based on DEM simulations at eight flowrates as given in Table 4.1. For the validation case (3.25 kg/h), absolute percentage error plots for the specific energy and collision frequency from kriging models are shown in Figure 4.6 (first row). Similarly, the error plots for the corresponding ANN based models for specific energy and collision frequency are also shown in Figure 4.6 (second row). The percentage maximum and minimum errors for these models are listed in Table 4.4. As done for case study 1, the effect of these surrogate models on hybrid model predictions are analyzed and the performance of these models is compared. For case study 2, comparison of particle size distribution of material inside and exiting the mill at steady state for kriging based model is shown in Figure 4.7 (first row). Figure 4.7 (second row) shows the comparison for an ANN based model. A comparison of the dynamic holdup for kriging based model and ANN based models are also shown in Figure 4.7. Similar to case study 1, SM based

model predictions agree well with DEM based model predictions. The constant kernel based predictions differ significantly from DEM based predictions in this case study as well.

The performance metrics for the surrogate models is listed in Table 4.5. The sum of square errors for PSD from Kriging-PBM approach, ANN-PBM approach and constant kernel models are $2.9\text{e-}4$, $1.2\text{e-}3$ and $1.1\text{e-}2$ respectively. For dynamic holdup, the sum of square errors for PSD from Kriging-PBM approach, ANN-PBM approach and constant kernel models are 0.04, 0.97 and 4.56 respectively. As for the previous case study, it is apparent that the surrogate models are successful in predicting PSD and holdup. In addition, the kriging model outperforms the ANN based model.

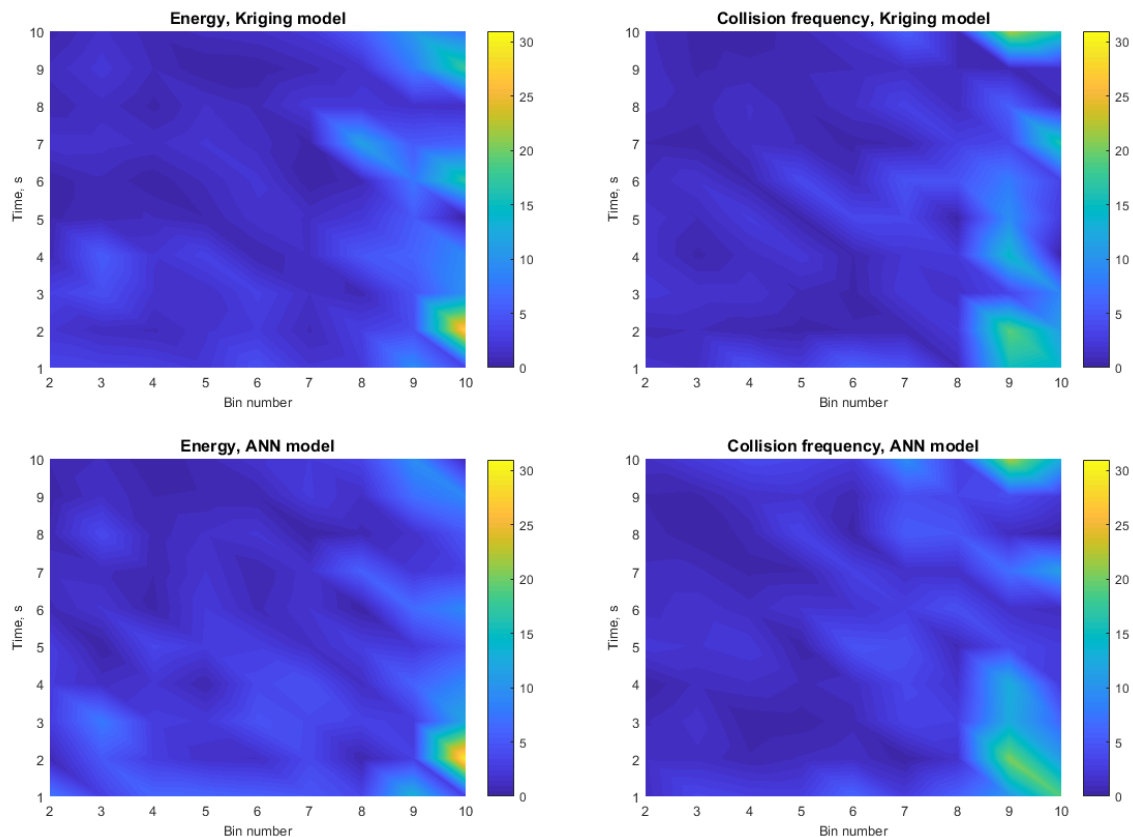


Figure 4.6 Percentage error surface plots for Energy and Collision surrogate models from Kriging (first row) and ANN (second row) for case study 2, Validation: 3.25 kg/h

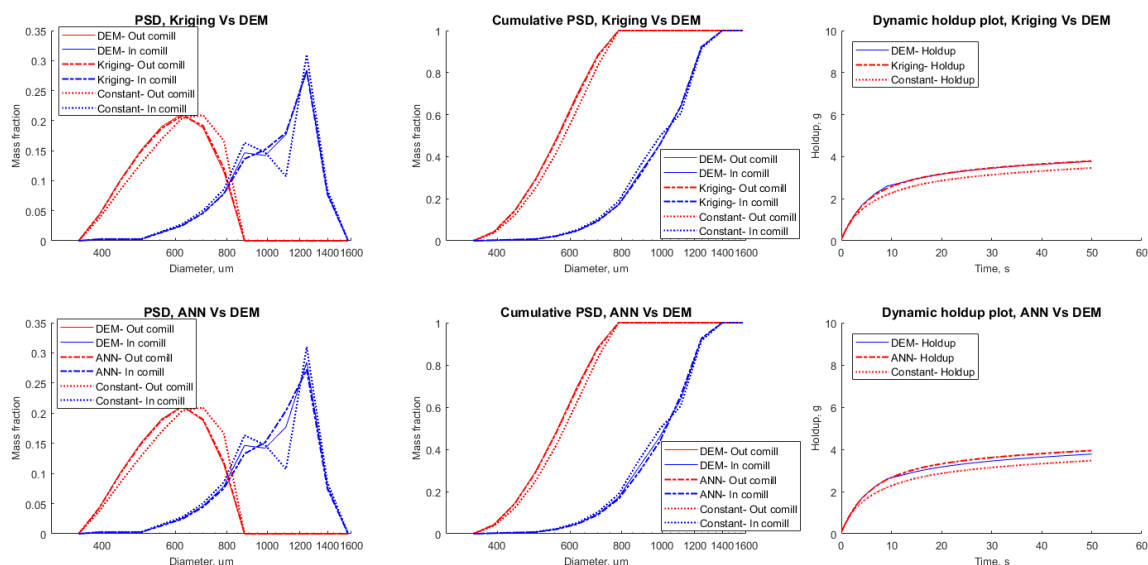


Figure 4.7 Comparison of PSD and holdup plots, DEM Vs SM Vs Constant kernel for case study 2, Validation: 3.25 kg/h. Kriging based surrogate (First row) and ANN based surrogate (second row).

Through the case studies detailed, the predictions from SM-PBM approach are shown to be comparable to DEM-PBM approach. The significance of the proposed hybrid framework lies in the drastic improvement seen in computational cost. The SM-PBM model takes few seconds to run in contrast to the DEM-PBM model that takes few days to run as a result of the high fidelity DEM model. In addition, the SM-PBM approach is shown to have capability to predict the mechanistic data at a new processing condition. This is a significant advantage as it eliminates the need to run DEM simulations when the processing condition is changed.

4.3.3 Implementation in integrated process modeling

The mill model developed using the SM-PBM framework as described in Section 4.2.4 was built in MATLAB using the DACE toolbox [169] and the ANN toolbox [170]. However, model integration is usually done in simulators such as gPROMSTM, as this platform allows dynamic simulation and dynamic propagation of disturbances from an upstream unit to the succeeding units.

gPROMSTM uses an equation-oriented approach instead of sequential modular approach. An overview of the equation-oriented techniques used in gPROMSTM platform and comparison with the sequential modular approach is given by Pantelides and Barton [171].

Surrogate models, for instance, a kriging model can be effectively incorporated in gPROMSTM along with the population balance model equations described in Section 4.2.2. For demonstration, the set of equations for the kriging models added to the PBM in gPROMSTM, along with the model parameters used are explained here. The design sites in the model are represented by a matrix X of size $m \times 3$ that are mean centered and univariate scaled, where $m=450$ for case study 1 (5 impeller speeds x 9 particle sizes x 10 time intervals) and $m=720$ (8 flowrates x 9 particle sizes x 10 time intervals) for case study 2. x^{new} is a vector representing the point at which the surrogate model needs to be evaluated i.e., $x^{new} = [\text{impeller speed, time in seconds, particle radius in mm}]^T$ for case study 1. The set of Equations 4.19 yields the kriging model predictor represented as $\hat{f}(x^{new})$ where γ , is a matrix of size $m \times 1$ that represents correlation factors given by $\gamma = R^{-1}(y - 1\beta)$.

Table 4.6 shows the parameters obtained for the energy as well as the collision frequency kriging model. Model parameters relevant for case study 2 are shown in Table 4.7.

$$dx(i, j) = \frac{x^{new}(j) - S_x(1, j)}{S_x(2, j)} - X(i, j), i = 1, 2 \dots m; j = 1, 2, 3$$

$$tt(i, j) = \theta(j) * |dx(i, j)|^{\theta(4)}, i = 1, 2, \dots m; j = 1, 2, 3$$

4.19

$$r(i) = e^{\sum_{j=1}^3 tt(i, j)}, i = 1, 2, \dots m$$

$$\hat{f}(x^{new}) = S_y(1) + S_y(2) * \left(\sum_{i=1}^m \gamma(i)r(i) + \beta \right)$$

Table 4.6 Kriging model parameters for case study 1

	Energy model	Collision model
Correlation model parameters, θ	[0.187, 0.111, 1.189, 0.397]	[1.059, 0.8848, 0.569, 0.910]
Regression model parameter, β	-0.119	0.337
Scaling factors for design responses, S_y	[352.6; 162.5]	[1.630; 0.637]
Scaling factors for design sites, S_x	$\begin{bmatrix} 1000 & 5.5 & 0.366 \\ 424.7 & 2.875 & 0.108 \end{bmatrix}$	$\begin{bmatrix} 1000 & 5.5 & 0.366 \\ 424.7 & 2.875 & 0.108 \end{bmatrix}$

Table 4.7 Kriging model parameters for case study 2

	Energy model	Collision model
Correlation model parameters, θ	[0.25, 0.0702, 2.00, 0.2806]	[0.236, 0.891, 0.749, 0.315]
Regression model parameter, β	-0.0794	0.186
Scaling factors for design responses, S_y	[354.7; 163.8]	[1.603; 0.559]
Scaling factors for design sites, S_x	$\begin{bmatrix} 4.25 & 5.5 & 0.366 \\ 1.146 & 2.874 & 0.108 \end{bmatrix}$	$\begin{bmatrix} 4.25 & 5.5 & 0.366 \\ 1.146 & 2.874 & 0.108 \end{bmatrix}$

Similarly, an artificial neural network surrogate model can be incorporated in gPROMSTM along with the population balance model equations as well. The model parameters i.e., weights and biases corresponding to the input layer and the hidden layers are obtained using the design points i.e., $m=450$ for case study 1 and $m=720$ for case study 2 using the MATLAB ANN toolbox. If x^{new} is a vector representing the point at which the surrogate model needs to be evaluated i.e., $x^{new} = [\text{impeller speed, time in seconds, particle radius in mm}]^T$ for case study 1, let $x^{scale,new}$ be the corresponding scaled variable. The surrogate model predictor can then be evaluated as given in Equation 4.20, where $w_{I \rightarrow H}(k, i)$ represents the weight from i^{th} neuron in the input layer to the k^{th} neuron in the hidden layer. $b_{I \rightarrow H}(k)$ represents bias from the input layer to the k^{th} neuron in the

hidden layer. The value of the k^{th} neuron in the hidden layer is represented as $HN(k)$ as given by Equation 4.20. $w_{H \rightarrow O}(k)$ represents weight from k^{th} neuron in the hidden layer to the neuron in the output layer. The weights and biases for all the layer connections for case study 1 are listed in Table 4.8. Model parameters for case study 2 are listed in the Table 4.9. Using the weights and bias from the hidden layer to the output layer, the scaled surrogate model predictor can be obtained.

$$HN(k) = b_{I \rightarrow H}(k) + \sum_{i=1}^3 w_{I \rightarrow H}(k, i) * x^{scale, new}(i), \quad k = 1, 2, \dots, 10$$

4.20

$$\hat{f}(x^{new}) = b_{H \rightarrow O} + \sum_{k=1}^{10} \text{tansig}(HN(k)) * w_{H \rightarrow O}(k)$$

Table 4.8 ANN model parameters for case study 1

Bias, input to hidden layer, $b_{I \rightarrow H}$	$\begin{bmatrix} 4.042 \\ -0.845 \\ -2.127 \\ -1.115 \\ -1.017 \\ 0.012 \\ -1.499 \\ 2.774 \\ -2.703 \\ 2.768 \end{bmatrix}$	$\begin{bmatrix} 2.791 \\ -1.484 \\ -0.839 \\ 0.804 \\ 1.336 \\ 0.518 \\ -0.415 \\ 3.138 \\ 1.498 \\ -1.673 \end{bmatrix}$
Weights, input to hidden layer, $w_{I \rightarrow H}$	$\begin{bmatrix} 0.495 & 2.787 & 0.236 \\ 0.005 & 1.841 & -1.615 \\ 3.362 & -0.054 & 2.388 \\ 1.679 & 1.654 & 0.925 \\ 0.168 & 1.886 & 0.068 \\ 0.024 & -0.161 & -1.345 \\ -0.416 & -3.157 & -2.367 \\ 1.389 & 3.154 & -0.184 \\ -1.273 & 0.258 & -2.246 \\ 0.862 & -0.581 & 2.307 \end{bmatrix}$	$\begin{bmatrix} -1.937 & 0.811 & -0.847 \\ 2.098 & -0.683 & -2.536 \\ 0.293 & 0.640 & -1.618 \\ -2.662 & 0.625 & 1.082 \\ 0.710 & -2.280 & 0.551 \\ 0.048 & -2.233 & -0.967 \\ -1.749 & 0.120 & -2.259 \\ 2.749 & 0.480 & -2.199 \\ -0.144 & -0.024 & -3.441 \\ -0.927 & -3.945 & 1.740 \end{bmatrix}$
Bias, hidden to output layer, $b_{H \rightarrow O}$	1.1716	-0.6761
Weights, hidden to output layer, $w_{H \rightarrow O}$	$\begin{bmatrix} -1.307 \\ 0.139 \\ -0.008 \\ 0.023 \\ -0.053 \\ 0.870 \\ -0.001 \\ 0.093 \\ -0.233 \\ -0.257 \end{bmatrix}$	$\begin{bmatrix} 0.129 \\ 0.042 \\ -0.123 \\ 0.044 \\ 0.022 \\ -0.059 \\ -0.035 \\ -0.119 \\ -0.234 \\ -0.041 \end{bmatrix}$

Table 4.9 ANN model parameters for case study 2

	Energy model	Collision model
Bias, input to hidden layer, $b_{I \rightarrow H}$	$\begin{bmatrix} -1.202 \\ -1.943 \\ -1.158 \\ -0.378 \\ -0.885 \\ 1.977 \\ 1.495 \\ -8.615 \\ -0.457 \\ -4.266 \end{bmatrix}$	$\begin{bmatrix} 2.958 \\ 1.615 \\ 0.317 \\ 2.678 \\ 0.439 \\ 0.750 \\ -2.557 \\ 1.868 \\ 3.422 \\ 3.538 \end{bmatrix}$
Weights, input to hidden layer, $w_{I \rightarrow H}$	$\begin{bmatrix} -0.063 & -1.459 & 1.079 \\ -0.02 & 2.116 & 0.823 \\ 1.857 & -0.429 & -1.537 \\ 0.02 & -0.065 & -0.802 \\ -0.167 & -3.522 & -0.041 \\ 0.017 & 0.180 & 2.748 \\ 2.459 & -3.961 & -0.537 \\ -4.921 & 1.795 & 16.342 \\ -0.918 & 0.3701 & -0.676 \\ -11.704 & 4.652 & -7.077 \end{bmatrix}$	$\begin{bmatrix} -0.512 & -2.165 & 2.021 \\ -0.643 & -2.990 & -0.280 \\ -0.013 & -0.211 & 2.378 \\ 0.215 & 2.644 & -0.711 \\ 2.859 & -1.453 & 0.077 \\ 3.205 & -1.615 & 0.594 \\ 0.041 & 0.002 & 5.724 \\ 1.308 & 1.325 & 2.122 \\ 0.221 & 2.577 & -0.438 \\ 1.483 & -2.086 & -1.619 \end{bmatrix}$
Bias, hidden to output layer, $b_{H \rightarrow O}$	0.508	1.017
Weights, hidden to output layer, $w_{H \rightarrow O}$	$\begin{bmatrix} 0.191 \\ 0.084 \\ -0.019 \\ 2.125 \\ -0.121 \\ 0.393 \\ 0.012 \\ 0.001 \\ 0.088 \\ -0.013 \end{bmatrix}$	$\begin{bmatrix} 0.067 \\ -0.059 \\ 0.218 \\ 0.936 \\ -0.072 \\ 0.071 \\ 0.310 \\ 0.002 \\ -2.462 \\ 0.064 \end{bmatrix}$

The surrogate models can thus be used to develop a mechanistic integrated mill and tablet press model in gRPOMSTM. While gPROMSTM uses an equation-oriented approach, in contrast, the solution of the population balance model developed in MATLAB uses explicit Euler integration method. Figure 4.8 shows evolution of particle size distribution percentiles d_{10} , d_{50} and d_{90} at 850 rpm and 4 kg/h (case study 1) obtained from gPROMSTM as well as MATLAB, which shows the solution methods yield comparable results.

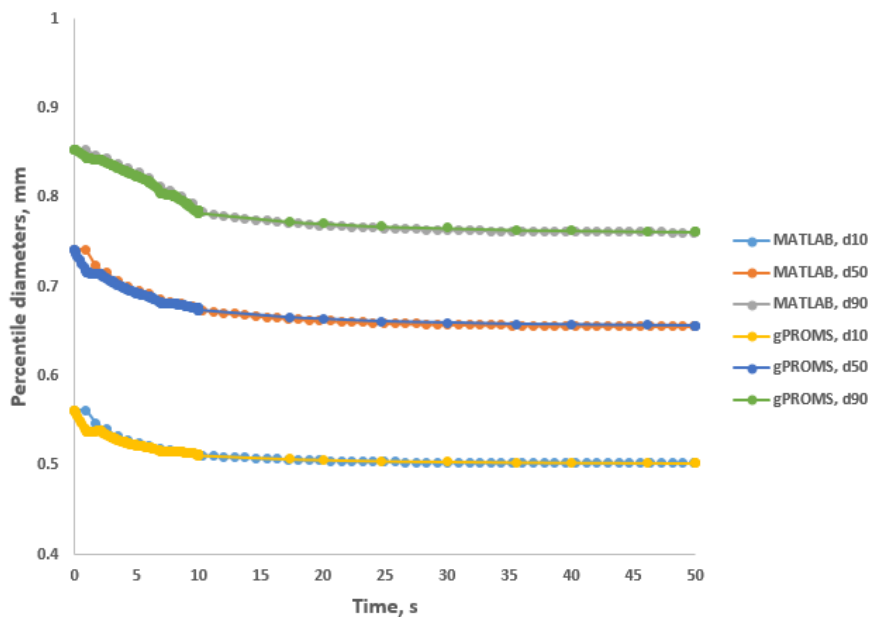


Figure 4.8 Comparison of evolution of milled product percentile diameters predictions from gPROMS and MATLAB, 850 rpm

With the integrated model thus implemented in gPROMSTM, Figure 4.9 shows the simulation of granule product bulk density evolution with time. Figure 4.10 shows the evolution of tablet hardness and tablet weight with time. This implementation of the mechanistic integrated model is intended to demonstrate that the surrogate model, once developed, is an effective replacement of the computationally expensive DEM simulations, and can be used in the development of a fully mechanistic flowsheet model for the continuous manufacturing line. Without the development of the surrogate model, such an inclusion into flowsheet modeling cannot be attained, thus limiting the utilization of full potential of mechanistic and multiscale modeling frameworks.

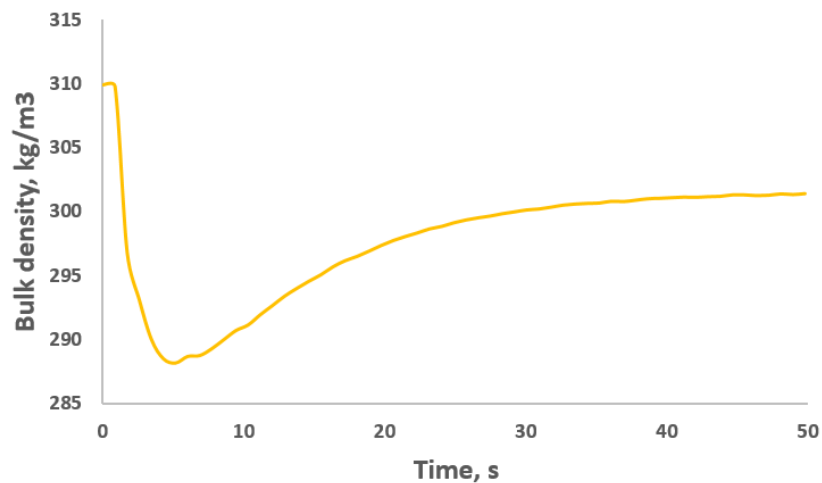


Figure 4.9 Profile of milled granule bulk density evolution with time from SM-PBM framework

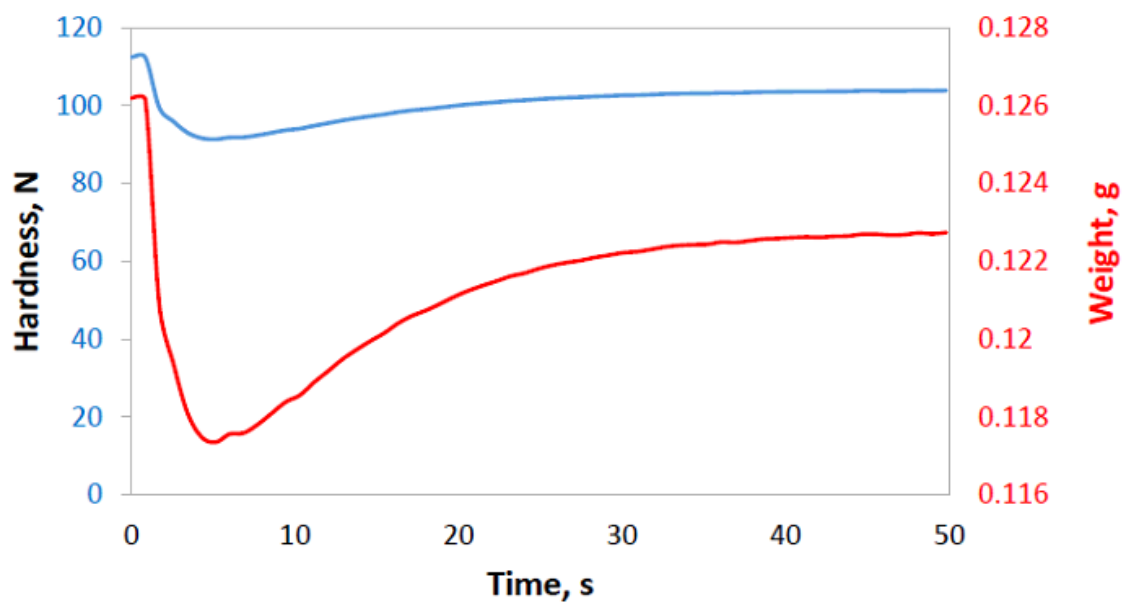


Figure 4.10 Profiles tablet hardness (left axis) and tablet weight (right axis) evolution with time from SM-PBM framework

4.4 Comparison between kriging and ANN surrogate models

The performance of Kriging and ANN surrogate models for predicting PSDs, dynamic holdup profiles are shown to be comparable, as discussed in Sections 4.3.1 and 4.3.2. However, it is worth comparing different surrogate modeling approaches in terms of aspects related to model building and implementation. For instance, unlike a Kriging model, training a neural network model has randomness associated with it that arises from random division of the dataset into training and validation sets. In this work, a fixed random seed generator is used for reproducibility of results. However, several methods [172-174] are available in neural networks literature to handle the randomness, which introduces additional steps in building an ANN model. Another notable difference between the modeling approaches is that Kriging is an interpolation method i.e., model prediction error is zero at the design points whereas the ANN model predictor may have an error at design points. This may lead to superior performance of Kriging model at design points. However, this is not a reflection of the model performance at other sample sites. In addition, a Kriging model provides an estimate of variance of prediction. This is a useful property as variance estimator helps identify additional sample points that need to be added for the purpose of improvement in accuracy of model prediction [175]. A Kriging model has lower number of model parameters when compared to an ANN model [176]. The higher number of model parameters in an ANN model are associated with weights and biases associated with every neuron connection. This is also reflected in relatively higher training time required for an ANN model when compared to a Kriging model. In terms of integration into gPROMSTM environment, both modeling approaches can be easily implemented.

4.5 Summary

In this work, a SM-PBM framework is proposed that replaces a computationally expensive DEM-PBM framework. The framework is implemented for a comilling system. Through this work, the methodology is shown to be applicable for complex processes that involve particle breakage. The application is all the more useful for such processes as the DEM simulations for a breakage process takes much longer than for a process that does not involve particle size change such as feeding, blending etc. The methodology is implemented for case studies involving feed flowrates and impeller speeds as the processing variable, since a change in either may be relevant in a pharmaceutical manufacturing process. The SM-PBM methodology is also shown to predict bulk properties such as particle size distributions and dynamic hold up. The bulk property predictions from the DEM-PBM approach is also compared to predictions from a model that is based on a constant kernel value that is independent of particle size or process time. The comparison shows the significance of considering dynamic change in breakage kernel to accurately model dynamic hold up evolution or particle size distribution. The surrogate modeling approach makes the inclusion of particle scale dynamics in unit operation modeling as well as integrated process modeling viable. The SM-PBM framework is implemented in an integrated mill and tablet press model that aids in simulation of dynamic bulk density and tablet properties such as hardness and weight. The implementation of the framework in the integrated model illustrates how multiscale frameworks using surrogate modeling methodologies can support development of a mechanistic flowsheet model.

The surrogate models not only efficiently represent the mechanistic data obtained from DEM simulations, but also eliminate the need to run the DEM simulation at a new processing condition. The improvement in computational expense is drastic as a DEM simulation takes days to run whereas the developed surrogate model takes few seconds. It is worth noting that the computational

expense needed to build the surrogate models is high, particularly because the DEM simulations include particle breakage. However, advances in the area of parallel computing is expected to release limitations on computational complexity to some extent [177].

The framework also aligns with QbD approach recommended by FDA as the effect of processing conditions, material properties are better captured into process modeling through inclusion of particle level information. The framework addresses issues with computational limitations and aids in the effort to utilize advanced modeling techniques for practical applications such as flowsheet modeling and prediction, sensitivity analysis, optimization and model predictive control.

Chapter 5

Hybrid model development for prediction of milled granule quality attributes

5.1 Background

Granule breakage in the comill occurs through weakening of pore structures within the agglomerate through stresses from a rotating impeller and collisions with equipment walls. The smaller sized granules thus obtained are discharged through a screen. The size distribution of the resulting granules is a CQA as it impacts the flow behavior and downstream product attributes. Non uniform flow of granules into a tablet press die could result in weight variability of the tablets. More significantly, the content uniformity of tablets is impacted which results in inconsistent drug dissolution profiles, an indicator of the drug bioavailability. In addition, the strength of tablet obtained from compaction is also impacted [178]. Literature published in the area of comminution focusses on predicting milled particle size distribution [40, 41, 43, 44]. Mentions of prediction of other CQAs such as bulk density, tapped density, friability etc., of the milled product are limited. It is important to note that these CQAs have an impact on the compaction behavior of granules and thus their effect on CQAs should be predicted.

In the current work, a hybrid modeling approach to predict particle size distribution and bulk density, tapped density, friability of the milled product is presented. Milled product particle size distribution is predicted through development of a population balance model. Prediction of other CQAs such as bulk density, tapped density and friability is pursued by using a Partial Least Squares (PLS) modeling approach which uses the milled product particle size distribution as one of the

input variables. The approach presented is also calibrated and validated using experimental data generated from milling pharmaceutical material. The specific objectives of this work are:

- Analyze the effect of the influence of process parameters on milled product properties.
- Develop a PBM that predicts milled product particle size distribution as well as milling dynamics.
- Develop a PLS model that predicts milled product CQAs such as bulk density, tapped density and friability.
- Calibrate and validate the PBM as well as PLS models, present statistical significance of model parameters, where applicable.
- Present a comprehensive modeling approach for the milling process that aids in flowsheet modeling.

5.2 Experiments

The model formulation consisted of two Active pharmaceutical ingredients (APIs) and Maize starch, powdered cellulose, pregelatinised starch, sodium starch glycolate as excipients. The formulation was processed using demineralized water as granulation liquid.

5.2.1 Design of Experiments

The study has been conducted using the ConsiGma™ system (GEA Pharma systems, Collette, Wommelgem, Belgium), which is an oral solid dosage manufacturing line based on continuous wet granulation. This study involved three consecutive unit operations of the continuous system: the twin-screw granulator, fluid-bed dryer and Granule Conditioning Unit (GCU). The twin-screw granulator consists of two 25 mm diameter co-rotating screws with a length-to-diameter ratio of 20:1. The powder premix enters the granulator barrel using a gravimetric twin-screw loss-in-weight feeder (KT20, K-Tron Soder, Niederlenz, Switzerland). In a next step, the powder premix is moved

forward using conveying elements. In this conveying compartment, prior to the first kneading compartment, granulation liquid is gravimetrically dosed into the screw chamber using two peristaltic pumps (Watson Marlow, Cornwall, UK) operating out of phase with silicon tubing (internal and external diameter of 1.6 and 4.8 mm, respectively) connected to 1.6 mm nozzles. The addition of granulation liquid takes place by injecting the liquid through two liquid feed ports located on the central top of each screw. The fixed screw configuration used in this study was composed of 2 kneading zones each consisting of 4 kneading elements ($L=D/4$ for each kneading element), staggered at an angle of 60 degrees. Both kneading zones were separated by a conveying element ($L=1.5D$). An extra conveying element ($L=1.5D$) was implemented after the second kneading block together with 2 narrow kneading elements ($L=D/6$ for each kneading element) in order to reduce the amount of oversized agglomerates.

In a next step, the produced wet granules are pneumatically transferred by means of a wet transfer line to the six-segmented fluid-bed dryer. This semi-continuous module uses a drying chamber which is divided in 6 identical cells, which are sequentially filled and discharged, hereby ensuring a continuous flow of incoming wet granules and exiting dried granules. After drying, the granules are pneumatically transported to the Granule Conditioning Unit (GCU). This module consists of a product control hopper (PCH) where the dried granules are collected. In a next step, the granulate material is gradually discharged to a conical mill using a metering valve, which ensures a consistent material flow. In this study, the conical mill is a U10 Quadro® Comil (Quadro, Ontario, Canada) which is equipped with a grater style screen and a square bar impeller. The diameter of the screen holes is 1016 μm . After the milling step, the resulting product is assembled in a buffer reservoir where it is released for the next process step.

An adequate Population Balance model calibration requires a thorough understanding of how granules with different characteristics behave during the milling operation. This is only possible by

intensively collecting experimental data, which captures the influence of input material properties and process variables during the milling process. De Leersnyder, Vanhoorne [179] have demonstrated that granules may undergo a significant amount of breakage during fluid-bed drying.

This makes it difficult to investigate the impact of the milling process upon breakage of the incoming granules. For this reason, this study uses oven-dried granules (collected after the twin-screw granulator) as well, since this material is assumed to undergo stronger breakage events during milling, allowing to study the underlying mill phenomena more precisely. Furthermore, the experimental part of this study takes into account several input material properties (granule size, granule strength and residual moisture content) and process settings (impeller speed) (see Table 5.1)

The first part of the experiments focuses on granules collected after twin-screw granulation and oven-dried (24h, 40 deg C) (experiments A-C in Table 5.1). To investigate the impact of incoming granule strength, granules were produced at three different liquid-to-solid (L/S) ratios. By increasing the L/S ratio, the amount of liquid bridges formed between solid particles grows, which results in stronger granules. Furthermore, to assess the effect of incoming granule size, granules were sieved in three different size classes (>2000 , $1000-2000$ and <1000 μm) using a Retsch VE 1000 sieve shaker (Haan, Germany) and fed separately on top of the mill. The second part of the experiments includes granules subjected to fluid-bed drying (experiments D-H in Table 5.1 Here, the impact of drying time (hence, residual moisture) upon granule breakage is examined. Lastly, granules are collected at the outlet of the twin-screw granulator and tray-dried at room temperature for two specific durations of time (i.e. 4h and 24h) with the goal of achieving two distinct moisture levels, which are within the processable range of milling (experiments I in Table 5.1).

Table 5.1 Overview of different milling experiments conducted in this study

ID	Sampling location	L/S ratio	Drying time (s)	Residual moisture (%)	Size class (µm)	Impeller speed (rpm)
A	TSG (oven dried)	26.7	N/A	1.35	<1000, 1000-2000, >2000, all	500, 1000, 1500
B	TSG (oven dried)	43.3	N/A	1.28	<1000, 1000-2000, >2000, all	500, 1000, 1500
C	TSG (oven dried)	60	N/A	1.34	<1000, 1000-2000, >2000, all	500, 1000, 1500
D	FBD	50	400	5.97	all	500, 1000, 1500
E	FBD	50	600	3.65	all	500, 1000, 1500
F	FBD	50	800	2.32	all	500, 1000, 1500
G	TSG (air dried)	50	N/A	6.43	all	500, 1000, 1500
H	TSG (air dried)	50	N/A	1.41	all	500, 1000, 1500
I	TSG (air dried)	50	N/A	1.70	all	300, 500, 700, 900, 1100, 1300, 1500

5.2.2 Test Methods

The granule size is measured via dynamic image analysis using a QICPIC particle size analyzer with WINDOX 5.4.1.0 software (Sympatec, GmbH, Clausthal-Zellerfeld, Germany). The resulting volumetric granule size distributions were calculated using the default M7 non-ISO size fractions.

Bulk density was determined by measuring the bulk volume of 50 g sample in a 250 mL graduated cylinder. In addition, the tapped volume after 500 taps was measured for the granule samples, using a tapping machine (J. Englesman, Ludwigshafen, Germany).

A portion of granules (with mass >10 g) is sieved at 150 µm and the fraction smaller than 150 µm is removed. 10 g is weighted from the fraction >150 µm (I_{WT}) and combined with 200 glass beads (diameter 4 mm) in a plastic drum of the friabilator (Pharmatest PTF E, Hainburg, Germany). This drum spins with a speed of 25 rpm for a duration of 10 minutes. After 10 minutes, content of the drum is sieved at 150 µm. The residual granules with size >150 µm are weighted (F_{WT}). Friability (F) was calculated using Equation 5.1.

$$F(\%) = \left(\frac{I_{WT} - F_{WT}}{I_{WT}} \right) \times 100 \quad 5.1$$

The residual moisture content within the granule samples was measured via Loss On Drying (LOD) using a moisture analyzer (Mettler LP16, Mettler-Toledo, Zaventem, Belgium) which includes an infrared dryer and a balance. A sample of 1 g was dried at 105 deg C until the weight was constant for 30 seconds.

5.3 Modeling methods

5.3.1 Population balance model

A population balance model (PBM) is implemented to track the change in mass of particles of various sizes over time as shown in Equation 6.1. $M(w, t)$ represents the mass of particles of volume w at time t , R_{form} and R_{dep} represent the rates of formation and depletion of particles respectively. \dot{M}_{in} and \dot{M}_{out} are the mass flow rates of particles entering and exiting the mill respectively. Several techniques are published in the literature to solve the PBM equation [180-182]. In this work, the cell average technique using discretization scheme as proposed by Chaudhury, Kapadia [183] and applied by Barrasso, Oka [44] is used to obtain the numerical solution to the set of equations in the PBM. The discretization scheme used is the same as the particle size bins used in the Qicpic analysis as described in Section 5.2.2.

$$\frac{dM(w, t)}{dt} = R_{form}(w, t) - R_{dep}(w, t) + \dot{M}_{in}(w, t) - \dot{M}_{out}(w, t) \quad 5.2$$

In this work, the comill unit used for collecting experimental data received feed from a hopper intermittently using an on-off valve. The PSD or the flow rate of the feed to the comill from the

hopper is unknown due to limitations in collecting this information. Hence, the hopper and the comill are considered as a single unit for the purpose of simulating the milling process. This assumption is equivalent to assuming the process is operating in a batch configuration. Hence, \dot{M}_{in} in the PBM Equation 6.1.

The formation and depletion of particles occur in the comill due to the breakage process. The rate of formation R_{form} and the rate of depletion R_{dep} is formulated in the model as given in Equations 5.3 and 5.4 respectively, using a breakage kernel and a breakage distribution function.

$$R_{form}(w, t) = \int_w^{\infty} K(u)M(u, t)b(u, w)du \quad 5.3$$

$$R_{dep}(w, t) = K(w)M(w, t) \quad 5.4$$

The breakage kernel $K(w)$ is used to represent the probability that a particle of volume w undergoes breakage. In this work, a classification kernel as given in Equation 5.5 is used. Here, v_{imp} is the impeller speed, $v_{imp,min}$ is the minimum impeller speed and the parameter β is estimated from experimental data. The kernel is formulated based on theory published by Vogel and Peukert [184] i.e., a particle breaks only if the energy lost by it from collisions is greater than a certain ‘Threshold energy’, which is a material specific property dependent on particle size. A smaller particle needs higher energy to break compared to a larger particle. In this kernel, particles below a certain size are not considered to break as the energy imparted by the impeller is considered insufficient. Another plausible theory is that small size particles exit the mill, and hence do not undergo breakage. The size limit below which the breakage kernel is assumed to be zero is obtained using a heuristic approach during calibration of the model. Particle size corresponding to the 24th bin (797 μm) in the discretization scheme was determined as the size limit in this work i.e., if the size of a

particle is less than 797 μm , the particle is assumed to remain unbroken. A similar classification kernel was also used by Reynolds [43]. However, Reynolds [43] considered the kernel value below a size limit as a constant and the effect of particle size was not considered.

$$K(w) = \begin{cases} \beta \left(\frac{v_{imp}}{v_{imp,min}} \right)^2 \left(\frac{w}{w_{ref}} \right) & \text{if } w \geq w_{ref} \\ 0 & \text{else} \end{cases} \quad 5.5$$

The breakage distribution function $b(u, w)$ represents the distribution of daughter particles formed when a particle of volume w undergoes breakage. Several breakage functions have been used to model milling process [109, 185]. In this work, a pragmatic approach was employed to determine the choice of breakage distribution function. Feed granules were sieved and granules of size >2000 μm were separated and milled. Since all the granules in this fraction are greater than the screen size used i.e., 1016 μm , the breakage of particles is assumed to be the dominant phenomenon affecting the milled product PSD, when compared to the effect of particles exiting the mill. The resulting milled product particle size distribution was fit to a PBM formulated from various breakage distribution functions to determine the choice that best fits the experimental data. In this work, an attempt was made to fit a log-normal [44], a uniform distribution, Hill-Ng distribution [186] and a combination of these distributions. The Hill-Ng distribution function was observed to fit the experimental data better than the other distribution functions tested. The distribution function $b(w, u)$ is given in Equation 5.6 where, w is the parent particle volume, u is the daughter particle volume and the parameters p, q are calibrated from experimental data. The parameters p and q also provide a fundamental understanding of the breakage process. The parameter p is the number of daughter fragments formed and the parameter q represents the fragment size dependence. A large value of q indicates fragmentation, whereas a small value of q indicates chipping or erosion mechanism. $B(q, r)$ refers to beta function with q and r as the arguments where $r = q(p - 1)$.

$$b(w, u) = \frac{p^u w^{q-1} (1 - \frac{u}{w})^{r-1}}{wB(q, r)} \quad 5.6$$

The mass flowrate out of the mill $\dot{M}_{out}(w, t)$ is formulated using a screen model as given in Equation 5.7. The feed particle size distribution entering the mill is denoted by d_{in} . A parameter $\Delta = d_{screen} * \delta$ is used, where δ is referred to as critical screen size ratio and d_{screen} is the screen size. The critical screen size ratio reflects the size limit below which the particle exits the mill instantaneously. If the size of a particle is greater than the screen size, the particle does not exit the mill. A linear model as given in Equation 5.8 is used to determine the flowrate of particles of various sizes exiting the mill. It is worth noting that the linear model considers the size of a particle relative to the lower and upper size limits of the particle size bins defined to discretize the PBM. This is an update to a linear model used in Barrasso, Oka [44] where the average size of the bin $x = \frac{x_{LL} + x_{UL}}{2}$ was used.

$$\dot{M}_{out}(w, t) = (R_{form}(w, t) - R_{dep}(w, t) + \gamma d_{in}(w, t))(1 - f_d) \quad 5.7$$

$$f_d(w) = \begin{cases} 0 & \text{for } x_{UL} \leq \Delta \\ \frac{x_{UL} - 0.5(d_{screen} + \Delta)}{x_{UL} - x_{LL}} & \text{for } x_{UL} > d_{screen}, x_{LL} < \Delta \\ \frac{x_{UL} - d_{screen} + \frac{(0.5x_{LL} + 0.5d_{screen} - \Delta)(d_{screen} - x_{LL})}{d_{screen} - \Delta}}{x_{UL} - x_{LL}} & \text{for } x_{UL} > d_{screen}, x_{LL} > \Delta \\ \frac{0.5(x_{UL} - \Delta)^2}{(d_{screen} - \Delta)(x_{UL} - x_{LL})} & \text{for } \Delta < x_{UL} < d_{screen}, x_{LL} < \Delta \\ \frac{x - \Delta}{d_{screen} - \Delta} & \text{for } x_{UL} < d_{screen}, x_{LL} > \Delta \\ 1 & \text{for } x_{LL} \geq d_{screen} \end{cases} \quad 5.8$$

In addition, a relationship between the critical screen size ratio δ and impeller speed v_{imp} is proposed as given in Equation 5.9. The relationship is reflective of the reduced apparent screen

size available for a particle to exit the mill as impeller speed increases. At higher impeller speeds, the particle motion tangential to the screen leads to a reduction in apparent screen size that is available for the particle to exit the mill.

$$\delta = \epsilon \left(\frac{v_{imp,min}}{v_{imp}} \right)^\alpha \quad 5.9$$

If the size of a particle is less than Δ , it exits the mill instantaneously. If the size of a particle is greater than the screen size, it does not exit the mill. And, if the size of a particle is within these limits, a linear function is used to determine the flow rate out of the mill as given in Equation 5.8. The parameters γ, ϵ, α are estimated from experimental data. The list of all the parameters in the PBM is tabulated in Table 5.2.

Table 5.2 List of parameters in the PBM

Significance in model	Parameter
Breakage kernel	β
Breakage distribution	p, q
Feed distribution coefficient	γ
Critical screen size parameters	ϵ, α

5.3.1.1 Parameter estimation and statistical measures

The model parameters are estimated by minimizing an objective function that is the sum of squares of differences between the experimental and model predicted values of milled product mass fractions for all ns particle size bins and n impeller speeds. The objective function $\phi(\theta)$ is given in Equation 5.10 where θ is the vector of model parameters. $f_{expt,i,j}, f_{sim,i,j}$ are the measured and simulated milled product mass fractions in the i^{th} bin milled at the j^{th} impeller speed respectively.

Sequential quadratic programming algorithm from 'fmincon' function in MATLAB® 2017a was used to perform the optimization.

$$\phi(\theta) = \sum_{i=1}^{ns} \sum_{j=1}^n (f_{expt,i,j} - f_{sim,i,j})^2 \quad 5.10$$

In order to test the statistical significance of the parameters estimated, standard errors of the model parameters are calculated from the diagonal elements of the covariance matrix obtained at the optimal parameter set θ^* . The covariance matrix $Cov(\theta^*)$ at the parameter set θ^* is obtained using Equation 5.11 [187] where s is the standard deviation and $J(\theta^*)$ is Jacobian estimated at the parameter set θ^* . The standard deviation s is calculated as given in Equation 5.11 based on residuals, which are the differences between model predicted and measured values. The sum of squared residuals is divided by the degrees of freedom $m - n$, where m is the number of comparisons made between the model predictions and measured values and n is the number of parameters in the model. The covariance matrix also requires values of the Jacobian at the parameter set θ^* . Each row of the Jacobian matrix consists of partial derivatives of the residual with respect to each model parameter. To estimate the Jacobian value, the partial derivatives are approximated using a finite-difference scheme using a perturbation of $1e-4$ as explained in Aster, Borchers [187]. Once the standard errors for the model parameters are obtained, 95% t value is calculated using standard errors of parameters calculated using Equation 5.11, and compared to the reference t-value t_{crit} of 2.15. A t-value higher than the t_{crit} indicates statistical significance at 95% confidence. The corresponding confidence intervals are obtained as shown in Equation 5.11.

$$\begin{aligned}
Cov(\theta_*) &= s^2(J(\theta_*))^T(J(\theta_*))^{-1} \\
s &= \sqrt{\frac{\sum_{z=1}^m r_z^2}{m-n}} \\
t_i &= \frac{\hat{\theta}_i}{SE_i} \\
SE_i &= \sqrt{Cov_{ii}} \\
CI_i &= [\hat{\theta}_i - t_{1-\frac{\alpha}{2}} SE_i, \hat{\theta}_i + t_{1-\frac{\alpha}{2}} SE_i]
\end{aligned}
\tag{5.11}$$

5.3.2 Partial least squares model

Since the formulated PBM only predicts granule size, an empirical Partial-Least Squares (PLS) model was constructed to connect the (predicted) particle size of the milled granules with their corresponding measured CQAs such as friability and bulk/tapped density. Furthermore, the residual moisture of the granulate material was included as input variable. This property is predicted by the PBM developed for the fluid-bed dryer. The granule size and residual moisture were separated in different blocks, allowing to calculate weights and scores for each independent block [188]. This MultiBlock PLS (MBPLS) approach was performed using SIMCA 15 software (Umetrics, Sartorius, Gottingen, Germany). Prior to analysis, the particle size data is weighted using mean centering. In addition, a unit variance (UV) scaling was applied on the residual moisture data. This model was calibrated and hence only valid for material which is representative for the integrated continuous granulation line. This implies that only granules, which have been subjected to fluid-bed drying, have been included.

To assess the model predictive performance, three external validation samples were produced, using the process parameters found in Table 5.3. Granulation parameters were varied in such a way

that the barrel filling ratio and hence the resulting granule density would change as much as possible. Dryer and mill settings were fixed during validation.

Table 5.3 Overview of experiments used for the external validation of the empirical PLS models

Experimental ID	Mass flow rate (kg/h)	L/S ratio	Screw speed (rpm)	Filling time (s)	Drying time (s)	Air flow (m ³ /h)	Inlet air temperature (°C)	Impeller speed (rpm)
A	10	0.08	900	180	660	430	45	800
B	20	0.18	450	180	660	430	45	800
C	20	0.15	900	180	660	430	45	800

With the PBM and PLS models described above, a comprehensive modeling framework as given in Figure 5.1 is developed to predict milled product particle size distribution, bulk density, tapped density and friability.

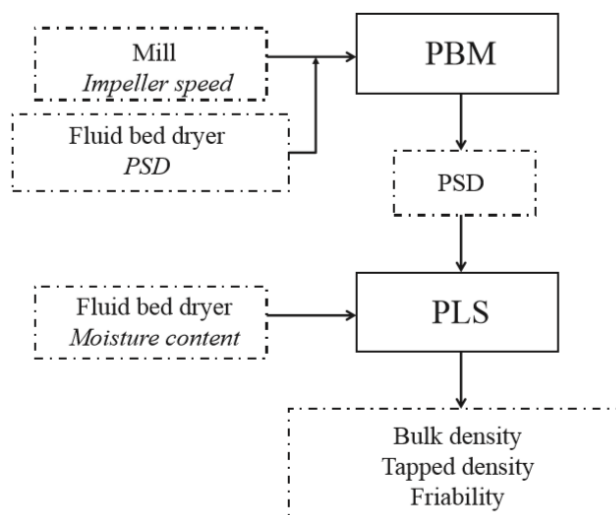


Figure 5.1 Modeling framework to predict milling product CQAs

5.4 Results and discussion

5.4.1 Experimental results

The influence of the degrees of freedom varied in the experiments on the PSD are assessed in this section by visual analysis of the experimentally obtained PSDs. This was done through a detailed

assessment of the change in PSD, which allowed building hypotheses on the influence of the varied degrees of freedom. The discussion is divided based on the drying method applied prior to milling.

5.4.1.1 Oven-dried granules

When other degrees of freedom were kept constant, the difference in milled product PSD by varying impeller speed was small, yet a consistent shift of the PSD to the smaller size range is obtained when augmenting the impeller speed. This trend is consistent over the different input granule properties that were applied. This is visible for the oven-dried granules in Figure 5.2.

A larger extent of breakage was found for the granules with the highest friability value (A in Table 5.1, whereas for the other friability levels the PSDs behaved more similar (Figure 5.2).

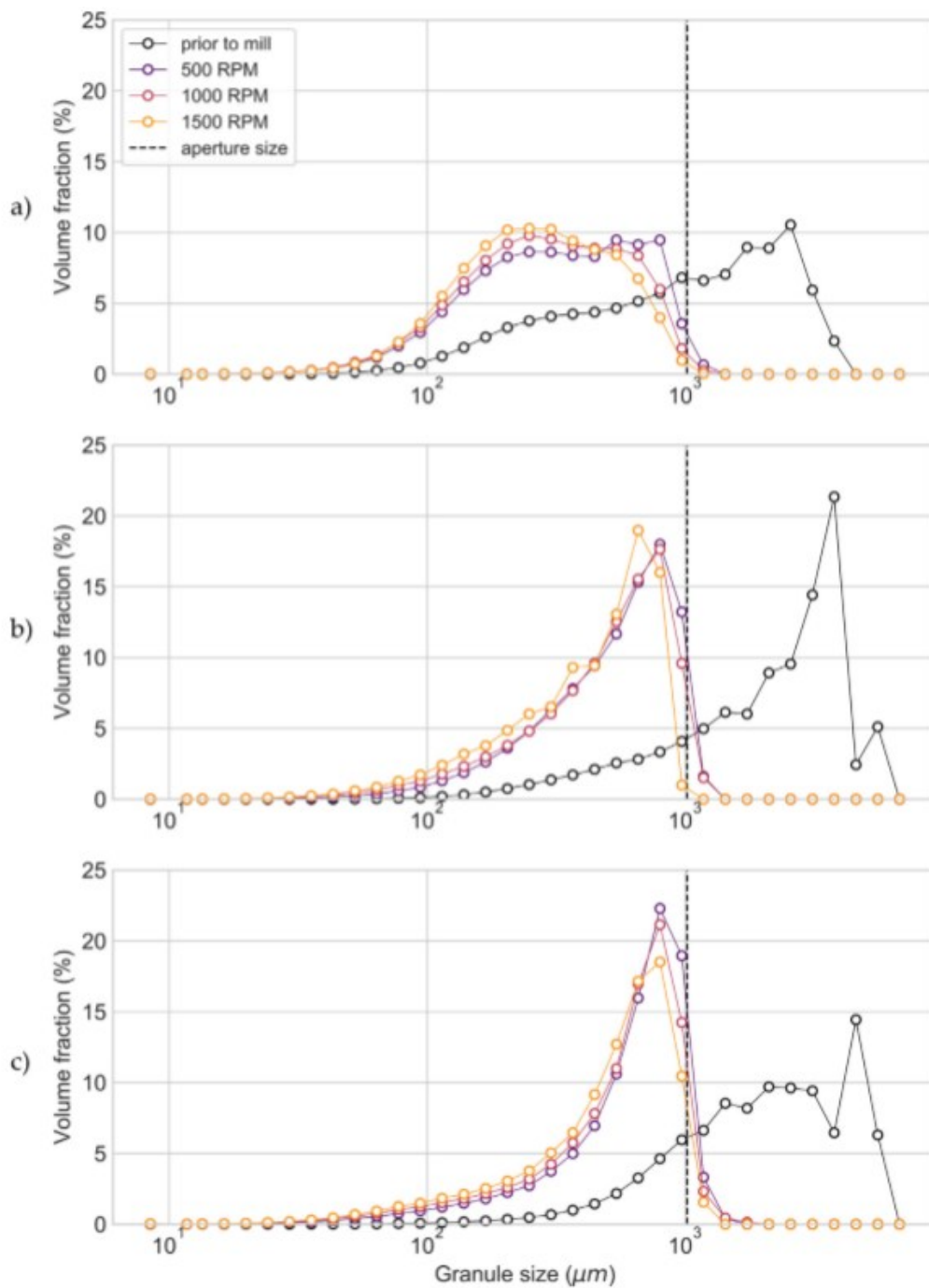


Figure 5.2 Particle size distributions of material prior to and after milling at different impeller speeds for oven-dried granules with, prior to milling, a friability of a) 19.19% b) 9.90% and c) 4.00%

The observations of applying separate sieve fractions of oven-dried granules to the comill are shown in Figure 5.3 and described below.

- Granules that are larger than the screen aperture are almost entirely held up in the mill. It can be observed that a small fraction of the milled granules is larger than 1000 μm . These are thought to be needle shaped, their mill passing depending on their orientation when facing the mill screen.
- Size fractions equal or slightly smaller than the screen aperture underwent ambiguous passing. A certain amount of granules of size 1000 μm is still present in the milled product.
- Size fractions significantly smaller than the screen aperture pass through the mill unmodified. The hypothesis is that the increase in the smaller size range in the milled product results only from breakage of granules with a size approaching the screen aperture size.

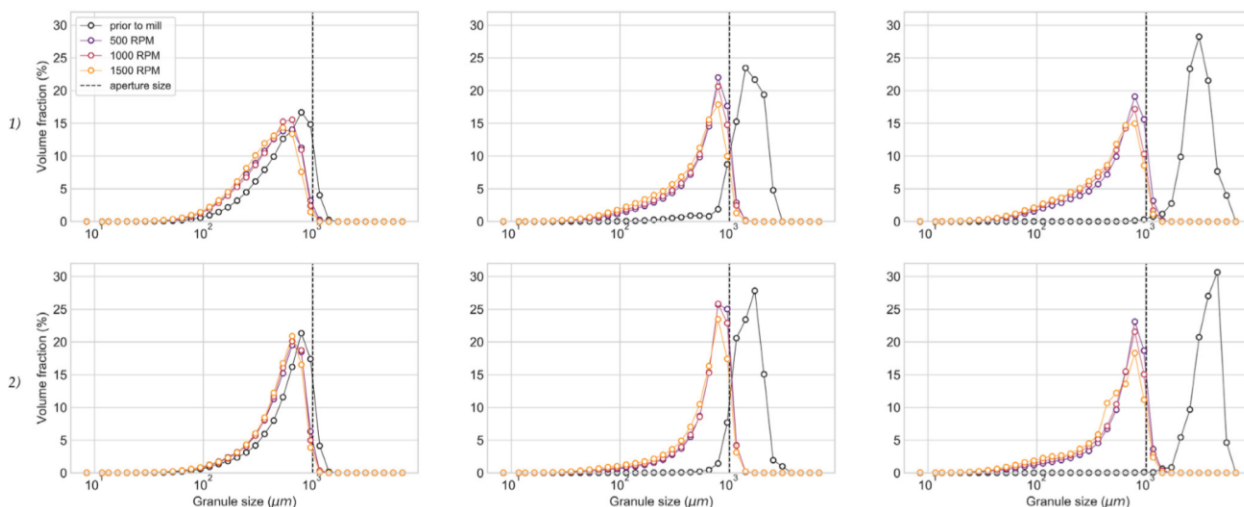


Figure 5.3 Particle size distributions of material prior to and after milling at different impeller speeds, for oven-dried granules with a friability of 9.90% on the first row (1) and 4.00% on the second row (2), classified in size fractions prior to milling of < 1000 μm (a), 1000-2000 μm (b) and >2000 μm (c).

Finally, in the literature it has been found that breakage of larger particles can result in more fines [39, 40]. This could not be verified in the experiments, as the applied size fractions 1000-2000 μm and $> 2000 \mu\text{m}$ result in similar distributions when milled, with only a small shift to the smaller size range noticeable Figure 5.3.

5.4.1.2 Fluid bed dried granules

Residual moisture content is a significant factor regarding the milling process. In the event that the granules contain too high a moisture level, 'smearing' of the screen will occur in the milling unit, and will cause several process issues. This maximally processable moisture content was chosen based on in-house expertise as 6.5 wt%. In the experiments detailed in this work, the residual moisture content was kept sufficiently low and no smearing was observed.

For the granules that were dried using the in-line fluid bed dryer, the drying time was varied according to experiments D-F in Table 5.1. As the drying time decreased, slightly more fines were generated, yet the PSDs were all very close to each other (Figure 5.4). This can be explained by the larger amount of solid bonds that are formed by crystallization of solubilized material during drying [179].

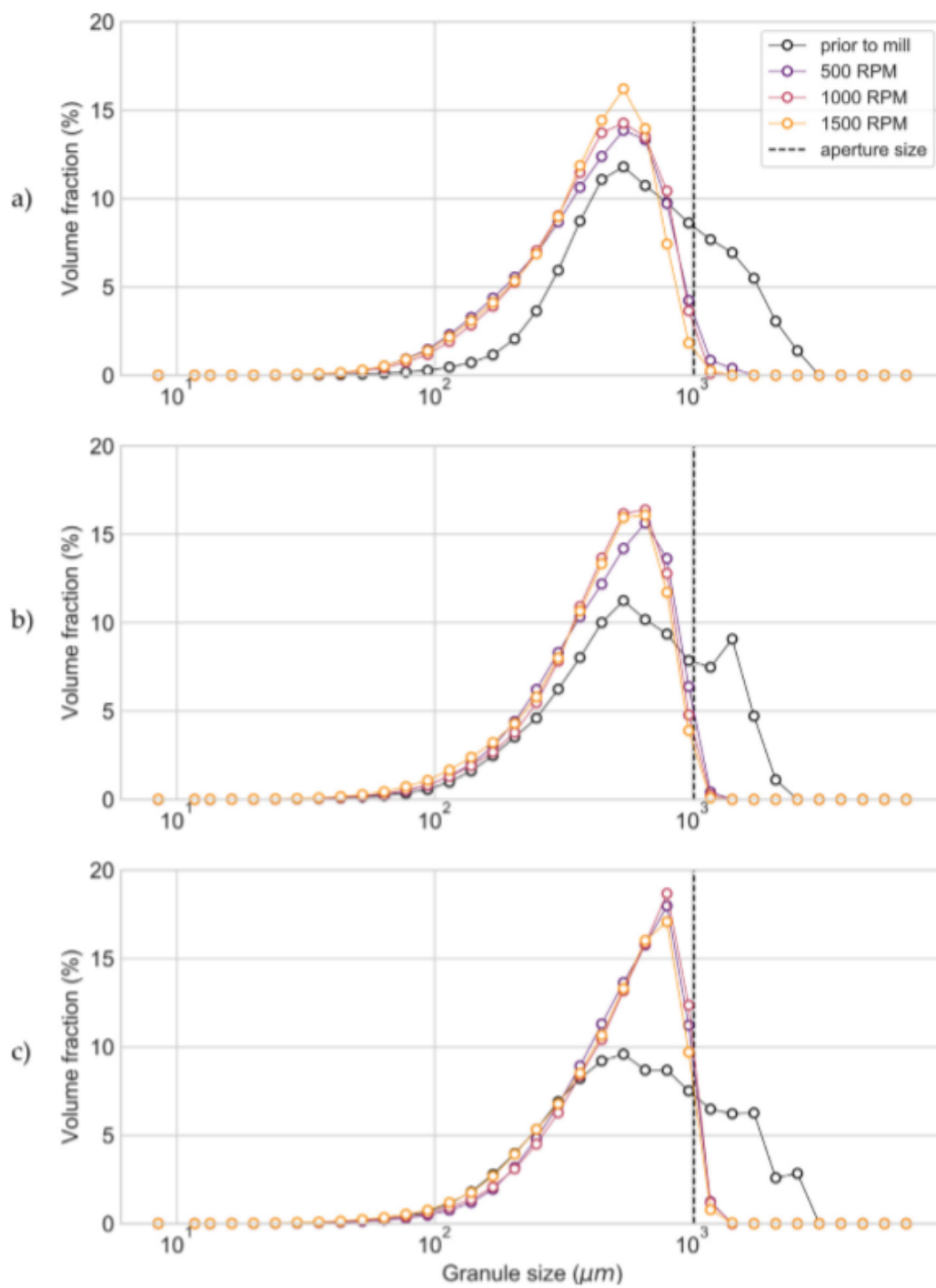


Figure 5.4 Particle size distributions of material prior to and after milling at different impeller speeds, for fluid bed dried granules after a fluid bed drying time of 400 μm (a), 600 μm (b) and 800 μm (c).

5.4.1.3 Air-dried granules

Part of the wet granules was left to dry at room temperature for two different time periods, in order to achieve two different residual moisture contents, 6.43% and 1.41% (respectively G and H in Table 5.1). A similar trend as in the case of fluid-bed-dried granules is noticeable, namely that there are slightly more fines generated when milling granules with a higher moisture content Figure 5.5). This is visible when milling at an impeller speed of 500 rpm, yet at an impeller speed of 1500 rpm the resulting PSDs are overlapping. This could be explained by the larger impact imposed on the granules at higher impeller speeds, which is enough to break an equal amount of bonds in the granules regardless of their difference in strength after drying (see Section 5.4.1.2).

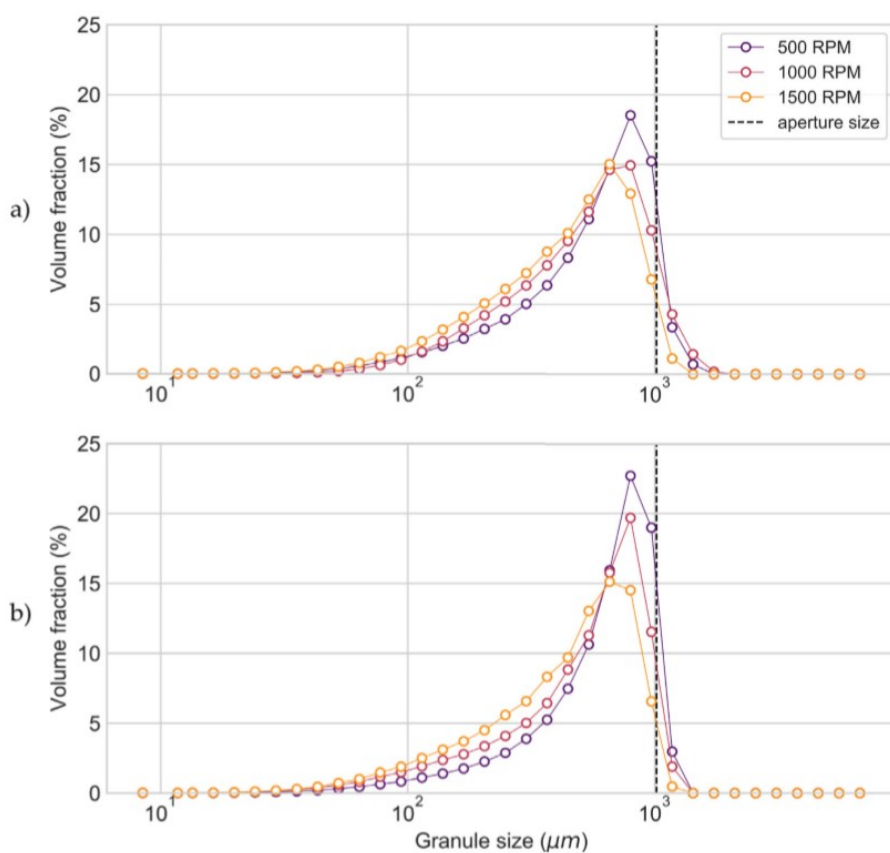


Figure 5.5 Particle size distributions of material after milling at different impeller speeds, for air dried granules with an RMC of 6.43% (a) and 1.41% (b).

Overall, impeller speed has the most influence on the milled product PSD, as the effect is clearly perceivable in the experiments conducted with all applied drying methods. Varying input granule friability and residual moisture content also show consistent changes in milled product PSD. However, in the former only the highest level of friability showed a very different product PSD from the other levels. Therefore this variable could not be quantitatively taken into account in the PBM calibration. In the case of residual moisture content, the differences are also too small to be taken into account for calibration of the PBM formulated in this study. A final observation was that the difference in milled PSDs was the smallest for the fluid bed dried granules, because of the low amount of oversized granules left after breakage through transport to and from the fluid bed dryer in the horizontal ConsiGma™-25 configuration [179].

5.4.2 PBM calibration and validation

The population balance model described in Section 5.3.1 is calibrated to estimate model parameters. The experimental data from milling air dried granules are used to estimate the model parameters. Granules produced from wet granulation process are air dried for two drying times producing two granule feeds with residual moisture contents (RMC) 6.4% and 1.4% (Experiment IDs G and H from Table 5.1). 1 kg of granule feeds are milled at three impeller speeds 500, 1000 and 1500 rpm. The PSD of the total milled product collected is used to calibrate the model and estimate parameters. The purpose of this exercise is to check if

- the model can successfully predict milled product particle size distribution
- the effect of impeller speed is reflected in the model predicted milled product particle size distribution

For this set of experiments, the dynamics of the process are not captured, i.e. the time taken for a fixed granule feed of 1 kg to mill, hereafter referred to as milling time, is not of interest. Since the

goal is to predict milled product PSD only, the breakage kernel parameter β is not estimated. An arbitrary high constant value of $\beta = 2 \text{ s}^{-1}$ is considered to simulate fast exit of granules from the mill.

The model parameters p, q, γ, ϵ and α are estimated using the objective function as given in Equation 5.10 and explained in Section 5.3.1.1. The list of model parameters estimated is tabulated in Table 5.4. Value of parameters p and q indicate an erosion or chipping mechanism being the dominant breakage process. Comparisons of predicted and experimental particle size distributions for milled granules from RMC 1.4% (Experiment ID H) processed at 500, 1000 and 1500 rpm are shown in Figure 5.6. Similar comparison for milled granules obtained from RMC 6.4% feed (Experiment ID G) are shown in Figure 5.7. In addition to particle size distributions, comparisons between experimental and simulated d10, d50 and d90 are shown in Figure 5.8. To quantify the success of prediction of the distribution percentiles d10, d50 and d90, R^2 value for fit between simulated and measured values are calculated to be 0.9976 and 0.9901 for RMC 1.4% and 6.4% feeds respectively.

Table 5.4 List of estimated parameter values in PBM using experimental data from RMC 1.4% and 6.4% granule feed, Experiment IDs G and H

	Parameter	1.4%	6.4%
Breakage distribution function	p	1.7904	2.4101
	q	0.3128	0.3151
Feed distribution coefficient	γ	1.7925	1.6111
Critical screen size parameters	ϵ	0.9834	0.9693
	α	0.0315	0.0001
SSE		0.00249	0.00309

The comparisons discussed reflect that the model formulated and described in Section 5.3.1 can successfully predict milled product particle size distributions, the distribution percentiles as well as capture the effect of impeller speed. In order to predict milling dynamics, another set of milling experiments are conducted at various impeller speeds, 300, 500, 700, 900, 1300 and 1500 rpm (Experiment ID I from Table 5.1). For this set of experiments, the milled product PSD as well as milling times were measured. Since the experiments were conducted at a range of impeller speeds, validation of the model is also done. In addition, the model parameter β is estimated as well. The statistical significance of all the estimated parameters is reported as explained in Section 5.3.1.1 and discussed. The parameter ϵ is considered as 1. From Equation 5.9 it is evident that the critical screen size ratio δ becomes equal to ϵ at the minimum impeller speed $v_{imp,min}$. At 300 rpm, the critical screen size is assumed to be equal to the screen size used i.e., $\epsilon = 1$. An independent calibration using data from 300 rpm only yields $\epsilon = 1$ as well. This is also a pragmatic approach to reduce the number of parameters to be estimated.

The objective function used to estimate the model parameters have the milling times also included in order to effectively estimate the kernel parameter. `fmincon` function in MATLAB® 2017a was used to perform the calibration using 300, 500, 700, 1300, 1500 rpm. 900 rpm is used as an independent check for validation purpose (Experiment ID I from Table 5.1). The list of parameters obtained from the calibration exercise is tabulated in Table 5.5. For brevity, comparison of measured and predicted distribution percentiles d10, d50 and d90 is shown in Figure 5.9. R^2 value of this fit is calculated as 0.9787. A comparison of measured and predicted milling times is also plotted in Figure 5.10. The R^2 value calculated for this fit is 0.7633. It is evident that the simulated values agree well with measured values at impeller speeds used for calibration as well as validation. For the model parameters estimated, t-values and their corresponding confidence intervals are listed in Table 5.5. All the model parameters p, q, γ, α except β show statistical significance. The parameter β effects the dynamics of the milling process. It is important to note that the model

structure is assumed as a batch process due to limitations in collecting data on the interaction between feed hopper and the comill. More information on the nature of feed variation with time might improve the model structure containing parameters that can all be estimated with statistical significance. With the assumptions considered, the current model structure is successful in predicting product PSD as well as milling times.

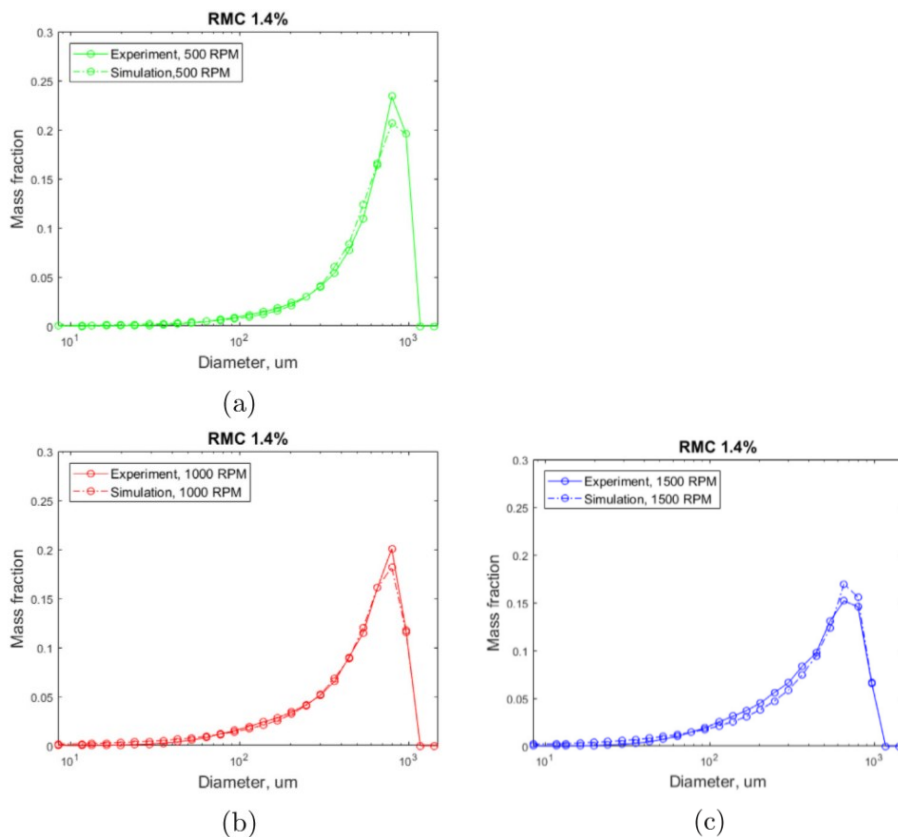


Figure 5.6 Comparison of predicted and experimental milled product PSD at (a) 500 rpm, (b) 1000 rpm and (c) 1500 rpm, granule feed RMC 1.4%

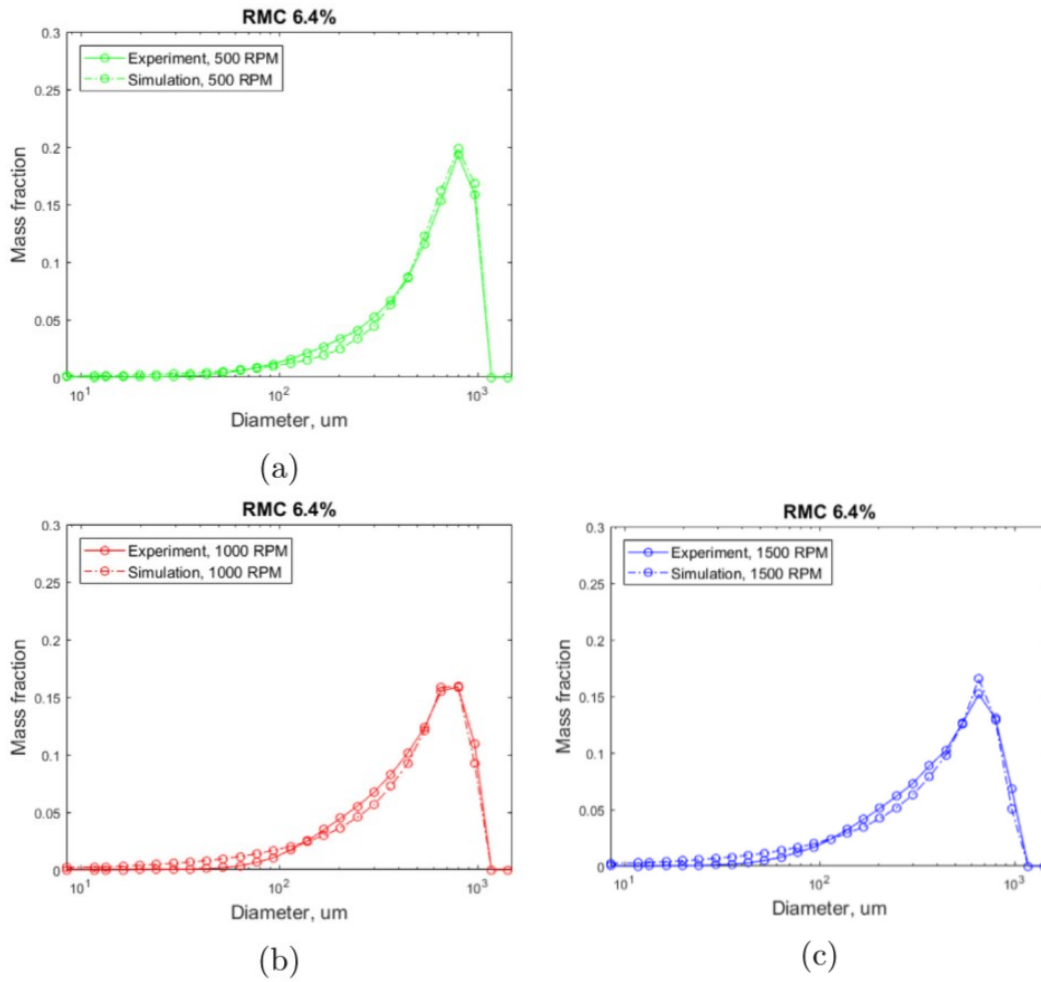
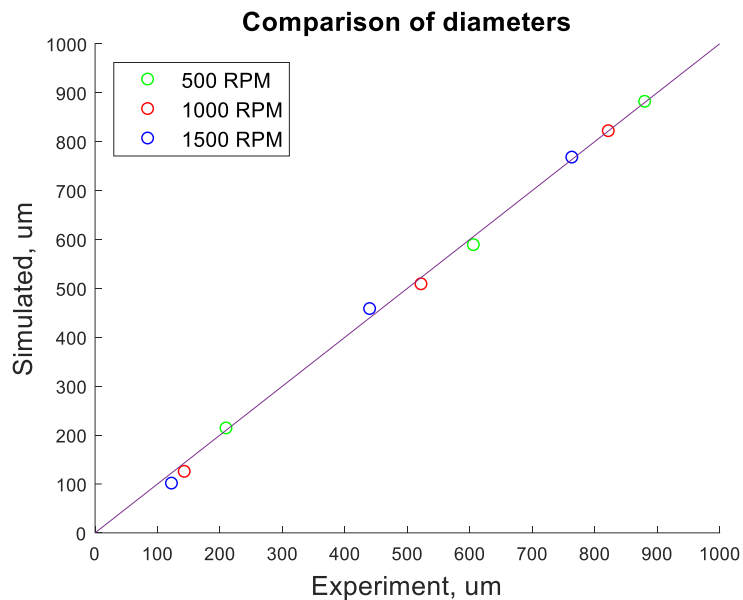
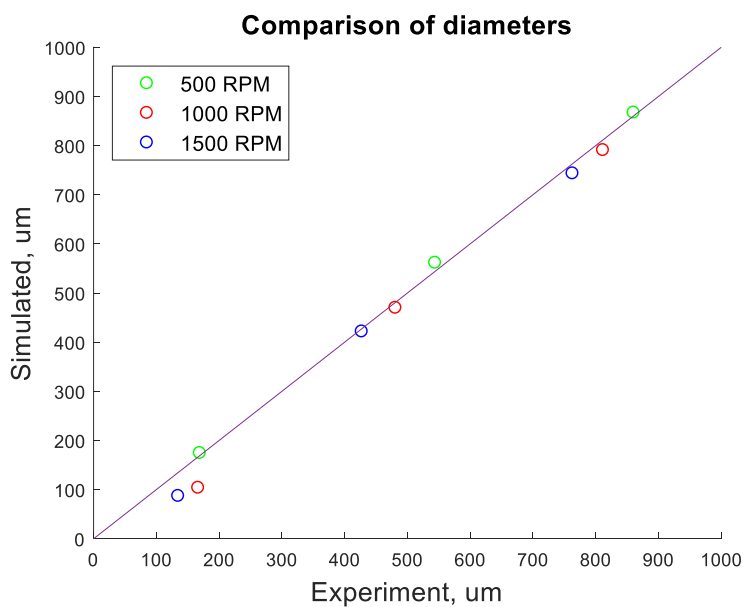


Figure 5.7 Comparison of predicted and experimental milled product PSD at (a) 500 rpm, (b) 1000 rpm and (c) 1500 rpm, granule feed RMC 6.4%



(a)



(b)

Figure 5.8 Comparison of predicted and measured D10, D50 and D90 of milled product at various impeller speeds (a) Feed RMC 1.4% (b) Feed RMC 6.4%

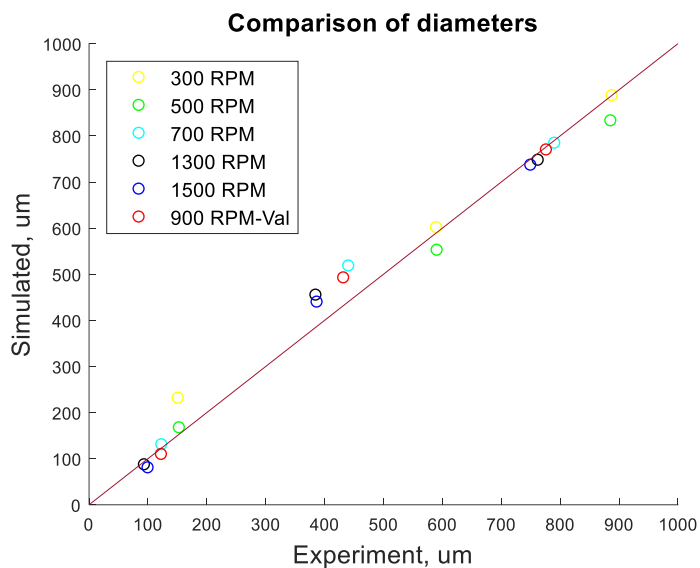


Figure 5.9 Comparison of predicted and measured D10, D50 and D90 of milled product at various impeller speeds. Red color refers to validation impeller speed of 900 rpm

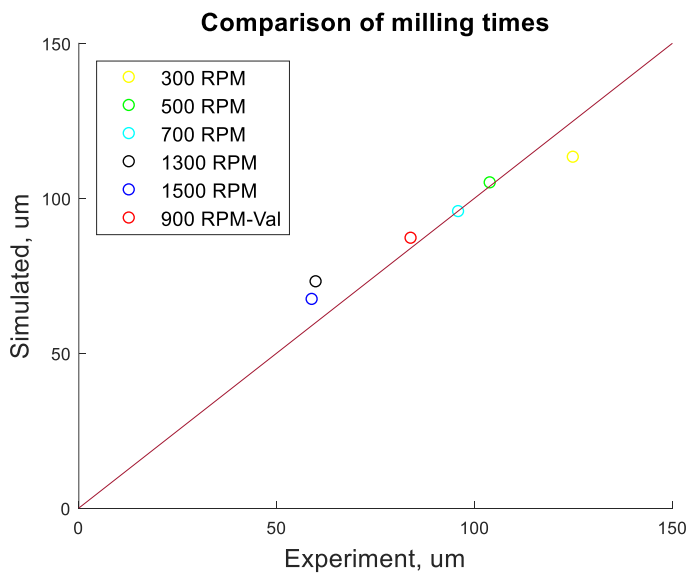


Figure 5.10 Comparison of predicted and measured milling times at various impeller speeds. Red color refers to validation impeller speed of 900 rpm

Table 5.5 Statistical significance of parameters estimated in the PBM, using data from Experiment ID I

Parameter	Value	t-value	95% CI
p	1.0262	46.09	(0.978, 1.073)
q	0.2404	5.80	(0.152, 0.328)
γ	0.0171	2.57	(0.0029,0.031)
ϵ	1	–	–
α	0.2324	4.79	(0.130,0.338)
β	0.1331	0.70	(-0.267 0.533)

The combination of PBM and PLS models can be used to predict the required CQAs. The bulk properties are important in modeling the tablet press unit operation as the densities are required to simulate pre-compression and main compression forces in the tablet press, as well as tablet hardness [84]. The proposed modeling framework thus enables the development of continuous process modeling by connecting the dryer, mill and tablet press operations. The modeling framework developed is generic. However, it is important to note that the model parameters need to be estimated and re-evaluated when changing the drug formulation or the design variables.

5.5 Summary

The comilling process is investigated thoroughly to understand the effect of the feed granule strength, feed granule size, moisture content on the milled product. Granules with low strength yielded bimodality in the milled product whereas stronger granules yielded unimodal milled product distribution. Effect of feed granule size is studied through separately milling portions of the feed. Smaller sized granules passed through the screen unmodified whereas granules larger than screen size are almost entirely held up. In addition, the effect of method of granule drying is studied.

To fully simulate the effect of mill operating parameters, experiments from air dried granules are used to calibrate and validate the mill model. A population balance modeling (PBM) approach is

employed to predict the mill dynamics and the milled product particle size distribution. The PBM is formulated using six parameters. Five out of six parameters are estimated with statistical significance and metrics for the same are presented. The model successfully predicts milled product particle size distribution as well as the milling time. Partial least squares (PLS) modeling approach is applied to predict other CQAs such as bulk density, tapped density and friability. The PLS model takes moisture content of the feed and particle size distribution of the milled product as the input and successfully predicts the product bulk density, tapped density and friability. There is a need to predict these CQAs as the bulk properties effect flowability, segregation and tableability of granules in the downstream tablet press compaction process. Thus, a comprehensive modeling approach using PBM and PLS models that predicts all the required CQAs aids in building flowsheet models.

In future, the model parameters can be estimated for various granulation and drying conditions and the dependence of the model parameters on these variables can be studied. In addition to granule and drying conditions, the effect of powder properties can be investigated. This has the potential to develop a generic and advanced modeling framework that predicts milled granules properties based on the formulation, granulation and drying conditions. Another avenue to explore is the use of mechanistic models that incorporate material properties in the modeling framework. Overall, the QbD approach in continuous manufacturing is advancing through the use of a model based approach in place of a trial and error based approach for predicting and thus providing a path to control the quality of the end product.

Chapter 6

Integrated model development and analysis of wet granulation continuous pharmaceutical tablet manufacturing process

6.1 Background

Flowsheet models are approximate mathematical representations of the manufacturing line. The incentives for flowsheet model development for the pharmaceutical industry have been described in the paper of Escotet-Espinoza, Singh [16]. Gernaey, Cervera-Padrell [189] also wrote extensively on the value of Process Systems Engineering for pharmaceutical process development, in which flowsheet models contribute to combine knowledge and models of different unit operations and different scales for a holistic understanding of the process. These boil down to the in-silico achievement of process design and optimization, control system design and optimization, and an accurate risk assessment tool that could be used for regulatory instances. The first step in attaining these benefits is by the development of a flowsheet model that captures the relevant mechanisms for assessing the desired product properties as a function of process settings and material properties. This foundation built in this work, comprised of several diverse unit operation models that capture critical mechanisms, as a function of the process inputs.

The flowsheet model simulation enables the assessment of unit operation outputs downstream in the process. This has the advantage that, instead of application of the unit operation models separately for model-based research, the flowsheet model allows for targeted optimization of unit operation performance as a part of the entire line. In terms of the QbD paradigm, a flowsheet model allows for investigating the influence of CPP in one unit to the CQA of material downstream in the process line. Namely, through the flowsheet model development, process phenomena are directly

linked to the final product quality downstream. Moreover, analysis of the developed model allows assessment of criticality of the various CPP of the process, and subsequently research effort can be targeted towards those most critical areas.

In this work, composing the integrated system requires extensive synchronization of the unit operation models themselves, as these need to run seamlessly in one simulation, regardless of the different time scales, variable magnitudes, or stiffness of the various models. Population balance models for example, require specific solution methods, and these need to run at par with other less computationally demanding models. This work therefore captures the research into the simultaneous simulation of these diverse models. In addition, process dynamics are included into the flowsheet model. This allows tracing the material properties throughout the entire line. This feature is included as the foundation of applying the model to assess the propagation of process disturbances, with respect to the product quality, i.e. which products needs to be discarded, or how fast can the process recover and return to a position where product CQA properties are within specification limits.

Previous work on the development of flowsheet models are restricted to direct compaction [12-14, 89] and dry granulation routes [15, 81] for continuous solid oral dosage manufacturing. Park, Galbraith [15] created a flowsheet model of continuous dry granulation and applied it for optimization. Boukouvala, Niotis [81] developed a flowsheet model for the wet granulation route. This model served as a proof-of-concept and with no connection to specific experimental data. Boukouvala, Chaudhury [90] also investigated a methodology for optimization of computationally expensive flowsheet models. Rogers and Ierapetritou [110] showed a flowsheet modeling case with hybrid models incorporating information from both detailed and reduced-order models.

The work presented in this manuscript includes models systematically developed based on experiments on units in the ConsiGma™ -25 line for continuous tablet manufacturing using the

same formulation and relevant materials across all the units. Specifically, the units involved are feeders, blender, twin screw granulator, fluidized bed dryer, comill and tablet press. Models for these processes are developed [164, 190-193] and included. Besides these, models for intermediate feeding and blending operations are also included. Transfer lines that lead to material holdup in between the units are added to the flowsheet model as well.

The specific objectives of this work are:

- Develop a flowsheet model approximating the ConsiGma™-25 wet granulation manufacturing line
- Demonstrate the use of the flowsheet model for simulating effects of disturbances in the continuous process
- Identify CPPs affecting the properties of intermediate and final product

Section 6.2.1 details various models used to build the flowsheet model. To enunciate how the flowsheet model can be used for propagation of information and disturbances across the units, a detailed discussion is provided in Section 6.3 along with supporting case studies in Section 6.4. In addition to building the flowsheet model, a detailed analysis of the developed model is provided. The scenario analysis, explained in Section 6.2.2 and 6.5, serves to ensure that the flowsheet model which is a complex set of equations from various modeling approaches, runs successfully at several values of process variables and the process responses thus obtained are aligned with process knowledge. Following this, CPP that affect product quality are identified through implementation of sensitivity analysis as explained in Sections 6.2.3 and 6.6.

6.2 Model development and analysis

The model formulation consisted of two API, a lubricant and four excipients. Hereafter, the two APIs and the four excipients are referred to as API 1, API 2 and Excipient A, B, C and D

respectively. The formulation was processed using demineralized water as granulation liquid. The formulation used in this work is given in Table 6.1.

Table 6.1 Formulation used for model development

Component Name	Weight %
API 1	75.58
API 2	8.72
Lubricant	0.58
Excipient A	6.05
Excipient B	1.51
Excipient C	6.05
Excipient D	1.51

6.2.1 Flowsheet Modeling

Since flowsheet models are approximate representations of the integrated manufacturing line, developing individual unit operation models aid in the development of a flowsheet model. In this work, the models developed are based on experiments conducted using the ConsiGmaTM-25 system (GEA Pharma systems, Collette, Wommelgem, Belgium), which is an oral solid dosage manufacturing line based on continuous wet granulation. In Section 6.2.1.1 to 6.2.1.8, the individual unit models used in this work are briefly described. Figure 6.1 pictorially shows transfer of information across the unit operations i.e., feeder, blender, granulator, dryer, mill and tablet press, in that order. Further, intermediate units are added and relevant information is transferred. These models are implemented in the software gPROMS FormulatedProducts v1.2.1 (PSE, London). It is a platform for flowsheet simulations that uses an equation-oriented approach. An overview on the equation-oriented techniques particular to the gPROMS platform is given in Pantelides, Nauta [194]

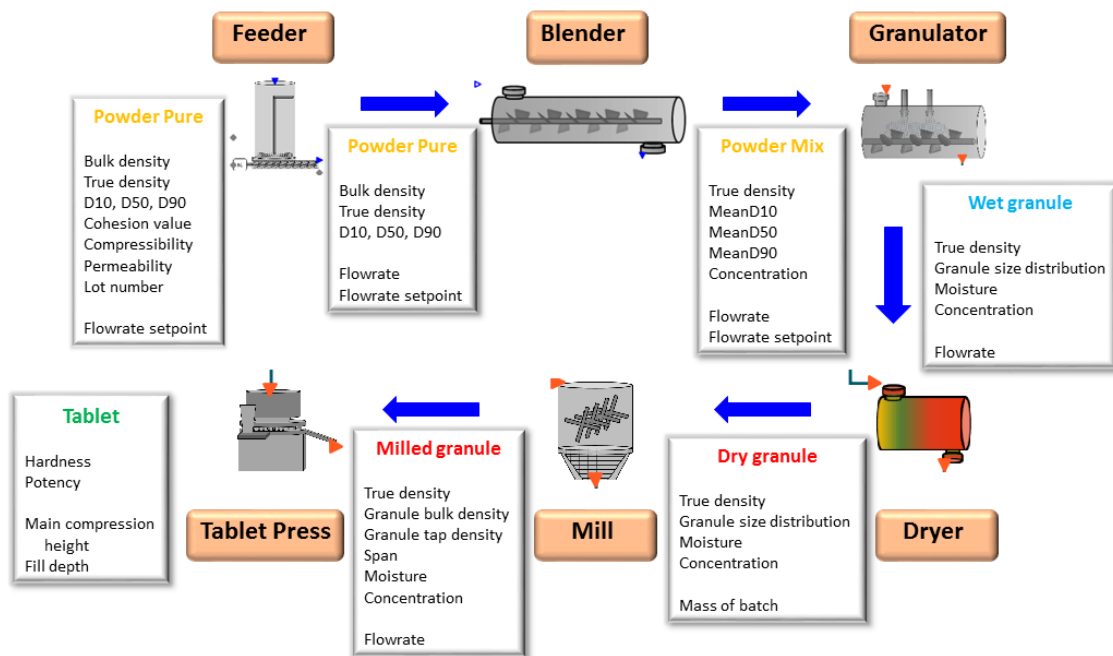


Figure 6.1 Schematic showing transfer of information between units required for flowsheet model development

6.2.1.1 Feeder

Loss-in-weight (LIW) feeders are used to feed the required powder components in the continuous manufacturing line. The feeder used in this work has a hopper and a conveying unit, a refill unit, and a PID controller. The hopper is used as a receptacle for the raw materials whereas the conveying system has a rotating screw that is used to move the material out of the feeder. The refill unit is used to feed material into the hopper when the fractional fill level in the hopper drops below a setpoint value. The PID controller enables the feeder to run in gravimetric mode i.e., the screw speed in the conveying unit is adjusted to maintain a constant mass flow rate out of the unit. The three models (refill, feeding and PID controller) work in conjunction to represent the overall feeding operation in the continuous line.

The mass flow rate out of the feeder is simulated using a feed factor model [12]. Feed factor is a time-dependent property ($ff(t)$), defined as maximum mass of powder fitting in a screw flight and has the unit of mass per screw revolution. It is found to be dependent on the amount of material in the hopper ($w(t)$) as given in Equation 6.1. The parameters ff_{max} , ff_{min} and β are dependent on the powder bulk density, compressibility, cohesion and permeability. More details on the feed factor model and its dependence on material properties are published in Escotet Espinoza [195]. The mass flow rate of the powder out of the feeder can then be obtained as given in Equation 6.2 where $\omega(t)$ is the screw speed that is manipulated by the PID controller.

$$ff(t) = ff_{max} + (ff_{min} - ff_{max})exp(-\beta w(t)) \quad 6.1$$

$$\dot{M}_{out}(t) = ff(t)\omega(t) \quad 6.2$$

6.2.1.2 Blender

Continuous blenders that are used to mix the powder components in the continuous line, dampen the flow rate variations from the feeding units. The build-up of mass in the blender $M(t)$ was found to be following a first order relationship as given in Equation 6.3, where M_{SS} is the steady state mass holdup and τ is the time constant. From the mass holdup and flow rate of the material into the blender \dot{M}_{in} , flow rate out of the unit \dot{M}_{out} , can be computed as given in Equation 6.4. An axial dispersion equation [12] is used to model the mixing calculation in the blending unit as a function of time. The equation as given in Equation 6.5 is subject to initial and boundary conditions (Equation 6.6). The coefficients of the axial dispersion model (τ_{ax} and Pe) are calculated based on their relationship to a CSTR-in-series model constant i.e., number of tanks n_t as given in Equation 6.7. Experimental data were used to develop regression models that predict the model constants

τ , n_t and M_{SS} as a function of flow rate and blade speed. More details on the blender model are available in Escotet Espinoza [195].

$$\tau \frac{dM(t)}{dt} + M(t) = M_{SS} \quad 6.3$$

$$\frac{dM(t)}{dt} = \dot{M}_{in} - \dot{M}_{out} \quad 6.4$$

$$\tau_{ax} \frac{dC_{out}^i}{dt} = \frac{1}{Pe} \frac{\partial^2 C_{out}^i}{\partial \xi^2} - \frac{\partial C_{out}^i}{\partial \xi} \quad 6.5$$

$$I.C : C_{out}^i = 0, t = 0$$

$$B.C : C_{out}^i = C_{in}^i, \xi = 0 \quad 6.6$$

$$\frac{dC_{out}^i}{dt} = 0, \xi = 1$$

$$Pe = n_t + (8n_t + n_t^2)^{1/2} \quad 6.7$$

6.2.1.3 Twin-Screw Wet Granulator

The modeling of the change in particle size distribution of the material through granulation is executed with the compartmental population balance model of [191]. The twin-screw granulator model mathematically links the aggregation and breakage behavior in the granulator barrel to the granulator process settings of mass flow rate, screw speed and liquid flow rate. It moreover distinguishes two compartments in the barrel: the wetting zone (i.e. the zone where the liquid is added to the dry powder blend) where only aggregation occurs, followed by the kneading zone (i.e.

kneading elements are present in the screws) with different aggregation behavior complimented with breakage. Each compartment is thus modeled by its own population balance model.

The PBM equation is given in Equation 6.8. The change in number of particles n of a certain size x over time t is thereby described based on aggregation kernel $\beta(t, x, \epsilon)$, breakage selection function $S(\epsilon)$ and breakage fragment distribution $b(x, \epsilon)$. The aggregation kernel $\beta(t, x, \epsilon)$ can be modeled as the product of aggregation efficiency β_0 with collision frequency $\beta(x, \epsilon)$, as the relation is in this case independent of time t .

The formula of the collision frequency in the first PBM, describing the wetting zone, is given in Equation 6.9. It comprises a two-dimensional stepping function and a product kernel in order to reach bimodal granule particle size distributions starting from a monomodal powder particle size distribution. Kernel parameters $\beta_0, R_1, R_2, top_1, top_2, \delta_1$ and δ_2 are needed to achieve this mathematical connection [191].

$$\begin{aligned} \frac{\delta n(t, x)}{\delta t} = & \frac{1}{2} \int_0^x \beta(t, x - \epsilon, \epsilon) n(t, x - \epsilon) n(t, \epsilon) d\epsilon \\ & - n(t, x) \int_0^\infty \beta(t, x, \epsilon) n(t, \epsilon) d\epsilon \\ & + \int_x^\infty b(t, x, \epsilon) S(t, \epsilon) n(t, \epsilon) d\epsilon - S(t, x) n(t, x) \end{aligned} \quad 6.8$$

$$\begin{aligned} \beta(x, \epsilon) = & \left(\frac{top_1}{2} \left(1 + \tanh \left(\frac{R_1^3 - (x^2 + \epsilon^2)^{1/2}}{\delta_1} \right) \right) \right) \\ & - \frac{top_1 - top_2}{2} \left(1 + \tanh \left(\frac{R_2^3 - (x^2 + \epsilon^2)^{1/2}}{\delta_2} \right) \right) \\ & \cdot \left(x^{1/3} \cdot \epsilon^{1/3} \right) \end{aligned} \quad 6.9$$

The breakage in the kneading zone is modeled by a linear breakage selection function:

$$S(\varepsilon) = S_0 \varepsilon^{1/3} \quad 6.10$$

and a breakage fragment distribution $b(x, \varepsilon)$ describing a combination of erosion and uniform breakage:

$$b(x, \varepsilon) = f_{prim} \frac{1}{\sqrt{2\pi}\sigma} e^{-\frac{(x^{1/3}-\mu)^2}{2\sigma^2}} \frac{\varepsilon}{\mu^3} \frac{1}{3x^{2/3}} + (1 - f_{prim}) \frac{2}{\varepsilon}, \quad 6.11$$

with ε the volume of the breaking particle, x the volume of the fragment, S_0 the breakage rate constant, σ and μ respectively the standard deviation and mean of the Gaussian distribution representing the size distribution of the small eroded particles and f_{prim} the volume fraction of erosion in the overall breakage (as opposed to a fraction $(1 - f_{prim})$ of uniform breakage).

Aggregation in this zone could be described by a sum kernel (Equation 6.12).

$$\beta(x, \varepsilon) = x + \varepsilon \quad 6.12$$

Overall, kernel parameters R_2, β_0 and top_1 in the wetting zone and $\beta_0, S_0, f_{prim}, \mu$ and σ in the kneading zone are linearly related to the process setting values in the units given in Table 6.2.

Table 6.2 Process setting ranges of validated twin-screw granulator model [191]

Process Setting	Lower Bound	Upper Bound
Mass flow rate (kg/h)	10	20
Screw speed (RPM)	500	900
Liquid/solid-ratio (kg/kg)	0.08	0.18

6.2.1.4 Dryer

The fluidized bed dryer (FBD) model consists of prediction of granule batch drying kinetics based on single granule drying kinetics for one dryer cell [193]. The single granule drying kinetics are governed by Stefan diffusion of water vapor through the granule pores, from the source of evaporation to the edge of the granule. The mass transfer rates are corrected with the equilibrium moisture content X_e . When the moisture content of the granule is larger than its pore fraction, the remaining liquid is modeled as a layer of water of uniform thickness around the granule, evaporating according to a droplet:

$$\dot{m}_v = h_D(\rho_{v,s} - \rho_{v,\infty})A_d \quad 6.13$$

with mass transfer rate \dot{m}_v (kg/s), mass transfer coefficient h_D (m/s), partial vapor density over the droplet surface $\rho_{v,s}$ (kg/m³), partial vapor density in the ambient air $\rho_{v,\infty}$ (kg/m³) and droplet surface area A_d (m²). The energy balance paired with this drying behavior is described by:

$$h_{fg}\dot{m}_v + c_{p,w}m_d\frac{dT_d}{dt} = h(T_g - T_d)4\pi R_d^2 \quad 6.14$$

with specific heat of evaporation h_{fg} specific heat capacity of the liquid $c_{p,w}$ droplet mass m_d , uniform droplet temperature T_d , heat transfer coefficient h , drying gas temperature T_g and droplet radius R_d . After this layer of water is depleted the wet granule enters the subsequent drying phase. Herein the moisture is conceptualized as a sphere with radius R_i , also referred to as the wet core, filling up the pore volume of the granule with radius R_p . The mass transfer rate \dot{m}_v in this stage is given by:

$$\dot{m}_v = -\frac{8\pi\epsilon^\beta D_{v,cr} M_w p_g}{\Re(T_{cr,s} + T_{wc,s})} \frac{R_p R_i}{R_p - R_i} \ln\left[\frac{p_g - p_{v,i}}{p_g - \left(\frac{\Re}{4\pi M_w h_D R_p^2} \dot{m}_v + \frac{p_{v,\infty}}{T_g}\right) T_{p,s}}\right] \quad 6.15$$

with ϵ the granule porosity (-), β an empirical coefficient, $D_{v,cr}$ the vapor diffusion coefficient, M_w the liquid molecular weight, p_g the pressure of the drying air, R the ideal gas constant, $T_{cr,s}$ and $T_{wc,s}$ respectively the temperature of solids at the granule surface and at the gas-liquid interface, $p_{v,\infty}$ and $p_{v,i}$ respectively the partial vapor pressure in the drying air and at the gas-liquid interface and $T_{p,s}$ the temperature of the particle solids. Equation 6.14 is assumed to apply for the energy balance of the granule during this drying phase. The physical properties of the solids were assumed to be at environment conditions of 25 deg C and atmospheric air pressure in the model, whereas liquid properties were modeled as those of pure water. A value of 35% was assumed for the granule porosity. Finally, the mass transfer rates \dot{m}_v are corrected with the effect of X_e :

$$\dot{m}_{v,res} = \frac{X - X_e}{X} \dot{m}_v \quad 6.16$$

Overall this means that the course of moisture content X of a granule amounts to:

$$\dot{X}_{SPDM} = \frac{\dot{m}_{v,res}}{m_p} \quad 6.17$$

with \dot{X}_{SPDM} the change in moisture content X over time and m_p the total mass of the granule (particle). This is solved from time $t = 0$ until the dryer cell drying time $t = t_{dry}$.

Connecting the single granule drying kinetics to those of the batch, along with the continuous filling of the batch, is done according to the following simplified approach. Drying curves are calculated for several size fractions of the granules, in which the arithmetic mean size is representative in the X_{SPDM} . Thus the average moisture content \bar{X}_f per size fraction f then equals the average moisture content of different drying curves, starting a certain time τ later over the cell filling time t_{fill} :

$$\bar{X}_f = \frac{\sum_{\tau=0}^{t_{fill}} X_{SPDM}(t - \tau)}{n_\tau} \quad 6.18$$

with n_τ the amount times τ that the drying curve was shifted over the cell filling time interval t_{fill} . A constant ideal fluidization behavior, constant relative air humidity in the dryer cell and atmospheric air properties in the drying chamber (with exception of the drying agent temperature) were assumed in the batch approach.

The dryer model discussion so far dealt with the drying behavior of the material, other material properties are directly governed by the dynamic output of the granulator model. For each dryer cell, these are mass-averaged over the drying cell filling period. This is illustrated in Equation 6.19 for the concentration of API in the dryer cell $C_{API,dryer}$, and is calculated the same way for the material true density, PSD} and the mass of the material in the dryer cell. They are weighted by the mass flow rate at which they are flowing from the granulator at time t ($MFR_{TSWG(t)}$).

$$C_{API,dryer} = \frac{\int_t^{t+t_{fill}} C_{API,TSWG}(u) MFR_{TSWG}(u) du}{\int_t^{t+t_{fill}} MFR_{TSWG}(u) du} \quad 6.19$$

After drying, the breakage of the material through pneumatic transport through a tube to the evaluation module is calculated by a PBM. As aggregation is assumed not to take place based on

the experimental work of De Leersnyder, Vanhoorne [192], only the last two terms in the right hand side of Equation 6.8 need to be used. The same breakage kernel as in the kneading zone of the granulator was found to apply, i.e. breakage rate $S(\varepsilon)$ from Equation 6.10 and breakage fragment distribution $b(x, \varepsilon)$ from Equation 6.11. Parameter S_0 from Equation 6.10 is linearly related to the remaining moisture content after drying.

Finally, the six cells are simulated in parallel with the filling-drying-emptying sequences according to the operation in the actual process. A cell is idle until the predecessor cell has been filled, at which point the current cell enters the filling stage. Hereafter, the remainder of the drying time is completed in the drying stage, where the mass flow rate at time t ($MFR_{TSWG(t)}$) in that cell is zero. In the final emptying stage, the mass transfer rates in Equations 6.13 and 6.15 are set to zero, and the change in PSD is calculated by the PBM based on the residual moisture content of the material. These material property values are thus those perceived at the inlet of the evaluation module.

6.2.1.5 Mill

In the wet granulation continuous manufacturing route, comilling is used to break the granulated product through collisions from a rotating impeller and walls. Granules that are broken to the required size exit the comill through a screen. In this work, the comill model published in Metta, Verstraeten [164] is used. Briefly, the mill model is a hybrid model that includes a PBM approach and a PLS approach. Trajectories of change in mass of particles of various sizes over time is predicted through the PBM as shown in Equation 6.20 where $M(w, t)$ represents the mass of particles of volume w at time t , R_{form} and R_{dep} represent the rates of formation and depletion of particles respectively. \dot{M}_{in} and \dot{M}_{out} are the mass flow rates of particles entering and exiting the mill respectively. The rate of depletion R_{dep} is defined in the model (Equation 6.21) using a breakage kernel $K(w)$, which represents the probability that a particle of volume w undergoes breakage.

A classification kernel as given in Equation 6.22 is used in this work, where v_{imp} is the impeller speed, $v_{imp,min}$ is the minimum impeller speed and the parameter β is calibrated using data from experiments. The rate of formation R_{form} as shown in Equation 6.23 uses the breakage kernel and a breakage distribution function. The breakage distribution function $b(w, u)$ represents the distribution of daughter particles formed when a particle of volume w undergoes breakage.

The Hill-Ng distribution function given in Equation 6.24 is used in this work, where the parameters p, q are estimated using experimental data. The mass flow rate out of the mill $\dot{M}_{out}(w, t)$ as given in Equation 6.25 is modeled using the feed particle size distribution (d_{in}) and a parameter $\Delta = d_{screen}\delta$, where d_{screen} is the screen size and δ is referred to as critical screen size ratio. A linear model is used to define the function f_d . The parameter δ is formulated as given in Equation 6.26 which represents the phenomenon of reduced apparent screen size available for a particle to exit the mill as impeller speed increases.

$$\frac{dM(w, t)}{dt} = R_{form}(w, t) - R_{dep}(w, t) + \dot{M}_{in}(w, t) - \dot{M}_{out}(w, t) \quad 6.20$$

$$R_{dep}(w, t) = K(w)M(w, t) \quad 6.21$$

$$K(w) = \begin{cases} \beta \left(\frac{v_{imp}}{v_{imp,min}} \right)^2 \left(\frac{w}{w_{ref}} \right) & \text{if } w \geq w_{ref} \\ 0 & \text{else} \end{cases} \quad 6.22$$

$$R_{form}(w, t) = \int_w^\infty K(u)M(u, t)b(u, w)du \quad 6.23$$

$$b(w, u) = \frac{p \frac{u}{w} q^{-1} (1 - \frac{u}{w})^{r-1}}{wB(q, r)} \quad 6.24$$

$$\dot{M}_{out}(w, t) = (R_{form}(w, t) - R_{dep}(w, t) + \gamma d_{in}(w, t))(1 - f_d) \quad 6.25$$

$$\delta = \epsilon \left(\frac{v_{imp, min}}{v_{imp}} \right)^\alpha \quad 6.26$$

Impeller speed showed little effect on the milled product when the comill feed is obtained from the fluid bed dryer because of breakage that occurs during transport to and from the fluid bed dryer in the horizontal ConsiGma™-25 configuration. Hence, v_{imp} is considered equal to $v_{imp, min}$ in the breakage kernel given in Equation 6.22.

The PBM is thus used to predict milled granule size distribution. The PLS model is an empirical modeling approach used to predict the milled product bulk density and tapped density, using the granule size distribution and moisture content as inputs. To use the mill model in the flowsheet model, batches of material are added to the milling unit each time the FBD completes a drying cycle and initiates an emptying cycle. When a batch of material is added to the existing material in the mill, breakage occurs. Properties of the material exiting the mill are obtained through mass averaging over the milling period t_{mill} . This is illustrated in Equation 6.27 for the bulk density of milled granules and is calculated the same way for the tapped density, span and true density of the material exiting the mill. The instantaneous bulk density $\rho_{bulk, PLS}$ is obtained from the PLS model and weighted by the total mass flow rate of material exiting the mill, $\dot{M}_{out, total}$ at time t .

$$\rho_{bulk,milled} = \frac{\int_t^{t+t_{mill}} \rho_{bulk,PLS}(x) \dot{M}_{out,total}(x) dx}{\int_t^{t+t_{mill}} \dot{M}_{out,total}(x) dx} \quad 6.27$$

6.2.1.6 Tablet Press

The tablet press model consists of four submodels. Firstly, a RTD model is used to describe the propagation of material properties through the powder dosing valve and the tablet press feed frame into the tablet die. The other models work with the material properties modeled as present in the die. The weight model relates material densities to the mean weight of the tablets semi-mechanistically (Equations 6.28 and 6.29). The tablet potency model is a first-principles model (Equation 6.31), and the tablet mean hardness model harbors literature empirical correlations related to tablet hardness and tensile strength (Equations 6.32 to 6.37).

Propagation of the material properties through the feed frame is modeled according to a series of a CSTR and a plug flow RTD model, with respective delay times t_{cstr} and t_d related to the feed frame turret speed. The solution of the feed frame model is performed in the same way as the transfer line models explained in Section 6.2.1.8.

The tablet mean weight model uses the tooling dimensions (cup volume V_{cup} , die surface A_{die} and punch cup depth D_{cup}), the material densities at the die (true density ρ_{true} , bulk ρ_{bulk} and tapped ρ_{tapped} density), a fill density factor $p_{\rho_{fill}}$ and the fill depth d_{fill} to calculate the mean tablet weight \bar{m} , according to the following equations.

$$\rho_{fill} = \rho_{bulk} + p_{\rho_{fill}} (\rho_{tapped} - \rho_{bulk}) \quad 6.28$$

$$\bar{m} = (V_{cup} + A_{die}d_{fill})\rho_{fill} \quad 6.29$$

The volume of the solids in the die V_{solid} is then:

$$V_{solid} = \bar{m} / \rho_{true} \quad 6.30$$

The potency P simply follows from the concentration C_{API} and \bar{m} :

$$P = \bar{m} C_{API} \quad 6.31$$

The hardness model in the end uses V_{solid} from the tablet mean weight model, the main compression height process setting MCH and the tablet dimensions (width W , thickness T and upper punch penetration upp) to calculate the tablet hardness through estimation of the tablet tensile strength. W and T are calculated according to:

$$W = MCH - upp \quad 6.32$$

$$T = (MCH - upp) + 2D_{cup} \quad 6.33$$

resulting in a tablet volume V_{tablet} and relative density ρ_{rel} through:

$$V_{tablet} = (WA_{die}) + 2V_{cup} \quad 6.34$$

$$\rho_{rel} = \frac{V_{solid}}{V_{tablet}} \quad 6.35$$

In order to relate the experimentally obtained hardness N values to the material properties for the biconvex tablets, a tensile strength σ_T normalization needs to be applied w.r.t. the tablet dimensions [196].

$$\sigma_T = \frac{10N}{\pi D^2} \left(2.84 \frac{t}{D} - 0.126 \frac{t}{W} + 3.15 \frac{W}{D} + 0.01 \right)^{-1} \quad 6.36$$

The tensile strength is linked to the critical density for tableting of the material ρ_c , and maximum achievable tensile strength σ_{max} [84]:

$$\sigma = \sigma_{max} \left[\rho_c - \rho_{rel} - \ln \left(\frac{1 - \rho_{rel}}{1 - \rho_c} \right) \right] \quad 6.37$$

The constants of σ_{max} and ρ_c are obtained through empirical linear correlations with the relative size span R_{span} of the material and the moisture content X .

Finally, two modes of using the tablet press model are defined. In the *process setting* mode, tablet press process setting values (fill depth and MCH) are supplied to the model along with the material properties. Tablet properties such as the mean weight and hardness then result from the combination of the user defined process setting values with the incoming properties. These might however not match and result in unrealistic tablet properties as well as infeasible calculations, such as in the case

where Equation 6.38 is not satisfied. In this mode, this is amended by the inclusion of a boolean variable that is only True when the input variables are such that condition Equation 6.38 is fulfilled.

$$\rho_c < \rho_{rel} < 1 \quad 6.38$$

Another mean weight control (MWC) mode was created to allow for the tablet press model to calculate its process setting values in order to achieve a certain mean weight and hardness. These two variables thus serve as an input to the model in the flowsheet model, and the fill depth and MCH are calculated. This allows avoidance of the situation where user-specified tablet press process settings are not compatible with the simulated material properties governed by the process setting values upstream, possibly leading to a long simulation where no tablet weights or hardnesses could be calculated.

6.2.1.7 Overview

Once the individual unit operation models are developed and parameterized, the flowsheet model is built via connecting the inlet of a unit to the outlet of the preceding unit. Required information (material properties, operating conditions etc.) are transferred from one unit to the succeeding unit as shown in Figure 6.1. The interaction between various modeling approaches in the individual unit operations is pictorially shown in Figure 6.2 to illustrate how empirical, semi-empirical, statistical and mechanistic models interact to yield a flowsheet model.

The system is solved using a backward differentiation solver with variable time steps, which is one of the two built-in solvers in gPROMS.

6.2.1.8 Intermediate feeders, blender and transfer line

The ConsiGma™-25 line includes an intermediate feeder for feeding powder blend from blender to the granulator (hereafter referred to as 'powder blend feeder'), and an intermediate feeder for feeding granulated material from the mill (hereafter referred to as 'granule feeder'). Thus to achieve a more accurate representation of the ConsiGma™-25 line, transfer lines and the intermediate feeder and blender units are also included in the flowsheet model. A key difference in the implementation of the feeder model to the intermediate units is that the powder blend feeder and granule feeder do not have refilling units assigned to them, as these units receive material from their preceding units (powder blend feeder receives material from the blender and granule feeder receives material from the mill).

In addition, a blending unit is also included to add lubricant to the granulated material from the mill. This intermediate blender will hereafter be referred to as 'granule blender'. The granule blender is modeled based on the axial dispersion equation as explained in Section 6.2.1.2. The blender is assumed to be filled with granulated material and the axial dispersion equation is used to transfer information regarding new or changing material properties from the upstream mill and the lubricant feeder. The true density of lubricated material from the granule blender is taken as weighted average of bulk densities of the milled granule product and lubricant.

In the dynamic flowsheet simulation, an accurate representation of the material properties at all times and at every location in the process would not be complete without accounting for material hold-up between unit operations. Hereto, transfer line models have been implemented to propagate variable values in between unit operation models. These models delay the propagated values according to a plug flow regime, assuming no back-mixing or axial dispersion is taking place during the transfer of materials between unit operations.

The plug flow propagation of these materials is often modeled applying a convolution of the inlet concentration profile at the modeled system, with the residence time distribution function of the material, as for instance described in Engisch and Muzzio [197]. This convolution requires information on the inlet concentration values over a range of time. For simplicity, this plug flow behavior is emulated using an axial dispersion model. A new simulation domain z is created to represent the normalized length of the transfer line under consideration, therefore this domain $[0, L]$ is always equal to $[0, 1]$. Over this domain, the change in input signal S over time t at $z = 0$ is propagated over the domain as in Equation 6.39 where the plug flow time delay is represented as τ_{delay} . The input and output of the transfer lines are hence given by $S(t, 0)$ and $S(t, 1)$ respectively. The smaller ∂z is chosen, the smoother and more accurate the signal will propagate through the domain z , yet more computational burden is involved with this choice of more grid points. A value of $1/1000$ for ∂z has been found to give a good balance between smoothness and computational burden. Finally, it has been found that normalization of the delayed signal S drastically improves CPU time in the gPROMS solvers.

$$\tau_{delay} \frac{dS(t, z)}{dt} = \frac{\partial S(t, z)}{\partial z} \quad 6.39$$

The above unit operation models are connected to develop the flowsheet model representing the ConsiGma™-25 line as shown in Figure 6.3. The flowsheet includes intermediate units and transfer lines as well. When the flowsheet model is simulated, it is important to have a clear understanding of the initial states of the model as it impacts the dynamic model state. For example, feeder hoppers could have various amounts of material at the start of the simulation. Similarly, the mill could start empty or have a certain amount of mass held up at the start of the simulation.

Table 6.3 gives an overview of initial and dynamic states of the various units in the developed flowsheet model. The full flowsheet model thus developed can be used to simulate the continuous process as described in Section 6.3. Two case studies are provided in Section 6.4 where the full flowsheet model is used to understand the effect of step changes in process settings. The flowsheet model can also be used for advanced process analyses as described in the next sections.

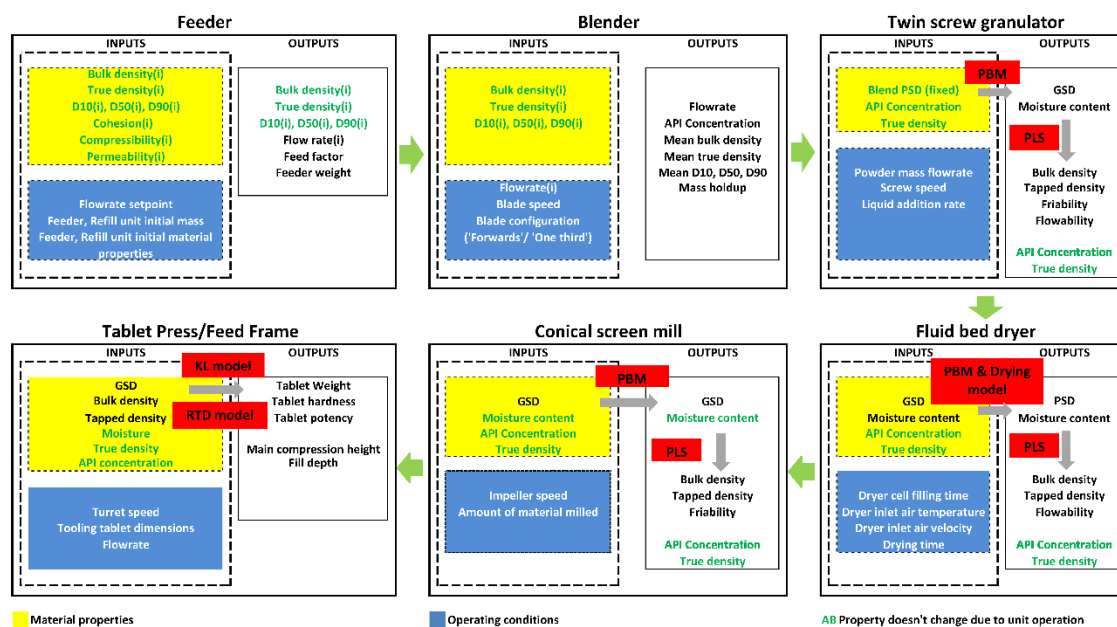


Figure 6.2 Schematic showing interaction between units and various modeling approaches

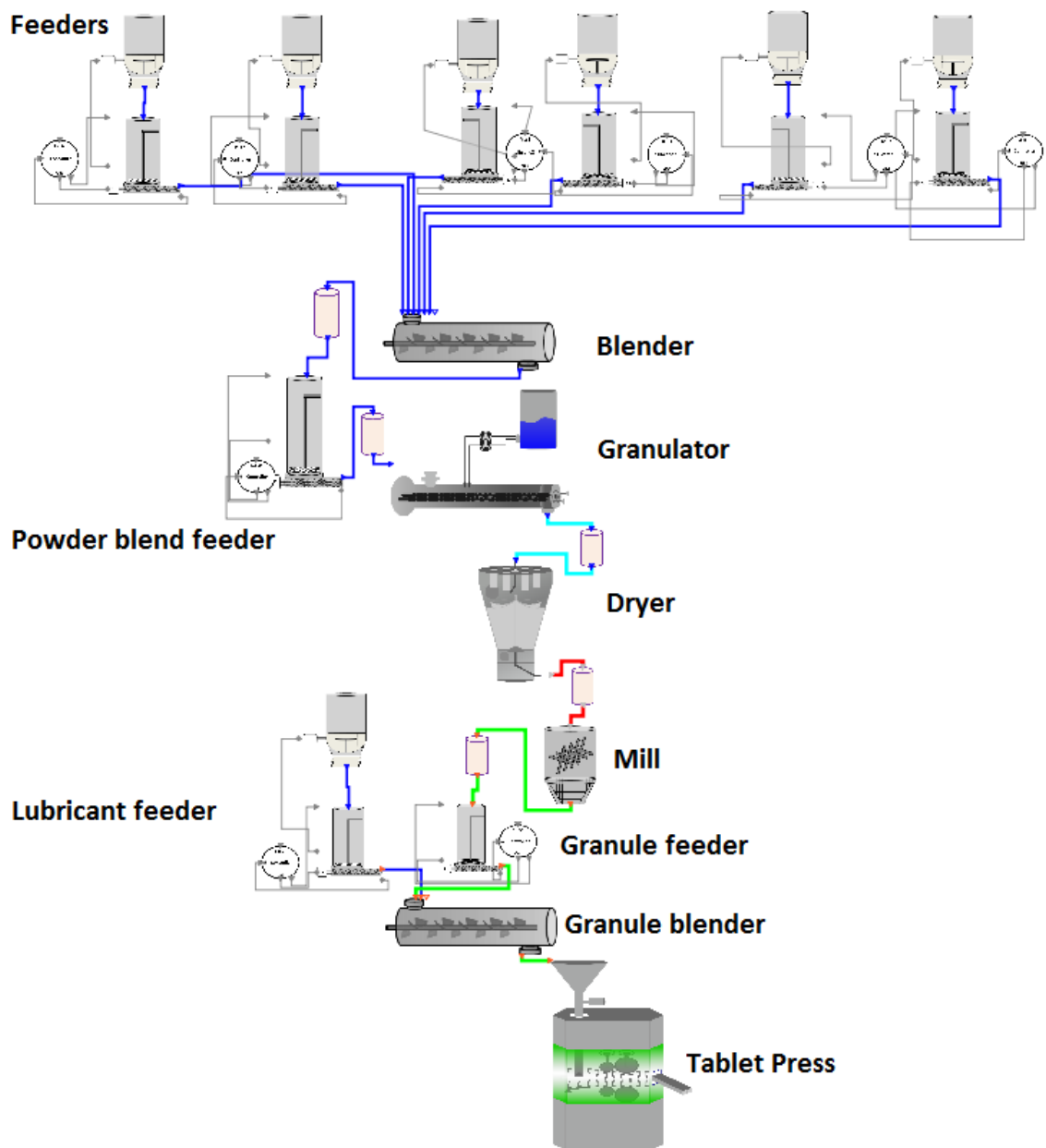


Figure 6.3 gPROMS Formulated Products schematic of the full flowsheet model developed

Table 6.3 State of unit models used in flowsheet model development

Unit	Initial State	Dynamic State
Feeders	Full	Refills when empty
Blender	Empty	Reaches steady state
Granulator	Empty	Output obtained when input is in studied range Plug flow delay added to instantaneous response
Dryer	Empty	Releases batches of material at the end of drying time
Mill	Empty	Releases material in semi-continuous mode
Tablet Press	Empty	Output obtained when input is in studied range Delay from RTD model in feed frame
Powder blend feeder	Full with powder blend	Continuous feed from blender
Granule feeder	Full with granules	Refill from mill
Granule blender	Always full	Delay from axial dispersion

6.2.2 Scenario Analysis

It is important to ensure that the flowsheet model developed successfully runs simulations at various process conditions. This affirms that the models are successfully integrated. In addition, it is important to verify that the process responses from these simulations are aligned with process knowledge. Scenario analysis provides a structured framework to achieve this, as several simulations at various combinations of process settings can be run in parallel and the resulting process responses can be analyzed. In this work, only process responses at the end of simulation i.e., steady state tablet properties are analyzed.

However, this exercise is computationally demanding as one simulation takes several hours to run. In this work, a more pragmatic approach is applied and the flowsheet model as given in Figure 6.4 is adapted in order to implement scenario analysis. Specifically, the intermediate units (powder blend feeder, granule feeder, granule blender) and the transfer lines are not considered. Since only the end of simulation responses are studied, the flowsheet model simplification is valid as the intermediate units and transfer lines do not affect the steady state process responses. The modified model lowers the computational expense and allows implementation of study required to affirm

that the process responses from integration of unit operation models are meaningful. The full flowsheet model takes approximately 4 h to run a six-cell drying cycle, whereas the modified model only takes approximately 7 min for the tablet properties to reach steady state. Hence, the adapted model as shown in Figure 6.4 is used for the implementation of scenario analysis. In addition, the factors used for the study are also chosen judiciously in order to keep the total number of flowsheet model evaluations low. For example, factors such as blender blade speed, mill impeller speed are not considered. The blender blade speed influences the mass holdup in the blender as explained in Section 6.2.1.2 but not the steady state flow rate, as this depends on the incoming feed flowrate. The mill impeller speed does not have an effect on granules obtained from a FBD [164]. Overall, the factors considered, their corresponding lower and upper bounds, and number of levels for each factor is listed in Table 6.4. In addition, the process responses that are recorded for each simulation run are also listed in Table 6.4. Three levels for flow rate setpoint, four levels for LS ratio, granulator screw speed, dryer air temperature, drying time are chosen. In Section 6.5, an analysis of process responses from the simulations run is discussed in detail.

While the adapted flowsheet model is useful in implementing further analyses, it is also important to understand its limitations. The simplified flowsheet does not capture the effects of the intermediate units. For example, effects of refilling and propagation of disturbances from the intermediate units are ignored. In addition, a successful scenario analysis on the simplified model does not capture scenarios where the full flowsheet model fails due to the intermediate units. The simplified flowsheet does not support study of dynamic behavior of the line. Analyses such as dynamic sensitivity analysis or identification of dynamic feasible region cannot be accomplished.

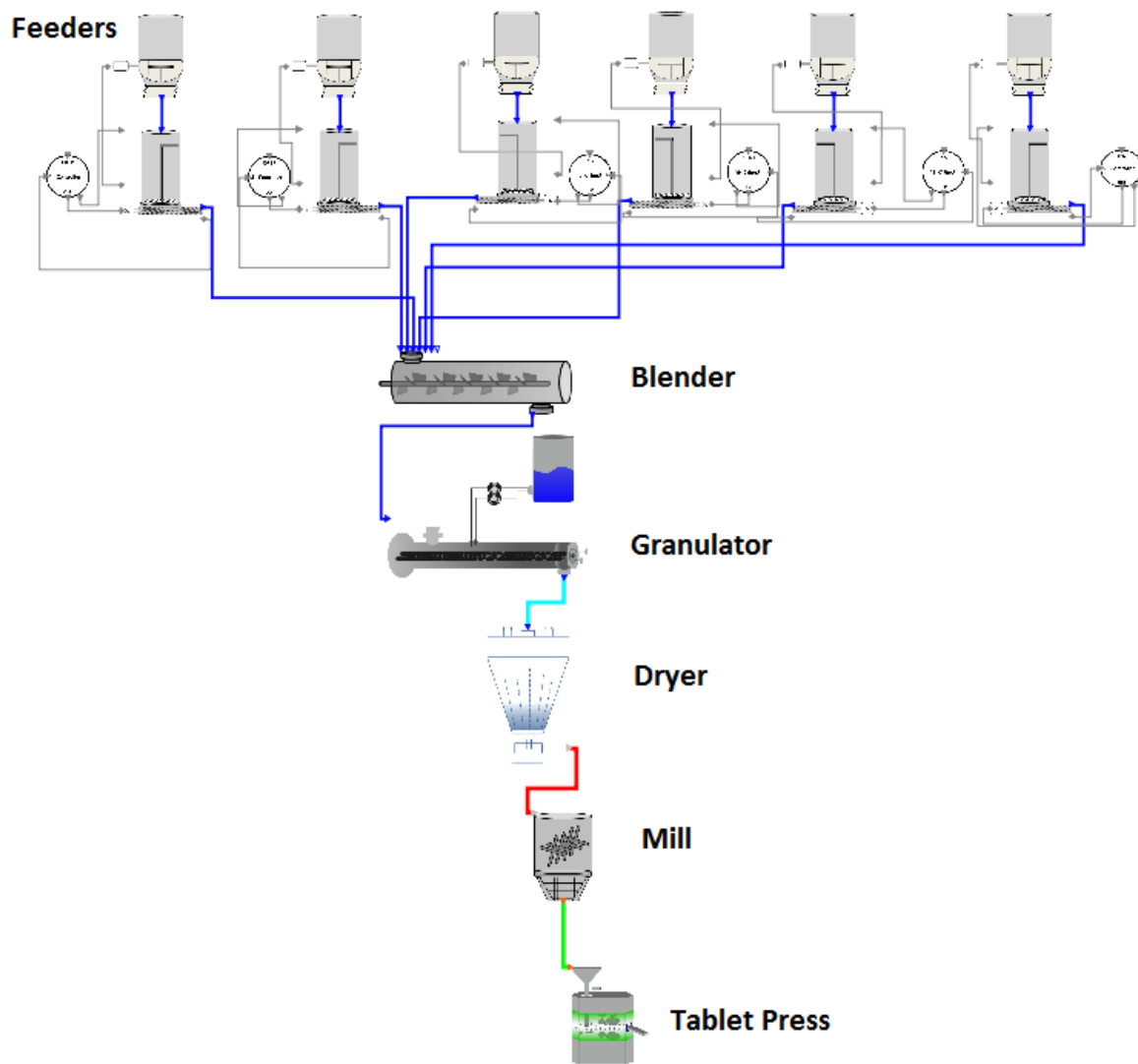


Figure 6.4 Schematic of the flowsheet model used for scenario analysis and sensitivity analysis

Table 6.4 Factors and responses for scenario analysis and sensitivity analysis

Unit	Factor	Bounds	Number of Levels	Response
Blender	flowrate setpoint, kg/h	[10, 20]	3	Mean Residence time Number of tanks
Granulator	LS ratio, kg/kg	[0.08, 0.18]	4	PSD: d10, d50, d90
	Screw speed, rpm	[500, 900]	4	Moisture content
Dryer	Air temperature, deg C	[40, 60]	4	PSD: d10, d50, d90
	Drying time, s	[200, 1080]	4	Moisture content
Mill				PSD: d10, d50, d90 Span Bulk density Tapped density
Tablet Press				Tablet hardness Tablet potency MCH Fill depth

6.2.3 Sensitivity Analysis

Sensitivity analysis is one of the key process systems engineering tools that can be used for quality risk assessment through identification of critical process variables. Sensitivity analysis is the investigation of how variability in the model inputs contributes to variations in model outputs [198]. It is an effective tool to rank and prioritize the process variables based on the effects they have on the output variables of interest. In the context of operation of a continuous manufacturing line, it helps identify the source of issues in meeting product quality or production demands. In the context of process model development, sensitivity analysis has been extensively used to identify the parameters that affect model outputs, thus helping focus experimental and model calibration efforts [198, 199]. This helps researchers identify the areas where further model development needs to be focused on. Specifically for a flowsheet model where there is high number of input factors, sensitivity analysis can be used to reduce the number of input factors that need to be studied further. This helps in simplifying a high dimensional problem by filtering out the variables that have

negligible effects on the outputs of interest. With this simplification, other tools can be applied for identification of design space of the process and its optimization [12].

Sensitivity analysis can be categorized into local and global methods. Local methods study the effect of input variables around a nominal point (or base case), whereas global methods study the effects over an entire input space. In this work, we focus on global sensitivity analysis as this is more relevant for pharmaceutical processes. For pharmaceutical processes, the input factors may include operating variables such as blender impeller speed, granulator screw speed etc. The output variables of interest may include product properties such as tablet hardness, granule mean particle sizes, or process variables such as mill mass hold up, total flow rate etc. There are various global sensitivity analysis methods available. The choice of method usually depends on the computational cost of evaluating the models, sampling budget available and the detail of sensitivity information desired. In this work, Elementary effects method and Variance based sensitivity analysis methods are used, details of which are described in the next section. These methods are chosen as they are available in gPROMS FormulatedProducts with parallel computing capability.

6.2.3.1 Morris Method

Morris method also referred to as Elementary effects method is categorized under screening methods for sensitivity analysis. Screening methods are the most effective way to identify the most influential factors with relatively fewer samples [198]. Morris method is based on OAT (one-at-a-time) design where each of the input factors is varied and effects on the model outputs are studied.

For a model with k number of inputs, at a selected base point (x_1, x_2, \dots, x_k) , the elementary effect EE_i of the i^{th} factor is given by Equation 6.40 where Δ_i is the step change in the i^{th} input factor, Y represents the model output and $0 \leq \Delta_i \leq 1$. In order to represent the sensitivity information accurately, the sample points must be spread in the input space.

$$EE_i = \frac{Y(x_1, x_2, \dots, x_i + \Delta_i, \dots, x_k) - Y(x_1, x_2, \dots, x_i, \dots, x_k)}{\Delta_i} \quad 6.40$$

Based on the calculation of EE_i , the sensitivity metrics as given in Equation 6.41 can be calculated, where r is the number of trajectories or radial base points for sampling. μ_i represents the average EE_i , σ_i^2 represents the variance and reflects non linearity or interactions in the i^{th} input. μ_i^* represents the average elementary effect using absolute EE_i to ensure the negative and positive effects do not cancel each other. It is suggested to look at all three metrics together to understand sensitivity information. Total sampling cost for this method is $r(k + 1)$ where r can be less than 20 [200]. Hence, it is especially useful for models with a large number of input factors (factor of ten) or when the model is computationally expensive. In this work, the value of r is chosen as 20.

$$\begin{aligned} \mu_i &= \frac{1}{r} \sum_{j=1}^r EE_i^j \\ \sigma_i^2 &= \frac{1}{r-1} \sum_{j=1}^r (EE_i^j - \mu_i)^2 \\ \mu_i^* &= \frac{1}{r} \sum_{j=1}^r |EE_i^j| \end{aligned} \quad 6.41$$

After the metrics are obtained, input factors with large μ_i and/or μ_i^* , σ_i^2 are considered to be significant. Practically, if the metric of an input factor is less than 10% of the largest value of this metric, the input factor is considered insignificant. While the method can be used to rank the factors, it does not quantify how much an input factor is more important than the other factors.

6.2.3.2 Variance-based method

In this category of methods, the variance of the output is decomposed into several components including the individual inputs and the interactions between the inputs [201]. For an independent set of input factors, the variance $V(y)$ is expressed as given in Equation 6.42 where V_i is the variance term solely due to the input factor x_i , $V_{i,j}$ is the variance term due to the interaction between the input factors x_i and x_j . Based on this variance decomposition, sensitivity measures can be defined as given in Equation 6.42.

$$\begin{aligned}
 V(y) &= \sum_{i=1}^k V_i + \sum_{1 \leq i < j \leq k} V_{i,j} + \dots + V_{i,j,\dots,k} \\
 S_i &= \frac{V_i}{V(y)} \\
 S_{ij} &= \frac{V_{i,j}}{V(y)} \\
 S_{Ti} &= \frac{V_i + \sum_{j \neq i} V_{i,j} + V_{1,2,\dots,k}}{V(y)} = 1 - \frac{V_{\sim i}}{V(y)}
 \end{aligned}
 \tag{6.42}$$

For the input x_i , S_i represents the ‘first-order sensitivity index’ whereas S_{ij} represents the ‘second-order sensitivity index’ which is the interaction effect of x_i and x_j on the process output. The metric S_{Ti} indicates the ‘total sensitivity index’, which accounts for the main effects as well as all the higher order interaction effects.

Specifically, this method uses Monte-Carlo techniques to compute the sensitivity indices as given in Equations 6.43 and 6.44 where $E(\cdot)$ is the expected value and $X_{\sim i}$ represents all possible combinations of input factors with i^{th} input factor X_i fixed. For this method, total number of samples required is $N(k + 2)$ where N is recommended to be at least 500 [198]. In this work, the value of N is chosen as 500.

$$S_i = \frac{V_{X_i}(E_{X_{\sim i}}(Y | X_{\sim i}))}{V(Y)} \quad 6.43$$

$$S_{Ti} = \frac{V_i + \sum_{j \neq i} V_{i,j} + V_{1,2,..,k}}{V(y)} = 1 - \frac{V_{X_{\sim i}}(E_{X_i}(Y | X_{\sim i}))}{V(y)} = \frac{E_{X_{\sim i}}(V_{X_i}(Y | X_{\sim i}))}{V(y)} \quad 6.44$$

For the variance based method, higher values of the metrics S_i and S_{Ti} indicate larger influence of the input factor. Also, S_i is always lower than or the same value as S_{Ti} . Hence, the difference between these metrics reflects interaction effects of the input factor with other factors. The adapted flowsheet model as explained in Section 6.2.2 is used for implementing the sensitivity analysis methods as well. In this work, details of factors and responses listed in Table 6.4 are also applicable for executing sensitivity analysis. In the next sections, results from simulating the flowsheet model, case studies to demonstrate dynamic simulation capabilities of the model and further analysis are presented and discussed.

6.3 Simulation results

The flowsheet model as described in Section 6.2.1 is simulated using process settings as given in Table 6.5. The flow rate setpoints for the feeders are based on the formulation given in Table 6.1 and a total flow rate of 15 kg/h. The operating variables for other units were set within the ranges that were used to develop the individual unit operation models. The flowsheet model is simulated for 1500 s to complete a drying cycle using six dryer cells. Feeder levels in the seven component feeders (two API, one lubricant and four excipient feeders) decrease until refill occurs at a fractional fill level of 0.1. The fill level in the powder blend feeder reduces until the blender starts feeding powder blend to it. The fill level in the granule feeder reduces until the mill starts feeding granules in a semi-continuous mode. Fill levels of all the component feeders and flow rate are shown in

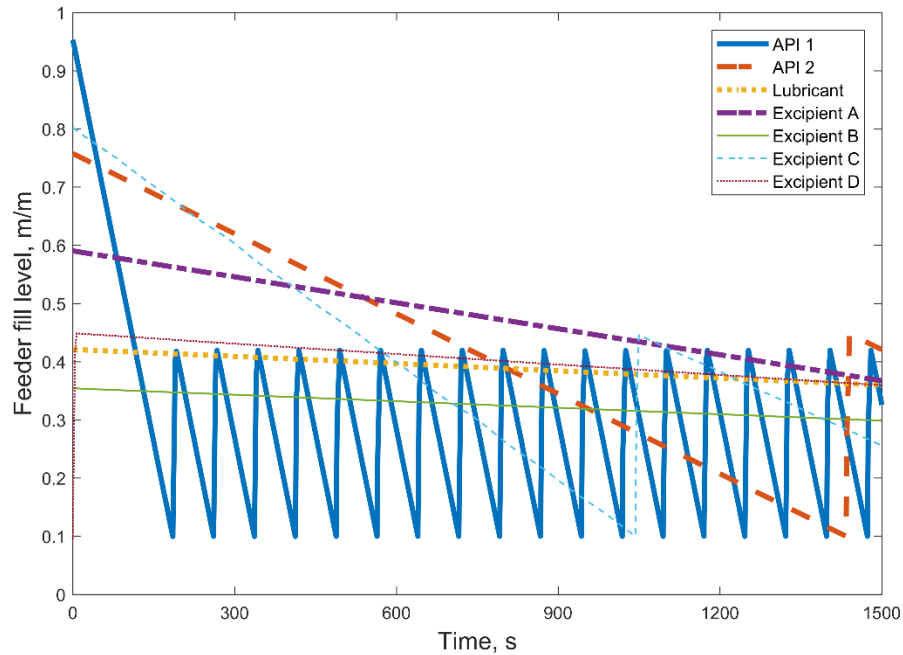
Figure 6.5. Figure 6.5c shows fill levels and flow rates of the two intermediate feeders, i.e. powder blend and granule feeder.

Table 6.5 Values of process variables used for simulating the flowsheet model

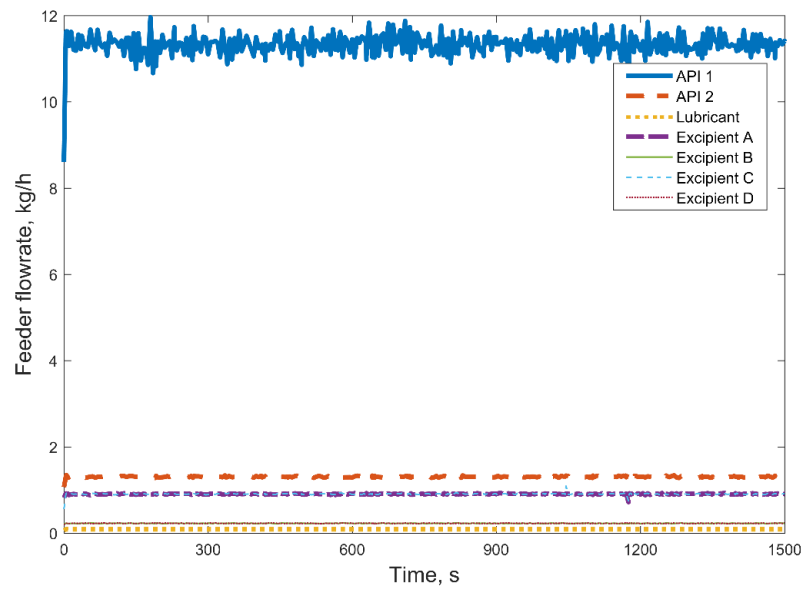
Unit	Process Variable	Units	Value
Feeders	API 1 flow rate	kg/h	11.337
	API 2 flow rate	kg/h	1.308
	Lubricant flow rate	kg/h	0.087
	Excipient A flow rate	kg/h	0.907
	Excipient B flow rate	kg/h	0.227
	Excipient C flow rate	kg/h	0.907
	Excipient D flow rate	kg/h	0.227
	Powder blend feeder flow rate	kg/h	14.913
	Granule feeder flow rate	kg/h	14.913
Blenders	Bladespeed	rpm	250
Granulator	Liquid-solid ratio	kg/kg	0.12
	Screw speed	rpm	500
Dryer	Air flow	m ³ /h	360
	Air temperature	deg C	40
	Drying time	s	450
	Filling time	s	180
Tablet Press	Turret speed	rpm	29.8
	Mean weight	g	0.43

Powder blend flows continuously to the granulator. Wet granules start filling the first cell of the dryer and drying begins. After a filling time of 180 s, the second dryer cell starts filling. Dried granules in the first cell are emptied to the mill after a total drying time of 450 s. Thus, the cycle of filling, drying and emptying continues for the duration of simulation. Batches of dried granules fed to the mill are broken and leave the mill. The left axis in Figure 6.6 shows flow rate of the blend from the granulator. The right axis in Figure 6.6a shows mass of the batches of dried granules fed to the mill and corresponding change in holdup in the mill due to granules entering and leaving the mill. Figure 6.6b shows the evolution of moisture content of wet granules from the granulator and dry granules from the dryer as simulation progresses. As the simulation of the drying behavior requires a moisture content value at the beginning of its simulation, the results for the first dried

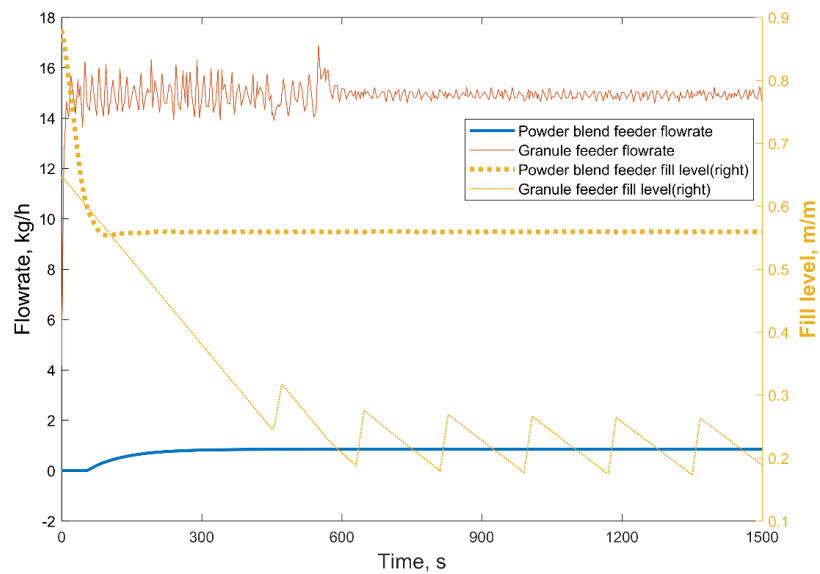
batch are not representative because the wet granule moisture content at time $t = 0s$ equaled zero. This is the moisture content output of the dryer model at time $t = 450s$, which just indicates that the first dryer cell has emptied. This should be improved towards the future so that the dryer model has a fully dynamic response towards its input.



(a)

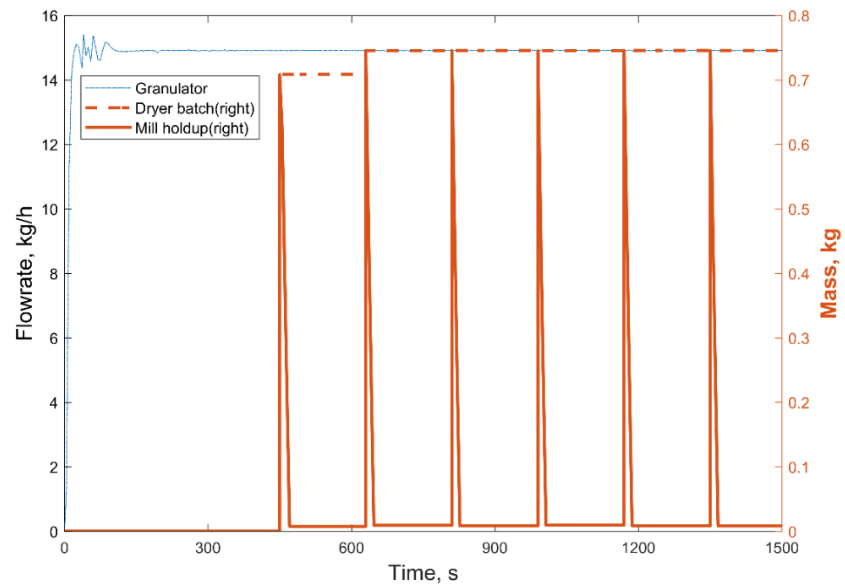


(b)

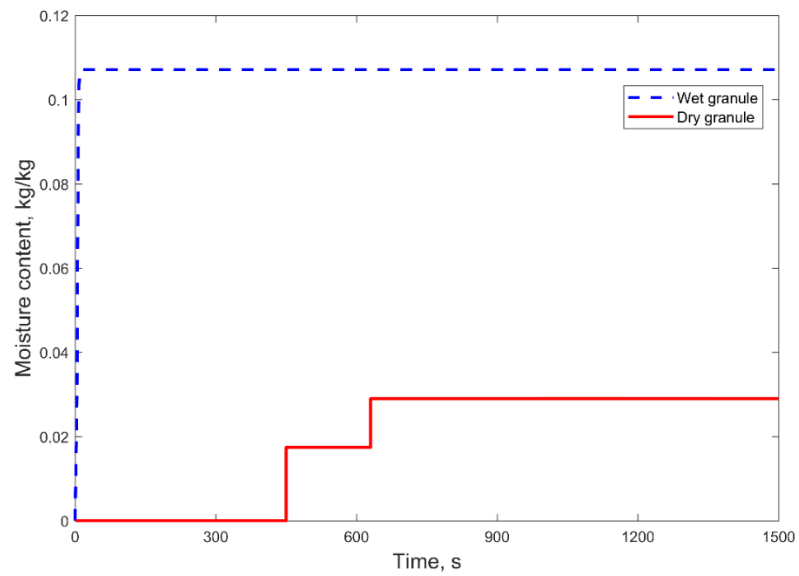


(c)

Figure 6.5 (a) Component feeder fill levels (b) Component feeder flow rates (c) Powder blend feeder and granule feeder fill levels and flow rates



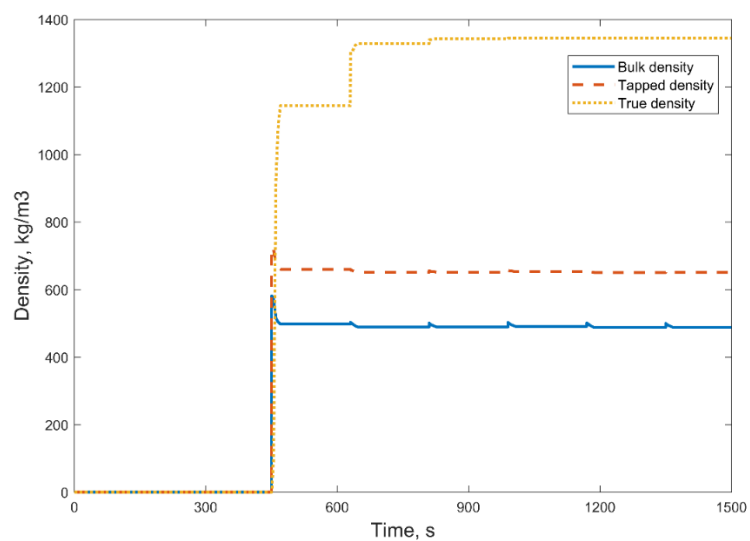
(a)



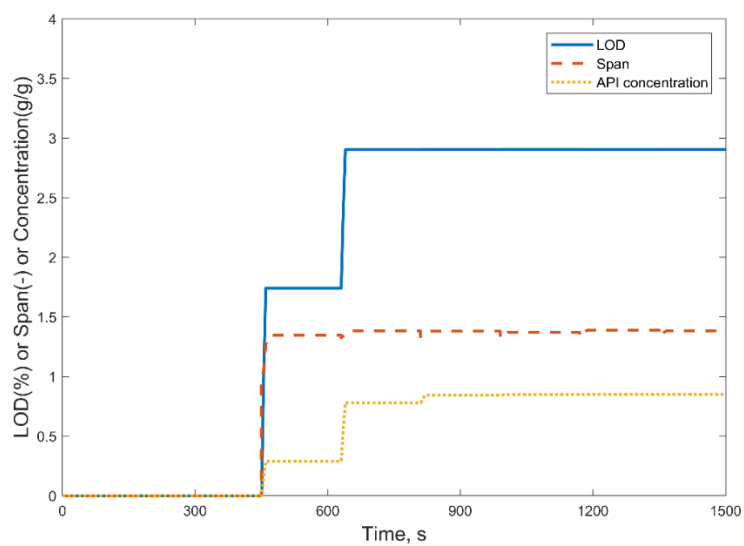
(b)

Figure 6.6 (a) Granulator flow rate, mass of granules from the dryer and holdup in mill (b) Moisture content of wet and dry granules

As milled granules exit the mill, properties of the batch of milled granules are mass averaged and this information is propagated to the subsequent units. Figure 6.7a shows profiles of bulk density, tapped density and true density of milled granules as the simulation progresses. Profiles of LOD, span and API concentration of the milled product are shown in Figure 6.7b. It can be observed that the true density, LOD and API concentration of milled product shows a step change around 600 s. This is because the intermediate powder blend feeder initially contains powder blend with a true density of 1291 kg/m³, at the start of the simulation. This is eventually replaced when the powder blend of true density of 1344 kg/m³, coming from the unit operations upstream, reaches that intermediate feeder in the simulation. Similarly, powder blend containing no API is replaced by a powder blend containing API 1 and API 2. This is reflected in the API concentration profile as shown in Figure 6.7b. In addition, LOD of the first batch of dried granules is lower (as shown in Figure 6.6b) which reflects in the milled granule LOD profile as well.



(a)

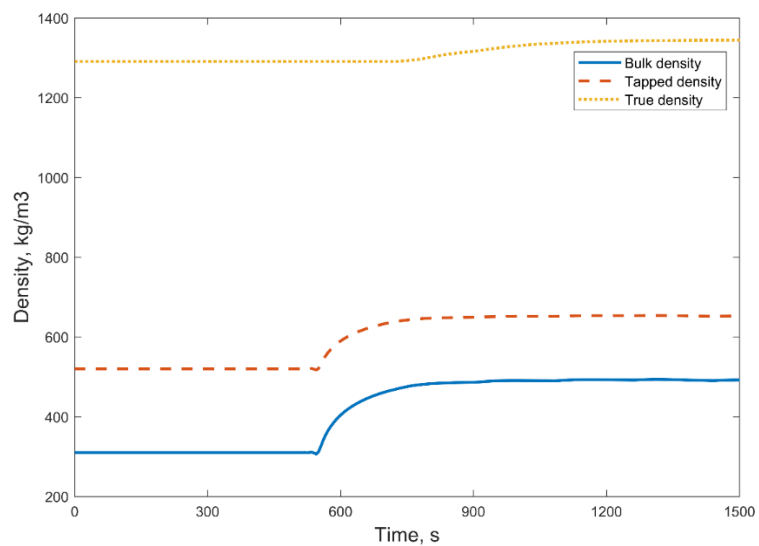


(b)

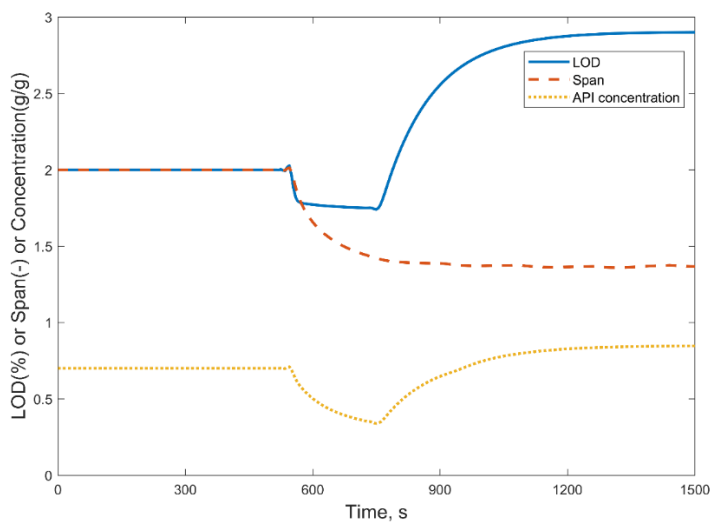
Figure 6.7 Profiles of milled granules (a) bulk density, tapped density and true density (b) LOD, span and API concentration

Milled granules fed to the granule feeder eventually replace granular material in it. Milled granules exiting the granule feeder are mixed in the granule blender with lubricant. Granules thus lubricated are sent to the feed frame, which is modeled as a PFR and CSTR in series. Propagation of properties (bulk density, tapped density, true density) in the granule feeder is shown in Figure 6.8a. The density profiles in this figure shows replacement of granules in the granule feeder with granules from the mill. Similarly, Figure 6.8b shows LOD, span and API concentration profiles that simulate replacement of material existing in the granule feeder (2% LOD, span of 2 and 0.7 fractional API concentration) with milled granules from the upstream unit. Figure 6.9a shows density profiles of granules entering and leaving the feed frame. Similarly, Figure 6.9b shows profiles of LOD, span and API concentration of granules entering and leaving the feed frame. The profiles changes seen in these figures is self explanatory based on the milled granule profiles (Figure 6.7) and granule feeder profiles (Figure 6.8).

The propagation of bulk density, tapped density, true density, API concentration, LOD and span affect the profiles of tablet properties namely, tablet hardness, weight and potency. Figure 6.10a shows dynamic evolution of tablet properties as powder from component feeders replace material existing in the intermediate units (powder blend feeder and granule feeder). The tablet press hardness model was developed for material with bulk density greater than 300 kg/m^3 . Hence, an initial tablet hardness of zero is shown in the hardness profile. In addition, since the tablet press is used in a mean weight control mode, main compression height and fill depth are adjusted as shown in Figure 6.10b in order to make tablets with a weight of 0.43 g.

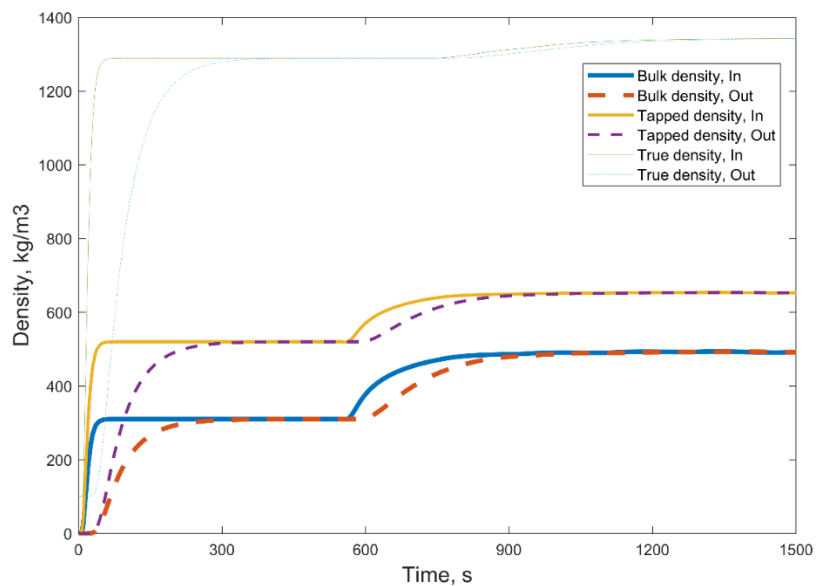


(a)

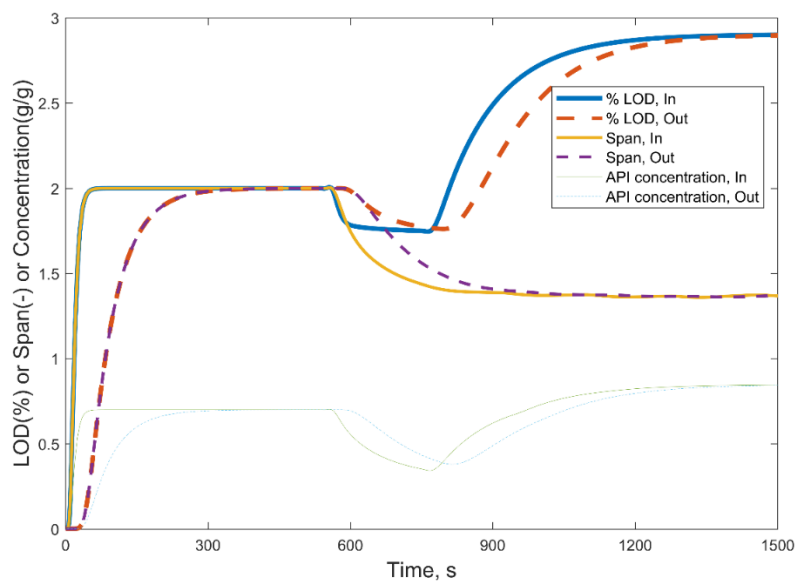


(b)

Figure 6.8 Profiles of (a) bulk density, tapped density and true density (b) LOD, span and API concentration of granules from the granule feeder.

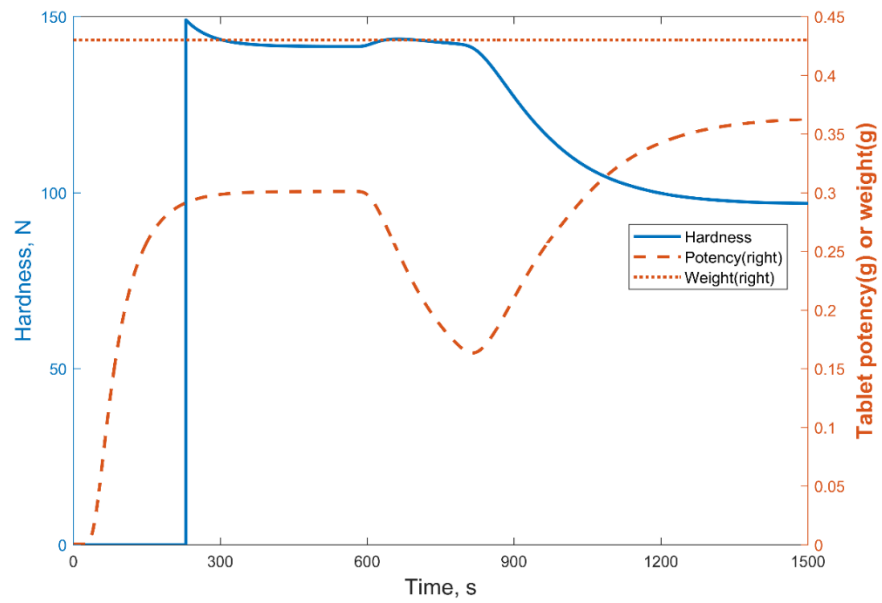


(a)

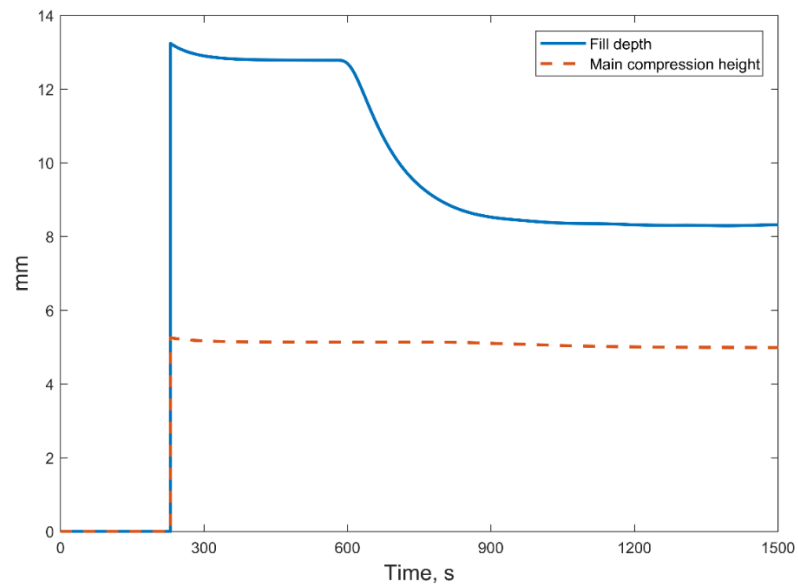


(b)

Figure 6.9 Profiles of (a) bulk density, tapped density and true density (b) LOD, span and API concentration of granules entering and leaving the feed frame.



(a)



(b)

Figure 6.10 Profiles of (a) tablet hardness, weight and potency (b) tablet press fill depth and main compression height

6.4 Case studies

To clearly demonstrate the use of the flowsheet model for dynamic simulation purposes, two case studies are presented in this section. In both case studies, the full flowsheet model developed as explained in Section 6.2.1 is used. The initial simulation process variable settings are the same as explained in Table 6.2. Later, in case study 1, a step change from 1.3 kg/h to 4 kg/h is made to the API 2 feeder flow rate setpoint at 200 s. In case study 2, a step change from 40 deg C to 50 deg C is made to the dryer air temperature at 455 s. A comparison between simulation results with and without the step changes implemented, and a demonstration of propagation of effects of the changes is discussed in the following sections.

6.4.1 Step change in feeder flow rate

A step change in API 2 feeder flow rate setpoint from an initial value of 1.3 kg/h to 4 kg/h is expected to lead to a change in API concentration (API 1 and API 2) in the powder blend, the granules and subsequently potency of the tablets. Figure 6.11 shows the step change made in setpoint at 200 s leads to a change in API 2 feeder flow rate.

A change in fractional API concentration at the blender outlet from 0.85 to 0.87 is seen in Figure 6.12a as a result of the step change. Figure 6.12a also shows a change in API concentration of the powder blend leaving the powder blend feeder as initial material in the feeder (with no API) is eventually replaced by powder blend with API concentration of 0.87. A comparison with profiles from the simulation explained in Section 6.3 is also shown in this. Since the change is made at 200 s, the first cell in the dryer is filled (dryer filling time = 180 s) with granules from powder blend already present in the powder blend feeder. Hence, profiles of API concentration from the outlet of granulator and dryer from the simulation explained in Section 6.3 and this case study are the same till the first dryer cell is emptied. This is shown in Figure 6.12b. Similarly, Figure 6.12c shows the

propagation of change in API concentration at the outlet of respectively the mill and the granule feeder. As a result of this, a change in API concentration profiles at the outlet of granule blender and the feed frame are shown in Figure 6.12d. Finally, due to the step change in the amount of API 2 in the feed components an eventual deviation in the potency of tablets from 0.364 g to 0.374 g is shown in Figure 6.13

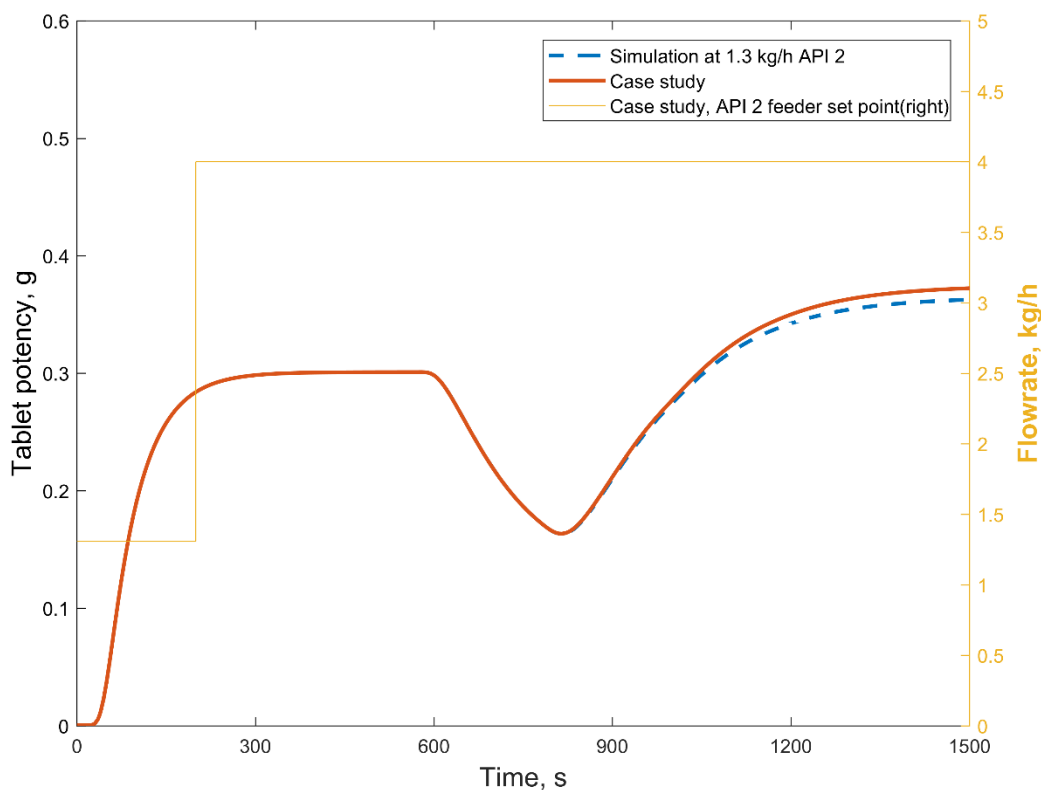


Figure 6.13. Thus, the case study demonstrates the use of the flowsheet model developed to track the effects of disturbances in upstream units on the final product quality.

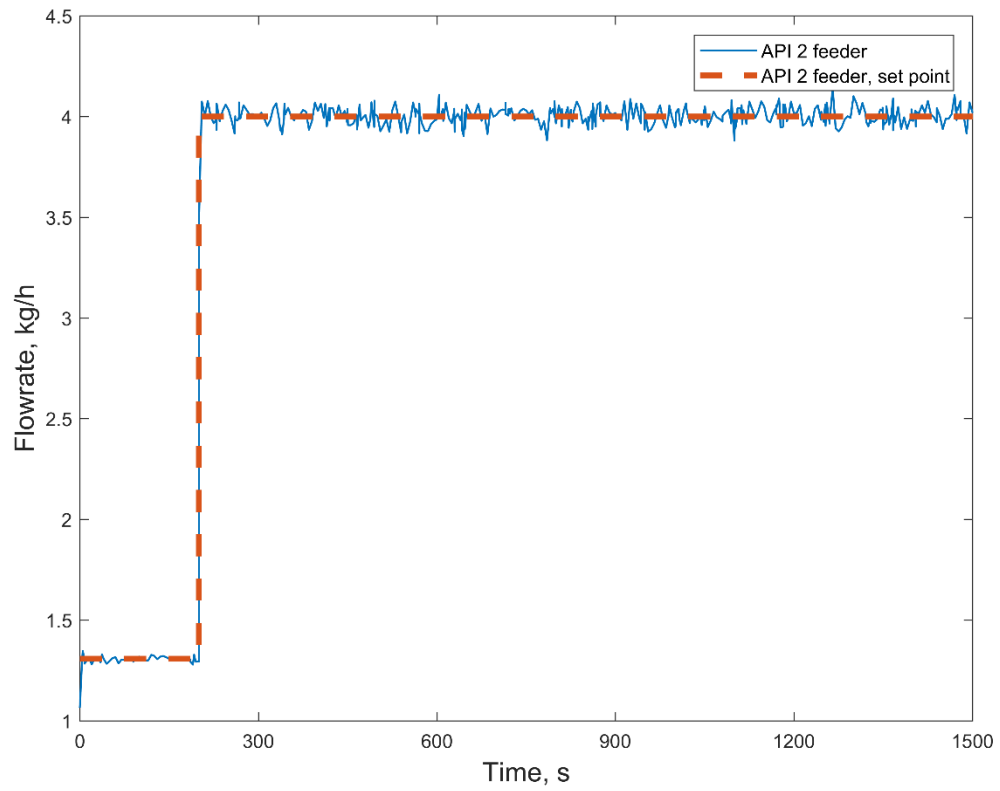
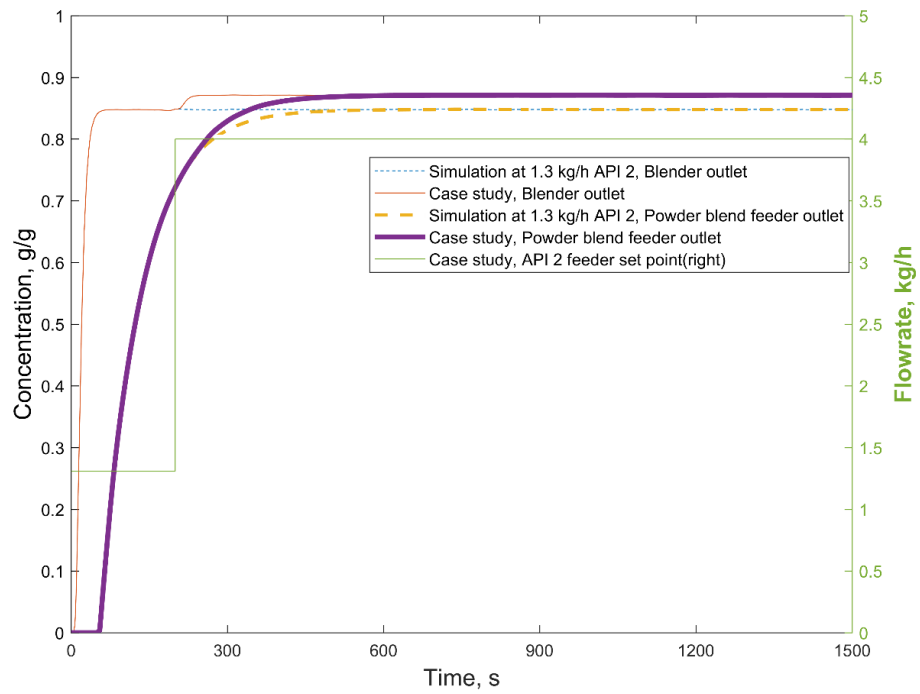
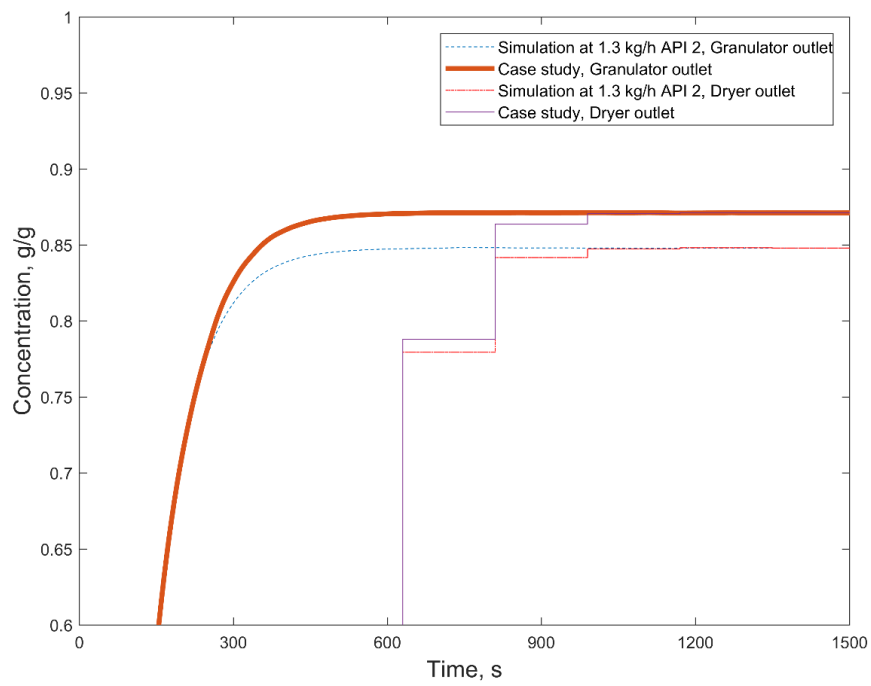


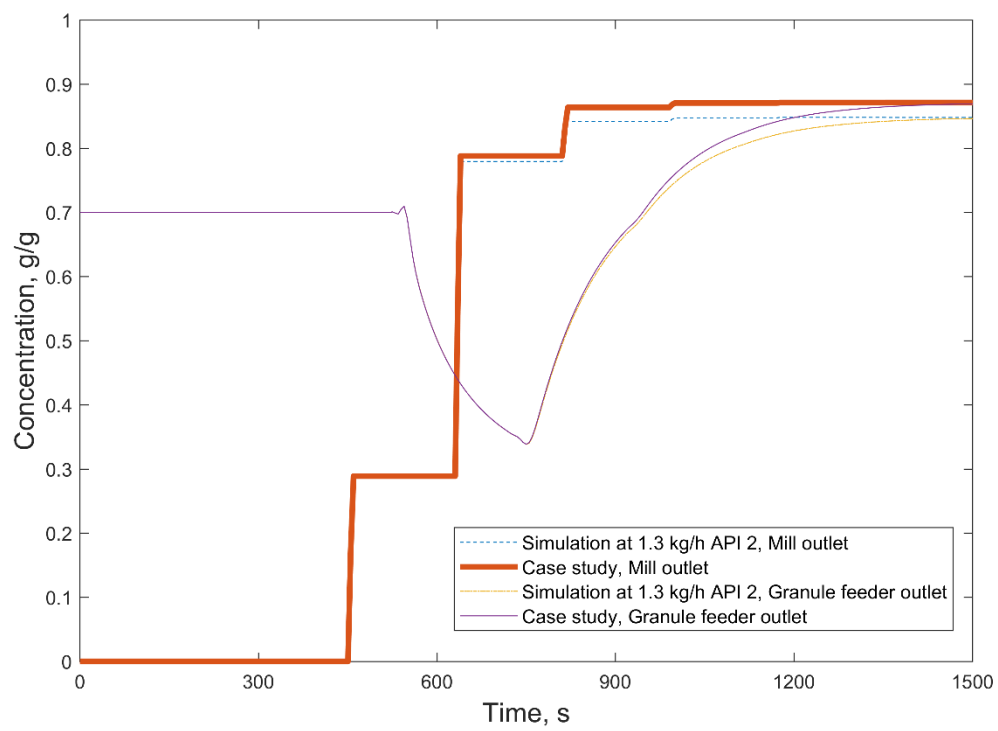
Figure 6.11 Step change in API 2 feeder flow rate setpoint showing an effect on the feeder flow rate



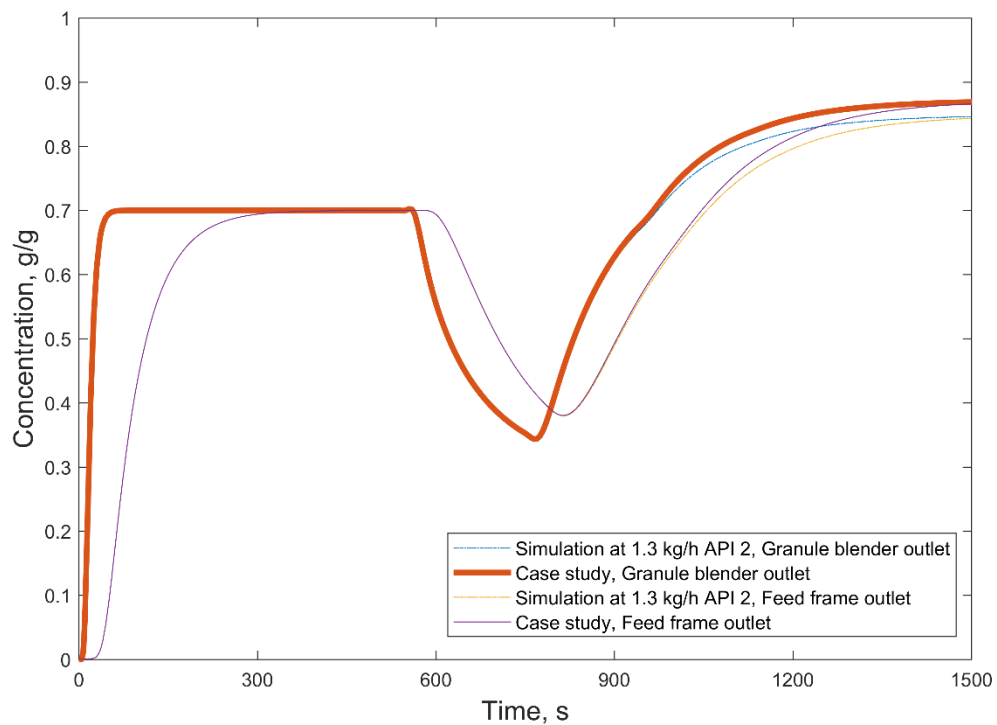
(a)



(b)



(c)



(d)

Figure 6.12 Comparison of API concentration profiles from simulations with fixed and step change in API 2 feeder flow rate setpoint for (a) blender and powder blend feeder (b) granulator and dryer (c) mill and granule feeder (d) granule blender and feed frame.

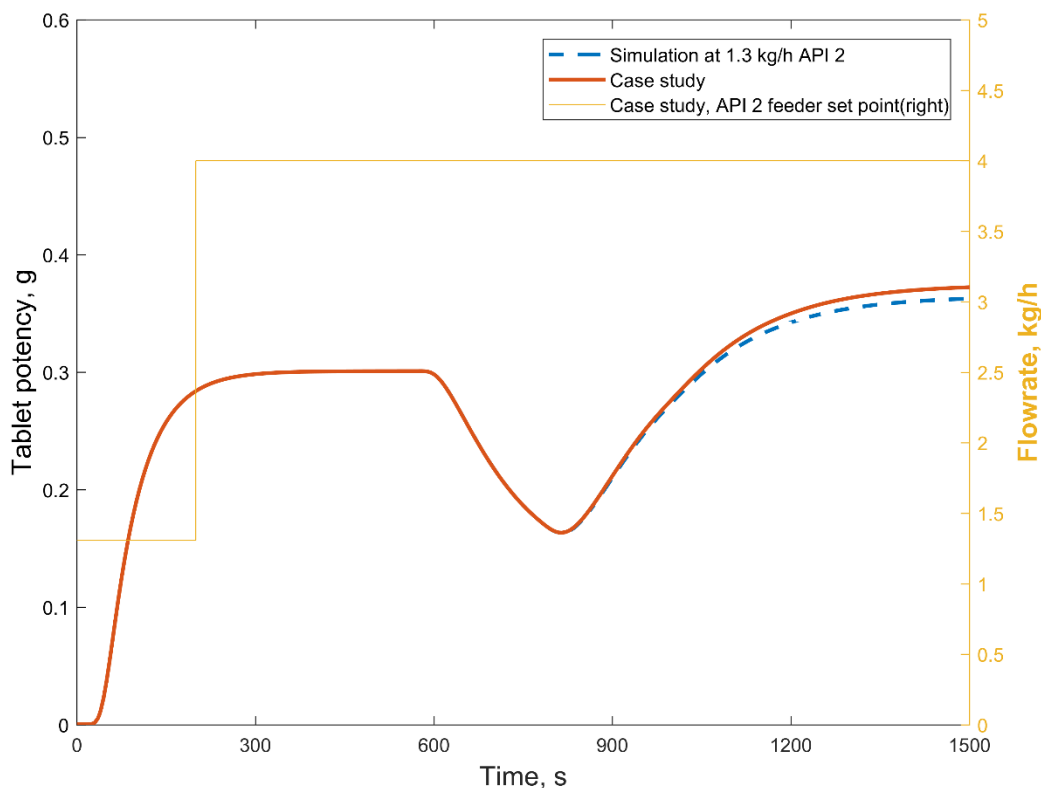


Figure 6.13 Comparison of tablet potency profiles from simulations with fixed and step change in API 2 feeder flow rate

6.4.2 Step change in dryer air temperature

In case study 2, a step change from 40 deg C to 50 deg C is made to the dryer air temperature. The step change is made at 455 s as shown in Figure 6.14 (right axis). At 455 s, filling, drying and emptying of the first cell is completed. In the second dryer cell, filling is completed and drying is in progress. In the third dryer cell, filling and drying are in progress. Profiles of dried granule moisture content from the simulation explained in Section 6.3 along with this case study is also plotted in Figure 6.14.

It can be observed that the dried granule moisture content from the first dryer cell is same in both cases as the step change occurs after emptying the first cell. In the second cell, dried granule

moisture content is lower in the case where the step change is imposed. This is because granules in this cell are exposed to a higher air temperature for a duration of 175 s ($180 \times 1 + 450 - 455$) which leads to a lower granule moisture content. In the third cell, dried granule moisture content is further lowered as drying at 50 deg C occurs for a longer duration of 355 s ($180 \times 2 + 450 - 455$). In the fourth cell, the moisture content is further lowered to a steady state value as all the granules are dried at 50 deg C.

Figure 6.15 shows propagation of LOD for both cases in the feed frame, which is the result of profile changes in the dryer and subsequent mill, feeder and blender units. It can be seen that the profiles follow the same path until about 750 s, after which a lower steady state value is reached for the case where step change to a higher air temperature occurs. The effect of difference in LOD profiles is also reflected in the tablet hardness as shown in Figure 6.16. Thus, implementation of the flowsheet model allows analysis of effects of such dynamic changes made to an upstream process variable on the final product quality of interest.

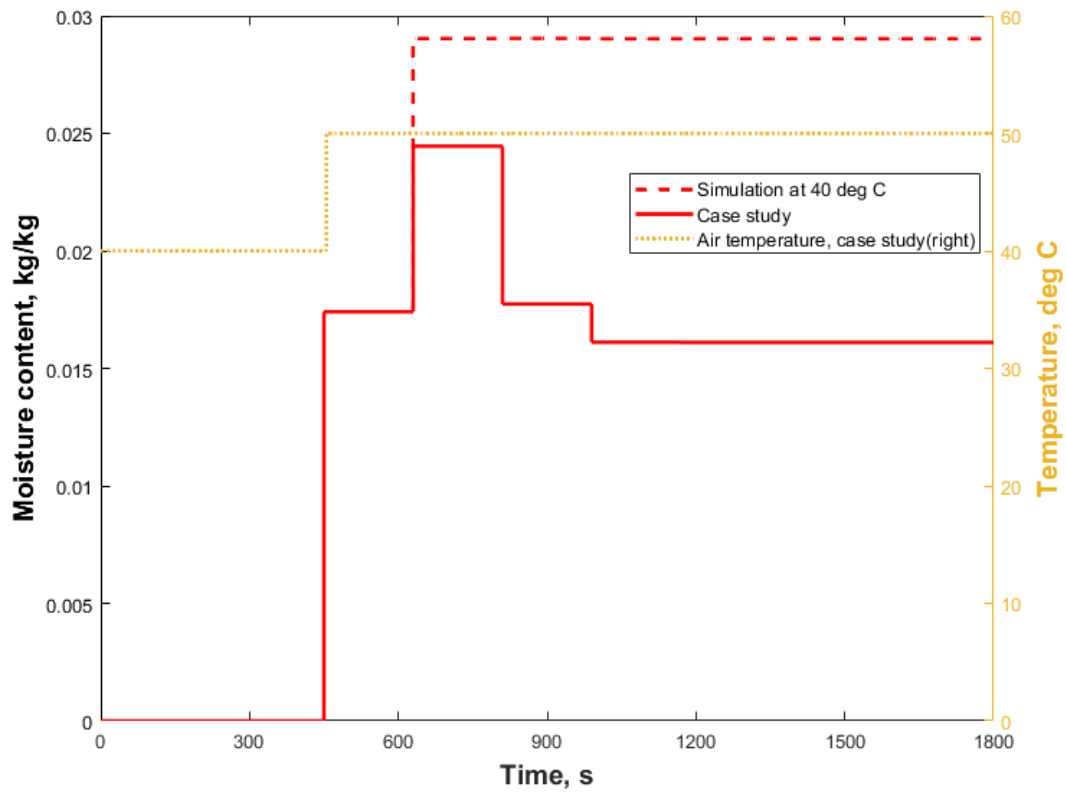


Figure 6.14 Comparison of dried granule moisture content profiles from simulations with fixed and step change in dryer air temperature

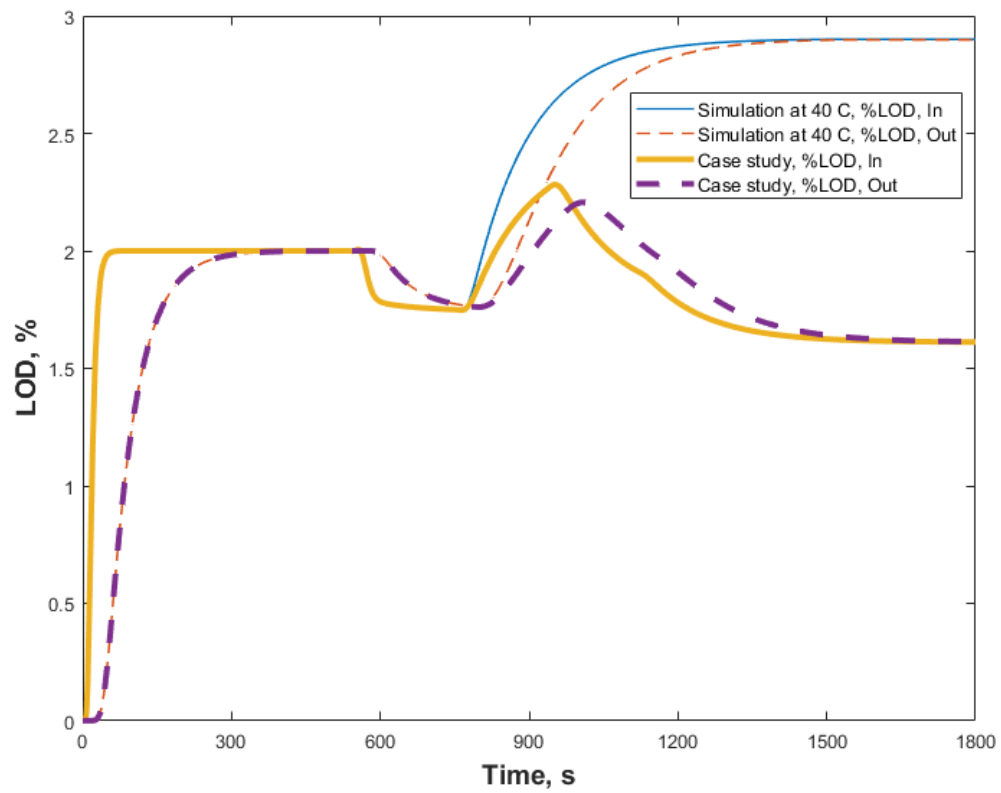


Figure 6.15 Comparison of moisture content of granules entering and leaving the feed frame from simulations with fixed and step change in dryer air temperature

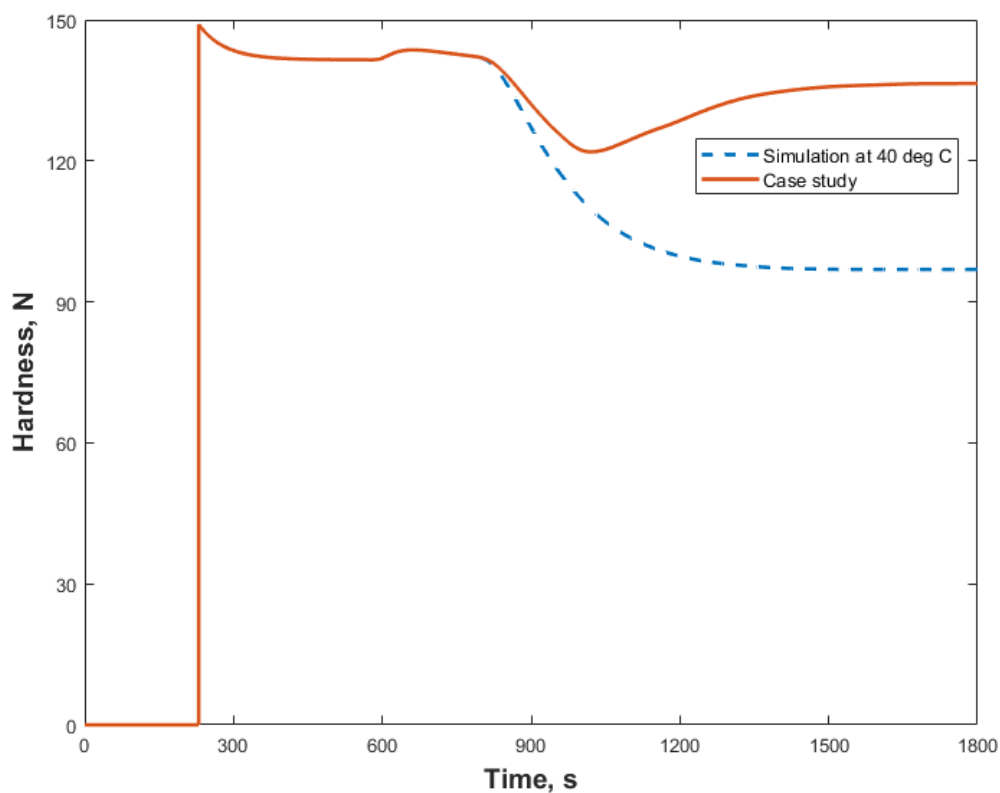


Figure 6.16 Comparison of tablet hardness profiles from simulations with fixed and step change in dryer air temperature

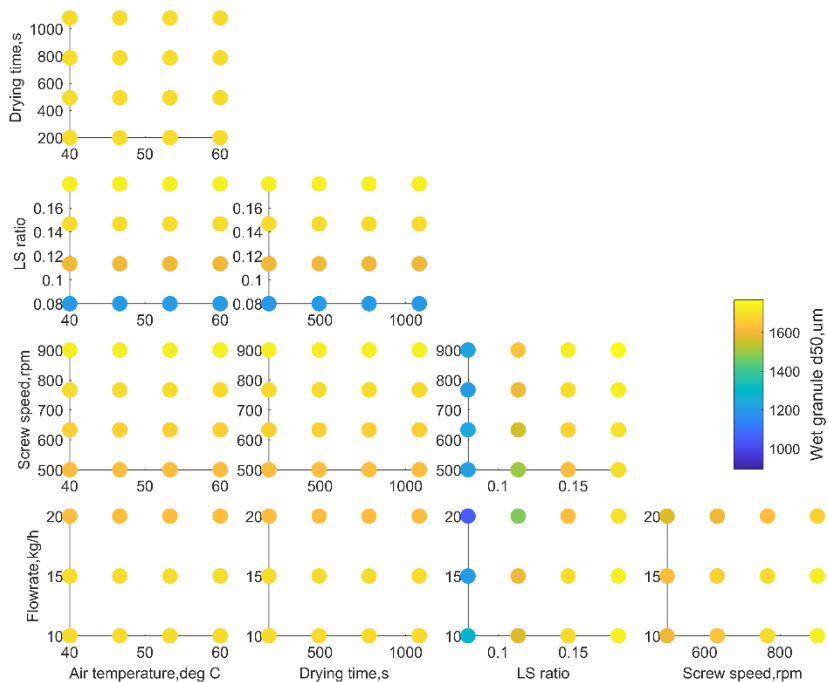
6.5 Scenario analysis of the integrated model

The adapted flowsheet model as shown in Figure 6.4 was used to implement a scenario analysis as explained in Section 6.2.2. Scenario analysis entails running the flowsheet model at various process setting values. It serves as a useful step before running a more computationally demanding sensitivity analysis. The flowsheet model is developed and errors are typically debugged at fixed values of process settings. However, this masks errors that may occur at other process setting values and does not provide confidence that the flowsheet model can run seamlessly. Debugging model errors at this stage before running more expensive analyses such as variance based sensitivity

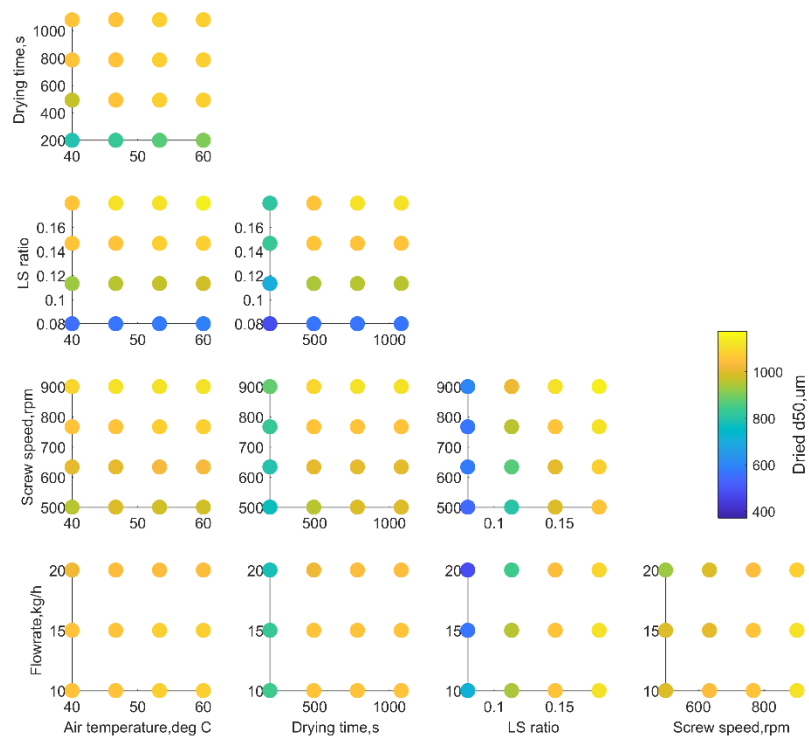
analysis serves as an effective modeling practice. Total flow rate, LS ratio, granulator screw speed, dryer air temperature and drying time as tabulated in Table 4 are the input factors considered for scenario analysis. A total of 768 simulations from three levels of total flow rate, four levels each for LS ratio, granulator screw speed, dryer air temperature, drying time ($3 \times 4 \times 4 \times 4 \times 4 = 768$) were successfully run. Process responses from blender, granulator, mill, dryer and tablet press models as given in Table 6.4 were recorded at the end of each simulation. For brevity, only few process responses are discussed in this section.

Specifically, wet granule d50, dry granule d50, dry granule LOD and tablet hardness are plotted and discussed. Since, this is a multivariate analysis (five variables) plotting and analyzing responses from simultaneous change in all the variables is not possible. Hence, a matrix of plots as shown in Figure 6.17 are used. The matrix consists of 10 plots, each of which shows process response plots from varying two distinct factors with the three other factors fixed at baseline values. Figure 6.17a can be used to visualize and understand the effect of the five variables on wet granule d50. It can be observed that wet granule d50 increases with LS ratio and screw speed, and decreases with flow rate. This is in accordance with the experimental data used for granulator model development [191]. Figure 6.17b and c can be used to understand effects on dry granule size and moisture content respectively. Figure 6.17c shows that moisture content decreases with drying time which is an expected phenomenon. Figure 6.17b shows that dry granule size increases with LS ratio, screw speed, drying time and air temperature, and decreases with flow rate. This is in accordance with experiments used for dryer model development [193]. Drying is expected to increase granule strength and lower breakage rate, which leads to a larger size. Hence, increase in drying time and air temperature increases granule size. The effect of flow rate, LS ratio and screw speed on the dry granule size is due to the propagation of effects of these variables on the size of the wet granule feed to the dryer. Similarly, the effect of changes in the variables on tablet hardness is plotted in Figure 6.17d. It can be observed that low drying time leads to tablets with very low hardness. In

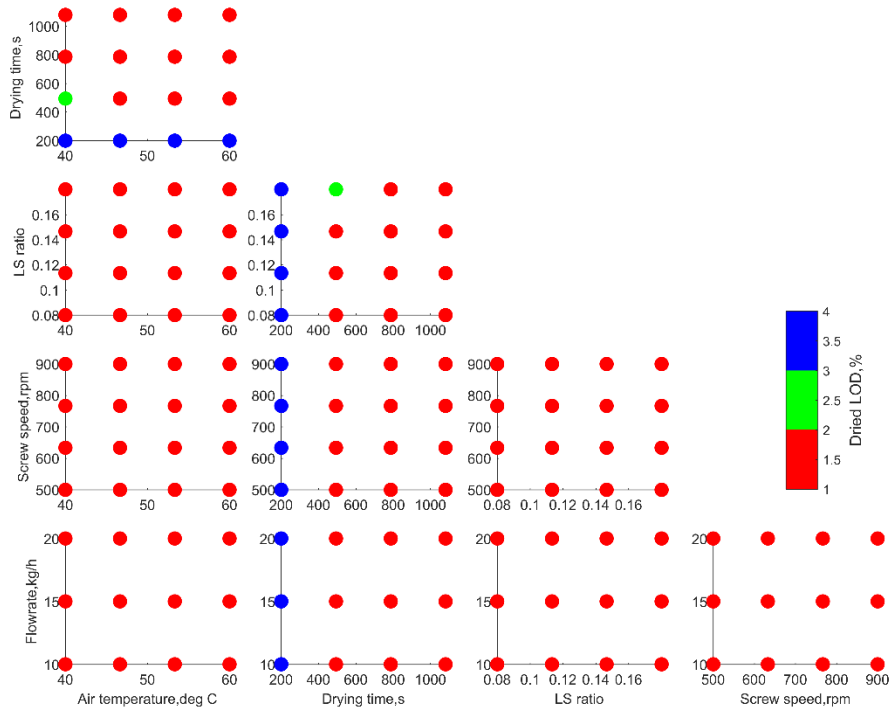
other words, granules with high moisture content cannot be used to make tablets. This is in accordance with process knowledge as gained from experiments. It is also worth noting that development of a flowsheet model has enabled study of the effect of change in a process variable in an upstream unit on the final product quality.



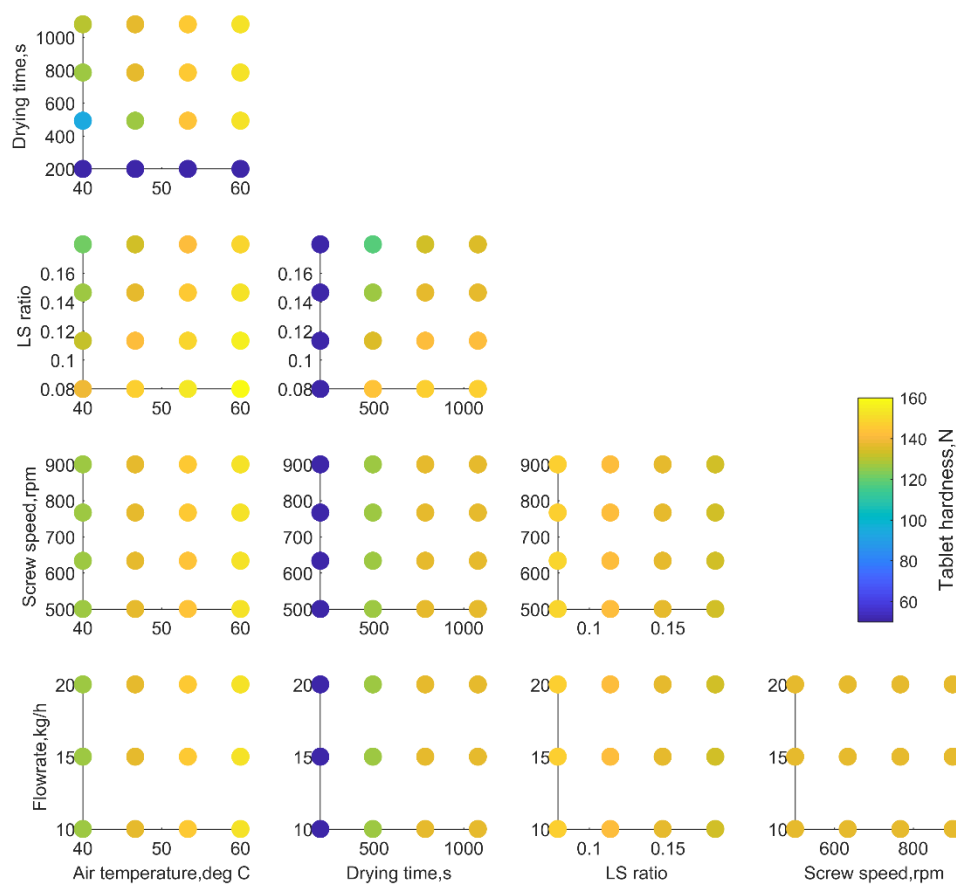
(a)



(b)



(c)



(d)

Figure 6.17 Scenario analysis plots for (a) wet granule d50 (b) dry granule d50 (c) dry granule LOD (d) tablet hardness

6.6 Sensitivity analysis of the integrated model

Sensitivity analysis was conducted using the adapted flowsheet model as explained in Section 6.2.2 and using five input factors, flow rate, LS ratio, granulator screw speed, dryer air temperature and drying time. The effect of these input factors on 20 model responses are studied. The list of factors and responses, ranges for the factors are tabulated in Table 6.4. The input factors are considered to

vary uniformly within these ranges. Morris analysis is implemented using 120 samples ($=20*(5+1)$). The results of the analysis are shown in Table 6.6 that lists the metrics μ , μ^* and σ . From the metrics, we observe that LS ratio influences wet granule moisture content, which is expected. Wet granule size is influenced by all three granulator process variables. This finding conforms with experiments that show effect of these variables on granulation rate [190]. For the dryer model outputs, flow rate and granulator screw speed do not show influence on dry granule moisture content and all five input factors show influence on dry granule size and dry granule properties (bulk density, tapped density and angle of repose). For the mill model outputs, LS ratio shows the most influence on milled granule size, bulk and tapped density. This is due to effect of LS ratio on size distribution of feed to the mill. The tablet press variables, main compression height and fill depth, are shown to be most influenced by air temperature, drying time and LS ratio. This is due to the effect of all these factors on the granule moisture content as granules with LOD higher than 3% cannot be used to make tablets. Thus, these factors also show an effect on tablet hardness.

Table 6.6 Morris method sensitivity analysis results

Granulator												
Output →	d10, μm			d50, μm			d90, μm			Moisture, kg/kg		
Input ↓	μ	μ^*	σ	μ	μ^*	σ	μ	μ^*	σ	μ	μ^*	σ
Air temperature	0.11	0.21	0.30	0.52	0.87	1.29	0.98	1.77	2.59	0.00	0.00	0.00
Drying time	0.10	0.22	0.37	0.34	0.80	1.26	0.64	1.51	2.39	0.00	0.00	0.00
LS ratio	407.42	407.42	103.79	458.99	458.99	246.00	656.49	656.49	296.79	0.08	0.08	0.02
Screw speed	37.45	37.45	14.53	127.43	127.43	70.74	115.23	121.95	111.01	0.00	0.00	0.00
Flow rate	-35.49	38.10	28.06	-145.43	148.57	138.75	-148.87	154.33	136.70	0.00	0.00	0.00

Dryer												
Output →	d10, μm			d50, μm			d90, μm			Moisture, %		
Input ↓	μ	μ^*	σ	μ	μ^*	σ	μ	μ^*	σ	μ	μ^*	σ
Air temperature	17.30	17.39	17.79	81.69	82.11	55.76	139.08	139.79	103.01	-2.01	2.01	1.64
Drying time	22.77	22.94	36.96	101.87	102.56	139.46	182.81	184.14	243.99	-2.77	2.77	3.50
LS ratio	273.71	273.71	81.03	410.60	410.60	206.75	307.38	326.94	200.84	1.50	1.50	1.93
Screw speed	18.03	18.03	7.37	121.74	121.74	53.72	86.86	86.86	48.09	0.00	0.00	0.00
Flow rate	-22.44	22.44	11.43	-109.86	115.99	99.38	-102.19	114.15	96.78	0.00	0.00	0.00

Output →	Bulk Density, Kg/m^3			Tapped Density, Kg/m^3			Angle of Repose, deg		
Input ↓	μ	μ^*	σ	μ	μ^*	σ	μ	μ^*	σ
Air temperature	-6.19	6.24	5.89	-4.75	4.78	4.53	0.79	0.80	0.62
Drying time	-8.30	8.33	12.12	-6.21	6.23	8.76	1.07	1.08	1.50
LS ratio	16.70	16.70	11.80	11.25	11.39	8.56	1.17	1.43	1.20
Screw speed	-14.25	14.25	5.73	-12.32	12.32	4.64	0.85	0.85	0.40
Flow rate	4.53	6.99	7.71	3.82	5.23	5.57	-0.63	0.80	0.76

Mill												
Output →	d10, μm			d50, μm			d90, μm			Span		
Input ↓	μ	μ^*	σ	μ	μ^*	σ	μ	μ^*	σ	μ	μ^*	σ
Air temperature	4.81	4.81	5.06	7.94	7.96	5.06	8.76	8.80	6.68	-0.02	0.02	0.01
Drying time	6.50	6.56	10.44	9.45	9.52	12.07	11.21	11.27	13.85	-0.02	0.02	0.03
LS ratio	146.63	146.63	46.95	252.14	252.14	68.84	83.55	83.55	31.47	-0.96	0.96	0.29
Screw speed	3.38	3.68	3.56	3.16	9.13	10.91	16.16	16.53	10.26	0.01	0.03	0.03
Flow rate	-7.63	8.39	8.91	-8.83	13.65	12.13	-16.54	19.73	23.27	0.01	0.05	0.06

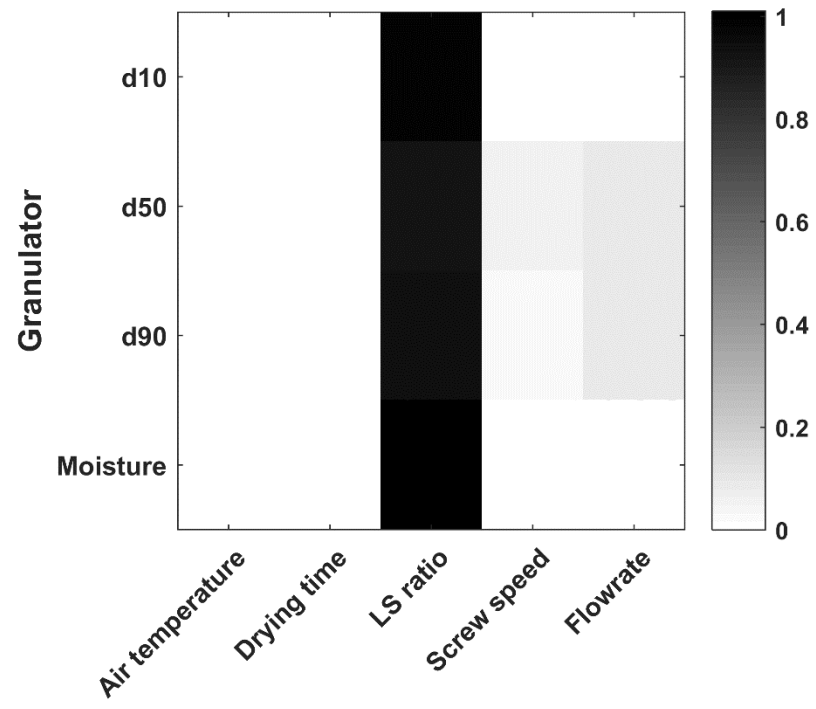
Output →	Bulk Density, Kg/m^3			Tapped Density, Kg/m^3		
Input ↓	μ	μ^*	σ	μ	μ^*	σ
Air temperature	4.93	4.93	3.24	4.09	4.09	2.54
Drying time	5.34	5.39	6.93	4.33	4.38	5.59
LS ratio	237.08	237.08	62.79	236.53	236.53	57.64
Screw speed	1.76	5.14	8.27	-16.09	17.69	14.84
Flow rate	-13.81	13.81	5.26	-8.02	12.52	14.14

Output →	Hardness, N			Potency, g			Compression Height, mm			Fill Depth, mm		
Input ↓	μ	μ^*	σ	μ	μ^*	σ	μ	μ^*	σ	μ	μ^*	σ
Air temperature	28.85	28.85	38.87	0.00	0.00	0.00	0.37	0.37	1.67	0.85	0.96	4.05
Drying time	84.89	84.89	100.13	0.00	0.00	0.00	2.62	2.62	3.71	4.57	4.63	6.83
LS ratio	-21.40	21.40	38.55	0.00	0.00	0.00	-0.37	0.37	1.67	-3.83	3.83	4.10
Screw speed	0.01	0.27	0.41	0.00	0.00	0.00	0.00	0.00	0.00	-0.02	0.14	0.24
Flow rate	0.06	0.49	0.66	0.00	0.00	0.00	0.00	0.00	0.00	0.22	0.22	0.21

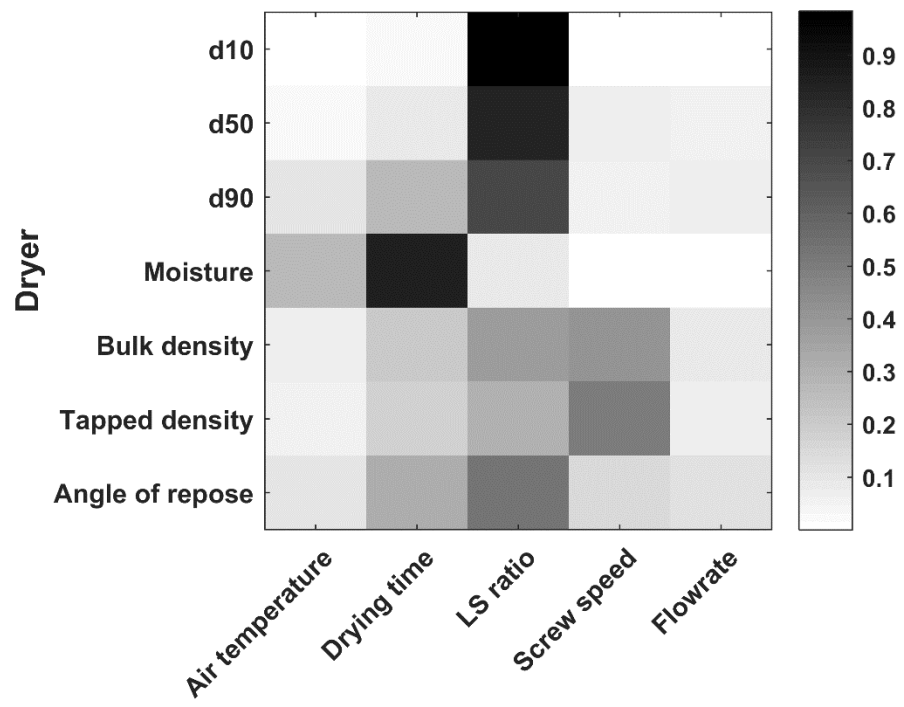
Output →	Time Constant, s			Number of Tanks			Steady State Holdup, kg		
Input ↓	μ	μ^*	σ	μ	μ^*	σ	μ	μ^*	σ
Air temperature	0.00	0.00	0.00	0.00	0.00	0.00	0.00	0.00	0.00
Drying time	0.00	0.00	0.00	0.00	0.00	0.00	0.00	0.00	0.00
LS ratio	-0.00	0.00	0.00	0.00	0.00	0.00	0.00	0.00	0.00
Screw speed	0.00	0.00	0.00	0.00	0.00	0.00	0.00	0.00	0.00
Flow rate	-15.53	15.53	3.68	-0.15	0.15	0.07	0.03	0.03	0.01

From Morris analysis, dryer air temperature, drying time and LS ratio are identified as the significant factors that influence tablet properties. Variance based analysis as explained in Section 6.2.3.2 can be applied to this subset of factors to obtain a quantitative understanding of their influence. However, for this work, variance based sensitivity analysis is performed using all five factors and compared to results obtained from Morris method. The analysis was implemented using 3500 (=500*(5+2)) samples. Here, only the total sensitivity indices, S_{Ti} are pictorially represented in Figure 6.18 as the first order effects S_i are close to S_{Ti} for responses from granulator, dryer, mill and blender units. The responses from tablet press show interactions for the factors air temperature, drying time and LS ratio. Generally speaking, findings from variance based sensitivity analysis agree with the findings from Morris analysis. The variance based method identified LS ratio as a significant factor for granulator. All five factors were identified as significant for dryer. LS ratio showed most influence for mill. All of these findings align with conclusions obtained from implementing Morris analysis. For tablet press, air temperature, drying time and LS ratio were identified as significant factors that influence tablet hardness, main compression height and fill

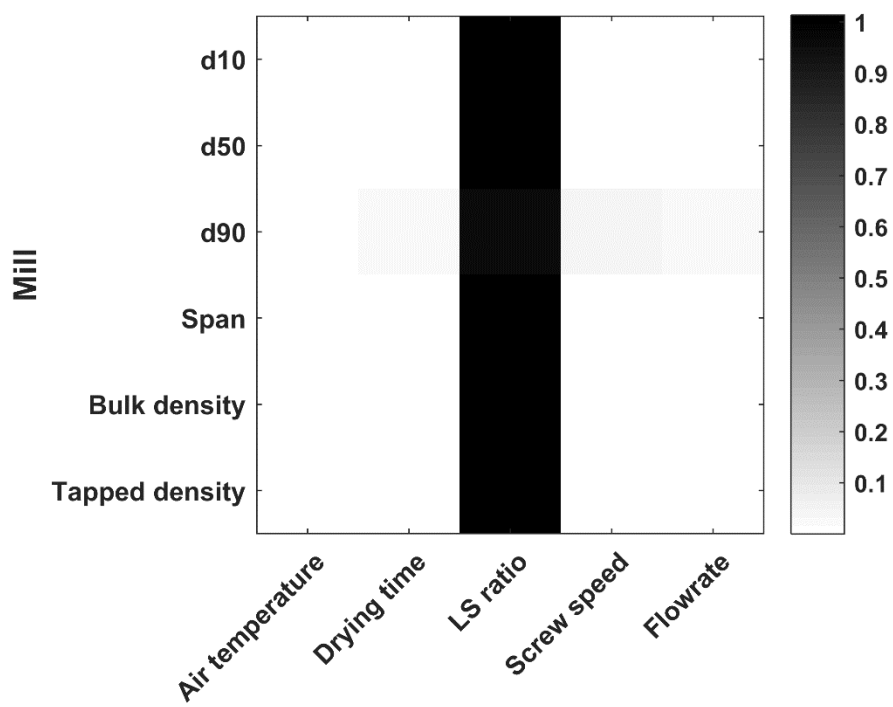
depth. In addition, all five factors were identified as significant for tablet potency. The influence of these factors on tablet potency was not observed from Morris analysis. This is because, in Morris analysis, the metrics are not dimensionless. For example, the metrics have a unit of g for tablet potency. Hence, any factor that shows an effect less than 0.01 g was identified as insignificant for Morris analysis. However, in variance based analysis, the metrics are dimensionless and the effect of various factors on the responses are normalized. A potency difference in the order of $1\text{e-}6\text{ g}$ is also accurately identified in the sensitivity indices. Overall, both Morris and Variance-based methods serve in identifying critical factors. While, the Morris method requires fewer samples and allows ranking the factors by the order of influence, it does not provide quantitative information on relative effects of the factors. On the other hand, variance based analysis requires much higher number of samples but can provide detailed and quantitative information on the relative effects of the factors. It is also important to note here that the factors shown as influential per the sensitivity analysis metrics is a direct result of the process models used. Hence, any assumptions and deficiencies in the model are also carried to the sensitivity analysis. Results from sensitivity analysis should thus be carefully scrutinized in conjunction with process knowledge in order to avoid drawing incorrect conclusions.



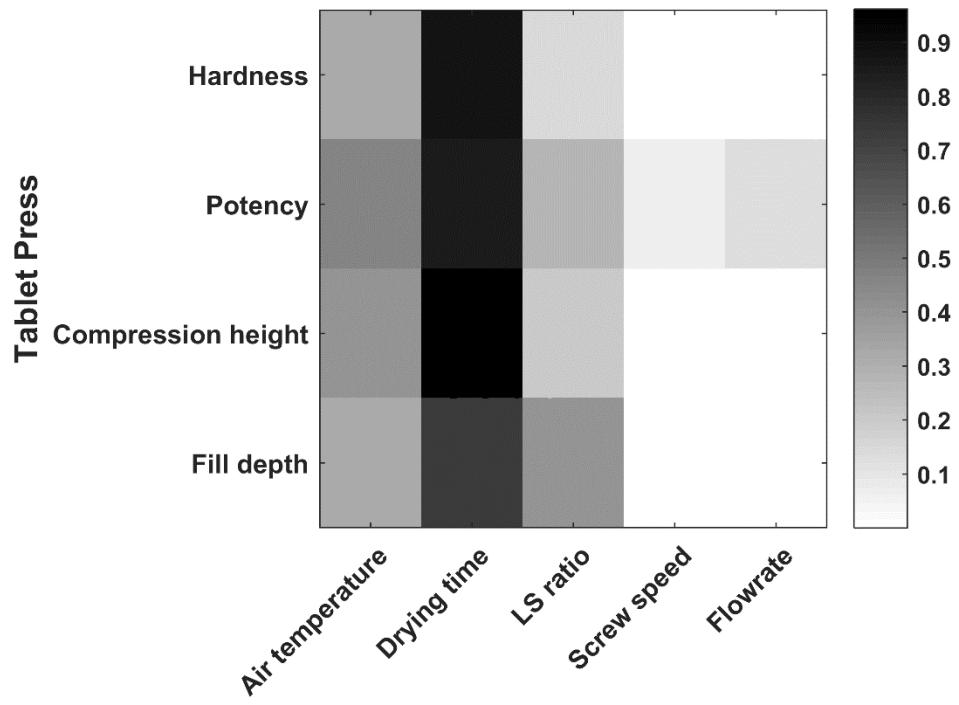
(a)



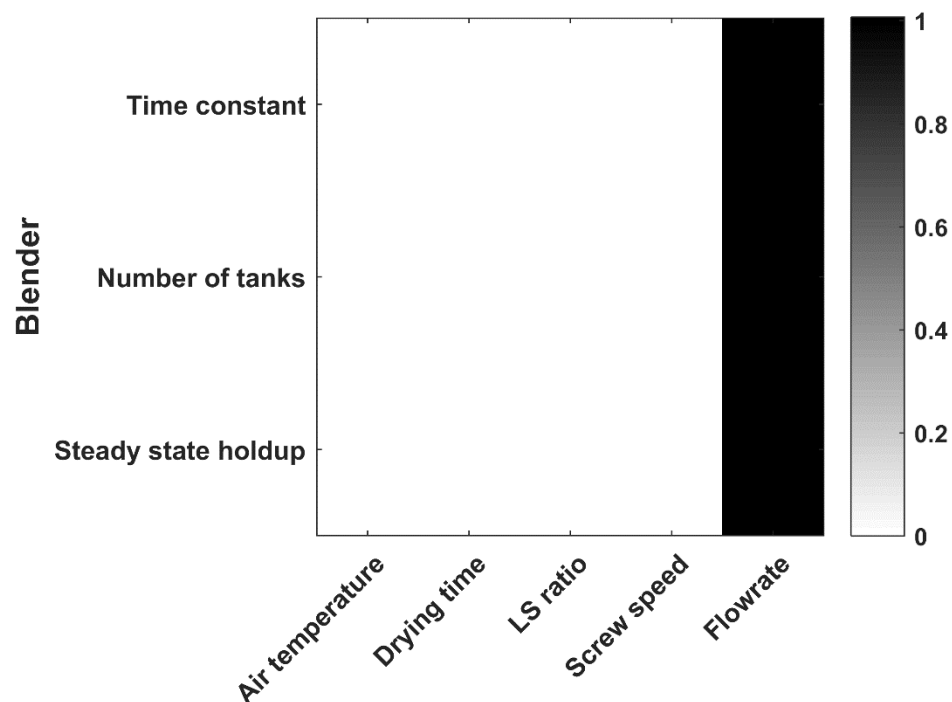
(b)



(c)



(d)



(e)

Figure 6.18 Total sensitivity index S_{Ti} plots for (a) Granulator (b) Dryer (c) Mill (d) Tablet press (e) Blender

6.7 Summary

In this work, a flowsheet model that approximates the ConsiGma™-25 line for continuous tablet manufacturing through the wet granulation route is developed. The flowsheet model is based on models that are developed from experimental runs on units included in the continuous line using the same formulation and materials. For a complete virtual representation of the continuous line, models for intermediate units (powder blend feeder, granule feeder and granule blender) as well as transfer lines are also included in the flowsheet model. The developed model successfully

demonstrates its ability to simulate the effect of changes in the process variables through case studies where step changes in API flow rate and dryer air temperature are implemented and their effect on final tablet properties is understood. Robustness of the developed model is established by systematically running the flowsheet model at several combinations of process settings and analyzing the corresponding process responses. The model is also used to identify critical process variables that affect intermediate and final product quality.

Throughout this article, several applications and capabilities of the developed flowsheet model have already been alluded to in the discussion. However, it is also worth noting some gaps in the developed model which helps throw light on areas where future research efforts can be focused on. For instance, the developed flowsheet model is computationally expensive. A simulation of about 1600 s takes approximately 4 h. While a simplified model is adapted in this work to implement steady state sensitivity analysis, it is not feasible to run dynamic sensitivity analysis using this model. Other areas of improvement include further development of the unit operation models. The blender model currently used predicts only 10%, 50% and 90% percentile diameters for the powder blend. However, a much higher resolution PSD is required in the granulator model. In addition, the granulator model predicts only steady state PSD output based on process setting values. For the dryer model used in this work, drying behavior is based on input material properties at the start of drying cycle of cell. This could be further improved by incorporating dynamic modeling of drying behavior. For the mill model, the model parameters used currently are not a function of drying time in the fluid bed dryer. In addition, some of the submodels for unit operations use empirical relationships which are formulation-specific. Another valuable verification of the model would be to check the mass balance over the entire system. The approximation of the axial dispersion models modeling the material flow propagation could thus be achieved. As research efforts continue on improving the unit operation models, the flowsheet model in its current state has already shown to be a useful tool in enhancing process understanding and enabling better decision making.

Overall, the developed flowsheet model is a prerequisite for identification of design space and optimization of the continuous line. Future research efforts should be focused on reducing computational expense of the model as well as improving capability of the unit models to capture dynamics as well as their applicability for other formulations suited for continuous solid oral dosage manufacturing.

Chapter 7

Design space identification of continuous pharmaceutical manufacturing processes

7.1 Background

Feasibility is the ability of a process to satisfy all production, operating, safety and quality constraints. Process models for manufacturing processes can be used to identify the feasible region i.e., the multivariate combination of CPPs and CMAs that satisfy the process and product constraints. During the past decade, the need to develop predictive models for complex processes accompanied by advances in computational capabilities has led to the evolution of higher fidelity models, which incur high computational cost. Traditional feasibility analysis methods [96, 97, 99, 100] cannot be applied to these models as they require high number of function calls which is prohibitive for such models. In addition, the constraints are not available in closed-form or function derivatives are difficult to evaluate. Surrogate based methods have gained prominence to address problems of such nature. In this class of methods, a surrogate model is used to approximate the computationally expensive model for identifying the feasible region. Banerjee, Pal [101] used a HDMR surrogate model to approximate the original model and used the computationally inexpensive surrogate to identify the feasible region. Kucherenko, Giamalakis [102] used HDMR as a metamodel to represent the design space in case of uncertainty in model parameters. Rogers and Ierapetritou [103] used kriging as the surrogate model to approximate the original function for identifying disjoint and nonconvex feasible regions with limited sampling. Wang and Ierapetritou [104] used RBF surrogate model which performed comparable to kriging surrogate model. In some of these approaches, an adaptive sampling methodology is used, where samples are identified in regions that are of high interest such as regions where the surrogate model prediction errors are

high or regions that are expected to be feasible. However, these approaches showed limitations or did not illustrate examples in identifying feasible regions in high dimensional problems.

In this work, we propose a surrogate based feasibility analysis method where an Artificial Neural Network (ANN) is used as the surrogate model to address problems that are computationally expensive or do not have constraints in closed form. Owing to their function approximation, classification and pattern recognition properties, ANNs have attracted attention in several fields such as chemical engineering [202, 203] biochemical engineering [204] to optimize processes, and pharmaceutical research [205]. For ANN applications related to process optimization, ANN is used as the surrogate model to approximate the original process model or the objective function and the developed surrogate model is used for subsequent optimization [206, 207]. In this work, we propose to use ANN as the surrogate model to approximate the feasibility function, which is a characterization of constraint violation or infeasibility in a problem. An adaptive sampling methodology is used. The goal of adaptive sampling in this work is to improve accuracy of the surrogate model that represents the feasible region while limiting the number of samples required to achieve this. Adaptive sampling in feasibility analysis problems entails identification of samples in regions of high surrogate model prediction variance or regions close to the feasible region boundary. In this work, the prediction error of the surrogate model is estimated using a statistical technique known as jack-knifing [208]. The identification of samples in the regions of interest is achieved by maximizing a modified expected improvement function proposed by Boukouvala and Ierapetritou [209]. The neural network based feasibility analysis method thus developed shows better performance compared to previously published kriging based method [103] for low as well as high dimensional problems.

In the following sections, the mathematical foundation and formulation of the surrogate based feasibility analysis method is described in Section 7.2. Following this, the feasibility analysis

methodology based on surrogate models used in this work, namely Kriging and Artificial Neural Networks are described in Sections 7.2.1 and 7.2.2 respectively. Section 7.3 illustrates implementation of the methodology in several low and high dimensional test problems. The implementation of the methodology on pharmaceutical manufacturing processes are then described in Sections 7.4 and 7.5.

7.2 Feasibility analysis methodology

The concept of process flexibility was introduced to have mathematical foundation for incorporating operability considerations at design stage [94]. For a process with design variables d , control variables z , and uncertain parameters θ , the constraints that represent feasible operation can be expressed as Equation 7.1.

$$g_j(d, z, \theta) \leq 0, \quad j \in J \quad 7.1$$

Feasibility of operation of a design d , operating at given values of uncertain parameters θ is determined by establishing whether proper adjustment of control variables z allows each inequality given by Equation 7.1 to hold. The control variable z is adjusted to maximize the largest value of g , which can be formulated as Equation 7.2, where ψ is defined as the feasibility function. If $\psi < 0$, the design is feasible for the given values of θ . If $\psi > 0$, that means any value of the control variable z cannot bring the process to a feasible operation. If $\psi = 0$, this indicates the process is at the boundary of feasible and infeasible operation.

$$\psi(d, \theta) = \min_z \max_{j \in J} g_j(d, z, \theta) \quad 7.2$$

The flexibility test problem uses this mathematical foundation to determine if a process is feasible for all possible values of θ , which is equivalent to checking if $\psi \leq 0$ for all values of θ . In mathematical terms, this is formulated as Equation 7.3 where χ is defined as the flexibility function. The flexibility test problem only determines whether a process is feasible or infeasible, and does not give a quantitative measure of feasibility, or information on the region where operation is feasible. In this work, our goal is to identify the feasible region i.e., given bounds on we need to identify the region of θ where the process is feasible ($\psi \leq 0$).

$$\chi(d) = \max_{\theta} \psi(d, \theta) = \max_{\theta} \min_z \max_{j \in J} g_j(d, z, \theta) \quad 7.3$$

If control variables are not considered, the feasibility function in Equation 7.2 is reformulated as Equation 7.4.

$$\psi(d, \theta) = \max_{j \in J} g_j(d, \theta) \quad 7.4$$

In cases where the constraints in the process model are black-box in nature or the process model is computationally expensive to run, surrogate based feasibility analysis methods are developed to fit an inexpensive surrogate model of the feasibility function. The sample points required to build the surrogate model need to be carefully chosen as the original model is expensive. Adaptive sampling strategies [172] are used to identify the samples that provide most useful information when building the surrogate model. At these sample points, the original process model is run, constraint violations are evaluated and the corresponding feasibility function value, which is the maximum of the constraint violation values, is used to update the surrogate model. In this work, a modified expected improvement function EI_{feas} [209] as given in Equation 7.5 is used to implement the adaptive

sampling strategy. Here, y and s are the surrogate model prediction and standard error of the prediction at x respectively.

$$EI_{feas}(x) = s \phi\left(-\frac{y}{s}\right) = s \frac{1}{\sqrt{2\pi}} e^{-0.5\left(\frac{y^2}{s^2}\right)} \quad 7.5$$

This function is modified from the EI function proposed by Jones, Schonlau [154] for surrogate based optimization problems. For surrogate based optimization problems, maximization of the EI function directs search towards the regions that are unexplored, which leads to regions of high uncertainty, or the regions where the surrogate model is minimized. Samples from these regions are used to improve the surrogate model accuracy, with the improvement focused towards identifying the optimum value. The modified EI function (EI_{feas}) has similar properties such that maximization of EI_{feas} identifies sample points close to the feasible region boundary or in the region of high prediction uncertainty. In this case, addition of these samples leads to higher accuracy of the surrogate model, with improvement focused towards identification of feasible regions. In the following sections, the surrogate modeling methods used in this work are explained, and their implementation in the feasibility analysis methodology is elucidated.

7.2.1 Kriging based feasibility analysis

Kriging also referred to as gaussian process regression [210] or stochastic process model [154] is a popular interpolating surrogate model used in several applications. An attractive feature of kriging model is an estimate of the model prediction error is inherently provided by the model. This is a useful feature in the implementation of adaptive sampling strategies as seen in optimization literature [211]. In Kriging, the predictor at an untested sample point is modeled as a function of process responses at previously tested points or design points. The kriging model prediction $\hat{f}(x^i)$ for a d dimensional input x^i is given as a realization of a regression model $\hat{\mu}(x^i)$ and an error term

$\hat{\varepsilon}(x^i)$ as given in Equation 7.6. Here, $\hat{\mu}(x^i) = \sum_p \beta_p g_p(x^i)$ i.e., a linear combination of p basis functions and represents the mean of process responses. The regression term takes the form of a polynomial, typically constant, linear or quadratic. The error ε is a deviation from the mean process response and is represented by a Gaussian process with zero mean and covariance $\sigma^2 \mathbf{R}(\theta, x^{(i)}, x^{(j)})$ between $\varepsilon(x^{(i)})$, $\varepsilon(x^{(j)})$ where \mathbf{R} is the correlation model.

$$\hat{f}(x^i) = \hat{\mu}(x^i) + \hat{\varepsilon}(x^i) \quad 7.6$$

The correlation model \mathbf{R} indicates that the errors in the predicted values are correlated as a function of the input variables. Several correlation models are available and used in literature [153]. In this work, linear, exponential or gaussian correlation models are considered as they have been successfully applied in previously published kriging based feasibility analysis methods [103]. The kriging model structure i.e., the order and type of regression and correlation model are chosen in the initial model building phase. In this phase, the domain is sampled using a space-filling design such as grid sampling or latin hypercube sampling. Several Kriging models are fit with the combinations of regression and correlation models. The mean squared error (MSE) between predicted data and target data for each kriging model is computed. The model structure corresponding to the kriging model that yields the least MSE is chosen. In this work, Kriging implemented in Design and Analysis of computer Experiment (DACE) [212], is used. Overall, the kriging-based feasibility analysis algorithm is depicted in Figure 7.2. Performance of the kriging-based feasibility analysis methodology is compared to the proposed ANN based methodology which is explained in the next section.

7.2.2 Artificial neural networks based feasibility analysis

ANNs constitute input and output variables as neurons that are connected using hidden neurons or nodes arranged in layers. An illustration of an ANN with one input layer, one hidden layer and one output layer is shown in Figure 7.1. The architecture given in the figure has three input neurons (represented as yellow circles), four neurons (represented as blue circles) in the hidden layer and one neuron in the output layer (represented as the green circle). In ANN, a neuron is weighed, and the weighted values are sent to neurons in the succeeding layer. In addition, a bias is applied with a constant weight of 1 (represented by yellow and blue squares) and sent to neurons in the succeeding layer. All the inputs to a neuron in the succeeding layer are summed and a transfer function is applied, the result of which is weighed again and sent to the next layer. To build an ANN as a function approximator, the weights and biases are estimated such that a cost function, which constitutes differences between ANN predictions and target values, is minimized. In this work, a feed-forward neural network trained with back propagation algorithm is used [213]. One input layer, one hidden layer and one output layer are used, as a single hidden layer feed-forward ANN is known to be good function approximator provided sufficient number of neurons in the hidden layer, also known as hidden neurons are used [214]. The number of hidden neurons is a variable to be determined in the network structure. Higher number of neurons may lead to overfitting issues. Overfitting of the network parameters are generally avoided using methods such as early stopping and Bayesian regularization [215]. Early stopping requires the dataset to be divided into training, validation and testing sets. The training of network parameters is stopped based on model prediction performance on the training and validation dataset. In Bayesian regularization, the cost function includes a penalty term for high weights and does not require validation dataset to estimate optimum network parameter. In this work, Bayesian regularization is used as this reduces potential oscillatory behavior between samples and reduces overfitting issues.

The number of hidden neurons is determined in the initial model building phase. In an approach similar to choosing the regression and correlation models in the kriging-based methodology, the domain is sampled using a space-filling design such as grid sampling or Latin hypercube sampling. Several ANNs are built with varying number of hidden neurons. The mean squared error (MSE) between predicted data and target data for each ANN is computed. The number of hidden neurons corresponding to the neural network that yields the least MSE is chosen.

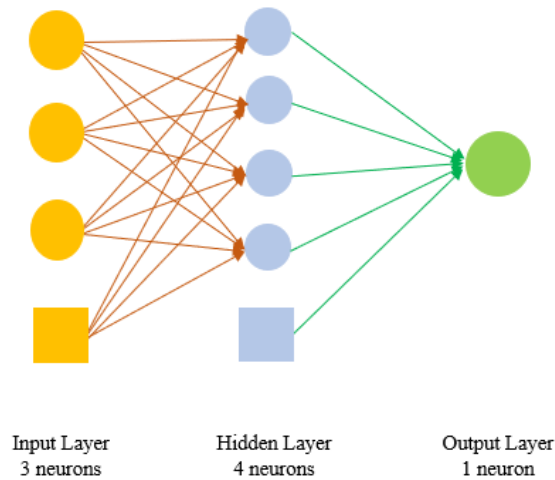


Figure 7.1 Schematic of a three-layer Artificial Neural Network

The implementation of feasibility analysis methodology includes maximization of the EI_{feas} function given in Equation 7.5. The standard error of ANN model prediction s needs to be estimated in order to implement the ANN based methodology. In this work, a statistical technique known as jack-knifing [208, 216] is used to estimate the variance σ of ANN model predictor y at a sample point x . The standard error s of the model predictor is then computed as $\sqrt{\sigma}$. Computation of the variance σ is achieved by creating subsamples of the parent sample set. Following are the steps to implement the jack-knifing method for ANN model prediction variance:

- Divide the sample set into K disjoint subsample sets of $1/K$ size each

- Leave out one subsample set each time and pool the remaining samples into a set. This leads to K disjoint sets
- Build K neural networks F_k ($k=1$ to K) using the K pooled disjoint sets
- Calculate variance of prediction from K neural networks

In mathematical terms, at a sample point x , if $U_k(x)$ is the predictor from the k^{th} ANN model, the variance of prediction is given by Equation 7.7.

$$\sigma(x) = \frac{1}{K} \sum_{k=1}^K \left(U_k(x) - \sum_{k=1}^K \frac{U_k(x)}{K} \right)^2 \quad 7.7$$

The standard error s of predictor needs to be scaled with respect to the model predictor y before it can be used in the EI_{feas} function. This is required to balance the magnitude of s compared to y . A similar scale factor has been used with a RBF based error prediction by Wang and Ierapetritou [104] which has resulted in successful function maximization for feasibility analysis problems. The scale factor is determined based on model fit to the initial sample set in the initial model building phase. If $n_{initial}$ is the initial number of samples chosen, U_0 is the predictor from the ANN model that is fit using the initial sample set and σ_0 is the variance of the prediction using jack-knifing, the scale factor δ is given by Equation 7.8:

$$\delta = \frac{\max(U_0)}{\max(\sigma_0)^{0.5} * n_{initial}} \quad 7.8$$

where $\max(U_0)$ is the maximum value of the initial model predictor, and $\max(\sigma_0)$ is the maximum value of the initial model prediction variance. The EI_{feas} function for the ANN based methodology uses the scaled value, $\delta s(x) = \delta \sqrt{\sigma(x)}$ instead of $s(x)$. The algorithm used for the implementation

of the proposed ANN based feasibility analysis is depicted in Figure 7.2. In order to evaluate the effectiveness of the ANN based feasibility analysis methodology, the feasible region predicted by the surrogate model could be visually compared to the actual feasible region. However, such visual evaluation is possible for two- or three-dimensional problems. For higher dimensional problems, visual representation of feasible regions is a challenge. Hence, for this work, we use performance of the surrogate model on untested data points as a means to quantify effectiveness of the methodology. Based on correct or incorrect identification of the untested sample points as feasible or infeasible, the accuracy of the kriging and ANN surrogate model can be evaluated and compared. Figure 7.3 is a two-dimensional hypothetical representation of various possibilities. Specifically, the untested sample points can belong to one of the following categories:

- Correctly identified feasible region (CF, dashed yellow): the sample is classified as feasible by the original model and feasible by the surrogate model as well
- Correctly identified infeasible region (CIF, white): the sample is classified as infeasible by the original model as well as the surrogate model
- Incorrectly identified feasible region (IC-F, yellow solid): the sample is classified as infeasible by the original model and feasible by the surrogate model.
- Incorrectly identified infeasible region (IC-IF, blue dashed): the sample is classified as feasible by the original model and infeasible by the surrogate model.

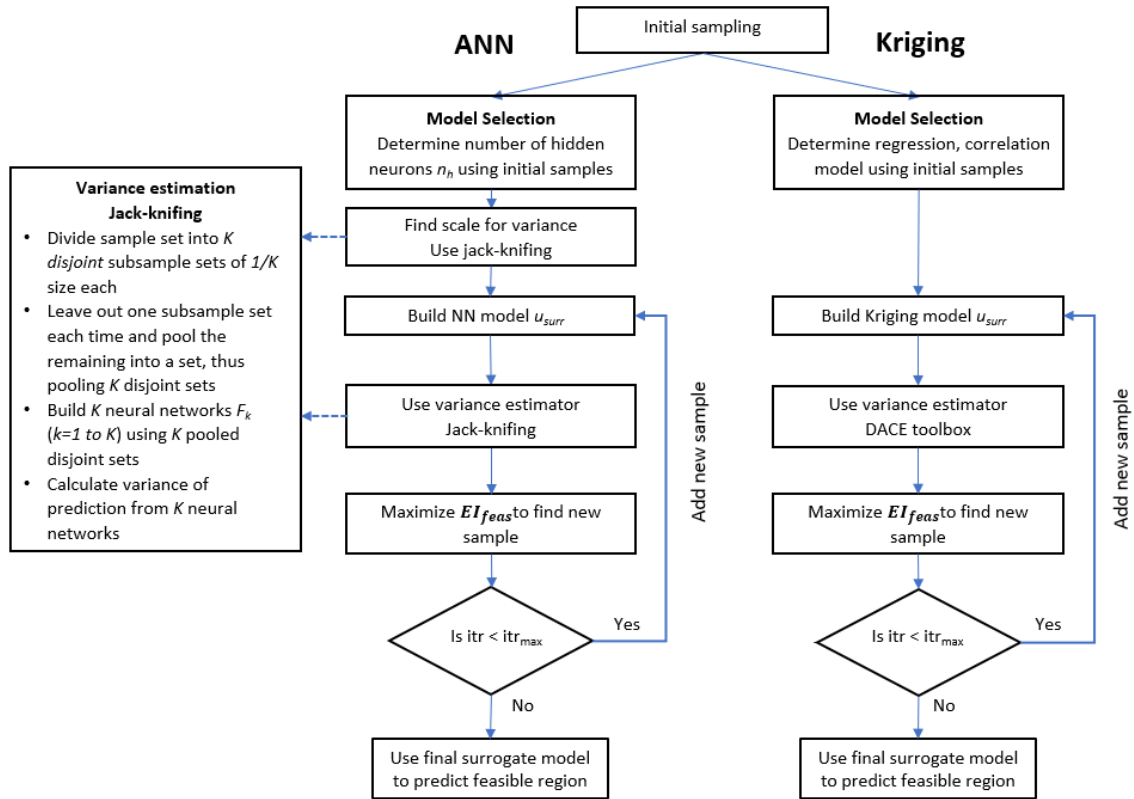


Figure 7.2 Algorithm for ANN and Kriging based feasibility analysis methodology

Based on the categories to which the untested samples may belong, we define three metrics namely, percentage of correct feasible region (CF%), percentage of correct infeasible region (CIF%) and percentage of not conservative feasible region (NC%). The respective calculations as given in Equation 7.9 are based on the number of sample points from the untested points that belong to each of the four categories as explained earlier. It is evident that accurate identification of feasible regions corresponds to CF% and CIF% of 100 and NC% of 0. To explain further, a high NC% is an indication of over-estimation of feasible region by the surrogate model whereas low CF% is an indication of under-representation of the feasible region.

$$CF\% = \frac{CF}{CF + ICIF} * 100$$

$$CIF\% = \frac{CIF}{CIF + ICF} * 100 \quad 7.9$$

$$NC\% = \frac{ICF}{ICF + CF} * 100$$

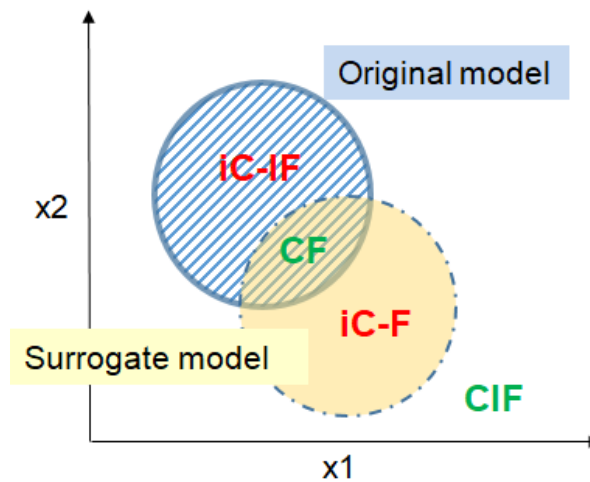


Figure 7.3 Illustration of surrogate model accuracy validation metrics

7.3 Test problems

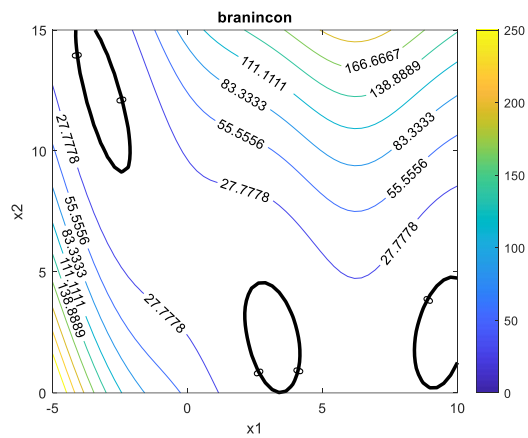
A thorough evaluation of the proposed ANN based feasibility analysis method is discussed in this section. The performance of the proposed method is compared with the kriging-based method through several low and high dimensional problems. The test problems chosen are standard and have been used in the literature extensively. In addition to the standard test problems, two additional test problems are formulated in high dimensions (four and six dimensions). The formulated test

problems serve to emulate a “flowsheet” problem, which is the case study discussed in sections 7.4 and 7.5. In the following section details on the test problems chosen for this work is given.

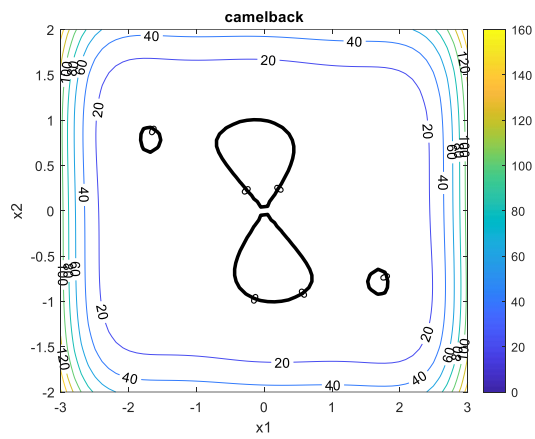
Four two dimensional problems listed in Table 7.1 are used in this work. The goal is to identify feasible regions for the test problems namely *branincon*, *camelback*, *ex3* [103] and *sasenacon* [217]. Table 7.1 provides details on the variable bounds along with the constraints that define the feasible region for these problems. All of the problems include non-linear constraints and the feasible regions are non-convex which are considered as difficult to identify. The *branincon*, *camelback* and *sasenacon* test problems also have disjoint feasible regions which adds difficulty in identifying the feasible region boundary. The feasible region boundaries for these problems are shown in bold black color in Figure 7.4. For these test problems, the performance of the ANN based and Kriging based methodologies are compared through visual analysis of the feasible regions as well as through validation metrics as explained in Section 7.2.

Table 7.1 Two-dimensional test problems with variable bounds and constraints

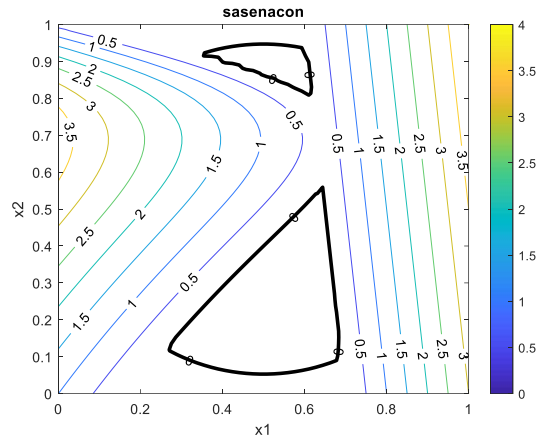
Test problem	Bounds	Constraint type	Constraints
<i>branincon</i>	$-5 \leq x_1 \leq 10$ $0 \leq x_2 \leq 15$	1 non-linear	$a(x_2 - bx_1^2 + cx_1 - d)^2 + h(1 - ff)\cos x_1 - 5 + h \leq 0$ $a = 1; b = \frac{5.1}{4\pi^2}; c = \frac{5}{\pi}; d = 6; h = 10; ff = \frac{1}{8\pi}$
<i>camelback</i>	$-3 \leq x_1 \leq 3;$ $-2 \leq x_2 \leq 2$	1 non-linear	$\left(4 - 2.1x_1^2 + \frac{x_1^4}{3}\right)x_1^2 + x_1x_2 + (-4 + 4x_2^2)x_2^2 \leq 0$
<i>sasenacon</i>	$0 \leq x_1 \leq 1;$ $0 \leq x_2 \leq 1$	1 linear, 2 non-linear	$10x_1 + x_2 - 7 \leq 0$ $(x_1 - 3)^2 + (x_2 + 2)^2 \exp(-x_2^2) - 12 \leq 0$ $(x_1 - 0.5)^2 + (x_2 - 0.5)^2 - 0.2 \leq 0$
<i>ex3</i>	$-10 \leq x_1 \leq 5;$ $-15 \leq x_2 \leq 15$	1 linear, 2 non-linear	$-2x_1 + x_2 - 15 \leq 0$ $\frac{x_1^2}{2} + 4x_1 - x_2 - 5 \leq 0$ $-\frac{(x_1 - 4)^2}{5} - \frac{x_2^2}{0.5} + 10 \leq 0$



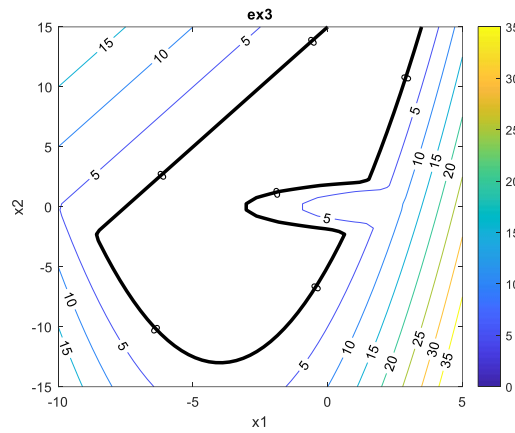
(a)



(b)



(c)



(d)

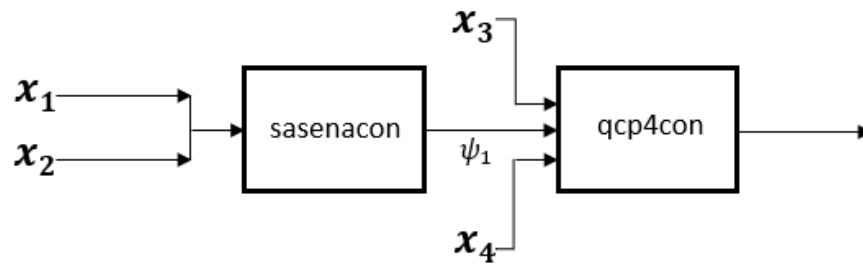
Figure 7.4 True feasible region boundaries of the test problems (a) braninon (b) camelback (c) sasenacon (d) ex3

In addition to the two dimensional problems listed in Table 7.1, three, five and six dimensional test problems listed in

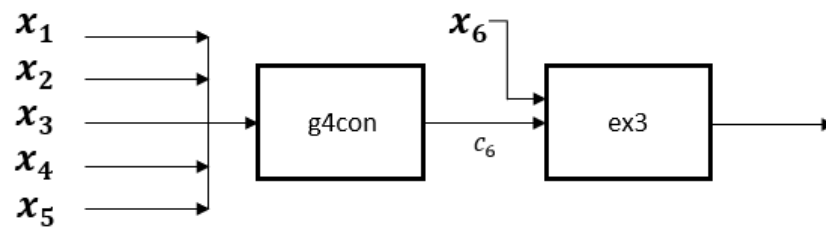
Table 7.2 namely *qcp4con*, *g4con* and *Hesse* [218] respectively are discussed here. Similar to the two dimension problems, the variable bounds and constraints are listed in the table. Two formulated test problems namely *4Dcomp* and *6Dcomp* are also used in this work. The purpose of these test problems is to simulate test cases similar to a flowsheet model. Flowsheet models are mathematical representations of continuous processes and are used to simulate dynamic behavior of the entire manufacturing line [219]. Flowsheet models have several unit operation models connected such that relevant information is transferred from a unit to the the succeeding unit. A flowsheet model representing the wet granulation continuous manufacturing process is the subject of case studies described in the Sections 7.4 and 7.5. Specifically, the flowsheet model constitutes process models for unit operations namely, granualtion, drying, milling and tablet compaction. Flowsheet models are computationally expensive and hence serve as excellent candidates for implementing the proposed surrogate based feasibility analysis method for identification of feasible regions. To test effectiveness of the proposed methodology in flowsheet models, the test problems *4Dcomp* and *6Dcomp* are formulated. The test problem *4Dcomp* is formulated using the *sasenacon* and *qcp4con* functions as shown in Figure 7.5(a). This leads to a four dimensional problem with six constraints. The test problem *6Dcomp* is formulated using the *g4con* and *ex3* functions as shown in Figure 7.5(b). This leads to a six dimensional problem with nine constraints. The performance of the ANN based and Kriging based methdologies for these test problems are compared through the validation metrics explained in Section 7.2.

Table 7.2 Standard high dimensional test problems with variable bounds and constraints

<i>d</i>	Test problem	Bounds	Constraints
3	<i>qcp4con</i>	$0 \leq x_1 \leq 2$ $0 \leq x_2 \leq 3$ $0 \leq x_3 \leq 3$	$x_1 + x_2 + x_3 - 4 \leq 0$ $3x_2 + x_3 - 6 \leq 0$ $x'A'Ax - 2y'Ax + \ y\ ^2 - 0.25\ b - z\ ^2 \leq 0$ $A = [0, 0, 1; 0, -1, 0; -2, 1, -1]; b = [3; 0; -4];$ $y = [1.5; -0.5; -5]; z = [0; -1; -6]; x = [x_1, x_2, x_3]'$
5	<i>g4con</i>	$78 \leq x_1 \leq 102$ $33 \leq x_2 \leq 45$ $27 \leq x_3 \leq 45$ $27 \leq x_4 \leq 45$ $27 \leq x_5 \leq 45$	$u - 92 \leq 0$ $-u \leq 0$ $v - 110 \leq 0$ $-v + 90 \leq 0$ $w - 25 \leq 0$ $-w + 20 \leq 0$ $u = 85.334407 + 0.0056858x_2x_5 + 0.0006262x_1x_4 - 0.0022053x_3x_5$ $v = 80.51249 + 0.0071317x_2x_5 + 0.0029955x_1x_2 + 0.0021813x_3^2$ $w = 9.300961 + 0.0047026x_3x_5 + 0.0012547x_1x_3 + 0.0019085x_3x_4$
6	<i>Hesse</i>	$0 \leq x_1 \leq 5$ $0 \leq x_2 \leq 4$ $1 \leq x_3 \leq 5$ $0 \leq x_4 \leq 6$ $1 \leq x_5 \leq 5$ $0 \leq x_6 \leq 10$	$4 - (x_3 - 3)^2 - x_4 \leq 0$ $4 - (x_5 - 3)^2 - x_6 \leq 0$ $x_1 - 3x_2 - 2 \leq 0$ $-x_1 + x_2 - 2 \leq 0$ $x_1 + x_2 - 6 \leq 0$ $2 - x_1 - x_2 \leq 0$



(a)



(b)

Figure 7.5 High dimensional test problems formulated (a) 4Dcomp (b) 6Dcomp

7.3.1 Two dimensional test problems

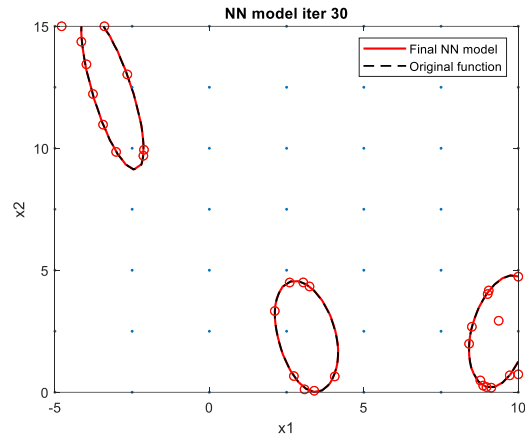
For ANN as well as kriging-based methods, a grid sampling scheme is used to build the initial surrogate model in the initial model selection phase. The performance of the methods is compared for different number of initial samples i.e., 49, 36, 25, 16 and 9 which correspond to 7, 6, 5, 4 and 3 levels respectively. After the initial surrogate model is built, the adaptive sampling strategy is implemented according to the algorithm in Figure 7.2 in order to improve the surrogate model accuracy. 100 adaptive sample points are chosen. The accuracy of the surrogate model is calculated using dense sampling of the variable space through 100^2 grid sampling. Table 7.3 lists the initial surrogate model and final surrogate model accuracies for ANN and kriging-based methods in the case of 49 initial samples. The number of adaptive samples required in order to reach an accuracy

of 99% CF, 99% CIF and 1% NC are also listed in Table 7.3. The feasible region boundaries identified by the final surrogate model are also plotted for both methods to aid visual analysis.

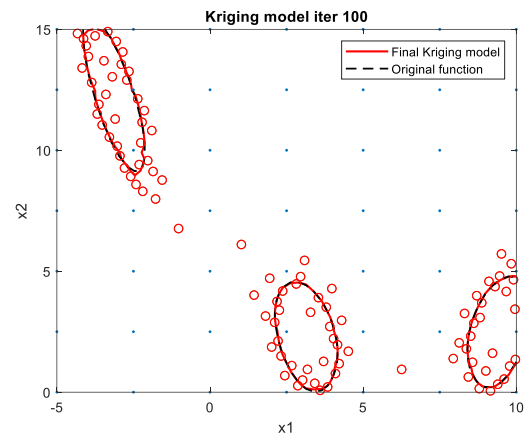
Table 7.3 Surrogate model accuracy metrics for two-dimensional test problems

Test problem	Surrogate model	Initial			Final			Adaptive samples
		CF%	CIF%	NC%	CF%	CIF%	NC%	
<i>branincon</i>	Kriging	26.10	100.00	0.00	97.86	99.89	1.20	100
	ANN	56.94	98.27	24.76	99.64	99.98	0.24	30
<i>camelback</i>	Kriging	99.39	76.21	77.44	96.47	99.28	9.63	100
	ANN	87.88	98.55	19.18	99.85	100.00	0.00	20
<i>sasenacon</i>	Kriging	58.03	98.06	17.85	88.14	99.62	2.73	100
	ANN	74.96	98.35	12.54	96.54	99.33	4.32	100
<i>ex3</i>	Kriging	91.53	98.25	3.22	98.38	99.50	0.88	100
	ANN	91.40	94.03	10.26	99.15	99.50	0.88	80

From Table 7.3, in terms of the surrogate model accuracy achieved, Kriging as well as ANN models are able to identify the feasible regions with high accuracy (>97% feasible regions and >99% infeasible regions are accurately identified) for *branincon* and *ex3* test problems, with ANN performing slightly better than Kriging in CF% and NC% and with fewer adaptive samples (*branincon*:30 and *ex3*:80). Figure 7.6 and Figure 7.7 show feasible region boundaries identified by the surrogate models compared to the actual feasible region boundaries for *branincon* and *ex3* problems respectively. The figures also show the location of adaptive samples. It is evident that the adaptive samples are placed close to the feasible region boundaries indicating the result of maximizing the modified expected improvement function EI_{feas} discussed in Section 7.2.

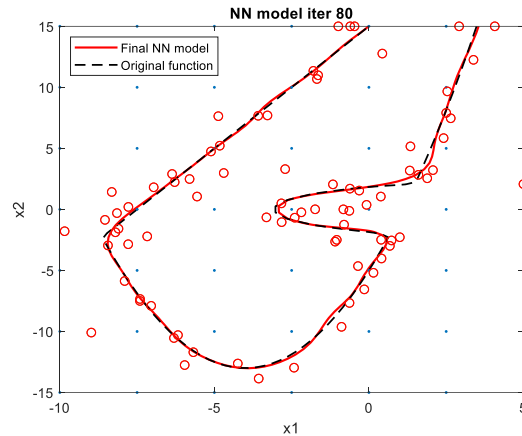


(a)

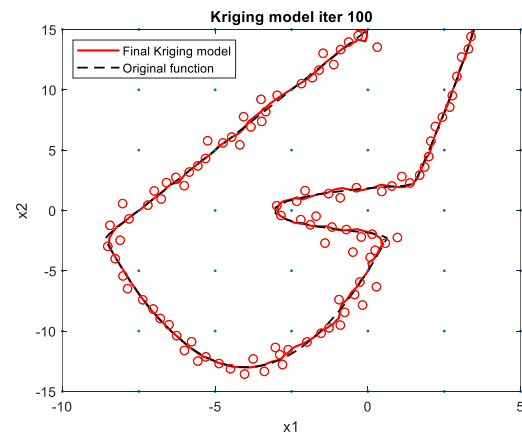


(b)

Figure 7.6 Visual comparison of the original model and surrogate model feasible region boundaries (a) ANN for branincon (b) Kriging for branincon (Initial samples are represented with dots and adaptive samples are represented with red circles. True feasible region boundary is represented as black dashed line and feasible region boundary predicted by the surrogate model is represented as red line)



(a)

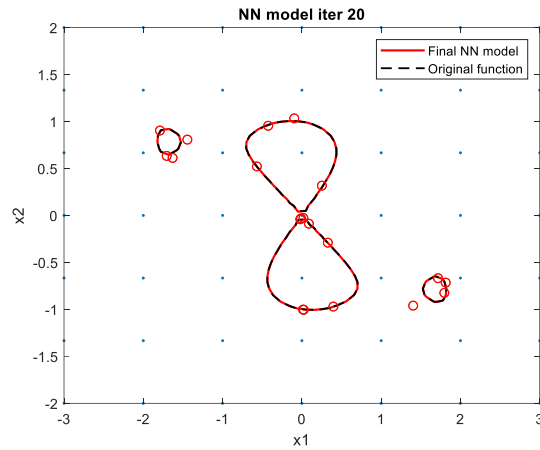


(b)

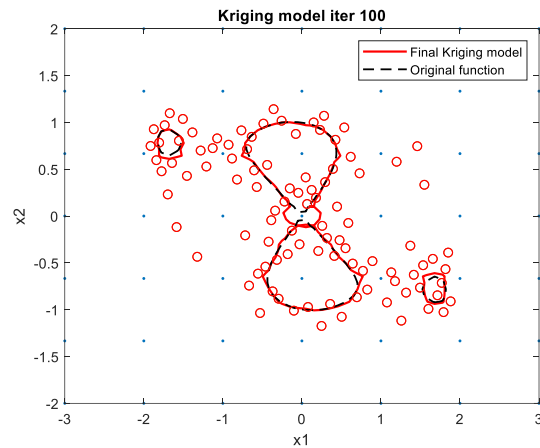
Figure 7.7 Visual comparison of the original model and surrogate model feasible region boundaries (a) ANN for ex3 (b) Kriging for ex3 (Initial samples are represented with dots and adaptive samples are represented with red circles. True feasible region boundary is represented as black dashed line and feasible region boundary predicted by the surrogate model is represented as red line)

For *camelback*, ANN performs significantly better in accurately identifying feasible regions. Kriging over estimates feasible region with 9.63 NC% compared to no over-estimation by ANN. This is also achieved by ANN with fewer adaptive samples (ANN: 20 and Kriging: 100). Figure

7.8 shows feasible region boundaries identified by the ANN and Kriging surrogate models respectively along with the placement of adaptive samples which shows very good prediction of feasible region boundaries by ANN.



(a)



(b)

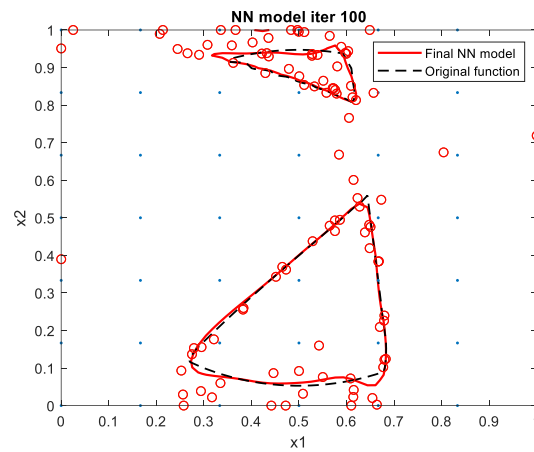
Figure 7.8 Visual comparison of the original model and surrogate model feasible region boundaries (a) ANN for camelback (b) Kriging for camelback (Initial samples are represented with dots and adaptive samples are represented with red circles. True feasible region boundary is represented as

black dashed line and feasible region boundary predicted by the surrogate model is represented as red line)

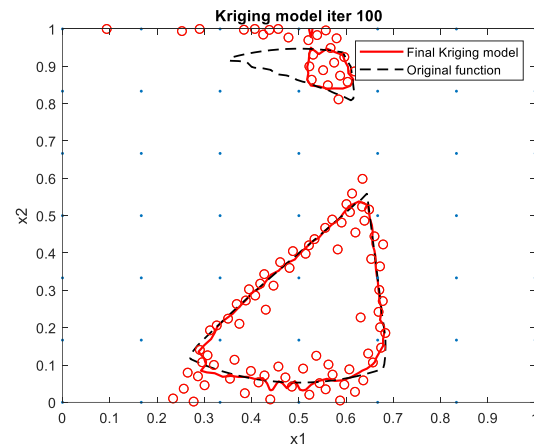
For *sasenacon*, significantly larger feasible region is identified by ANN (ANN: 96.54 CF% and Kriging: 88.14 CF%), which is also accompanied by slight over estimation when compared to Kriging (ANN: 4.32 NC% and Kriging: 2.73 NC%). Figure 7.9(a) and (b) shows performance of ANN and Kriging methods respectively for this test problem. It can be observed that in ANN method, the adaptive samples added are distributed between the larger and smaller feasible regions where in Kriging method, the adaptive samples are concentrated more towards the larger feasible region.

The results discussed thus far include surrogate models built with 49 initial samples. In order to show the effectiveness of the proposed ANN based algorithm, results for the performance of the methods using a different number of initial samples for the four test problems are plotted in Figure 7.10. In order to aid plotting of all the metrics i.e., CF%, CIF% and NC% on the same scale, $NC' = 100 - NC$ is plotted instead of NC. Since a low value of NC indicates accurate identification of feasible region, this implies a high value of NC' is desired. Figure 7.10 also shows the initial model accuracy and an improvement or degeneration in the accuracy attained due to the adaptive samples. From the plots, it can be observed that the accuracy of the ANN model is comparable or better than Kriging model for all four test problems at all levels considered. This is true for CF%, CIF% and NC%. It is also worth noting that the performance of ANN is better than Kriging irrespective of the accuracy of the initial model. For example, for *branincon* at 25 initial samples (levels=5), the initial ANN model accuracy reflected in CF% is significantly lower than initial Kriging model accuracy. However, with adaptive sampling, the final ANN model accuracy is better than Kriging. Similarly, for *camelback* with 36 initial samples (levels=6), the initial ANN model CF% is lower than initial Kriging model accuracy. However, the final model accuracies are comparable for both methods.

Another interesting observation is the loss in model accuracy particularly in Kriging model with adaptive sampling as seen in negative accuracy gain i.e., accuracy loss values. This is possibly due to interpolating nature of the Kriging model which may lead to oscillations with large number of closely located samples.



(a)

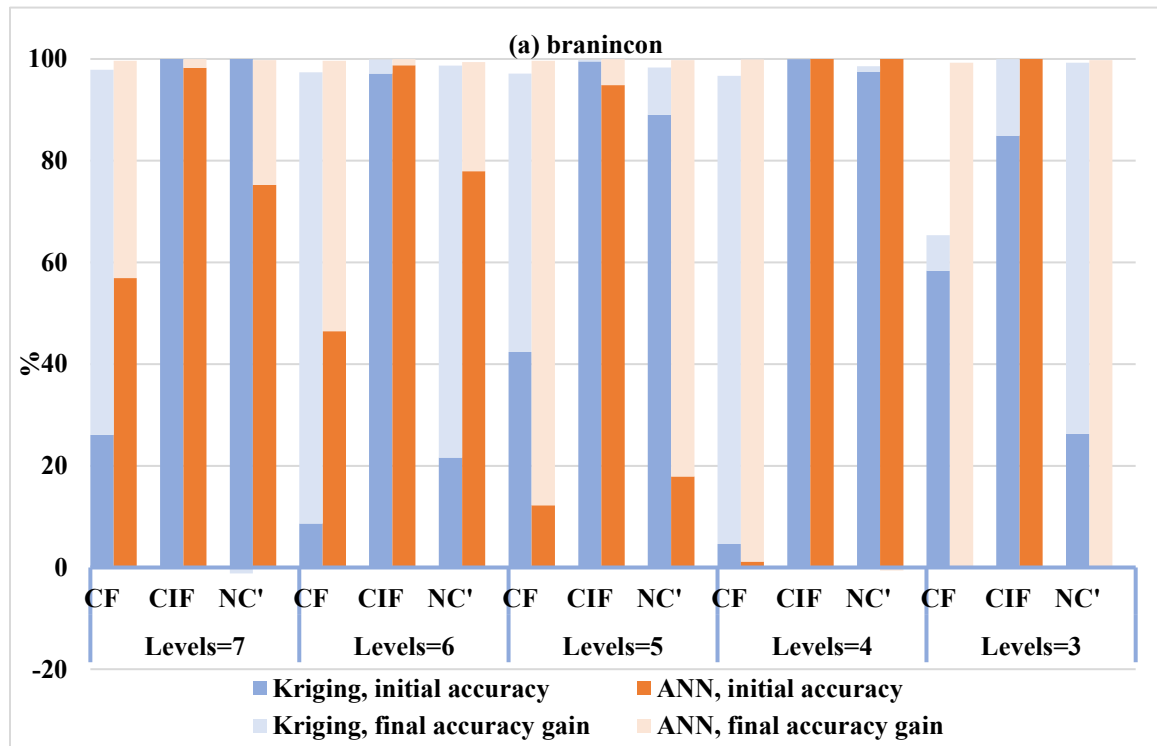


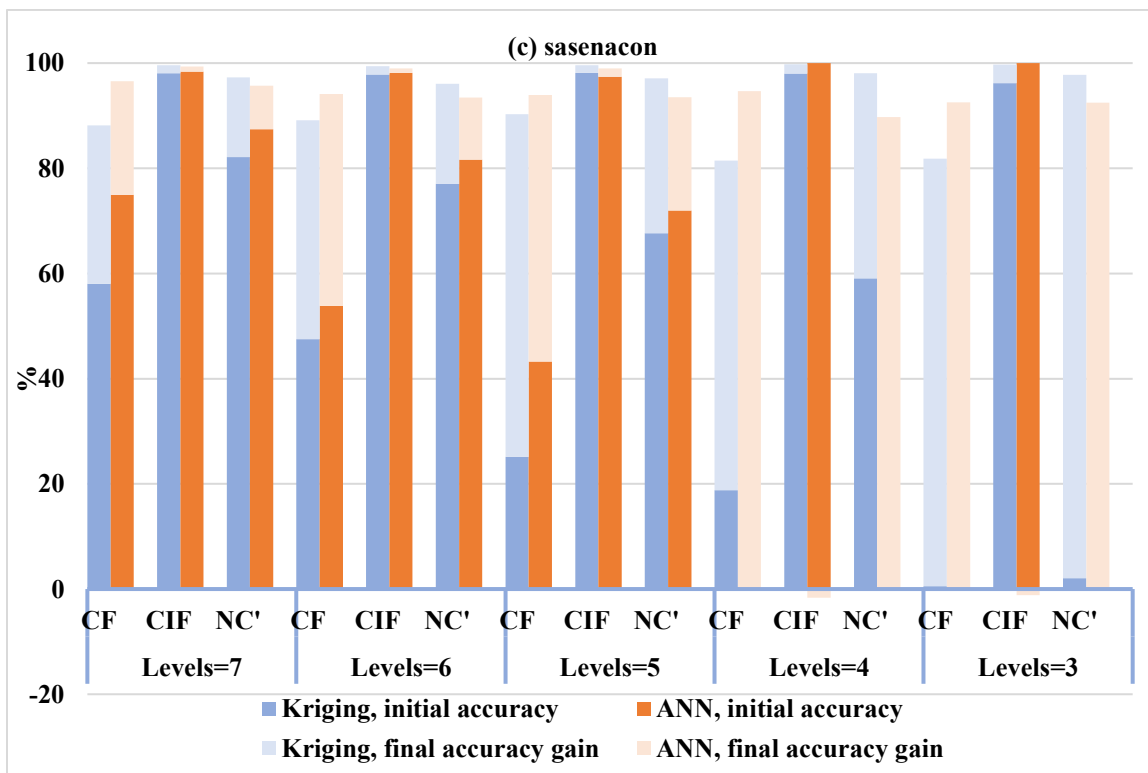
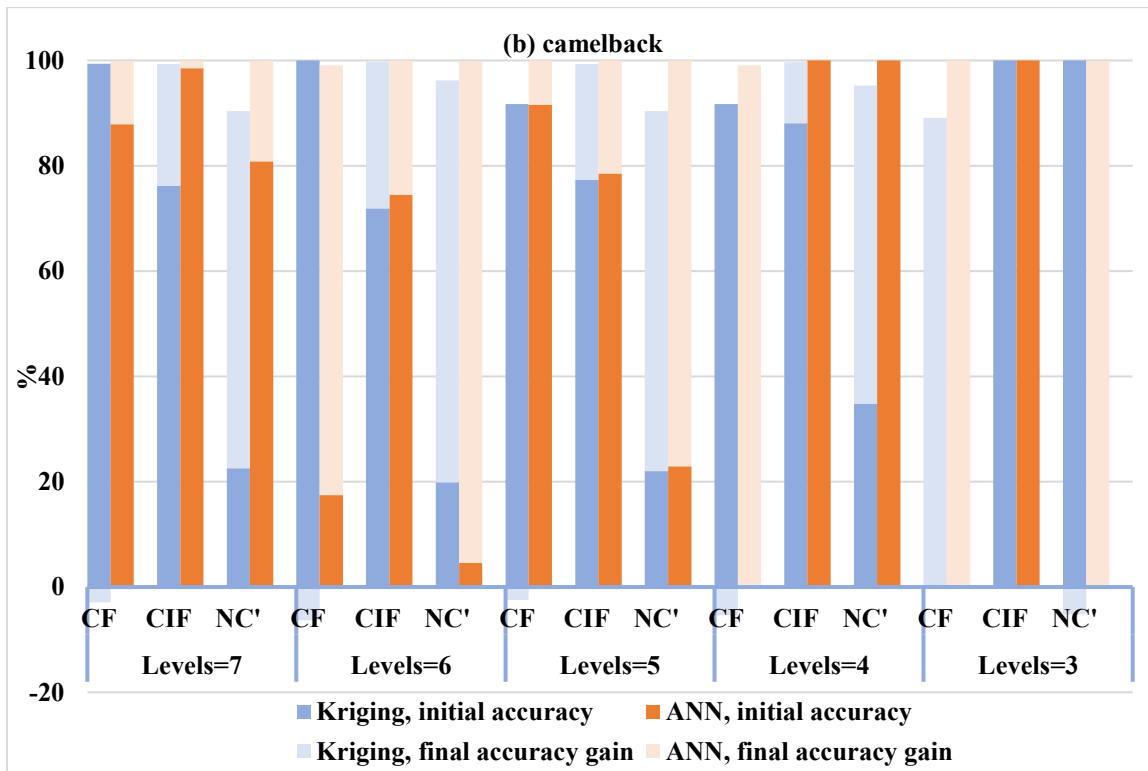
(b)

Figure 7.9 Visual comparison of the original model and surrogate model feasible region boundaries

(a) ANN for sasenacon (b) Kriging for sasenacon (Initial samples are represented with dots and

adaptive samples are represented with red circles. True feasible region boundary is represented as black dashed line and feasible region boundary predicted by the surrogate model is represented as red line)





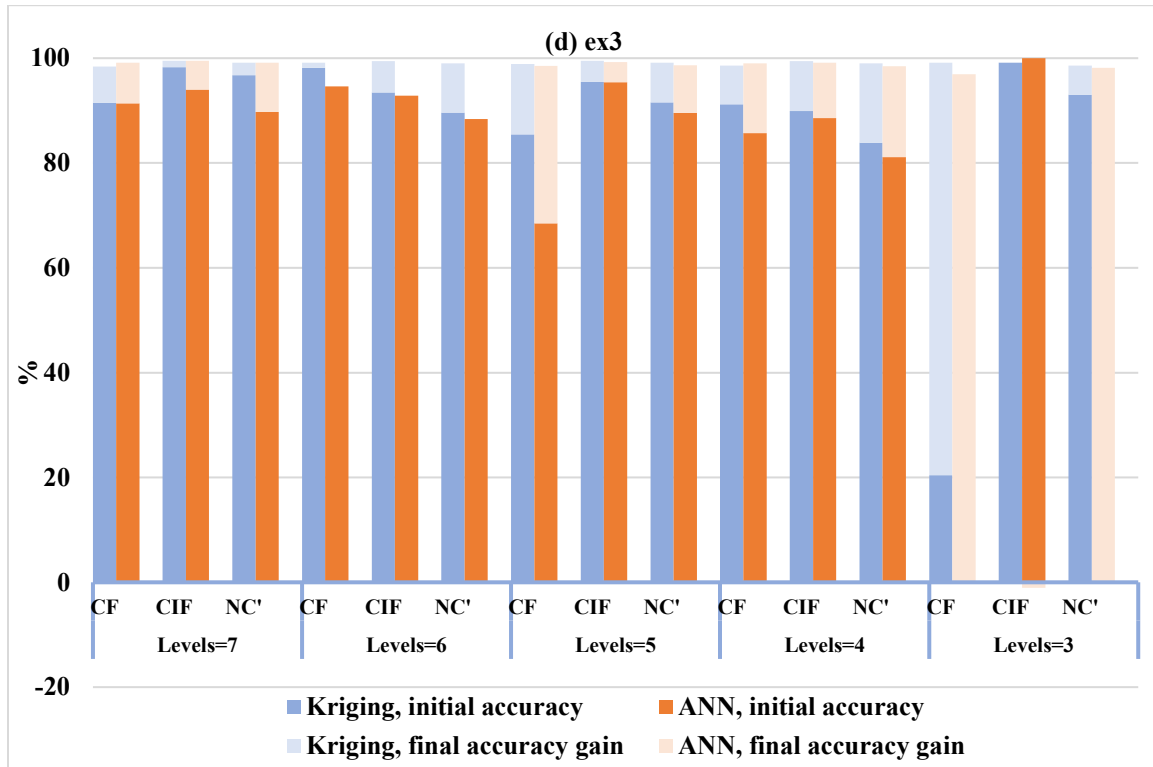


Figure 7.10 Comparison of ANN and Kriging model accuracy metrics for different levels of initial samples (a) *branincon* (b) *camelback* (c) *sasenacon* (d) *ex3*

The results listed in Table 7.3 show that generally ANN requires fewer adaptive samples compared to Kriging to attain a surrogate model accuracy of >99% CF, >99% CIF and <1% NC. Specifically, Kriging utilizes the sampling budget of 100 adaptive samples whereas ANN requires considerably less number of adaptive samples for *branincon* (30 samples) and *camelback* (20 samples). For these test problems, this is also true when lower number of initial samples are used. The total number of adaptive samples used by the test problems at different levels of initial samples are plotted in Figure 7.11. The plot shows that for *branincon*, at levels 6, 5, 4, and 3, ANN requires 20, 30, 30, and 40 adaptive samples respectively, whereas kriging uses the entire sampling budget of 100 adaptive samples. For *camelback* at levels 6, 5, 4, and 3, ANN requires 10, 20, 50, and 60 adaptive samples respectively, while all 100 adaptive samples are used by kriging. For *ex3* problem, ANN as well as Kriging use the entire sampling budget at 5, 4, and 3 levels. In the *sasenacon* problem, kriging as

well as ANN require 100 adaptive samples at all the levels considered. Overall, the proposed ANN methodology uses the same or a smaller number of adaptive samples when compared to the Kriging methodology at various levels of initial samples considered. This is particularly useful for implementation of the methodology in identifying feasible regions for computationally expensive problems.

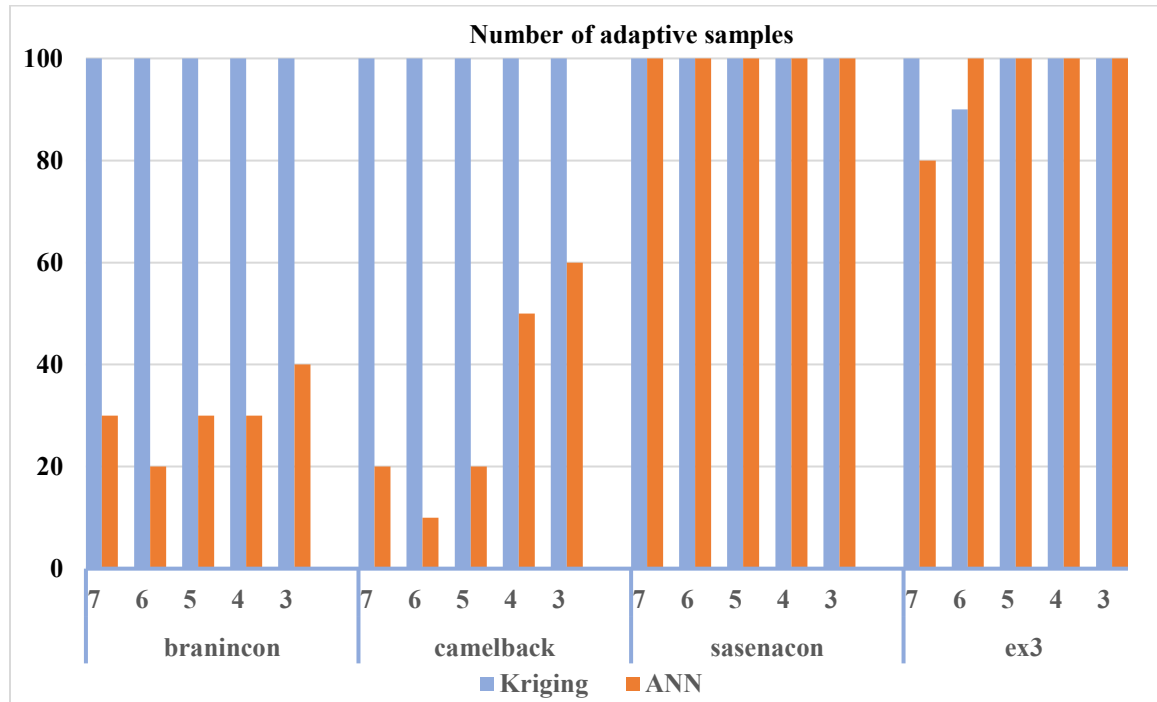


Figure 7.11 Comparison of number of adaptive samples required by ANN and Kriging based methodologies for different levels of initial samples

To take a closer look at the performance of the methods, the accuracy metrics of the ANN and Kriging surrogate models are also computed every 10 iterations. This also aids in evaluating effect of adaptive sampling on the metrics. The Kriging and ANN CF%, CIF% and NC% evolution with adaptive samples are plotted for the four test problems in Figure 7.12-Figure 7.15. Generally, the metrics improve with the addition of adaptive samples i.e., CF%, CIF% increase and NC% decreases. There may be oscillations in the trends which is the result of improvement in ability of

the models to predict feasible regions as more samples are added. For example, in the Kriging based implementation for the *camelback* problem the initial model predicts a large portion of the variable space as feasible as noted by high CF%. However, this is an over-estimation of the feasible region which reflects in the high initial NC% as well. As samples are added, CF% decreases as well as NC% decrease i.e., the model recognizes infeasible regions as well. After 20 iterations, the CF% begins to improve and the over-estimation of the feasible region is reduced as well. In addition, one may observe slightly more oscillation in trends with the ANN based method when compared to Kriging method. The oscillations in ANN based method can also be attributed to randomized nature of the ANN i.e., the optimized ANN network parameters depend on the initial values of weights and biases which are randomly chosen in contrast to the deterministic nature of model parameters in the Kriging model. Overall, for two dimensional problems, the ANN based method performs better than the Kriging based method in identifying feasible regions and with fewer adaptive samples.

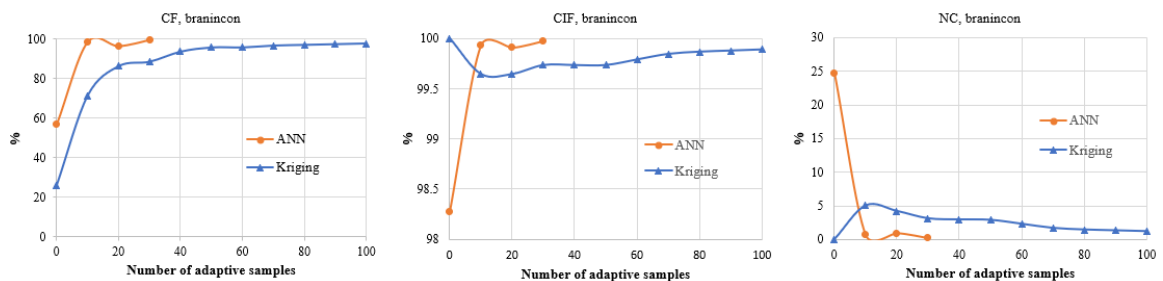


Figure 7.12 Comparison of ANN and Kriging model accuracy validation metrics by number of adaptive samples for branincon (a) CF% (b) CIF% (c) NC%

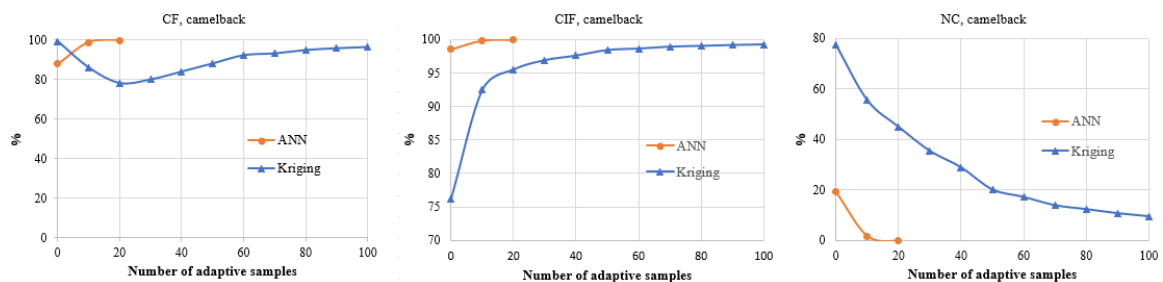


Figure 7.13 Comparison of ANN and Kriging model accuracy validation metrics by number of adaptive samples for camelback (a) CF% (b) CIF% (c) NC%

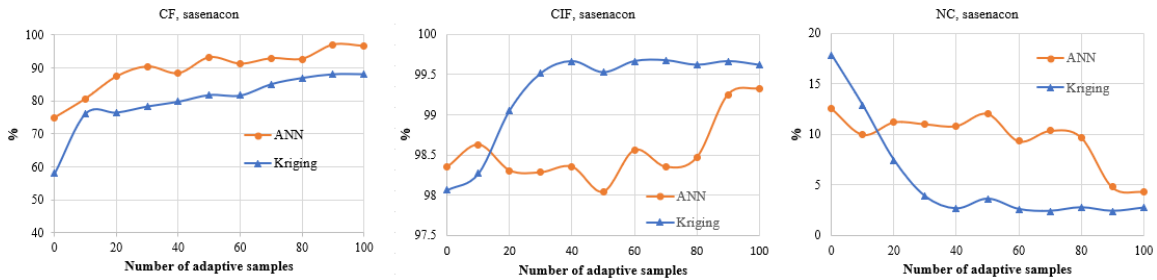


Figure 7.14 Comparison of ANN and Kriging model accuracy validation metrics by number of adaptive samples for sasenacon (a) CF% (b) CIF% (c) NC%

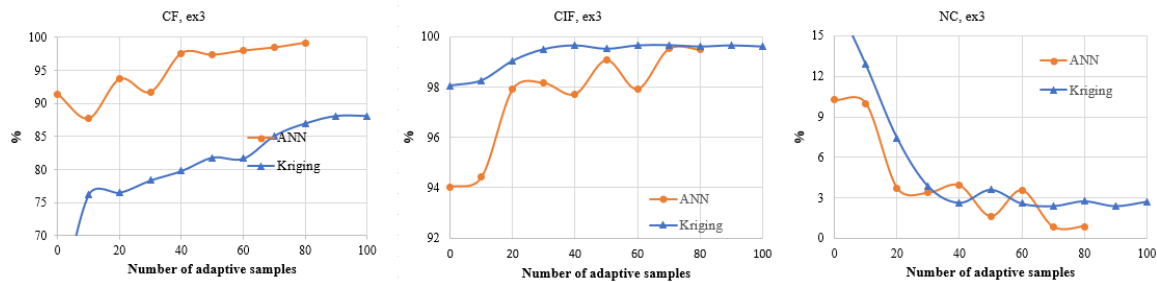


Figure 7.15 Comparison of ANN and Kriging model accuracy validation metrics by number of adaptive samples for ex3 (a) CF% (b) CIF% (C) NC%

7.3.2 Higher dimensional test problems

The high dimensional standard test problems are listed in

Table 7.2 and the formulated test problems are shown in Figure 7.5. Kriging and ANN based methodologies are applied and compared for these problems as well. To build the initial model in the initial model selection phase, Latin hypercube sampling scheme is used as it is known to provide better space filling property when compared to grid sampling for high dimensional domain [102, 104]. If d is the dimension of the variable domain, 2^d samples are chosen to fit the initial surrogate model. For problems with four or higher dimensions, exhaustion of 500 adaptive samples is chosen as the stopping criteria. A higher number of adaptive samples are chosen when compared to the two-dimensional test problems as high dimensional problems are considered difficult to solve and are known to require large number of samples (*curse of dimensionality*). The accuracy of the surrogate models is evaluated using untested samples in the variable space. For four, five and six dimensional problems, 7^4 , 6^5 , 5^6 points respectively are chosen through grid sampling. Table 7.4 lists the initial surrogate model and final surrogate model accuracy metrics for ANN and kriging-based methods. The ANN and Kriging based methods are also compared through computation of the surrogate model accuracy metrics every 25 iterations to closely observe the effect of adaptive sampling.

From the results, it is evident that the ANN-based method performs better than kriging in identifying feasible regions. ANN model yields good performance with untested points even when the initial surrogate model accuracy is considerably poorer than the initial kriging model. For example, in the five-dimensional *g4con* test problem, the initial Kriging model identifies the feasible points reasonably well (CF%: 83, CIF%: 95.85 and NC%: 12.4). The initial ANN model for this test problem is unable to identify any of the feasible regions (CF%: 0, CIF%: 100). However, with 500 adaptive sample points, the performance of the ANN model improves significantly (ANN: 90.88 CF% and 4.45 NC%) and the performance of the final Kriging model is worse than the final ANN model (Kriging: 86.23 CF% and 7.39 NC%). In the *6Dcomp* problem, the initial ANN model performance is very poor compared to the initial Kriging model. However,

with addition of 500 adaptive samples, the final ANN model is able to identify significantly more feasible points when compared to Kriging (ANN: 90.53 CF% and Kriging: 76.61 CF%). However, this is also accompanied by an over-estimation of the feasible region by the ANN model (ANN: 11.73 NC% and Kriging: 7.97 NC%).

In the *4Dcomp* problem, the initial ANN and Kriging surrogate model performance metrics are comparable. At the end of 500 adaptive samples, the final ANN model accuracy metrics are better than Kriging in the identification of feasible region as well as low over-estimation (ANN: 90.88 CF% and 4.45 NC%; Kriging: 86.23 CF% and 7.39 NC%). For the six-dimensional *Hesse* problem, a lower initial ANN model performance is significantly improved through adaptive sampling (Initial ANN: 45.89 CF%; Final ANN: 96.56 CF%). However, an over-estimation of the feasible region is observed for this case when compared to the Kriging model (ANN: 5.76 NC%; Kriging: 0.79 NC%).

Table 7.4 Surrogate model accuracy metrics for high dimensional test problems

<i>d</i>	Test problem	Surrogate model	Initial			Final		
			CF%	CIF%	NC%	CF%	CIF%	NC%
3	<i>qcp4con</i>	Kriging	94.29	98.36	16.06	98.33	99.82	1.96
		ANN	94.08	99.35	7.19	98.89	99.50	5.39
4	<i>4Dcomp</i>	Kriging	56.35	76.36	74.10	86.23	99.00	7.39
		ANN	55.05	79.94	71.31	90.88	99.38	4.45
5	<i>g4con</i>	Kriging	83.49	95.85	12.40	97.92	99.22	2.22
		ANN	0.00	100.00	NA	99.26	99.67	0.94
6	<i>Hesse</i>	Kriging	74.84	87.12	48.24	96.11	99.87	0.79
		ANN	45.89	86.23	62.96	96.56	98.86	5.76
6	<i>6Dcomp</i>	Kriging	15.04	95.58	66.23	76.61	99.01	7.97
		ANN	3.44	98.94	67.29	90.52	98.04	11.73

Figure 7.16-Figure 7.20 show trends of the surrogate model accuracy metrics every 25 iterations for *4Dcomp*, *g4con*, *6Dcomp* and *Hesse* problems respectively. Similar to the two-dimensional test problems some oscillations are seen in the trends for Kriging and ANN models. The oscillations

observed in the first few iterations may be attributed to the unreliability of the surrogate model. The initial surrogate model is unable to identify the feasible region as seen from the poor initial CF% metrics in the *g4con* and *Hesse* problems. In the first few iterations adaptive sampling explores the variable domain landscape to eventually identify more feasible regions. This is particularly noticeable in the oscillations with first few iterations in the *g4con* test problem. From here on, the adaptive sampling proceeds with exploitation phase where the focus is on identifying the feasible region boundary with more accuracy. This also results in the oscillations being eventually dampened as more samples are added. Also, the oscillations generally are more for the ANN model which may be attributed to randomization effect of the ANN model building i.e., initialization of the ANN network parameters random in nature. The following section describes the implementation of the ANN based methodology on a four-dimensional problem of the continuous wet granulation process.

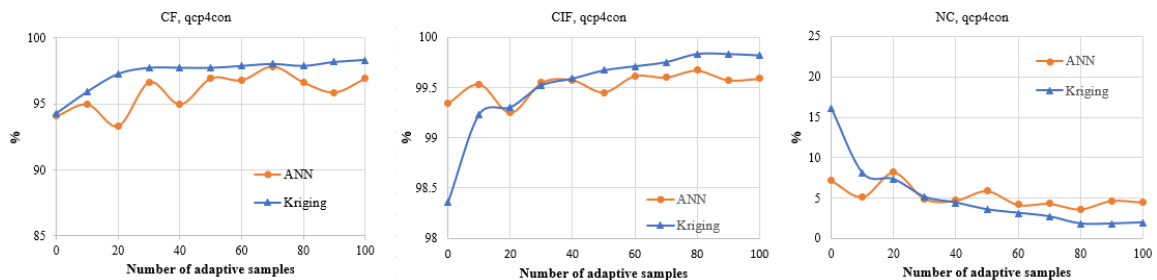


Figure 7.16 Comparison of ANN and Kriging model accuracy validation metrics by number of adaptive samples for qcp4con (a) CF% (b) CIF% (c) NC%

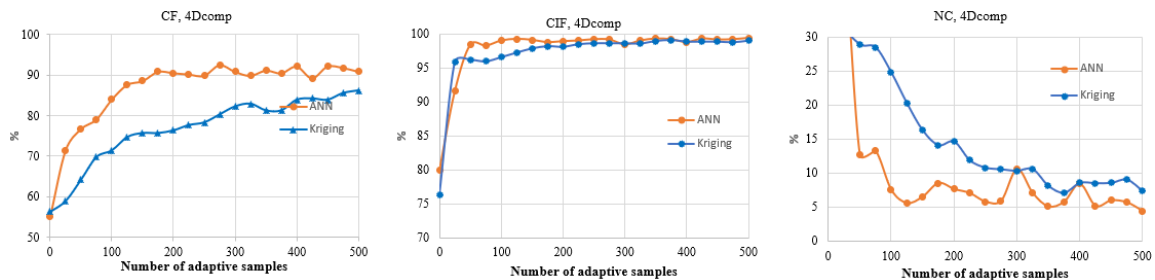


Figure 7.17 Comparison of ANN and Kriging model accuracy validation metrics by number of adaptive samples for 4Dcomp (a) CF% (b) CIF% (c) NC%

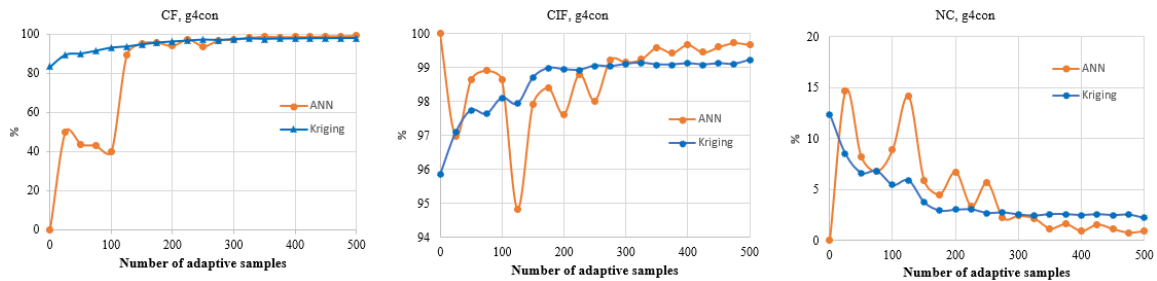


Figure 7.18 Comparison of ANN and Kriging model accuracy validation metrics by number of adaptive samples for g4con (a) CF% (b) CIF% (c) NC%

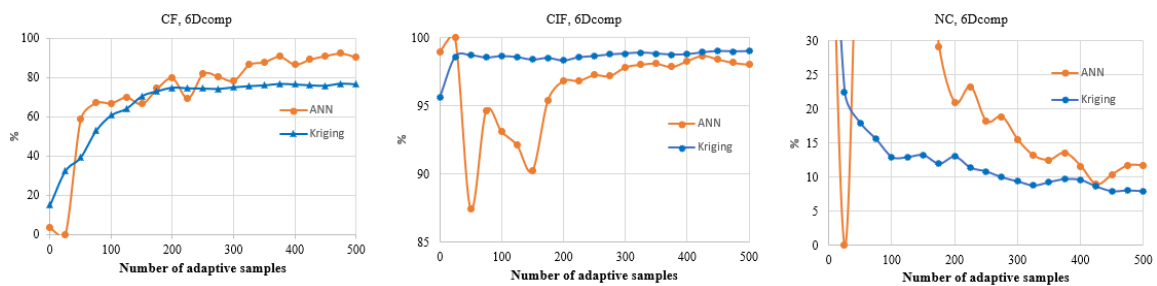


Figure 7.19 Comparison of ANN and Kriging model accuracy validation metrics by number of adaptive samples for 6Dcomp (a) CF% (b) CIF% (c) NC%

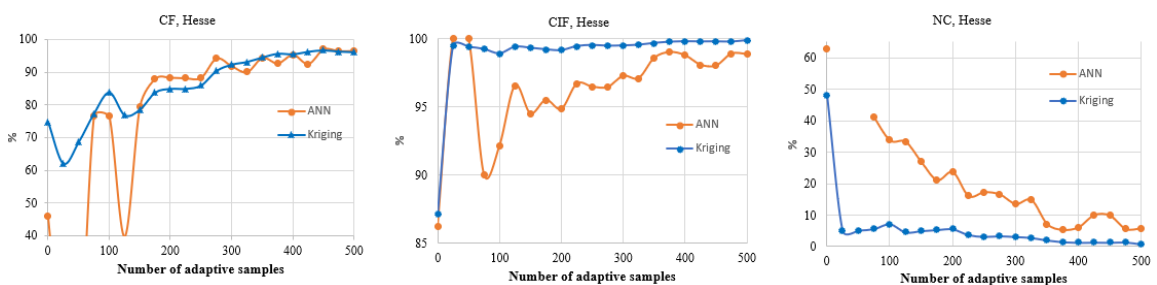


Figure 7.20 Comparison of ANN and Kriging model accuracy validation metrics by number of adaptive samples for Hesse (a) CF% (b) CIF% (c) NC%

7.4 Design space of a continuous direct compaction process

In this section, the proposed methodology is applied to identify feasible regions in a continuous direct compaction process. The performance of the methodology is also compared to the kriging-based methodology. The tablet manufacturing process via direct compaction route includes feeders, blender, comill and tablet press units. In this process, the formulation ingredients are introduced into the blender through the feeder units. The comill unit delumps the powder material before it is introduced into the blending unit. The blended components are then compacted to form tablets in the tablet press unit. A schematic of the continuous direct compaction process is shown in Figure 7.21. The process model representing the continuous direct compaction process is explained by Wang, Escotet-Espinoza [12]. The unit operation models are briefly explained here.

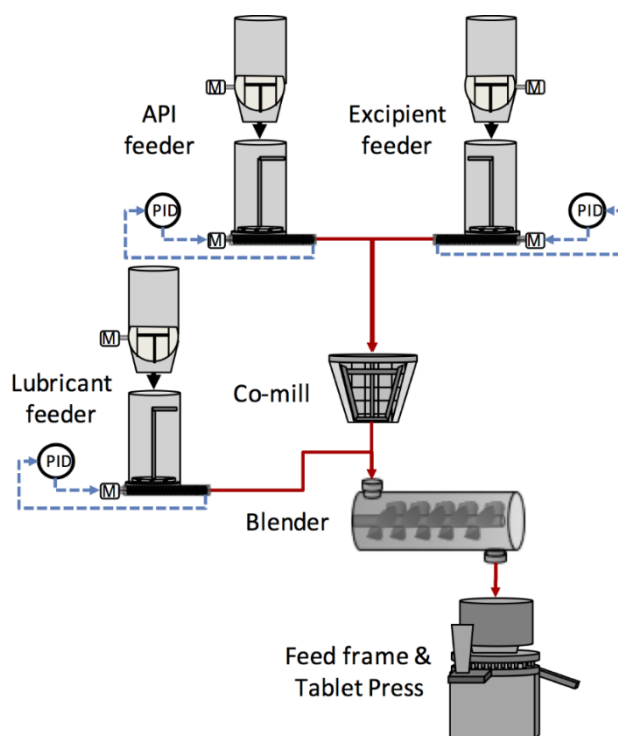


Figure 7.21 Schematic of a continuous direct compaction process

7.4.1 Unit process models

Feeder

In this work, the feeder model as given in Wang, Escotet-Espinoza [12] is used. A semi-empirical equation was used to dynamically model the mass flowrate out of the feeder $\dot{F}_{out}(t)$ using 7.10, where $\omega(t)$ is the screw speed; $ff(t)$ is the feed factor, defined as the maximum mass of powder fitting in a screw flight and is expressed in Equation 7.11, where $\rho_{effective}$ is the effective density of materials in the screw pitch with a volume $V_{ScrewPitch}$.

$$\dot{F}_{out}(t) = ff(t)\omega(t) \quad 7.10$$

$$ff(t) = \rho_{effective}(t)V_{ScrewPitch} \quad 7.11$$

ff was found to be dependent on the amount of material in the hopper, as the effective density of powder entering the screws is expected to change due to change in pressure exerted by static head of the material above. This relationship was determined to be following a pseudo-first-order as expressed in Equation 7.12, where ff_{level}^{sat} is the saturated feed factor; ff_{level}^{min} is the minimum feed factor; and β is the feed factor exponential decay constant. These parameters are regressed from experimental data and can be related to material properties such as bulk density, permeability, compressibility, cohesion [220].

$$ff(W(t)) = ff_{level}^{sat} - e^{-\beta W(t)}(ff_{level}^{sat} - ff_{level}^{min}) \quad 7.12$$

Blender

In this work, the mass balance in the blender is modeled assuming the hold up in the blender reaches a steady state asymptotically i.e., it follows a first-order. The flowrate out of the system, which is used as an input in the downstream unit, can thus be modeled as given in Equations 7.13 and 7.14, where, the parameters n , τ , M_{ss} depend on inlet flowrate and blade speed, and are estimated from experimental data.

$$\bar{\tau} \frac{dM(t)}{dt} + M(t) = M_{ss} \quad 7.13$$

$$\frac{dM(t)}{dt} = M_{in}^{total} - M_{out}^{total} \quad 7.14$$

Comill

The comill model considered here includes a mass balance equation and first order holdup dynamics similar to the blender model. The time constant that defines the holdup evolution is modeled to depend on the comill speed and flow rate of powders as given in Equation 7.15 . Here ω refers to the mill impeller speed, and the parameters a and b are estimated using experimental data.

$$\tau = \tau_{max} \left(1 - \exp \left(- \frac{a}{\omega_{comill} - \omega_{min}} - \frac{b}{M_{in}^{total}} \right) \right) \quad 7.15$$

Tablet press

The tablet hardness is modeled using the Kuentz-Luenberger equation as given in Equations 7.16 and 7.17 where ρ_r is the relative density. The parameters $\rho_{r,cr}$ and H_{max} are to be fitted from

experimental data. Escotet-Espinoza, Vadodaria [87] estimated these co-efficients from experimental data and developed empirical equations to relate these parameters to the original blend properties.

$$H = H_{max}(1 - \exp(\rho_r - \rho_{r,cr} + \lambda_H)) \quad 7.16$$

$$\lambda_H = \ln\left(\frac{1 - \rho_r}{1 - \rho_{r,cr}}\right) \quad 7.17$$

Overall, the unit process models are used to develop a flowsheet model representing the direct compaction process using MATLAB™ platform.

7.4.2 Feasibility problem for the continuous direct compaction process

The critical process parameters namely API and excipient flow rates, comill impeller speed, blender blade speed and tablet press fill depth and tablet thickness set point are considered as uncertain parameters. These are chosen as the variables for the feasibility problem based on sensitivity analysis performed by Wang, Escotet-Espinoza [12] that identifies these as the critical variables and aid sin reducing the dimensionality of the problem to few key variables. The lower and upper bounds of these are listed in Table 7.7. The constraints defining the feasibility problem are listed in Table 7.8. Overall, this is a six-dimensional problem with 20 inequality constraints, which is solved using the ANN-based as well as the kriging-based feasibility analysis methodology. 2^6 Latin Hypercube samples are used in the initial model selection phase. For the ANN method, the initial samples are used and the number of hidden neurons are varied in the initial model selection phase. 8 hidden neurons yield the least sum of squared errors between predicted and target feasibility function values. 500 samples are iteratively added using the adaptive sampling strategy. In terms of the metrics for the model accuracy, 5^6 samples chosen as five level grid samples are tested using

the original model as well as the surrogate models. Subsequently, metrics are computed as explained in Section 7.2. The ANN-based methodology yields 92.7 CF%, 99.8 CIF% and 3.1 NC% compared to 71.6 CF%, 99.7 CIF% and 6.7 NC% obtained from the kriging-based methodology. It is evident that the proposed ANN-based methodology performs significantly better than the kriging-based methodology. In addition to the metrics at the end of adaptive sampling, the metrics are also computed for every 25 adaptive samples added and plotted as shown in Figure 7.22. The plots show that with the addition of adaptive samples, the performance of the ANN as well as kriging models improve. The ANN model is able to capture significantly more feasible regions when compared to the kriging model, which is also accompanied by over-estimation of the feasible regions. However, with the addition of samples, the accuracy of the feasible region boundaries is improved and the over-estimation reduces to a level that is comparable to the conservativeness from the kriging model.

Since this is a high dimensional problem, visualizing the feasible region is a challenge. This is represented using a matrix of contour plots of feasibility function values as shown in Figure 7.23. For each contour plot, only two factors are varied and the remaining two factors are set at operating values. The feasible region boundary predicted by the final ANN model is represented using a red line. Feasible region boundary from the original process model is also plotted using a red dashed line. Good agreement between the original and predicted feasible regions is evident. Based on the feasible region plotting, it can also be interpreted that fill depth and tablet thickness settings should be carefully controlled in the tablet manufacturing process followed by mill impellor speed. The process is largely feasible in the ranges of API and Excipient flow rates, blender blade speed considered.

Table 7.5 Variable bounds for the continuous direct compaction process feasibility case study

Factors	Units	Nominal	LB	UB
API flowrate	kg/h	3	2.85	3.15
Excipient flowrate	kg/h	26.7	25.36	28.03
Mill impeller speed	rpm	1120	1064	1176
Blender blade speed	rpm	250	237.5	262.5
Fill depth	m	0.01	0.0095	0.0105
Thickness	m	0.0025	0.002375	0.002625

Table 7.6 Constraints for the continuous direct compaction process feasibility case study

Unit operation	Variable	Units	Limits based on % of nominal value
Blender	Mean residence time	s	+/- 20%
	Delay time	s	
	Mass hold SS	kg	
	Mean bulk, true density	kg/m ³	
	Mean d10, d50, d90	µm	
Comill	Mean d10, d50, d90	µm	+/-20%
	Mean bulk, true density	kg/m ³	
	Mean residence time	s	
	Mass holdup SS	kg	
	Tablet Press	Concentration	%
	Weight	kg	+/-10%
	Hardness	kp	
	Main compression pressure	MPa	
	Pre compression pressure	MPa	

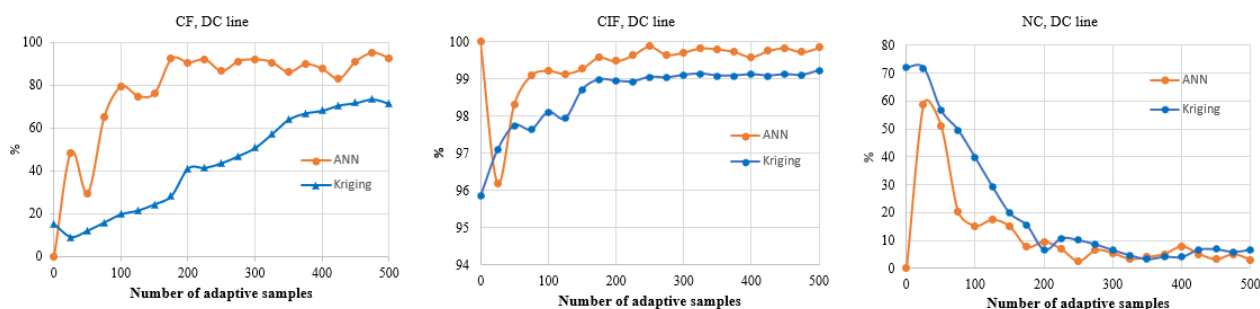


Figure 7.22 Comparison of ANN and Kriging model accuracy validation metrics by number of adaptive samples for the direct compaction process model (a) CF% (b) CIF% (c) NC%

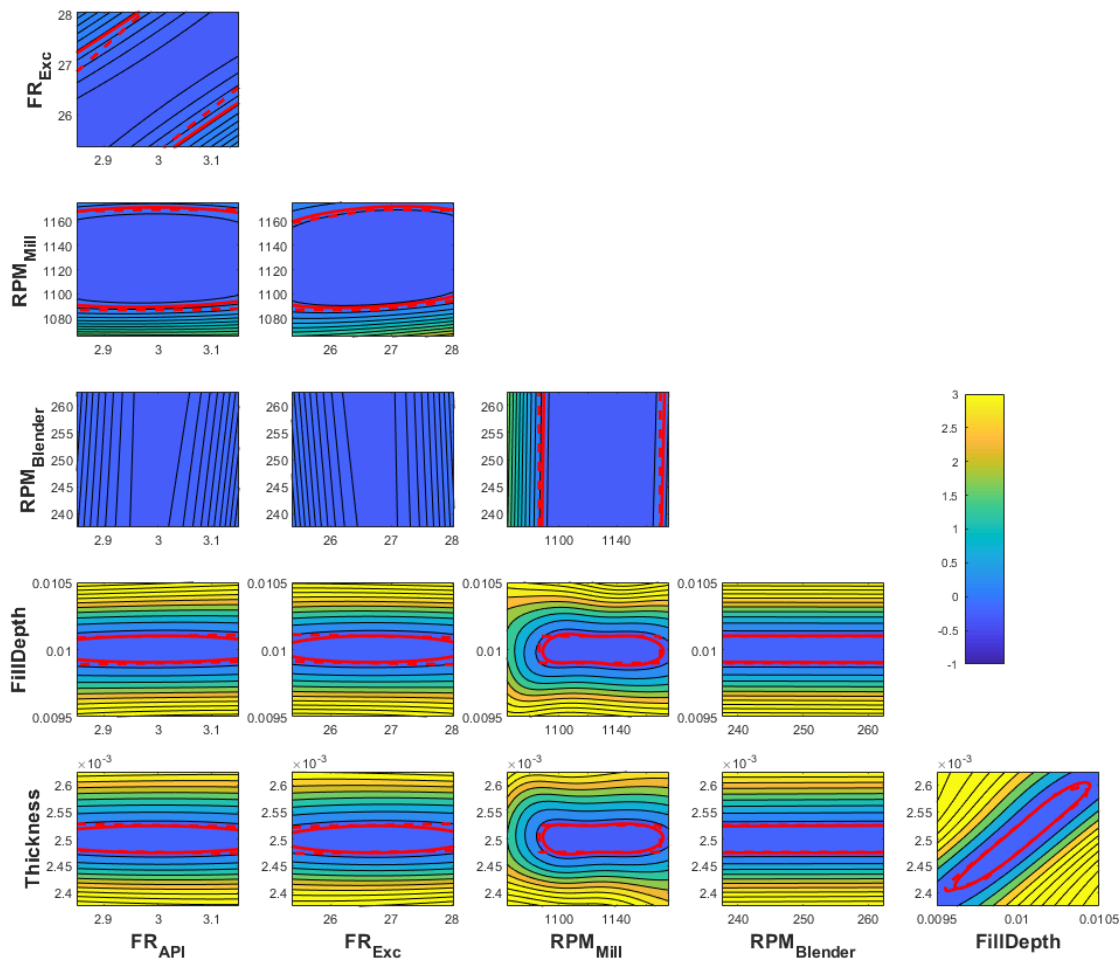


Figure 7.23 Matrix of feasibility function contour plots representing the feasible region of the continuous direct compaction process case study (Feasible region boundary from the original model and predicted by the ANN model are represented as red dashed lines and red solid lines respectively)

7.5 Design space of a continuous wet granulation process

In this section, the effectiveness of the proposed ANN based methodology in the continuous wet granulation manufacturing process is illustrated. The tablet manufacturing process via continuous wet granulation route is explained in detail in Chapter 6. Briefly, in this process, the formulation ingredients in powder form are blended and introduced as feed to a granulation unit. Liquid binder

is added to the granulation unit which aids in the production of uniform granules. The wet granules are dried in a fluidized bed drying unit through contact with hot air for a certain duration. These granules are subsequently broken to smaller sizes in a commilling unit through the action of a rotating impeller. The smaller sized granules are compacted to produce tablets in a tablet press unit. A schematic of the continuous process used in this work is shown in Figure 7.24. For this work, the twin screw granulator, fluidized bed dryer, mill and tablet press units are considered. The unit operations simulated by the process models are developed and validated with experimental data and are explained in detail in Chapter 6. The models are briefly explained here.

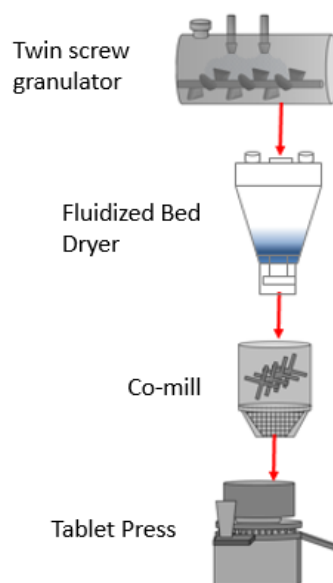


Figure 7.24 Schematic of a continuous wet granulation process

7.5.1 Unit process models

Twin screw granulation

The change in particle size distribution of the powder blend is modeled using a population balance modeling (PBM) approach as described by Van Hauwermeiren, Verstraeten [221] and given in Equation 7.18. Mass flow rate of powder, twin screw speed and liquid to solid ratio (also known

as binder addition rate) are modeled to impact granule aggregation and breakage. Change in number of particles n of size x at time t is modeled through an aggregation kernel $\beta(t, x, \epsilon)$, a breakage selection function $S(\epsilon)$ and breakage distribution function $b(x, \epsilon)$ where ϵ is the volume of the breaking particle. The parameters in the model are linearly related to the process variables i.e., powder mass flow rate, twin screw speed and liquid binder addition rate.

$$\begin{aligned} \frac{\delta n(t, x)}{\delta t} = & \frac{1}{2} \int_0^x (t, x - \epsilon, \epsilon) n(t, x - \epsilon) n(t, \epsilon) d\epsilon \\ & - n(t, x) \int_0^\infty \beta(t, x, \epsilon) n(t, \epsilon) d\epsilon \\ & + \int_x^\infty b(t, x, \epsilon) S(t, \epsilon) n(t, \epsilon) d\epsilon - S(t, x) n(t, x) \end{aligned} \quad 7.18$$

Fluidized bed dryer

The fluidized bed dryer consists of six dryer cells which are subjected to cycles of filling of granules from granulator, drying through hot air and emptying to milling unit. The drying model used in this work predicts properties of batch of granules based on single granule drying kinetics for one dryer cell. The mass transfer rate of liquid layer \dot{m}_v around the granule to the surrounding hot air is given by Equation 7.19, where h_D , $\rho_{v,s}$ and $\rho_{v,\infty}$ are the mass transfer co-efficient, partial vapor density over the droplet surface area A_d , partial vapor density in the ambient air respectively.

$$\dot{m}_v = h_D (\rho_{v,s} - \rho_{v,\infty}) A_d \quad 7.19$$

After this layer of liquid is dried, the remaining moisture is assumed to be a sphere referred to as the wet core. The mass transfer rate in this stage is given by Ghijs, Schäfer [193]. The affect of dryer air temperature and the duration of drying are included in the model using an energy balance. For each dryer cell, the properties of the batch of granules are mass averaged over the filling time in

the dryer. The dried granules are transported to the succeeding comilling unit through a tube pneumatically. Breakage was observed to occur during this transport which is modeled using a population balance model. 7.18 with only the last two terms in the right hand side are applicable here as aggregation does not occur.

Mill

Milling operation which constitutes breakage of granules through a rotating impeller and exit of granules through a screen is modeled using a hybrid modeling approach [164]. A PBM is used to simulate the breakage behavior in the mill and a partial least squares (PLS) model is used to predict granule quality attributes such as bulk density and tapped density. The mass based population balance model used is given in Equation 7.20, where $M(w, t)$ represents the mass of particles of volume w at time t , R_{form} and R_{dep} represent the rates of formation and depletion of particles respectively. \dot{M}_{in} and \dot{M}_{out} are the mass flow rates of particles entering and exiting the mill respectively. R_{form} and R_{dep} are modeled using a breakage kernel $K(w)$ and a breakage distribution function $b(w, u)$ where w and u are the volumes of the parent and daughter particles respectively. The breakage kernel $K(w)$ and mass flow rate exiting the mill \dot{M}_{out} are modeled as a function of impeller speed.

$$\frac{dM(w, t)}{dt} = R_{form}(w, t) - R_{dep}(w, t) + \dot{M}_{in}(w, t) - \dot{M}_{out}(w, t) \quad 7.20$$

The PBM is thus used to predict milled granule size distribution. The PLS model is an empirical modeling approach used to predict the milled product bulk density and tapped density, using the granule size distribution and moisture content as inputs.

Tablet Press

Tensile strength of the tablet is modeled using Equation 7.21 [84], where ρ_{rel} is the relative density of the material defined as the ratio of volume of solid in the tablet and geometric volume of the tablet. Here, ρ_c is the critical density of the material and σ_{max} is the maximum achievable tensile strength. These are obtained through empirical correlations with span of the milled material and moisture content.

$$\sigma = \sigma_{max} \left[\rho_c - \rho_{rel} - \ln \left(\frac{1 - \rho_{rel}}{1 - \rho_c} \right) \right] \quad 7.21$$

The hardness values H are related to tablet tensile strength and tablet and tooling dimensions (thickness T , width W , punch cup depth D) using the Equation 7.22 [196]. The tablet press is operated using a weight control mode.

$$\sigma = \frac{10N}{\pi D^2} \left(2.84 \frac{t}{D} - 0.126 \frac{t}{W} + 3.15 \frac{W}{D} + 0.01 \right)^{-1} \quad 7.22$$

The process models described are used to develop a flowsheet model where relevant information is transferred from a unit model to the downstream units. The flowsheet model is developed in gFormulatedProducts [222] and takes approximately 4.5 minutes to reach steady state.

7.5.2 Feasibility problem for the continuous wet granulation process

The flowsheet model simulating the continuous wet granulation process can be used to capture and study the effects of several process variables. Techniques such as sensitivity analysis can be applied to the flowsheet model for identifying the critical process parameters. The feasible region is then identified considering the chosen critical process parameters as the variable space. For this work,

the factors used to define the feasibility problem are listed in Table 7.7. These factors are chosen based on results of sensitivity analysis performed and published in Metta, Ghijs [219]. Specifically, the factors liquid to solid ratio (LS ratio), dryer air temperature ($Temp_{dryer}$), drying time ($Time_{dryer}$) and mill impeller speed (RPM_{Mill}) are considered. The bounds on these variables, considered as +/- 5% of the operating values are also listed in the table. The process constraints that define the feasible region are listed in Table 7.8. Constraints related to the quality of the granules such as size (d_{10}, d_{50}, d_{90}), moisture content and density are considered. The final tablet hardness value is allowed to vary up to 5% i.e., (84.9 N-93.8 N) from the targeted value of 89.4 N. The feasibility analysis problem thus formulated is solved using the proposed ANN based feasibility analysis methodology. The problem is four-dimensional and has 13 black-box constraints. 2^4 samples from a Latin hypercube sampling scheme are used to build the initial ANN model. As adaptive sampling points are identified, the flowsheet model is called to the MATLAB environment using gOMATLAB. A stopping criteria of 300 adaptive samples is chosen considering the computational expense of the flowsheet model. Due to the high computational expense of the flowsheet model, only 4^4 (= 256) grid samples are run in order to be used as validation points. The feasibility analysis algorithm thus implemented takes approximately 36 h to complete using 3 cores. After exhaustion of the sampling budget, the final ANN model the feasibility metrics are 98.75 CF%, 98.29 CIF% and 3.65 NC%. Since this is a high dimensional problem, the feasible region is represented using a matrix of contour plots of feasibility function values shown in Figure 7.25. For each contour plot, only two factors are varied and the remaining two factors are set at operating values. The feasible region boundary predicted by the final ANN model is represented using a red line. To aid visual analysis of the accuracy of the surrogate model, feasible region boundary from the original flowsheet model for $Time_{dryer}$ and $Temp_{dryer}$ contour plot is also plotted using green dashed line. This is identified using 20^2 runs of the original process model with only $Time_{dryer}$ and $Temp_{dryer}$ as the variables. It is evident that the feasible region boundary

predicted by the ANN model agrees very well with the feasible region boundary per the original flowsheet model. In addition, a better understanding of the feasible region can be achieved by observing the matrix of contour plots. The process is feasible for the range of mill impeller speed considered. Dryer temperature is an important factor that needs to be controlled well for the process to remain in feasible region. Also, the drying time needs to be set based on the dryer air temperature and LS ratio in the granulator. The ranges of feasible operation can thus be easily obtained and understood. In addition, the ANN surrogate model is computationally inexpensive and can be used to test feasibility of operation at desired combinations of the variables.

Table 7.7 Variable bounds for the continuous wet granulation process feasibility case study

Factors	Units	Nominal	LB	UB
LS ratio	kg/kg	0.12	0.114	0.126
Dryer air temperature	deg C	42.1	40	44.2
Drying time	s	450	427.5	472.5
Mill impeller speed	rpm	1000	950	1050

Table 7.8 Constraints for the continuous wet granulation process feasibility case study

Unit operation	Property	Units	Limits based on % of nominal value
Granulator	Mean d10, d50, d90	µm	+/- 10%
Dryer	Mean d10, d50, d90	µm	+/- 10%
	Moisture content	%	
Comill	Mean d10, d50, d90	µm	+/-10%
	Mean bulk density	kg/m ³	
	Mean tapped density	kg/m ³	
Tablet Press	Hardness	kP	+/-5%

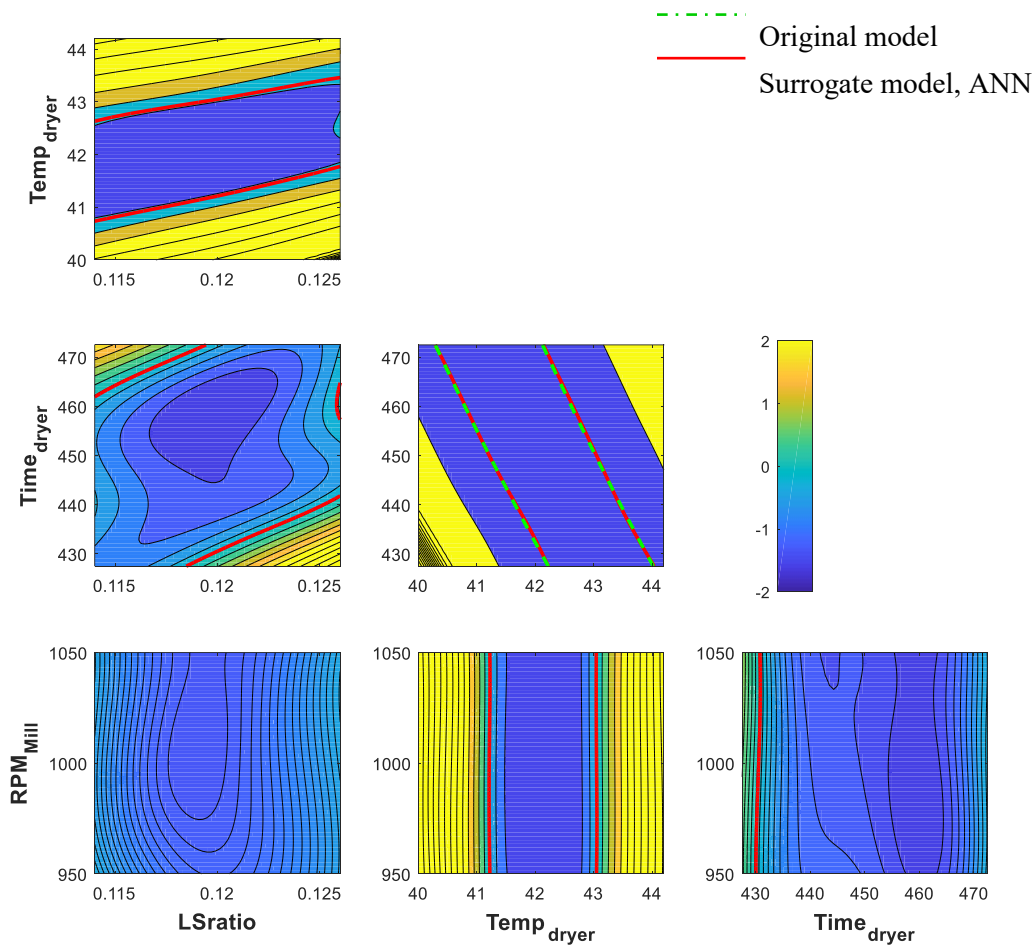


Figure 7.25 Matrix of feasibility function contour plots representing the feasible region of the continuous wet granulation process case study (Feasible region boundary from the original model and predicted by the ANN model are represented as green dashed line and red line respectively)

7.6 Summary

In this work, a novel ANN based methodology is proposed. The methodology utilizes an adaptive sampling technique to identify feasible regions of processes treated as a black-box. The adaptive samples are identified through the maximization of a modified Expected Improvement function.

This requires estimation of the ANN model prediction variance which is estimated using a statistical approach, Jack-knifing. The adaptive sampling allows exploration of the variable space to identify feasible regions and exploitation of the regions to identify the boundaries more accurately. The proposed ANN-based methodology performs better than the Kriging based approach in identifying the feasible region boundaries for two dimensional as well as high dimensional problems. For low dimensional problems, the ANN-based methodology requires lesser or comparable number of adaptive samples than the kriging-based methodology. The accuracy of the identified feasible region boundary is also better for the tested low dimensional problems. For high dimensional problems, the ANN-based methodology performed better than the kriging-based approach for classifying feasible points. The effectiveness of the ANN based methodology is also tested to a realistic pharmaceutical process of a continuous wet granulation that is simulated using a computationally expensive model where constraints are not available in closed form. The proposed ANN-based methodology accurately identifies the feasible region boundary with limited number of samples.

Chapter 8

Conclusions and future work

In this dissertation, several modeling approaches for simulating pharmaceutical drug product manufacturing processes are explored. The strengths of the individual approaches are captured through development of a hybrid modeling framework for a milling process. Several unit process models are integrated to develop a flowsheet model representing the continuous wet granulation pharmaceutical manufacturing process. Process systems engineering tools such as sensitivity analysis and feasibility analysis are implemented to identify the critical process parameters and design space of the process. An efficient methodology to identify design space of high dimensional and computationally expensive models is proposed and applied to the integrated process models.

An outline of the major contributions in this dissertation is given below. Following this, recommendations on areas that need further research focus are given.

- A multi-scale DEM-PBM model which incorporates particle scale information and the effect material properties is developed for a continuous milling process (Chapter 3). The model also accounts for the effect of mill geometry such as screen thickness, aperture size and impeller design. The framework replaces a model that uses an empirical kernel. A methodology to identify the material specific kernel parameters in the model is proposed.
- Computational limitations from inclusion of a high fidelity DEM model is addressed through the development of a surrogate model-PBM framework for a continuous milling process (Chapter 4). The improvement in computational expense is drastic as a DEM simulation takes days to run whereas the developed surrogate model takes few seconds. The hybrid model is implemented in an integrated mill and tablet press model, thus demonstrating its practical applications.

- For a milling process, a framework to predict particle size distributions as well as other CQAs such as bulk and tapped densities is developed using a comprehensive PBM-PLS hybrid modeling approach (Chapter 5), where the parameters are identified using experimental data. The hybrid model addresses the need to predict the bulk properties as they affect flowability, segregation and tableability of granules in the downstream tablet press compaction process.
- An integrated process model simulating a plant scale continuous tablet manufacturing process through wet granulation is developed (Chapter 6). The flowsheet model is based on models that are developed from experimental runs on units included in the continuous line using the same formulation and materials. The model is used to successfully demonstrate the effect of changes in the process variables on product properties through case studies. The model is also used to identify critical process variables that affect intermediate and final product quality. Overall, the developed flowsheet model is a prerequisite for identification of design space and optimization of the continuous line.
- A neural network based adaptive sampling methodology is developed (Chapter 7) to identify design space of low as well as high dimensional problems. The methodology is shown to be more efficient and accurate than a kriging-based approach for several test problems and case studies. The methodology is successfully applied for identifying the design space of integrated pharmaceutical process models including the flowsheet model developed in Chapter 6. The models are high dimensional, computationally expensive and do not have constraints in closed form, which are considered difficult to solve.

Based on the extensive research in this dissertation, below are few recommendations on the directions in which future research work could be focused on:

- The research work in this dissertation focused on incorporating the effect of material properties on the breakage kernel of a PBM. The other elements in the PBM such as the form of the distribution function (eg., normal distribution, log-normal distribution, specialized distributions) are still chosen on a heuristic basis. Research work on establishing a mechanistic basis for the choice of distribution function is an important area that merits focus.
- Currently, the DEM-PBM or the SM-PBM framework established in this dissertation is based on one-way coupling, i.e., DEM simulations are run for a specific amount of time and mechanistic data is used as input to the PBM. The idea is to include the effects of proximity of particles to the screen. It is interesting to compare this performance to a two-way coupling approach [223], where DEM simulations are run for a fixed time step. The required mechanistic data is given as input to the PBM and particle size distribution is updated at the end of the time step through the PBM. The updated particle size distribution can be used as input to the DEM simulations again at the end of every time step. The coupling approach is expected to be cumbersome and does not capture the effects of particle positioning relative to the screen on the particle population inside the mill. However, the computational burden on the DEM simulations is lowered due to absence of breakage implementation. A trade-off between computational burden and the effect of the particle proximity to the screen on the results can be explored.
- In this dissertation, artificial neural network models are used as the surrogate model for implementing the feasibility analysis methodology using adaptive sampling. An important aspect of this methodology is the use of a statistical approach for estimation of surrogate model prediction uncertainty. This is interesting as the methodology for variance estimation is independent of the type of surrogate model used. This allows exploring other surrogate models for identifying the feasible region.

- The feasibility analysis methodology proposed in this dissertation is tested on deterministic scenarios i.e., the original process model does not consider probabilistic uncertainties that may be associated with the model parameters. In stochastic scenarios, several model evaluations may be needed to map the feasible region boundaries as well as variance in the process responses. Further work is required to evaluate the applicability of the ANN model in such cases.
- Another area of research focus includes determination of a suitable stopping criteria for the feasibility analysis methodology. Currently, a fixed sampling budget is used as the stopping criteria. An alternative stopping criteria that is based on model performance would help choose the number of samples needed on the basis of the problem to be solved.

Acknowledgement of prior publications

Several chapters of the thesis have been published or being prepared for publications. Parts of the publications are modified to avoid redundancy and improve readability. The following publications are acknowledged.

Parts of Chapter 2 are being prepared for publication under the citations

- Metta, N., Yohannes, B., Kotamarthy, L., Ramachandran, R., Romañach, R., & Cuitino, A. Roller compaction
- Metta, N., Ierapetritou, M. Developing process models of an open-loop integrated system

Parts of Chapter 3 have been published under the citation

- Metta, N., Ierapetritou, M., & Ramachandran, R. (2018). A multiscale DEM-PBM approach for a continuous comilling process using a mechanistically developed breakage kernel. *Chemical Engineering Science*, 178, 211-221.

Chapter 4 has been published under the citation

- Metta, N., Ramachandran, R., & Ierapetritou, M. (2019). A Computationally Efficient Surrogate-Based Reduction of a Multiscale Comill Process Model. *Journal of Pharmaceutical Innovation*.

Chapter 5 has been published under the citation

- Metta, N., Verstraeten, M., Ghijs, M., Kumar, A., Schafer, E., Singh, R., . . . Ramachandran, R. (2018). Model development and prediction of particle size distribution, density and friability of a comilling operation in a continuous pharmaceutical manufacturing process. *International Journal of Pharmaceutics*, 549(1), 271-282.

Chapter 6 has been published under the citation

- Metta, N., Ghijs, M., Schäfer, E., Kumar, A., Cappuyns, P., Van Assche, I., . . . Nopens, I. (2019). Dynamic Flowsheet Model Development and Sensitivity Analysis of a Continuous Pharmaceutical Tablet Manufacturing Process Using the Wet Granulation Route. *Processes*, 7(4), 234.

Chapter 7 is being prepared for publication under the citations

- Metta, N., Ramachandran, R., & Ierapetritou, M. A Novel Adaptive Sampling Based Methodology for Feasible Region Identification of Expensive Models Using Neural Networks.
- Bhalode, P., Metta, N., Chen, Yingjie., & Ierapetritou, M. Efficient Data-based Methodology for Model enhancement and Flowsheet analyses for Continuous Pharmaceutical Manufacturing

Bibliography

1. Fisher, A.C., et al., Advancing pharmaceutical quality: An overview of science and research in the U.S. FDA's Office of Pharmaceutical Quality. *International Journal of Pharmaceutics*, 2016. **515**(1): p. 390-402.
2. Lee, S.L., et al., Modernizing Pharmaceutical Manufacturing: from Batch to Continuous Production. *Journal of Pharmaceutical Innovation*, 2015. **10**(3): p. 191-199.
3. Rockoff, J.D., Drug making breaks away from its old ways. *The Wall Street Journal*, 2015. **8**.
4. Yu, L.X. and M. Kopcha, The future of pharmaceutical quality and the path to get there. *International Journal of Pharmaceutics*, 2017. **528**(1): p. 354-359.
5. Teżyk, M., et al., Recent progress in continuous and semi-continuous processing of solid oral dosage forms: a review. *Drug Development and Industrial Pharmacy*, 2016. **42**(8): p. 1195-1214.
6. Shah, N., Pharmaceutical supply chains: key issues and strategies for optimisation. *Computers & Chemical Engineering*, 2004. **28**(6): p. 929-941.
7. Contract Pharma. Solid Dosage Manufacturing Trends. 2015–2018]; Available from: https://www.contractpharma.com/issues/2015-03-01/view_features/solid-dosage-manufacturing-trends--724749.
8. Lee, S. Present and Future for Continuous Manufacturing: FDA perspective. in 3rd FDA/PQRI Conference on Advancing Product Quality. 2017.
9. Matsunami, K., et al., Decision Support Method for the Choice between Batch and Continuous Technologies in Solid Drug Product Manufacturing. *Industrial & Engineering Chemistry Research*, 2018. **57**(30): p. 9798-9809.
10. Schaber, S.D., et al., Economic Analysis of Integrated Continuous and Batch Pharmaceutical Manufacturing: A Case Study. *Industrial & Engineering Chemistry Research*, 2011. **50**(17): p. 10083-10092.
11. Badman, C. and B.L. Trout, Achieving Continuous Manufacturing. May 20–21, 2014 Continuous Manufacturing Symposium. *Journal of Pharmaceutical Sciences*, 2015. **104**(3): p. 779-780.
12. Wang, Z., M.S. Escotet-Espinoza, and M. Ierapetritou, Process analysis and optimization of continuous pharmaceutical manufacturing using flowsheet models. *Computers & Chemical Engineering*, 2017.
13. Galbraith, S.C., et al., Flowsheet Modeling of a Continuous Direct Compression Tableting Process at Production Scale. *Proceedings of the Foundations of Computer Aided Process Operations/Chemical Process Control*, Tucson, AZ, USA, 2017: p. 8-12.
14. García-Muñoz, S., et al., A flowsheet model for the development of a continuous process for pharmaceutical tablets: An industrial perspective. *AIChE Journal*, 2018. **64**(2): p. 511-525.
15. Park, S.-Y., et al., Prediction of critical quality attributes and optimization of continuous dry granulation process via flowsheet modeling and experimental validation. *Powder technology*, 2018. **330**: p. 461-470.
16. Escotet-Espinoza, M.S., et al., Flowsheet Models Modernize Pharmaceutical Manufacturing Design and Risk Assessment. *Pharmaceutical Technology*, 2015. **39**(4): p. 34-42.
17. FDA, U., Guidance for Industry. Q8 (R2) Pharmaceutical Development. 2009, Department of Human and Human Services, Silver Spring, MD, USA.
18. Yu, L.X., et al., Understanding Pharmaceutical Quality by Design. *The AAPS Journal*, 2014. **16**(4): p. 771-783.
19. Rogers, A., Process systems engineering methods for the development of continuous pharmaceutical manufacturing processes. 2015.

20. Samanta, A.K., K.Y. Ng, and P.W.S. Heng, Cone milling of compacted flakes: Process parameter selection by adopting the minimal fines approach. *International Journal of Pharmaceutics*, 2012. **422**(1-2): p. 17-23.
21. Yin, S.X., et al., Bioavailability enhancement of a COX-2 inhibitor, BMS-347070, from a nanocrystalline dispersion prepared by spray-drying. *Journal of Pharmaceutical Sciences*, 2005. **94**(7): p. 1598-1607.
22. Loh, Z.H., A.K. Samanta, and P.W.S. Heng, Overview of milling techniques for improving the solubility of poorly water-soluble drugs. *Asian journal of pharmaceutical sciences*, 2015. **10**: p. 255-274.
23. M., A., Assessment of biopharmaceutical properties, in *Pharmaceutics: the science of dosage form design*, A. M, Editor. 2002, Churchill Livingstone: London. p. 253-273.
24. Naik, S. and B. Chauduri, Quantifying Dry Milling in Pharmaceutical Processing: A Review on Experimental and Modeling Approaches. *Journal of Pharmaceutical Sciences*, 2015. **104**: p. 2401-2413.
25. Pinder, R.M., *Fundamentals of Early Clinical Drug Development. From Synthesis Design to Formulation* Edited by AF Abdel-Magid and Stéphane Caron. John Wiley & Sons, New York. 2006. xv+ 323 pp. 16× 24 cm. ISBN 0-471-69278-6. \$99.95. 2006, ACS Publications.
26. Vanarase, A., et al., Effects of mill design and process parameters in milling dry extrudates. *Powder Technology*, 2015. **278**: p. 84-93.
27. Yu, S., et al., Experimental Investigation of Milling of Roll Compacted Ribbons, in *Particulate Materials: Synthesis, Characterisation, Processing and Modelling*. 2012, The Royal Society of Chemistry. p. 158-166.
28. Parrott, E.L., Milling of pharmaceutical solids. *Journal of Pharmaceutical Sciences*, 1974. **63**(6): p. 813-829.
29. Heywood, H., Some notes on grinding research. 1950.
30. Shekunov, B.Y., et al., Particle Size Analysis in Pharmaceutics: Principles, Methods and Applications. *Pharmaceutical Research*, 2007. **24**(2): p. 203-227.
31. Merkus, H.G., Particle size measurements: fundamentals, practice, quality. Vol. 17. 2009: Springer Science & Business Media.
32. Silva, A.F.T., et al., Particle sizing measurements in pharmaceutical applications: Comparison of in-process methods versus off-line methods. *European Journal of Pharmaceutics and Biopharmaceutics*, 2013. **85**(3, Part B): p. 1006-1018.
33. Chan, L.W., L.H. Tan, and P.W.S. Heng, Process Analytical Technology: Application to Particle Sizing in Spray Drying. *AAPS PharmSciTech*, 2008. **9**(1): p. 259-266.
34. Sangshetti, J.N., et al., Quality by design approach: Regulatory need. *Arabian Journal of Chemistry*, 2014.
35. De Beer, T., et al., Near infrared and Raman spectroscopy for the in-process monitoring of pharmaceutical production processes. *International Journal of Pharmaceutics*, 2011. **417**(1): p. 32-47.
36. Vercruyse, J., et al., Continuous twin screw granulation: Influence of process variables on granule and tablet quality. *European Journal of Pharmaceutics and Biopharmaceutics*, 2012. **82**: p. 205-211.
37. Wei Meng, et al., Statistical analysis and comparison of a continuous high shear granulator with a twin screw granulator: Effect of process parameters on critical granule attributes and granulation mechanisms. *International Journal of Pharmaceutics*, 2016. **513**: p. 357-375.
38. Vendola, T.A. and B.C. Hancock, The effect of mill type on two dry-granulated placebo formulations. *Pharmaceutical Technology*, 2008. **32**(11): p. 72-86.
39. Schenck, L.R. and R.V. Plank, Impact milling of pharmaceutical agglomerates in the wet and dry states. *International Journal of Pharmaceutics*, 2008. **348**(1): p. 18-26.

40. Verheezzen, J.J.A.M., et al., Milling of agglomerates in an impact mill. *International Journal of Pharmaceutics*, 2004. **278**(1): p. 165-172.
41. Samanta, A.K., K.Y. Ng, and P.W.S. Heng, Cone milling of compacted flakes: Process parameter selection by adopting the minimal fines approach. *International Journal of Pharmaceutics*, 2012. **422**(1): p. 17-23.
42. Kumar Akkisetty, P., et al., Population Balance Model-Based Hybrid Neural Network for a Pharmaceutical Milling Process. *Journal of Pharmaceutical Innovation*, 2010. **5**(4): p. 161-168.
43. Reynolds, G.K., Modelling of pharmaceutical granule size reduction in a conical screen mill. *Chemical Engineering Journal*, 2010. **164**(2-3): p. 383-392.
44. Barrasso, D., et al., Population Balance Model Validation and Prediction of CQAs for Continuous Milling Processes: toward QbD in Pharmaceutical Drug Product Manufacturing. *Journal of Pharmaceutical Innovation*, 2013. **8**(3): p. 147-162.
45. Wang, M.H., R.Y. Yang, and A.B. Yu, DEM investigation of energy distribution and particle breakage in tumbling ball mills. *Powder Technology*, 2012. **223**: p. 83-91.
46. Cleary, P.W., M.D. Sinnott, and R.D. Morrison, DEM prediction of particle flows in grinding processes. *International Journal for Numerical Methods in Fluids*, 2008. **58**(3): p. 319-353.
47. Zhang, C.S., G.D. Nguyen, and J. Kodikara, An application of breakage mechanics for predicting energy-size reduction relationships in comminution. *Powder Technology*, 2016. **287**: p. 121-130.
48. Weerasekara, N.S., et al., The contribution of DEM to the science of comminution. *Powder Technology*, 2013. **248**: p. 3-24.
49. Kotake, N., et al., Experimental study on the grinding rate constant of solid materials in a ball mill. *Powder Technology*, 2002. **122**(2-3): p. 101-108.
50. Mishra, B.K. and R.K. Rajamani, SIMULATION OF CHARGE MOTION IN BALL MILLS .1. EXPERIMENTAL VERIFICATIONS. *International Journal of Mineral Processing*, 1994. **40**(3-4): p. 171-186.
51. Bonfils, B., G.R. Ballantyne, and M.S. Powell, Developments in incremental rock breakage testing methodologies and modelling. *International Journal of Mineral Processing*, 2016. **152**: p. 16-25.
52. Deng, X., et al., Discrete element method simulation of a conical screen mill: A continuous dry coating device. *Chemical Engineering Science*, 2015. **125**: p. 58-74.
53. Capece, M., E. Bilgili, and R. Dave, Insight into first-order breakage kinetics using a particle-scale breakage rate constant. *Chemical Engineering Science*, 2014. **117**: p. 318-330.
54. Capece, M., E. Bilgili, and R.N. Dave, Formulation of a physically motivated specific breakage rate parameter for ball milling via the discrete element method. *Aiche Journal*, 2014. **60**(7): p. 2404-2415.
55. Wang, Y.F., et al., Predicting feeder performance based on material flow properties. *Powder Technology*, 2017. **308**: p. 135-148.
56. Boukouvala, F., F.J. Muzzio, and M.G. Ierapetritou, Design Space of Pharmaceutical Processes Using Data-Driven-Based Methods. *Journal of Pharmaceutical Innovation*, 2010. **5**(3): p. 119-137.
57. Rogers, A. and M.G. Ierapetritou, Discrete element reduced-order modeling of dynamic particulate systems. *AIChE Journal*, 2014. **60**(9): p. 3184-3194.
58. Liu, X.Y., et al., DEM study on the surface mixing and whole mixing of granular materials in rotary drums. *Powder Technology*, 2017. **315**: p. 438-444.
59. Sarkar, A. and C.R. Wassgren, Effect of Particle Size on Flow and Mixing in a Bladed Granular Mixer. *Aiche Journal*, 2015. **61**(1): p. 46-57.
60. Boukouvala, F., et al., Reduced-order discrete element method modeling. *Chemical Engineering Science*, 2013. **95**: p. 12-26.

61. Sen, M., et al., Multi-scale flowsheet simulation of an integrated continuous purification-downstream pharmaceutical manufacturing process. *International Journal of Pharmaceutics*, 2013. **445**(1-2): p. 29-38.
62. Oka, S., et al., The effects of improper mixing and preferential wetting of active and excipient ingredients on content uniformity in high shear wet granulation. *Powder Technology*, 2015. **278**: p. 266-277.
63. X. Liu, L. and J. D. Litster, Population balance modelling of granulation with a physically based coalescence kernel. *Chemical Engineering Science*, 2002. **57**(12): p. 2183-2191.
64. Immanuel, C.D. and F.J. Doyle, Solution technique for a multi-dimensional population balance model describing granulation processes. *Powder Technology*, 2005. **156**(2): p. 213-225.
65. Poon, J.M.H., et al., A three-dimensional population balance model of granulation with a mechanistic representation of the nucleation and aggregation phenomena. *Chemical Engineering Science*, 2008. **63**(5): p. 1315-1329.
66. Hapgood, K.P., J.D. Litster, and R. Smith, Nucleation regime map for liquid bound granules. *Aiche Journal*, 2003. **49**(2): p. 350-361.
67. Barrasso, D. and R. Ramachandran, Qualitative Assessment of a Multi-Scale, Compartmental PBM-DEM Model of a Continuous Twin-Screw Wet Granulation Process. *Journal of Pharmaceutical Innovation*, 2016. **11**(3): p. 231-249.
68. Cameron, I.T., et al., Process systems modelling and applications in granulation: A review. *Chemical Engineering Science*, 2005. **60**(14): p. 3723-3750.
69. Madec, L., L. Falk, and E. Plasari, Modelling of the agglomeration in suspension process with multidimensional kernels. *Powder Technology*, 2003. **130**(1): p. 147-153.
70. Matsoukas, T., T. Kim, and K. Lee, Bicomponent aggregation with composition-dependent rates and the approach to well-mixed state. *Chemical Engineering Science*, 2009. **64**(4): p. 787-799.
71. Barrasso, D. and R. Ramachandran, A comparison of model order reduction techniques for a four-dimensional population balance model describing multi-component wet granulation processes. *Chemical Engineering Science*, 2012. **80**: p. 380-392.
72. Barrasso, D., A. Tamrakar, and R. Ramachandran, Model Order Reduction of a Multi-scale PBM-DEM Description of a Wet Granulation Process via ANN. *Procedia Engineering*, 2015. **102**: p. 1295-1304.
73. Mortier, S., et al., Mechanistic modelling of fluidized bed drying processes of wet porous granules: A review. *European Journal of Pharmaceutics and Biopharmaceutics*, 2011. **79**(2): p. 205-225.
74. Mezhericher, M., A. Levy, and I. Borde, Theoretical drying model of single droplets containing insoluble or dissolved solids. *Drying Technology*, 2007. **25**(4-6): p. 1025-1032.
75. Mortier, S., et al., Mechanistic modelling of the drying behaviour of single pharmaceutical granules. *European Journal of Pharmaceutics and Biopharmaceutics*, 2012. **80**(3): p. 682-689.
76. Mortier, S., et al., Reduction of a Single Granule Drying Model: an Essential Step in Preparation of a Population Balance Model with a Continuous Growth Term. *Aiche Journal*, 2013. **59**(4): p. 1127-1138.
77. Aghbashlo, M., S. Hosseinpour, and A.S. Mujumdar, Application of Artificial Neural Networks (ANNs) in Drying Technology: A Comprehensive Review. *Drying Technology*, 2015. **33**(12): p. 1397-1462.
78. Ketterhagen, W.R., Simulation of powder flow in a lab-scale tablet press feed frame: Effects of design and operating parameters on measures of tablet quality. *Powder Technology*, 2015. **275**: p. 361-374.

79. Mateo-Ortiz, D. and R. Mendez, Microdynamic analysis of particle flow in a confined space using DEM: The feed frame case. *Advanced Powder Technology*, 2016. **27**(4): p. 1597-1606.
80. Mateo-Ortiz, D. and R. Mendez, Relationship between residence time distribution and forces applied by paddles on powder attrition during the die filling process. *Powder Technology*, 2015. **278**: p. 111-117.
81. Boukouvala, F., et al., An integrated approach for dynamic flowsheet modeling and sensitivity analysis of a continuous tablet manufacturing process. *Computers & Chemical Engineering*, 2012. **42**: p. 30-47.
82. Mendez, R., F. Muzzio, and C. Velazquez, Study of the effects of feed frames on powder blend properties during the filling of tablet press dies. *Powder Technology*, 2010. **200**(3): p. 105-116.
83. Patel, S., A.M. Kaushal, and A.K. Bansal, Effect of particle size and compression force on compaction behavior and derived mathematical parameters of compressibility. *Pharmaceutical Research*, 2007. **24**(1): p. 111-124.
84. Kuentz, M. and H. Leuenberger, A new model for the hardness of a compacted particle system, applied to tablets of pharmaceutical polymers. *Powder technology*, 2000. **111**(1-2): p. 145-153.
85. Paul, S. and C.C. Sun, The suitability of common compressibility equations for characterizing plasticity of diverse powders. *International Journal of Pharmaceutics*, 2017. **532**(1): p. 124-130.
86. Singh, R., K.V. Gernaey, and R. Gani, ICAS-PAT: A software for design, analysis and validation of PAT systems. *Computers & Chemical Engineering*, 2010. **34**(7): p. 1108-1136.
87. Escotet-Espinoza, M.S., et al., Modeling the effects of material properties on tablet compaction: A building block for controlling both batch and continuous pharmaceutical manufacturing processes. *International Journal of Pharmaceutics*, 2018. **543**(1): p. 274-287.
88. Ramachandran, R., et al., Model-Based Control-Loop Performance of a Continuous Direct Compaction Process. *Journal of Pharmaceutical Innovation*, 2011. **6**(4): p. 249-263.
89. Rogers, A.J., C. Inamdar, and M.G. Ierapetritou, An Integrated Approach to Simulation of Pharmaceutical Processes for Solid Drug Manufacture. *Industrial & Engineering Chemistry Research*, 2014. **53**(13): p. 5128-5147.
90. Boukouvala, F., et al., Computer-aided flowsheet simulation of a pharmaceutical tablet manufacturing process incorporating wet granulation. *Journal of Pharmaceutical Innovation*, 2013. **8**(1): p. 11-27.
91. Souihi, N., et al., Design Space Estimation of the Roller Compaction Process. *Industrial & Engineering Chemistry Research*, 2013. **52**(35): p. 12408-12419.
92. Chatzizacharia, K.A. and D.T. Hatzivramidis, Design Space Approach for Pharmaceutical Tablet Development. *Industrial & Engineering Chemistry Research*, 2014. **53**(30): p. 12003-12009.
93. Debevec, V., S. Srčić, and M. Horvat, Scientific, statistical, practical, and regulatory considerations in design space development. *Drug development and industrial pharmacy*, 2018. **44**(3): p. 349-364.
94. Grossmann, I.E., B.A. Calfa, and P. Garcia-Herreros, Evolution of concepts and models for quantifying resiliency and flexibility of chemical processes. *Computers & Chemical Engineering*, 2014. **70**: p. 22-34.
95. Grossmann, I.E. and M. Morari, Operability, resiliency, and flexibility: process design objectives for a changing world. 1983.
96. Halemane, K.P. and I.E. Grossmann, Optimal process design under uncertainty. *AIChE Journal*, 1983. **29**(3): p. 425-433.
97. Grossmann, I.E. and C.A. Floudas, Active constraint strategy for flexibility analysis in chemical processes. *Computers & Chemical Engineering*, 1987. **11**(6): p. 675-693.

98. Laky, D., et al., An Optimization-Based Framework to Define the Probabilistic Design Space of Pharmaceutical Processes with Model Uncertainty. *Processes*, 2019. **7**(2): p. 96.
99. Goyal, V. and M.G. Ierapetritou, Determination of operability limits using simplicial approximation. *AIChE Journal*, 2002. **48**(12): p. 2902-2909.
100. Banerjee, I. and M.G. Ierapetritou, Feasibility Evaluation of Nonconvex Systems Using Shape Reconstruction Techniques. *Industrial & Engineering Chemistry Research*, 2005. **44**(10): p. 3638-3647.
101. Banerjee, I., S. Pal, and S. Maiti, Computationally efficient black-box modeling for feasibility analysis. *Computers & Chemical Engineering*, 2010. **34**(9): p. 1515-1521.
102. Kucherenko, S., et al., Computationally efficient identification of probabilistic design spaces through application of metamodeling and adaptive sampling. *Computers & Chemical Engineering*, 2020. **132**: p. 106608.
103. Rogers, A. and M. Ierapetritou, Feasibility and flexibility analysis of black-box processes Part 1: Surrogate-based feasibility analysis. *Chemical Engineering Science*, 2015. **137**: p. 986-1004.
104. Wang, Z. and M. Ierapetritou, A novel feasibility analysis method for black-box processes using a radial basis function adaptive sampling approach. *AIChE Journal*, 2017. **63**(2): p. 532-550.
105. Xu, L., et al., Application of Population Balance Model in the Simulation of Slurry Bubble Column. *Industrial & Engineering Chemistry Research*, 2014. **53**(12): p. 4922-4930.
106. Lichter, J., et al., New developments in cone crusher performance optimization. *Minerals Engineering*, 2009. **22**(7-8): p. 613-617.
107. Choi, K.Y., X. Zhao, and S.H. Tang, POPULATION BALANCE MODELING FOR A CONTINUOUS GAS-PHASE OLEFIN POLYMERIZATION REACTOR. *Journal of Applied Polymer Science*, 1994. **53**(12): p. 1589-1597.
108. Nagy, Z.K., M. Fujiwara, and R.D. Braatz, Modelling and control of combined cooling and antisolvent crystallization processes. *Journal of Process Control*, 2008. **18**(9): p. 856-864.
109. Klimpel, R.R. and L.G. Austin, The back-calculation of specific rates of breakage from continuous mill data. *Powder Technology*, 1984. **38**(1): p. 77-91.
110. Rogers, A. and M. Ierapetritou, Challenges and opportunities in modeling pharmaceutical manufacturing processes. *Computers & Chemical Engineering*, 2015. **81**: p. 32-39.
111. Barrasso, D., et al., Population Balance Model Validation and Prediction of CQAs for Continuous Milling Processes: toward QbD in Pharmaceutical Drug Product Manufacturing. *Journal of Pharmaceutical Innovation*, 2013. **8**(3): p. 147-162.
112. Meier, M., et al., Generally applicable breakage functions derived from single particle comminution data. *Powder Technology*, 2009. **194**(1): p. 33-41.
113. Epstein, B., Logarithmico-Normal Distribution in Breakage of Solids. *Industrial & Engineering Chemistry*, 1948. **40**(12): p. 2289-2291.
114. Falola, A., A. Borissova, and X.Z. Wang, Extended method of moment for general population balance models including size dependent growth rate, aggregation and breakage kernels. *Computers & Chemical Engineering*, 2013. **56**: p. 1-11.
115. Weerasekara, N.S., L.X. Liu, and M.S. Powell, Estimating energy in grinding using DEM modelling. *Minerals Engineering*, 2016. **85**: p. 23-33.
116. Deng, X.L., et al., Discrete element method simulation of a conical screen mill: A continuous dry coating device. *Chemical Engineering Science*, 2015. **125**: p. 58-74.
117. Cundall, P.A. and O.D.L. Strack, DISCRETE NUMERICAL MODEL FOR GRANULAR ASSEMBLIES. *Geotechnique*, 1979. **29**(1): p. 47-65.
118. Mindlin, R.D., Compliance of elastic bodies in contact. *ASME Journal of Applied Mechanics*, 1949. **16**: p. 259-268.

119. Hertz, H., *J. reine angew. Math.* 92, 156. Reprinted. English, in Hertz's Miscellaneous paper, 1881.
120. O'Sullivan, C. and L. Cui, Micromechanics of granular material response during load reversals: Combined DEM and experimental study. *Powder Technology*, 2009. **193**(3): p. 289-302.
121. Marigo, M., et al., A numerical comparison of mixing efficiencies of solids in a cylindrical vessel subject to a range of motions. *Powder Technology*, 2012. **217**(Supplement C): p. 540-547.
122. Maione, R., et al., Axial segregation of a binary mixture in a rotating tumbler with non-spherical particles: Experiments and DEM model validation. *Powder Technology*, 2017. **306**: p. 120-129.
123. Flores-Johnson, E.A., et al., Discrete element simulation of dynamic behaviour of partially saturated sand. *International Journal of Mechanics and Materials in Design*, 2016. **12**(4): p. 495-507.
124. Hovad, E., et al., Simulating the DISAMATIC process using the discrete element method - a dynamical study of granular flow. *Powder Technology*, 2016. **303**: p. 228-240.
125. Datta, A. and R.K. Rajamani, A direct approach of modeling batch grinding in ball mills using population balance principles and impact energy distribution. *International Journal of Mineral Processing*, 2002. **64**(4): p. 181-200.
126. Cleary, P.W., Recent advances in dem modelling of tumbling mills. *Minerals Engineering*, 2001. **14**(10): p. 1295-1319.
127. Vogel, L. and W. Peukert, Breakage behaviour of different materials—construction of a mastercurve for the breakage probability. *Powder Technology*, 2003. **129**(1–3): p. 101-110.
128. Loreti, S., et al., DEM-PBM Modeling of Impact Dominated Ribbon Milling. *Aiche Journal*, 2017. **63**(9): p. 3692-3705.
129. DEM, S., *EDEM 2.7 Programming Guide, Revision 0*. 2015: Edinburgh, UK.
130. Saltelli, A., S. Tarantola, and F. Campolongo, Sensitivity analysis as an ingredient of modeling. *Statistical Science*, 2000. **15**(4): p. 377-395.
131. Ramachandran, R., et al., A mechanistic model for breakage in population balances of granulation: Theoretical kernel development and experimental validation. *Chemical Engineering Research & Design*, 2009. **87**(4A): p. 598-614.
132. Cryer, S.A. and P.N. Scherer, Observations and process parameter sensitivities in fluid-bed granulation. *Aiche Journal*, 2003. **49**(11): p. 2802-2809.
133. Saltelli, A., et al., Variance based sensitivity analysis of model output. Design and estimator for the total sensitivity index. *Computer Physics Communications*, 2010. **181**(2): p. 259-270.
134. Saltelli, A., Making best use of model evaluations to compute sensitivity indices. *Computer Physics Communications*, 2002. **145**(2): p. 280-297.
135. Rao, K.S., Understanding the relationship between process parameters and critical quality attributes of tablets produced by batch and continuous granulation for a low-dose caffeine formulation using design of experiments approach. 2017.
136. Vogel, L. and W. Peukert, Modelling of Grinding in an Air Classifier Mill Based on a Fundamental Material Function. *KONA Powder and Particle Journal*, 2003. **21**: p. 109-120.
137. Capece, M., E. Bilgili, and R. Dave, Identification of the breakage rate and distribution parameters in a non-linear population balance model for batch milling. *Powder Technology*, 2011. **208**(1): p. 195-204.
138. Austin, L.G. and P. Bagga, An analysis of fine dry grinding in ball mills. *Powder Technology*, 1981. **28**(1): p. 83-90.
139. Austin, L.G., et al., An analysis of ball-and-race milling. Part I. The hardgrove mill. *Powder Technology*, 1981. **29**(2): p. 263-275.

140. Delaney, G.W., et al., Predicting breakage and the evolution of rock size and shape distributions in Ag and SAG mills using DEM. *Minerals Engineering*, 2013. **50–51**: p. 132-139.
141. Meng, W., et al., Statistical analysis and comparison of a continuous high shear granulator with a twin screw granulator: Effect of process parameters on critical granule attributes and granulation mechanisms. *International Journal of Pharmaceutics*, 2016. **513**(1): p. 357-375.
142. Bouhlel, M.A., et al., Improving kriging surrogates of high-dimensional design models by Partial Least Squares dimension reduction. *Structural and Multidisciplinary Optimization*, 2016. **53**(5): p. 935-952.
143. Forrester, A.I.J. and A.J. Keane, Recent advances in surrogate-based optimization. *Progress in Aerospace Sciences*, 2009. **45**(1): p. 50-79.
144. Bhosekar, A. and M. Ierapetritou, Advances in surrogate based modeling, feasibility analysis, and optimization: A review. *Computers & Chemical Engineering*, 2018. **108**: p. 250-267.
145. Shvartsman, S.Y., et al., Order reduction of nonlinear dynamic models for distributed reacting systems. *Dynamics & Control of Process Systems 1998, Volumes 1 and 2*, ed. C. Georgakis. 1999. 637-644.
146. Wang, Z. and M. Ierapetritou, Surrogate-based feasibility analysis for black-box stochastic simulations with heteroscedastic noise. *Journal of Global Optimization*, 2018: p. 1-29.
147. Jia, Z., et al., Predictive Modeling for Pharmaceutical Processes Using Kriging and Response Surface. *Journal of Pharmaceutical Innovation*, 2009. **4**(4): p. 174-186.
148. Lang, Y.D., et al., Reduced Order Model Based on Principal Component Analysis for Process Simulation and Optimization. *Energy & Fuels*, 2009. **23**(3-4): p. 1695-1706.
149. Fei, Y., et al., Evaluation of the potential of retrofitting a coal power plant to oxy-firing using CFD and process co-simulation. *Fuel Processing Technology*, 2015. **131**(Supplement C): p. 45-58.
150. Smith, J.D., et al., CFD-Based Optimization of a Flooded Bed Algae Bioreactor. *Industrial & Engineering Chemistry Research*, 2013. **52**(22): p. 7181-7188.
151. Kleijnen, J.P.C., Kriging metamodeling in simulation: A review. *European Journal of Operational Research*, 2009. **192**(3): p. 707-716.
152. Basheer, I.A. and M. Hajmeer, Artificial neural networks: fundamentals, computing, design, and application. *Journal of Microbiological Methods*, 2000. **43**(1): p. 3-31.
153. Sacks, J., et al., Design and analysis of computer experiments. *Statistical Science*, 1989. **4**(4): p. 409-423.
154. Jones, D.R., M. Schonlau, and W.J. Welch, Efficient global optimization of expensive black-box functions. *Journal of Global Optimization*, 1998. **13**(4): p. 455-492.
155. Wesolowski, M. and B. Suchacz, Artificial Neural Networks: Theoretical Background and Pharmaceutical Applications: A Review. *Journal of Aoac International*, 2012. **95**(3): p. 652-668.
156. Akkisetty, P.K., et al., Population Balance Model-Based Hybrid Neural Network for a Pharmaceutical Milling Process. *Journal of Pharmaceutical Innovation*, 2010. **5**(4): p. 161-168.
157. Looney, C.G., Advances in feedforward neural networks: demystifying knowledge acquiring black boxes. *IEEE Transactions on Knowledge and Data Engineering*, 1996. **8**(2): p. 211-226.
158. MATLAB, Neural Network Toolbox User's Guide, version 10.0 (R2017a). 2017: The Mathworks Inc.
159. Yan, Z., et al., Discrete element modelling (DEM) input parameters: understanding their impact on model predictions using statistical analysis. *Computational Particle Mechanics*, 2015. **2**(3): p. 283-299.

160. Metta, N., M. Ierapetritou, and R. Ramachandran, A multiscale DEM-PBM approach for a continuous comilling process using a mechanistically developed breakage kernel. *Chemical Engineering Science*, 2018. **178**: p. 211-221.
161. Galbraith, S.C., et al. *Flowsheet Modeling of a Continuous Direct Compression Tableting Process at Production Scale*. 2016.
162. Seo-Young Park, S.C.G., Huolong Liu, HaeWoo Lee, Bumjoon Cha, Zhuangrong Huang, Thomas O'Connor, Sau Lee, Seongkyu Yoon, Prediction of critical quality attributes and optimization of continuous dry granulation process via flowsheet modeling and experimental validation. *Powder Technology*, 2018. **330**: p. 461-470.
163. Boukouvala, F., et al., Computer-Aided Flowsheet Simulation of a Pharmaceutical Tablet Manufacturing Process Incorporating Wet Granulation. *Journal of Pharmaceutical Innovation*, 2013. **8**(1): p. 11-27.
164. Metta, N., et al., Model development and prediction of particle size distribution, density and friability of a comilling operation in a continuous pharmaceutical manufacturing process. *International Journal of Pharmaceutics*, 2018. **549**(1): p. 271-282.
165. Gabbott, I.P., F. Al Husban, and G.K. Reynolds, The combined effect of wet granulation process parameters and dried granule moisture content on tablet quality attributes. *European Journal of Pharmaceutics and Biopharmaceutics*, 2016. **106**: p. 70-78.
166. Miyamoto, Y., et al., Optimization of the granulation process for designing tablets. *Chemical & Pharmaceutical Bulletin*, 1998. **46**(9): p. 1432-1437.
167. Sandler, N. and D. Wilson, Prediction of Granule Packing and Flow Behavior Based on Particle Size and Shape Analysis. *Journal of Pharmaceutical Sciences*, 2010. **99**(2): p. 958-968.
168. Yajima, T., et al., Optimization of size distribution of granules for tablet compression. *Chemical & Pharmaceutical Bulletin*, 1996. **44**(5): p. 1056-1060.
169. Lophaven, S.N., H.B. Nielsen, and J. Søndergaard, *DACE: A MATLAB Kriging Toolbox, Version 2.0*. 2002.
170. Beale, M.H., M.T. Hagan, and H.B. Demuth, *Neural Network Toolbox User's Guide*. 2017.
171. Pantelides, C.C. and P.I. Barton, EQUATION-ORIENTED DYNAMIC SIMULATION CURRENT STATUS AND FUTURE PERSPECTIVES. *Computers & Chemical Engineering*, 1993. **17**: p. S263-S285.
172. Jin, Y., et al., Adaptive Sampling for Surrogate Modelling with Artificial Neural Network and its Application in an Industrial Cracking Furnace. *The Canadian Journal of Chemical Engineering*, 2016. **94**(2): p. 262-272.
173. Kohavi, R., A study of cross-validation and bootstrap for accuracy estimation and model selection, in *Proceedings of the 14th international joint conference on Artificial intelligence - Volume 2*. 1995, Morgan Kaufmann Publishers Inc.: Montreal. p. 1137-1143.
174. Wolpert, D.H., Stacked generalization. *Neural Networks*, 1992. **5**(2): p. 241-259.
175. Wang, Z.L. and M. Ierapetritou, A novel feasibility analysis method for black-box processes using a radial basis function adaptive sampling approach. *Aiche Journal*, 2017. **63**(2): p. 532-550.
176. Rogers, A., A. Hashemi, and M. Ierapetritou, Modeling of Particulate Processes for the Continuous Manufacture of Solid-Based Pharmaceutical Dosage Forms. *Processes*, 2013. **1**(2): p. 67.
177. Sampat, C., et al., A parallel unidirectional coupled DEM-PBM model for the efficient simulation of computationally intensive particulate process systems. *Computers & Chemical Engineering*, 2018. **119**: p. 128-142.
178. Šantl, M., et al., A compressibility and compactibility study of real tableting mixtures: the effect of granule particle size. 2012. **62**(3): p. 325.

179. De Leersnyder, F., et al., Breakage and drying behaviour of granules in a continuous fluid bed dryer: Influence of process parameters and wet granule transfer. *European Journal of Pharmaceutical Sciences*, 2018. **115**: p. 223-232.
180. Garcia, A.L., et al., A Monte Carlo simulation of coagulation. *Physica A: Statistical Mechanics and its Applications*, 1987. **143**(3): p. 535-546.
181. Wright, D.L., R. McGraw, and D.E. Rosner, Bivariate Extension of the Quadrature Method of Moments for Modeling Simultaneous Coagulation and Sintering of Particle Populations. *Journal of Colloid and Interface Science*, 2001. **236**(2): p. 242-251.
182. Marshall, C.L., P. Rajniak, and T. Matsoukas, Numerical simulations of two-component granulation: Comparison of three methods. *Chemical Engineering Research and Design*, 2011. **89**(5): p. 545-552.
183. Chaudhury, A., et al., An extended cell-average technique for a multi-dimensional population balance of granulation describing aggregation and breakage. *Advanced Powder Technology*, 2013. **24**(6): p. 962-971.
184. Vogel, L. and W. Peukert, Breakage behaviour of different materials - construction of mastercurve for the breakage probability. *Powder Technology*, 2003. **129**(1-3): p. 101-110.
185. Diemer, R.B. and J.H. Olson, A moment methodology for coagulation and breakage problems: Part 3—generalized daughter distribution functions. *Chemical Engineering Science*, 2002. **57**(19): p. 4187-4198.
186. Hill, P.J. and K.M. Ng, Statistics of multiple particle breakage. *AIChE Journal*, 1996. **42**(6): p. 1600-1611.
187. Aster, R.C., B. Borchers, and C.H. Thurber, *Parameter estimation and inverse problems*. 2018: Elsevier.
188. Westerhuis, J.A., T. Kourti, and J.F. MacGregor, Analysis of multiblock and hierarchical PCA and PLS models. *Journal of Chemometrics*, 1998. **12**(5): p. 301-321.
189. Gernaey, K.V., A.E. Cervera-Padrell, and J.M. Woodley, A perspective on PSE in pharmaceutical process development and innovation. *Computers & Chemical Engineering*, 2012. **42**: p. 15-29.
190. Verstraeten, M., et al., In-depth experimental analysis of pharmaceutical twin-screw wet granulation in view of detailed process understanding. *International journal of pharmaceutics*, 2017. **529**(1-2): p. 678-693.
191. Van Hauwermeiren, D., et al., On the modelling of granule size distributions in twin-screw wet granulation: Calibration of a novel compartmental population balance model. *Powder technology*, 2019. **341**: p. 116-125.
192. De Leersnyder, F., et al., Breakage and drying behaviour of granules in a continuous fluid bed dryer: Influence of process parameters and wet granule transfer. *European Journal of Pharmaceutical Sciences*, 2018. **115**: p. 223-232.
193. Ghijs, M., et al., Modeling of Semicontinuous Fluid Bed Drying of Pharmaceutical Granules With Respect to Granule Size. *Journal of Pharmaceutical Sciences*, 2019. **108**(6): p. 2094-2101.
194. Pantelides, C.C., et al., *Equation-Oriented Process Modelling Technology : Recent Advances & Current Perspectives*. 5th Annual TRC-Idemitsu Workshop, 2015(February).
195. Escotet Espinoza, M., *Phenomenological and residence time distribution models for unit operations in a continuous pharmaceutical manufacturing process*. 2018, Rutgers University-School of Graduate Studies.
196. Pitt, K., et al., The Material Tensile Strength of Convex-faced Aspirin Tablets. *Journal of pharmacy and pharmacology*, 1989. **41**(5): p. 289-292.
197. Engisch, W. and F. Muzzio, Using residence time distributions (RTDs) to address the traceability of raw materials in continuous pharmaceutical manufacturing. *Journal of pharmaceutical innovation*, 2016. **11**(1): p. 64-81.

198. Saltelli, A., et al., Global Sensitivity Analysis. The Primer. Vol. 304. 2008.
199. Cryer, S. and P. Scherer, Observations and process parameter sensitivities in fluid-bed granulation. *AIChE journal*, 2003. **49**(11): p. 2802-2809.
200. Iooss, B. and P. Lemaître, A review on global sensitivity analysis methods. *Uncertainty Management in Simulation-Optimization of Complex Systems*, in *Operations research/computer science interfaces series 59*. 2015, Springer US. p. 101-122.
201. Helton, J.C. and F.J. Davis, Latin hypercube sampling and the propagation of uncertainty in analyses of complex systems. *Reliability Engineering & System Safety*, 2003. **81**(1): p. 23-69.
202. Leperi, K.T., et al., 110th Anniversary: Surrogate Models Based on Artificial Neural Networks To Simulate and Optimize Pressure Swing Adsorption Cycles for CO₂ Capture. *Industrial & Engineering Chemistry Research*, 2019. **58**(39): p. 18241-18252.
203. Fernandes, F.A., Optimization of Fischer-Tropsch synthesis using neural networks. *Chemical Engineering & Technology: Industrial Chemistry-Plant Equipment-Process Engineering-Biotechnology*, 2006. **29**(4): p. 449-453.
204. Smith, J.D., et al., CFD-based optimization of a flooded bed algae bioreactor. *Industrial & Engineering Chemistry Research*, 2012. **52**(22): p. 7181-7188.
205. Agatonovic-Kustrin, S. and R. Beresford, Basic concepts of artificial neural network (ANN) modeling and its application in pharmaceutical research. *Journal of Pharmaceutical and Biomedical Analysis*, 2000. **22**(5): p. 717-727.
206. Chambers, M. and C.A. Mount-Campbell, Process optimization via neural network metamodeling. *International Journal of Production Economics*, 2002. **79**(2): p. 93-100.
207. Meireles, M.R.G., P.E.M. Almeida, and M.G. Simoes, A comprehensive review for industrial applicability of artificial neural networks. *IEEE Transactions on Industrial Electronics*, 2003. **50**(3): p. 585-601.
208. Kleijnen, J.P.C. and W.C.M.v. Beers, Application-driven sequential designs for simulation experiments: Kriging metamodeling. *Journal of the Operational Research Society*, 2004. **55**(8): p. 876-883.
209. Boukouvala, F. and M.G. Ierapetritou, Feasibility analysis of black-box processes using an adaptive sampling Kriging-based method. *Computers & Chemical Engineering*, 2012. **36**: p. 358-368.
210. Quiñonero-Candela, J. and C.E. Rasmussen, A unifying view of sparse approximate Gaussian process regression. *Journal of Machine Learning Research*, 2005. **6**(Dec): p. 1939-1959.
211. Liu, H., Y.-S. Ong, and J. Cai, A survey of adaptive sampling for global metamodeling in support of simulation-based complex engineering design. *Structural and Multidisciplinary Optimization*, 2018. **57**(1): p. 393-416.
212. Lophaven, S.N., et al., A matlab kriging toolbox. Technical University of Denmark, Kongens Lyngby, Technical Report No. IMM-TR-2002-12, 2002.
213. Rumelhart, D.E., G.E. Hinton, and R.J. Williams, Learning representations by back-propagating errors. *Cognitive modeling*, 1988. **5**(3): p. 1.
214. Hornik, K., M. Stinchcombe, and H. White, Multilayer feedforward networks are universal approximators. *Neural Networks*, 1989. **2**(5): p. 359-366.
215. Burden, F. and D. Winkler, Bayesian regularization of neural networks, in *Artificial neural networks*. 2008, Springer. p. 23-42.
216. Eason, J. and S. Cremaschi, Adaptive sequential sampling for surrogate model generation with artificial neural networks. *Computers & Chemical Engineering*, 2014. **68**: p. 220-232.
217. Sasena, M.J., P. Papalambros, and P. Goovaerts, Exploration of metamodeling sampling criteria for constrained global optimization. *Engineering optimization*, 2002. **34**(3): p. 263-278.

218. Amine Bouhlef, M., et al., Efficient global optimization for high-dimensional constrained problems by using the Kriging models combined with the partial least squares method. *Engineering Optimization*, 2018. **50**(12): p. 2038-2053.
219. Metta, N., et al., Dynamic Flowsheet Model Development and Sensitivity Analysis of a Continuous Pharmaceutical Tablet Manufacturing Process Using the Wet Granulation Route. *Processes*, 2019. **7**(4): p. 234.
220. Escotet-Espinoza, M.S., Cathy Pereira, G.,D. Román-Ospino, A., Muzzio, F., Ierapetritou, M.,. Feeder Characterization and Model Development Accounting for Incoming Material Properties. in *AICHe Annual Meeting*. 2017. Minneapolis, MN.
221. Van Hauwermeiren, D., et al., On the modelling of granule size distributions in twin-screw wet granulation: Calibration of a novel compartmental population balance model. *Powder Technology*, 2019. **341**: p. 116-125.
222. Process Systems Enterprise, gFormulatedProducts. 1997-2019.
223. Barrasso, D., et al., A multi-scale, mechanistic model of a wet granulation process using a novel bi-directional PBM–DEM coupling algorithm. *Chemical Engineering Science*, 2015. **123**: p. 500-513.